TiO_2 LOADED ON REDUCED GRAPHENE OXIDE NANOSHEETS AS EFFICIENT ELECTRODES IN DYE-SENSITIZED SOLAR CELL

LOW FOO WAH

INSTITUTE OF GRADUATE STUDIES
UNIVERSITY OF MALAYA
KUALA LUMPUR

2018

TiO_2 LOADED ON REDUCED GRAPHENE OXIDE NANOSHEETS AS EFFICIENT ELECTRODES IN DYE-SENSITIZED SOLAR CELL

LOW FOO WAH

THESIS SUBMITTED IN FULFILMENT OF THE REQUIREMENTS FOR THE DEGREE DOCTOR OF PHILOSOPHY

INSTITUTE OF GRADUATE STUDIES
UNIVERSITY OF MALAYA
KUALA LUMPUR

2018

UNIVERSITY OF MALAYA
ORIGINAL LITERARY WORK DECLARATION

Name of Candidate: LOW FOO WAH

Matric No: HHC 130013

Name of Degree: Doctor of Philosophy (Science)

Title of Thesis: TiO_2 Loaded on Reduced Graphene Oxide Nanosheets as Efficient Electrodes in Dye-Sensitized Solar Cell

Field of Study:

I do solemnly and sincerely declare that:

(1) I am the sole author/writer of this Work;
(2) This Work is original;
(3) Any use of any work in which copyright exists was done by way of fair dealing and for permitted purposes and any excerpt or extract from, or reference to or reproduction of any copyright work has been disclosed expressly and sufficiently and the title of the Work and its authorship have been acknowledged in this Work;
(4) I do not have any actual knowledge nor do I ought reasonably to know that the making of this work constitutes an infringement of any copyright work;
(5) I hereby assign all and every rights in the copyright to this Work to the University of Malaya ("UM"), who henceforth shall be owner of the copyright in this Work and that any reproduction or use in any form or by any means whatsoever is prohibited without the written consent of UM having been first had and obtained;
(6) I am fully aware that if in the course of making this Work I have infringed any copyright whether intentionally or otherwise, I may be subject to legal action or any other action as may be determined by UM.

Candidate's Signature   Date:

Subscribed and solemnly declared before,

Witness's Signature   Date:

Name:

Designation:

TIO_2 LOADED ON REDUCED GRAPHENE OXIDE NANOSHEETS AS EFFICIENT ELECTRODES IN DYE-SENSITIZED SOLAR CELL

ABSTRACT

The formation of graphene oxide (GO) and reduced graphene oxide (rGO) nanosheet are a vital two dimensional (2D) material for highly efficient in dye-sensitized solar cell (DSSC) application. Comprehensive investigations on different parameters were conducted in order to control lateral size of nanosheet. Highly carbon content and thin film of rGO nanosheet in thickness controlled were successfully synthesized under 72 h and 1200 rpm, respectively. In specific, the large production and thin film of rGO nanosheet (≈46 nm) was achieved under high speed of 1200 rpm and 72 h reaction time. Continuous efforts have been exerted to further improve the power conversion efficiency (PCE) of DSSC performance by incorporating an optimum content of Titanium Dioxide (TiO_2) with rGO nanosheet using one-step hydrothermal and advanced implantation techniques in order to facilitate the injected electrons from N719 dye to the conduction band of TiO_2 and rGO based on its Fermi Level. It was found that optimum TiO_2 content of 0.3% incorporated with rGO nanosheet via one-step hydrothermal technique established well Ti-O-C bonds and achieved photocurrent density of ≈28.36 mA/cm^2 with PCE ≈7.20%. However, another useful ion implantation technique was applied which Ti^{3+} ions were sputtered onto rGO nanosheet with sputtering duration at 40s and lastly achieved the maximum PCE ≈8.78%. Herein, the higher performance of TiO_2-rGO nanocomposite (NC) as photoanode in DSSC application with advanced implantation technique than one-step hydrothermal technique (improved of 3.17%). These findings revealed that the Ti^{3+} ions species have been modified by rGO surface and even its lattice by high applied power (advanced implantation technique). Furthermore, the electron transfer rate was also noted to be the fastest due to the highest availability of the carbon-atom vacancy holes for Ti^{3+} replacement. On top of that, it may assigned that Ti^{3+} ion was fully loaded onto rGO nanosheet leading to the highest interactions with the O-H functional group in NC or Ti^{3+} could react with the epoxide or phenolic groups in rGO forming the Ti-O-C/Ti-O-Ti bonds. Besides, the incorporated of rGO with Ti^{3+} ions by calcination reaction (one-step hydrothermal technique) was gained lower PCE as compared with advanced implantation technique due to the higher electron-hole pairs charge recombination and thus increases of interior resistance. However, the excess incorporation of Ti^{3+} ions content (0.4 wt%, 0.5 wt%, 200 W, 250 W, 60s) onto rGO lattice leading poor PCE attributed to the over photocatalytic reation occurred leaving extra holes on the counter electrode and hence increased the charge transport resistance at the KI electrolyte/N719 dye/rGO/TiO_2 interfaces.

Keywords: Reduced Graphene Oxide (rGO), Titanium Dioxide (TiO_2), Dye-Sensitized Solar Cell (DSSC), Advanced Implantation Technique

TIO_2 DIMUATKAN KE ATAS KEPINGAN NANO GRAFIN OKSIDA TERTURUN SEBAGAI ELEKTROD CEKAP DALAM SEL SURIA TERPEKA/SENSITIF PEWARNA

ABSTRAK

Pembentukan grafin oksida (GO) dan kepingan nano grafin oksida terturun (rGO) merupakan bahan dua dimensi (2D) penting yang berkecekapan tinggi dalam aplikasi Sel Suria Terpeka/Sensitif Pewarna (DSSC). Penyiasatan komprehensif pada parameter yang berbeza telah dilaksanakan bagi mengawal saiz sisi kepingan nano. Kandungan karbon yang tinggi dan kawalan ketebalan filem nipis kepingan nano rGO telah berjaya dihasilkan masing-masing pada 72 jam dan 1200 putaran seminit (rpm). Secara khusus, pengeluaran besar dan filem nipis kepingan nano rGO ($\approx$46 nm) telah dicapai pada kelajuan tinggi 1200 rpm dan masa tindak balas 72 jam. Usaha berterusan telah dilaksanakan bagi meningkatkan prestasi DSSC dalam kecekapan penukaran kuasa (PCE) dengan menggabungkan kandungan optima Titanium Dioksida (TiO_2) dengan kepingan nano rGO menggunakan teknik hidrotermal satu-langkah dan teknik implantasi/penanaman termaju untuk memudahkan penyuntikan elektron dari Pewarna N719 ke jalur konduksi TiO_2 dan rGO berdasarkan Aras Fermi. Telah didapati bahawa kandungan TiO_2 optimum sebanyak 0.3% yang digabungkan dengan kepingan nano rGO melalui teknik hidrotermal satu-langkah telah membentuk ikatan Ti-O-C yang baik dan mencapai ketumpatan fotoarus $\approx$ 28.36 mA/cm^2 dengan PCE $\approx$ 7.20. Walau bagaimanapun, teknik lain juga turut digunakan iaitu teknik implantasi/penanaman ion yang mana ion Ti^{3+} dipercit ke atas kepingan nano rGO dengan tempoh percitan selama 40 saat dan akhirnya mencapai PCE maksimum $\approx$8.78%. Seterusnya, penghasilan fotoanod komposit nano (NC) TiO_2-rGO daripada teknik implantasi/penanaman termaju menunjukan prestasi yang lebih tinggi dalam aplikasi DSSC berbanding teknik penghasilan hidrotermal satu-langkah (peningkatan sebanyak 3.17%). Penemuan ini mendedahkan bahawa spesies ion Ti^{3+} dan kekisinya telah diubahsuai oleh permukaan rGO dengan menggunakan kuasa yang tinggi (teknik implantasi/penanaman termaju). Tambahan pula, kadar pemindahan elektron juga mencatatkan bacaan terpantas kerana terdapat ketersediaan yang tinggi bagi kekosongan lubang atom karbon untuk penggantian Ti^{3+}. Di samping itu, didapati ion Ti^{3+} telah dimuat sepenuhnya ke atas kepingan nano rGO dan ini membawa kepada interaksi tertinggi dengan kumpulan berfungsi O-H dalam NC atau Ti^{3+} boleh bertindak balas dengan kumpulan epoksida atau fenolik dalam rGO bagi membentuk ikatan Ti-O-C/Ti-O –Ti. Selain itu, gabungan rGO dengan ion Ti^{3+} oleh reaksi kalsinasi (teknik hidrotermal satu-langkah) memberi PCE yang lebih rendah berbanding dengan teknik implantasi/penanaman termaju kerana penggabungan semula caj pasangan elektron-lubang yang lebih tinggi dan sekaligus meningkatkan rintangan dalaman. Walau bagaimanapun, penambahan secara berlebihan kandungan ion Ti^{3+} (0.4% peratus berat, 0.5% peratus berat, 200 W, 250 W, 60saat) ke atas kekisi rGO menyebabkan penghasilan PCE yang lemah disebabkan oleh reaksi fotopemangkinan, membawa kepada lubang tambahan pada elektrod kaunter dan seterusnya meningkatkan rintangan pengangkutan caj pada antaramuka elektrolit KI/pewarna N719/rGO/TiO2.

Kata Kunci: Grafin Oksida Terturun (rGO), Titanium Dioksida (TiO_2), Sel Suria Terpeka/Sensitif Pewarna (DSSC), Teknik Implantasi/Penanaman Termaju

ACKNOWLEDGEMENTS

First and foremost, I would like to express my sincere gratitude to my supervisors, Dr. Lai Chin Wei, Prof. Dr. Sharifah Bee Abdul Hamid, and Assoc. Prof. Dr. Juan Joon Ching for their motivation, patience, and immense knowledge support throughout my PhD research study journey.

In addition, I would like to convey grateful appreciation to all the fellow colleagues and teammates in NANOCAT research centre, for their stimulating discussions and always willing to lend me a hand during in difficult moment. Without their kind assistance this research would not be possible to complete smoothly. In particularly, I would like to thank Ministry of Higher Education Malaysia provided me the MyPhD scholarship neither in funding of entire program nor allowance financial support to gain the opportunity to inevitably broaden my knowledge and perspective.

Last but not least, I would like to thank my family and lovely wife for spiritually support me throughout my thesis writing to accomplish my final stage of full time PhD research program.

Thank You.

TABLE OF CONTENTS

CHAPTER 5: ONE-STEP HYDROTHERMAL TECHNIQUE OF TiO_2-rGO NANOCOMPOSITE IN DSSCS

CHAPTER 6: ION-IMPLANTATION TECHNIQUE OF TiO_2-rGO NANOCOMPOSITE IN DSSCS

CHAPTER 7: CONCLUSION..171

LIST OF FIGURES

LIST OF TABLES

LIST OF SYMBOLS AND ABBREVIATIONS

2D : 2-Dimensional

AFM : Atomic Force Microscopy

CO_2 : Carbon Dioxide

CVD : Chemical Vapour Deposition

CB : Conduction Band

Jmp : Current Density at Maximum Power

N719 : Di-tetrabutylammonium cis-bis(isothiocyanato)bis(2,2’-bipyridyl-4,4’-dicarboxylato)ruthenium(II)

E_0 : Direct Interband Gap

DSSCs : Dye-Sensitized Solar Cells

EIS : Electrochemical Impedance Spectroscopy

EDX : Energy Dispersion X-ray

FESEM : Field Emission Scanning Electron Microscopy

FF : Fill Factor

FTO : Fluorine-Doped Tin Oxide Glass

FTIR : Fourier Transform Infrared Spectroscopy

V_g : Gate Voltage

GO : Graphene Oxide

HRTEM : High-Resolution Transmission Electron Microscopy

Pin : Input Power

I^- : Iodide

Pmax : Maximum Power

NC : Nanocomposite

NS : Nanosheets

Voc : Open Circuit Voltage

J-V	:	Photocurrent density-voltage
PL	:	Photoluminescence Spectroscopy
PCE	:	Power Conversion Efficiency
RF	:	Radio Frequency
rGO	:	Reduced Graphene Oxide
rpm	:	Rotation Per Minute
η_D	:	Refractive Index
SEM	:	Scanning Electron Microscopy
Jsc	:	Short Circuit Current Density
TPV	:	Thermo Photovoltaic
3D	:	Three Dimensional
Ti	:	Titanium
Ti^{3+}	:	Titanium (III) Ion
TiO_2	:	Titanium Dioxide
I_3^-	:	Tri-iodide
UV-Vis	:	Ultraviolet-Visible Spectroscopy
VB	:	Valence Band
Vmp	:	Voltage at Maximum Power
XRD	:	X-ray Diffraction
XPS	:	X-ray Photoelectron Spectroscopy
0D	:	Zero Dimensional

CHAPTER 1: INTRODUCTION

1.1 Introduction

Renewable solar cell energy is a key target for sustainable energies development, which are inexhaustible and non-polluting for energy system. Dye-sensitized solar cells (DSSCs) is one of the promising prospects for efficient renewable resources. In order to make the DSSCs to the point of commercial readiness and viability in terms of performance and cost, substantial research on the development of high efficient DSSCs system is necessary. Recently, nanocrystalline porous Titanium Dioxide (TiO_2) has emerged as photoanode in DSSCs due to its strong photocatalytic activity. However, the wide bandgap of TiO_2 affect the higher electron-hole pairs charge recombination. Recent studies have indicated that reduced graphene oxide (rGO) is a relatively novel material with unique properties that could apply in DSSCs as efficient photoanode. rGO is a 2D material and also known as zero band gap material with monolayer with hexagonal carbon network which provides outstanding electrical, optical, high specific surface area, and incredibly high mobility of charge carriers. Continuous efforts have been exerted to further enhance the electronic properties of rGO by loading an optimum content of photocatalyst to gain higher power conversion efficiency (PCE) of DSSCs performance. In contrast, synthesized rGO material possess poor photocatalytic properties and structural lattice defects. Since the synthesized rGO enable to form with few layers of graphene, electron transfer/path in the vertical direction against layers also decreases (Benson et al., 2014). Therefore, the hybridization between TiO_2 and rGO as photoanode in DSSCs is needed to improve the photocatalytic performance of TiO_2 in terms of migration of photo-induced charge carriers and its electrons transportation rate from TiO_2 to rGO nanosheets (NS) (Zhu et al., 2012). Furthermore, rGO could effectively suppresses the recombination losses and leaving more hole carriers within the TiO_2 lattice in this binary hybrid photoelectrode (Liang et al., 2010). In this chapter, introduction section begins by illustrating the essentials of TiO_2 and rGO material as selected candidate to support the high mobility charge carriers transport, as well as TiO_2 incorporation with rGO to improve PCE of DSSCs performance. This chapter will cover research background, problem statements, research objective, scope of research, and outline of the entire thesis.

1.2 Research Background

Recently, the global need for energy coupled depletion is ever increasing. The emergence of energy demands poses a serious threat to the conventional energy sources (oil, gas, coal) due to growth in the world's population and the techno-economic growth of the countries especially developing countries (Armaroli and Balzani, 2007). The energy crisis is getting worst by major concerns about global warming from greenhouse gas emission due to increasing of fossil fuels consumption. The global warming from greenhouse effect resulting probably causes erratic weather incidents like floods, draughts, melts of ice/snow and rises of sea level (Cai et al., 2014; Coumou and Rahmstorf, 2012).

One of the steps taken by many countries to aid the earth and minimizing environmental problems, development of clean and green alternative sustainable energy is needed (Kothari et al., 2010; Panwar et al., 2011). It seems that sustainable development is a strategic goal of modern society reflecting contemporary demand for economic, social, political and environmental development towards the ambition point of a low-carbon future (Bridge et al., 2013). Therefore, change-readiness capability for generating green and renewable energy resource has been the passion for scientists, which can provide us energy in sustainable manner (Mitchell and Walinga, 2017). The finding of alternative clean energy source is crucial in leading a high quality of life, which is in harmony with nature.

The best option of clean external source is sun's energy, which is infinite and non-hazardous source to obey all the alternative energy strategies (Asif and Muneer, 2007; Panwar et al., 2011). The clean and efficient source of sun energy able to convert the natural renewable energy forms into a controllable and useful energy form such as electricity fossil fuel free like hydrogen consumption is a promising solution to the energy challenge in this 21st century (Larcher and Tarascon, 2015; Oh et al., 2010). It remarkable that sustainable development is a strategic goal of modern society reflecting contemporary demand for economic, social, political and environmental development.

Since the solar power could rapidly provide a total yearly human energy consumption when harvesting by the solar irradiation within 10 mins onto the Earth's surface, therefore, it is considered to be one of the best sustainable energies for future generations (Yum et al., 2011). To date, the photovoltaic technology has been dominated by solid-state junction devices such as silicon, amorphous or crystalline materials based solar cells, which are readily available and the renewable resources from the semiconductor industry. However, silicon based solar cells is required a high manufacturing cost, high temperature and vacuum processes (Jeon et al., 2014; Taguchi et al., 2014). Hence, the prominent of third generation solar cells with inorganic solid-state junction has been developed to overcome drawbacks of the previous photovoltaic technology, like low-cost and simple integration of DSSCs (Grätzel, 2001; Hou et al., 2010; Maeda et al., 2010).

In 1991, Professor Grätzel is first reported that a working DSSCs with nanoporous film into dye-derived wide band semiconductor and a breakthrough with high PCE achievement (O'regan and Grätzel, 1991). DSSCs also remarkable as energy conversion device, which is able to convert solar energy into electricity (Grätzel, 2003). In 2011, an astonishing achievement of PCE with 12.3% was recorded by novel dye modification of

YD2-o-C8 with Y123 in DSSCs (Yella et al., 2011). This breakthrough was attracted numerous researchers in order to explore a new modification of materials.

To date, rGO has attracted tremendous interest as a great candidate in DSSCs photoanode research due to the fast electron transfer ability, good transparency, and high Young's modulus. As addition, rGO NS also can apply in surface modification of materials like TiO_2 to reduce the charge recombination and benefit the improvement of photoanode thus resulting PCE of DSSCs (Guo et al., 2015; Huang et al., 2012a; Li et al., 2011d; Wu et al., 2013; Zhu et al., 2010). Besides, the assistant of rGO NS to the TiO_2 also could increase the dye absorption, which is increased the light harvesting and encountered the increased in photocurrent (Sun et al., 2010b; Tang et al., 2010). However, an obvious hindrance to the widespread use of rGO to the TiO_2 as photoanode did not sense the change in dye absorption or some researchers proved that recorded of higher photocurrent for the lower absorption (Chen et al., 2012; Tang and Hu, 2012). In other words, factor of dye absorption is definitely independent with the photocurrent. The large increased in photocurrent (~29%) can be done by solvothermally reduce the rGO and incorporation with TiO_2 and absorbed 44% more light at the dye's (N719) absorption peaks within ~370 – 500 nm (Durantini et al., 2012). Making intuitive guesses on their properties are more or less impossible, and a focused research on the area is a very challenging task.

To get a better photovoltaic performance under ultraviolet and visible light range, the incorporation of rGO in the TiO_2 has received much more attention in the literatures recently due to the interesting and synergistic features such as more light harvest, enhanced dye-absorption capacity, and more efficient separation of photogenerated transport (e.g. electron-hole pairs) within TiO_2 surface and further increase the active charge carriers at photoanode part. In this manner, coupling of semiconductor materials

($rGO-TiO_2$ composite) is necessary to form heterojunction to ensure that the electrons and holes are separated via interfacial charge transfer (He et al., 2015).

1.3 Problem Statements

Global warming is a critical topic for human concerned where the large-scale emission of carbon dioxide (CO_2) and expansion of the greenhouse effect. The excess of CO_2 in atmosphere and consumption of non-renewable energy sources (petroleum, natural gas, coal, fossil fuels, and other minerals) resulting blanket, trapping heat radiating from Earth toward space and hence warming the planet (Yamasaki, 2003). Continuous efforts have been exerted to further reduce the emissions of CO_2 by carbon capture and geological sequestration technologies but required extraneous energy input (Hasaneen et al., 2014; Tan et al., 2013b). In order to resolve such energy and environmental problems, photovoltaic technology has been intensively explored. It is an ideal energy source as compared to wind, bioenergy and geothermal because of its natural friendly and endless supply to the Earth. According to the International Energy Agency (IEA), 20 % of the world's energy supply comes from solar energy in 2050 and expected to increase up 60 % in 2100 (Liu et al., 2013b).

Henceforth, the development of renewable energy with fossil fuels-free is a promising alternative way to address problems in global matter like Wind (Pena et al., 1996), Solar Thermal (Tritt et al., 2008), Biomass (Hoogwijk et al., 2003), Hydropower (Sipahutar et al., 2013) as well as photovoltaics (Araújo and Martí, 1994) energy have been widely exploited. The converting of natural renewable energy like sun resource into controllable and useful energy where its everlasting, potential damage/pollution free to the environment, large source of energy, and also clean energy source. However, the production cost, device sizes, stability, repeatability, reproducibility, and also its efficiencies yet to approach the green and sustainable technology in future (Raj and Prasanth, 2016).

Rather than developing new sensitizers, the rGO (carbon material) is another approach to improve the electron migration within the film. The rGO has unique properties such as electronic conductivity (2000 S/cm), high surface area (>2600 m^2/g), high electron mobility (15,000 cm^2/Vs), and good mechanical properties with Young's modulus of 1 TPa (Bo et al., 2012; Luan et al., 2013; Singh et al., 2011; Wang et al., 2012a). In specific, the unique combination of high electrical conductivity and optical transparency of rGO has emerged as the leading candidate in DSSCs application (Gwon et al., 2011; Huang et al., 2012a; Machado and Serp, 2012; Zhu et al., 2010). A single sheet of rGO is a superior electron mobility and delocalised over high specific surface area, and lower sheet resistance, which means that the charge scattering does not occur. The zero-bandgap of rGO has caused the rate of recombination process of electron-hole pairs to be almost instantaneous on the TiO_2 surface and thus enhance the photocatalytic activity (Gwon et al., 2011; Huang et al., 2012a; Machado and Serp, 2012; Zhu et al., 2010). Generally, rGO can be assembled into a film electrode with low roughness. However, in practical, rGO films produced via solution processing such as conventional Hummer's method contains structural defects and grain boundaries that act as recombination centers and decrease the electrical conductivity of the material significantly (Blanita and Lazar, 2013; Vicarelli et al., 2015; Yang et al., 2010b). In addition, rGO only can absorb 2.3% of visible light from the solar illumination (Huang et al., 2012a; Machado and Serp, 2012). Thus, the thicker or multilayer of rGO to obtain desired resistance is needed. At last but not least, to bring the DSSCs based rGO photoanode in commercialised purpose, the large scale production should be emphasized. However, the difficulty of peeling of pyrolytic rGO process is very tough (Sur, 2012).

To overcome the problems above, continuous efforts have been exerted to further improve the rGO textural and electronic properties by loading an optimum content of TiO_2 as photocatalyst for enhancing of photocatalytic activity in DSSCs (Momeni, 2016; Park et al., 2013). As the paradigm in this respect, TiO_2-rGO as photoanode has become a potential candidate for high efficient DSSCs in order to improve the photogenerated electron transport (Kusumawati et al., 2014; Song et al., 2011).

The high efficiency of TiO_2-rGO as a photoanode in a DSSCs application requires a suitable architecture such as nano-scale materials (rGO NS), higher crystallinity, and low interfacial/sheets resistance that minimizes electron loss at nanostructure connections and maximizes photon absorption (Liang et al., 2010). In order to improve the immigration of photo-induced charge carriers, the dopant effect and surface modification of materials has to be revealed to increase the PCE performance of DSSCs under solar illumination.

1.4 Research Objective

The objectives of this study are listed as follow:-

1. To study the integral properties (e.g., functional groups, aspect ratio, crystal structure, optical properties, and morphology) of pure rGO NS based electrical characteristic.
2. To study the formation of TiO_2-rGO NC using one-step hydrothermal technique and ion implantation technique.
3. To study the DSSCs photovoltaic characteristics (e.g., photocurrent density, fill factor, PCE, and EIS) of TiO_2-rGO NC based photoanode in DSSCs application.

1.5 Scope of Research

Improved Hummer's method is the most feasible method for synthesis of GO and rGO reduce by the chemical process in order to obtain large lateral size. Thus, lateral size with controlled dimensional features, physical and chemical properties of rGO are essential factors to explore prior to incorporation of rGO with other semiconductors composite.

Since the rGO material as photoanode act as lattice defects and grain boundaries, therefore, in the present study, the formation of rGO NS in TiO_2 was investigated. The dopant effect of the TiO_2 on the rGO (e.g., concentration) were studied in order to understand its integral properties for high efficient photoanode in DSSCs. Moreover, formation of TiO_2-rGO NC by one-step hydrothermal process is relatively enhance the dye absorption, improvements of charge separation electron-hole pairs further improve the photo-induced electrons transport. Among the various preparation techniques available, hydrothermal by one-step technique is a simple, low-cost, shorter time production, higher crystallinity, and high uniformity coating method for the preparation of TiO_2-rGO NC photoanode. Furthermore, the use of TiO_2-rGO NC photoanode was found to be beneficial in addressing recombination of electron-hole pairs and resulting low photocurrent density problems. The growth mechanism between rGO and TiO_2 was intensively discussed.

The next study are conducted the coupling mechanism of TiO_2-rGO NC via radio frequency (RF) sputtering technique to facilitate the Ti^{3+} species by the impact of high-energy ions accelerated with high voltage in shorter time on rGO surface. The advantages of supply this implantation technique are aimed to obtain homogeneous ion current distribution across the target surface, and are often used to construct uniform, well crystallized, and large-area composite films. The thin film thickness, composition and structure can be easily controlled by adjusting the sputtering power from target to the substrate. To the best of our knowledge, incorporation of TiO_2-rGO NC using radio frequency (RF) sputtering technique (ion implantation technique) can be considered as pioneer work where the Ti^{3+} ions were implanted onto rGO nanostructure surface and even lattice by sputtering power. Thus, a comprehensive study was conducted to optimize the photosensitivity (e.g., sputtering power) to obtain the desired PCE, resulting in best DSSCs performance.

In physical properties aspect, the surface morphologies and lattice of the rGO-TiO_2 were viewed by scanning electron microscopy (SEM), field emission scanning electron microscopy (FESEM), and high-resolution transmission electron microscopy (HRTEM), respectively. Surface topology of the sample was carried out by atomic force microscopy (AFM). The elemental analysis was determined with energy dispersion X-Ray (EDX). Besides, X-Ray diffraction (XRD) was used to investigate the crystallinity and phase transition of the sample. The ultraviolet-visible spectroscopy (UV-Vis) was used to investigate the optical properties of samples such as band gap energy observation. In chemical properties aspect, the functional groups of sample was determined by fourier transform infrared spectroscopy (FTIR) whereas the phase formation of sample was determined by Raman spectroscopy and photoluminescence spectroscopy (PL). The last characterization of sample was using X-Ray photoelectron spectroscopy (XPS) to determine the element compositions and chemical state of the sample. In DSSCs application, the PCE was measured by Autolab instrument whereas the electrochemical characterization and interfacial electrical properties were determined using electrochemical impedance spectroscopy (EIS).

1.6 Outline of Thesis

This thesis is organized in seven chapters consecutively. In Chapter 1, the introduction of this research work, research objectives, problem statement, the scope of research as well as thesis overview are presented. In Chapter 2, a summary of selected photoanode materials are reviewed based on properties, preparations approaches, mechanism of materials as working electrodes, as well as photovoltaic applications. This section are emphasize in research fundamentals and their direction path from scientific literature as pointer in order to accomplish every objectives in this research project. Regarding to this research project, it is organized compactly in an article-based format. Subsequently, the details of research methodology work were discussed in Chapter 3. In Chapter 4, synthesis and characterization of GO and rGO are presented as well as electrical characteristic was carried up. In Chapter 5, effect of TiO_2-rGO NC formation in different concentration and the summarized findings are presented to enhance the PCE of DSSCs. Consequently, the effect of applied power of Ti ion implanted and related findings were summarized and presented in Chapter 6. Chapter 7 summarizes the conclusion of the study as well as several suggestions and recommendations for the future work. Such finding will aid in building the fundamentals of photovoltaic solar in the development of photoanode based TiO_2-rGO NC for sustainable energy system.

CHAPTER 2: LITERATURE REVIEW

2.1 Introduction

Nowadays, public concern about the environmental impact of coal based energy, which have given rise to the urgent need of fostering development in the area of renewable energies, which are inexhaustible and non-polluting. The carbon-free sources of energy such as hydropower, solar thermal, biomass, and solar energy are one of the most promising prospects for efficient renewable resources (Schiermeier et al., 2008). Among all the renewable energy technologies, photovoltaic technology considered as most promising alternative energy due to its capable to generate electricity from the most reliable source of sun energy. To bring solar energy production in terms of performance and cost, substantial research on the development of sustainable technology is necessary.

Generally, solar cells technology has three core generations. Silicon (Si) wafer based is categorized as the first generation or conventional solar cell. The second generation is thin film solar cell whereas the third generation is the latest emerging solar cell technologies like multi-junction, organic, dye-sensitized (DSSCs), GaAs and thermo-photovoltaics (TPV) having the conversion efficiencies beyond the theoretical Schokley Queisser limit (Green et al., 2015). Specifically, Table 2.1 tabulates the solar cells performance, while Figure 2.1 displays the solar photovoltaic technologies in terms of conversion efficiency. It is noteworthy that the multijunction solar panels composed of III-V and silicon material shows the highest efficiency and better stability compared to that of those in the market. However, these multijunction solar panels have the limitations in terms of (i) huge size, i.e., 28 cm-squared with four-junction hybridization, (ii) costly materials used for production, (iii) fragile panel, and (iv) complex manufacturing as compared to that of other types of solar cells. On top of multijunction solar panels, Si-based solar cells, thin films solar cells, and III-V solar cells technologies have also received numerous attractions and attentions. However, these solar cells also suffer from shortcomings in terms of relatively high production cost, complex inner working panel, and time consuming.

Table 2.1: Performance of solar cell measured under AM 1.5 spectrum (1000 W/m^2)

Classification	Active Area, A (cm^2)	Open Circuit Voltage, V_{oc} (V)	Short Circuit Current Density, J_{sc} (mAcm^{-2})	Fill Factor, FF (%)	PCE, η (%)	Reference
Mono Si	180.43	0.7438	42.25	83.8	26.3 ±0.5	(Corporation, 2016)
Poly Si	242.74	0.6678	39.80	80.0	21.3 ±0.4	(Zhang et al., 2015)
Amorphous Si	1.001	0.896	16.36	69.8	10.2 ±0.3	(Matsui et al., 2013)
III-V	0.9927	1.122	29.68	86.5	28.8 ±0.9	(Kayes et al., 2011)
CdTe	1.0623	0.8759	30.25	79.4	21.0 ±0.4	("First Solar Builds the Highest Efficiency Thin Film PV Cell on Record,")
CIGS	0.9927	0.757	35.70	77.6	21.0 ±0.6	(Release, 2014)
DSSCs	1.005	0.744	22.47	71.2	11.9 ±0.4	(Komiya et al., 2011)
Organic	0.992	0.780	19.30	74.2	11.2 ±0.3	(Mori et al., 2015)
Perovskite	0.9917	1.104	24.67	72.3	19.7 ±0.6	(Yang et al., 2015)

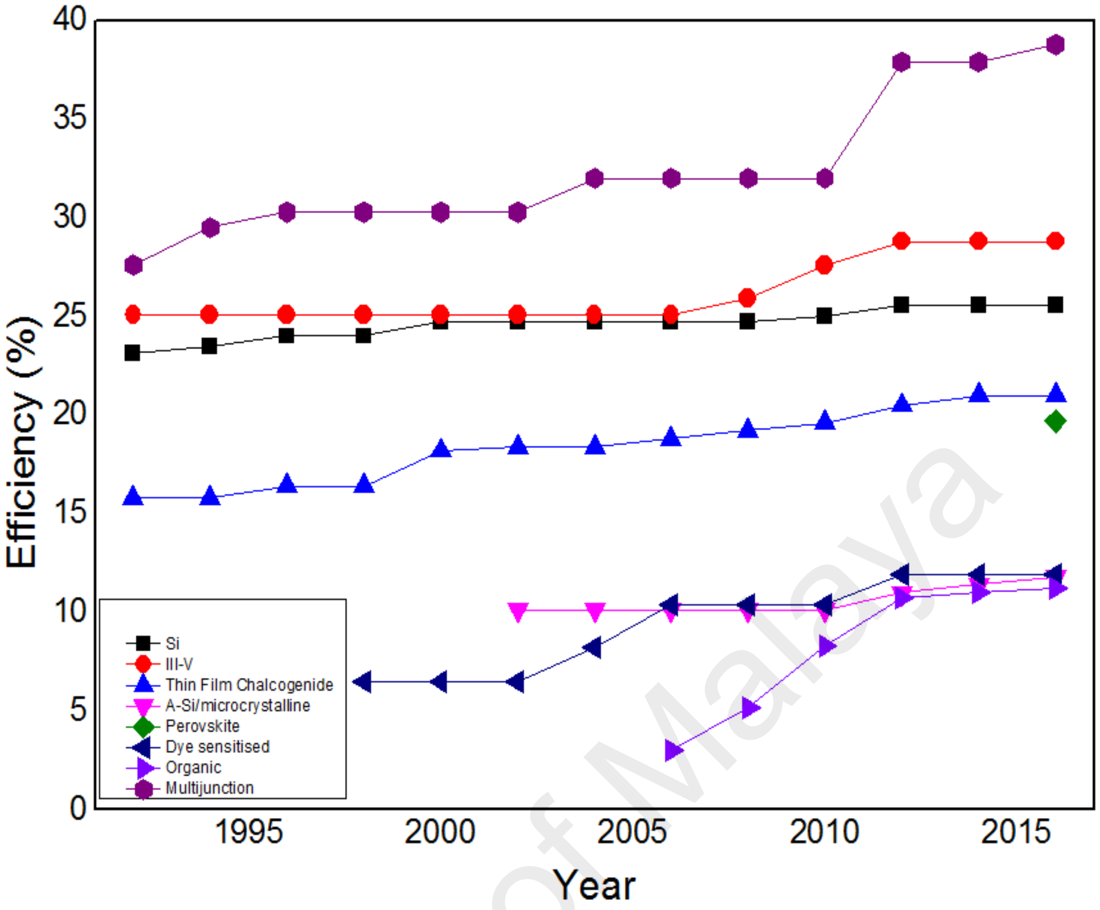

Figure 2.1: Solar cells efficiency reported based on several technologies

Recent studies have indicated that DSSCs has emerged as the leading candidate as third generation photovoltaic technologies because of its tunable optical properties, ease of fabrication, and cost effectiveness. Basically, mesoporous TiO_2 semiconductor which is commonly used as a photoanode in a DSSCs (Kumari et al., 2016). However, the practical photovoltaic of TiO_2 semiconductor have wide band gap energy (~3.2 eV) and recombination of photogenerated electron-holes pairs (Hamadanian and Jabbari, 2011). In order to further improve the photo conversion efficiency (PCE) performance of DSSCs, reduced graphene oxide (rGO) should introduce so that can minimizes band gap energy and maximizes dye absorption capability.

Lately, an interesting and unique features of semiconductor- NC -materials system as photoanode in DSSCs have gained intensive research interest and reflected a tremendous favourite research matter among various groups of scientists. The relationship between

TiO_2 on rGO as well as their growth mechanism with PCE performance was still a matter of debate and remains unclear. It was noted that the properties of this TiO_2-rGO NC primarily depend on the nature of the preparation method and the role of optimum TiO_2 content incorporated with the rGO. Therefore the development of PCE performance remains to be determined. In this chapter, an overview regarding TiO_2-rGO NC film as efficient photoanode for working principle of DSSCs is briefly reviewed in detail on several aspects:

- Historical overview of DSSCs
- Basic principle of DSSCs
- Material selection of TiO_2-rGO NC in DSSCs
- Work done by the various researchers of TiO_2-rGO NC in applied DSSCs

2.2 Historical Overview of DSSCs

Date to the 1960s the idea developed that the organic dye could function most efficiently to generate electricity at oxide electrode in electrochemical cells (Gerischer et al., 1968). The preliminary concept was imitated as plants photosynthesis process and explored by University of California at Berkeley with chlorophyll extracted from spinach (bio-mimetic or bionic approach) (Tributsch and Calvin, 1971). In 1972, the electric power generation experiments was started and demonstrated regarding principle of DSSCs (TRIBUTSCH, 1972). The following two decades, the instability in terms of PCE still remains a major challenge although porosity of the photo-electrode was optimized by the fine oxide powders (Matsumura et al., 1980). A modern of DSSCs utilized porous layer of TiO_2 nanoparticles as photo-electrode and covered with organic dye for sunlight absorption purpose. Eventually, it is obeyed the chorophyl in green leaves concept. Besides, the electrolyte solution is placed between the anode (TiO_2) and cathode (Pt) in DSSCs. In other words, the principle also similar to the conventional alkaline battery.

In 1991, the innovation of third generation of photovoltaic technology named DSSCs was inspired and breakthrough with ~7.1 % (O'regan and Grfitzeli, 1991) under solar illumination. The evolution has continued progressively in aspect of structural, substrate morphology, dye modification, and also electrolyte solution and thus obtained the latest improved performance with ~13 % (Mathew et al., 2014), there are revealed that up to twice times improvement of the PCE with the various methods, components, and materials applied. Semiconductor materials of photoanodes played an essential component in DSSCs to perform the great conversion PCE with agreement to the thin nanostructured mesoporous film, maximum transparency of the thin layer, rapid electron transportation with low resistance, and the porous photoanode can be completely accessible for the electrolyte (Hagfeldt, 2012).

To date, DSSCs has been aroused due to its large availability and low–cost material especially in term of low processing temperature. DSSCs also could integrated in portable devices as well as indoor facilities like chargers, solar key boards, and solar bags (Raj and Prasanth, 2016). In 2006, Poortmans and co-researchers reported that lifetime of DSSCs is around 20 years but the leakage of the liquid electrolyte still remain a challenge (Poortmans and Arkhipov, 2006).

2.3 Basic Principle of DSSCs

Technically, DSSCs are generally considered as the solid-state photovoltaics or photo-electrochemical cells imitating the concept of plants' photosynthesis process. The core concept of DSSCs is photoanode covered by the dye sensitizer (Figure 2.2). In DSSCs configuration, light is absorbed by the dye sensitizers and the charge carriers are transported to the wide band gap nanocrystalline semiconductor. Considering these facts, the construction of nanostructured semiconductor could improve the PCE by means of increased charge collection and light absorption enhancement. The rate of photogeneration (production of holes and electrons (redox reactions) and carrier lifetime from space quantization) could be enhanced as well.

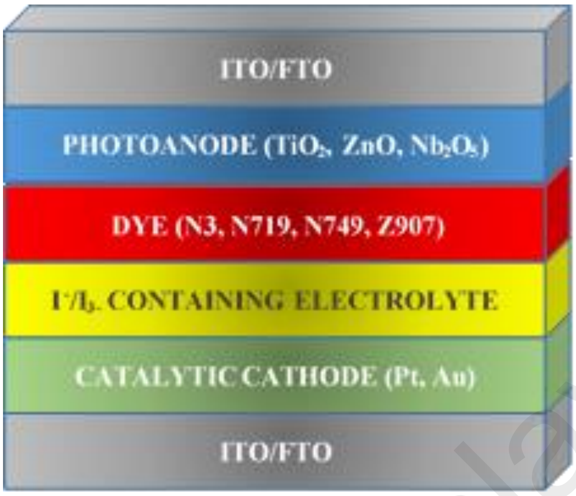

Figure 2.2: Schematic diagram of DSSCs structure

2.3.1 DSSCs Mechanism

Figure 2.3 shows the DSSCs mechanism. Accordingly, HOMO of the dye, S will release an excited electron, S* at the LUMO upon the light absorption under AM 1.5 spectrum. The S* will then transfer to the photoanode (conduction band) via photoexcitation Equation (2.1). Next, the S* will carry forward an electron and S^+ will flow along the outer circuit to the cathode of the cell Equation (2.2). The regeneration process occurs via the redox reaction when S^+ oxidizes the liquid electrolyte of iodide, I^- to form tri-iodide, I_3^- and neutralizes the state of sensitizer, S Equation (2.3). In the meantime, the electron also reduces the I_3^- to I^- Equation (2.4). The mechanism is shown below:

Photoanode:

$$S + h\nu \rightarrow S^* \qquad \textbf{Equation (2.1)}$$

$$S^* \rightarrow S^+ + e^-(\mathrm{TiO_2}) \qquad \textbf{Equation (2.2)}$$

$$S^+ + \tfrac{3}{2}I^- + e^- \rightarrow S + \tfrac{1}{2}I_3^- \qquad \textbf{Equation (2.3)}$$

Cathode:

$$I_3^- + 2e^-(\text{Pt/Au}) \rightarrow 3I^- \qquad \textbf{Equation (2.4)}$$

Henceforth, DSSCs promote an overall conversion of photon, hν to useful electricity with constantly non-ageing materials resulting in long lasting solar cells.

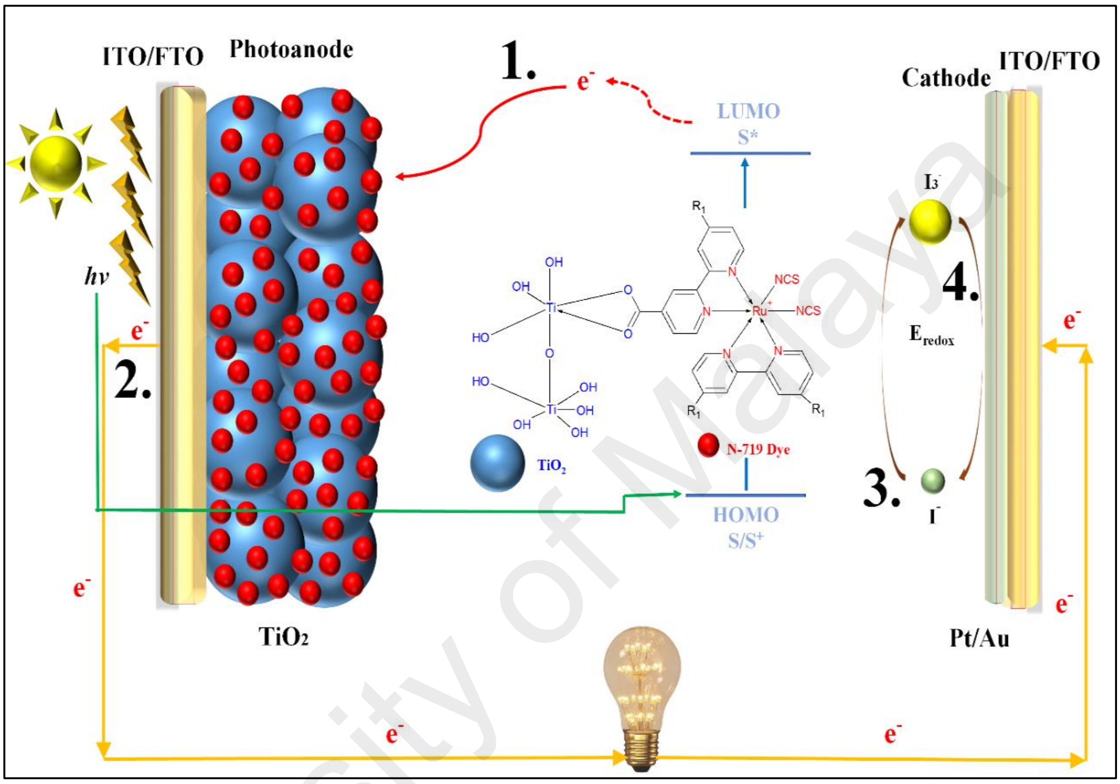

Figure 2.3: Schematic of the charge transfer reaction in DSSCs. 1. Upon light harvesting on DSSCs, the absorption of a photon by a dye molecule (S) is promoted into the exited state (S*). Within a short time (fs), an electron (e^-) goes into wide bandgap semiconductor film (TiO_2) while S* oxidised into S^+. 2. An e^- is flow through the TiO_2 film by diffusion and pass-through outer circuit to the Cathode. 3. The oxidised S^+ is reduced to S by the gaining electrons from the electrolyte. Electrolyte containing iodide (I^-) and tri-iodide (I_3^-) redox system in which I^- ions are oxidised to I_3^- ions and hence formed neutral state of S. 4. In Cathode part, after diffusion through the catalytic (Pt/Au) film, I_3^- ions releases its charge thus being reduced back to their I^- ions state

In the past two decades, DSSCs have attained the highest conversion efficiency of 14% (Mathew et al., 2014). In spite of suffering from drawbacks such as low efficiency compared to that of the current photovoltaic technologies, the cells in DSSCs could be integrated into low power gadgets (Islam et al., 2016). Continuous efforts have also been exerted in recent years to improve the cell performance of DSSCs on every aspects of each components and to reduce the product cost further. In order to achieve these goals, the flexible glass which has lighter weight, lower resistance and cheaper cost than that of the rigid glass was adopted (Sheehan et al., 2015). Additionally, a commercially cheaper and efficient organic dye with high absorption strength was also used to improve the performance of DSSCs (Zeng et al., 2010). Also, a composite of material for photoanode was introduced due to its various synergetic and intrinsic properties (Chen et al., 2012; Mao et al., 2016; Yen et al., 2015). An electrolyte with a better long-term stability and rapid charge carrier transport was obligatory (Sauvage et al., 2011; Yusuf et al., 2017). Cheaper alternative materials such as Pt- and TCO-free could be used as counter electrodes with high catalytic activities (Lee et al., 2010b).

2.3.2 Energy Diagram

As shown in Figure 2.7, rGO has the potential to improve the performance of DSSCs and also increases their electron lifespan. For the traditional TiO_2 photoanode without rGO materials, the recombination by the photogenerated hole and the back-electron transport (TiO_2 photoanode-electrolyte interface) is high when the photogenerated electrons flow through the TiO_2 thin film before arriving at FTO substrate. Figure 2.4 also indicates that the work function of the incorporated of rGO material (-4.4 eV) is closer to that of the FTO substrate (-4.7 eV) and the CB of TiO_2 (-4.2 eV). This will facilitate the photogenerated electrons flow from dye molecules-CB of rGO-TiO_2-FTO interfaces to the outer circuit (Yang et al., 2010a). In this corporation, rGO could provide a better dye adsorption and improved charge separation, coupled with accelerating the photogenerated electron transport to minimize the charge recombination (Chen et al., 2013b). Correspondingly, Eshaghi and co-researchers (Eshaghi and Aghaei, 2015) reported that the rGO material in TiO_2 will influence its surface morphology, resulting in more active sites for dye molecule loading. This means that there are more photogenerated electrons being injected from the excited state of the dye into the CB of TiO_2 and thereby enhancing the PCE of the DSSCs (Subramanian et al., 2013). In contrast, an excessive rGO material content would reduce the PCE of DSSCs owing to the reduction of the light absorption of dye as TiO_2 was covered by the rGO. Nevertheless, an excessive rGO content will also increase the electron-hole pairs' recombination rather than generate electrons pathway in DSSCs.

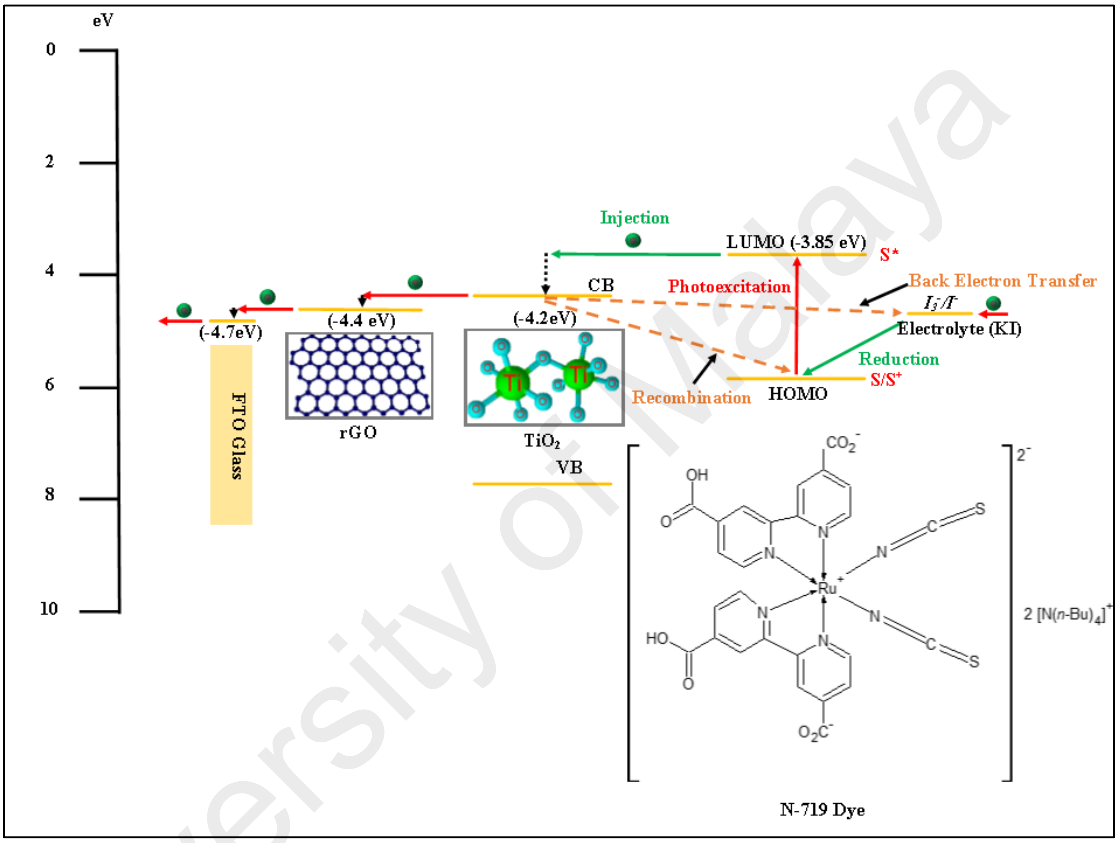

Figure 2.4: Schematic of energy levels and mechanism of photocurrent generation in DSSCs constructed by TiO_2-rGO NC

2.3.3 PCE Calculation

Performance of DSSCs, η Equation (2.6) by the sub-expressions such as Open Circuit Voltage, V_{oc}, Short Circuit Current Density, J_{sc}, and Fill Factor, FF Equation (2.5) could be determined from the photocurrent density-voltage (J-V) curves. The derivations of these equations are shown below.

$$FF = \frac{V_{mp}J_{mp}}{V_{oc}J_{sc}} \qquad \textbf{Equation (2.5)}$$

$$\eta = \frac{P_{max}}{P_{in}} = \frac{V_{OC}J_{SC}FF}{P_{in}}$$ **Equation (2.6)**

Where;

Voc = Open-circuit voltage; *Isc* = Short-circuit current density; *Vmp* = Voltage at maximum power; *Jmp* = Current density at maximum power; *FF* = Fill factor; *Pin* = 100 mWcm^{-2} with AM 1.5G spectrum (1 Sun)

Based on *J-V* curves, the recombination rate and the adsorption strength of the sensitizer will influence the *Voc* parameter. Specifically, *Voc* is defined as the difference between Fermi level of metal oxide semiconductor (e.g. TiO_2) and the redox potential of the electrolyte (e.g. I^-/I_3^-) in Figure 2.4 (De Angelis et al., 2007). Moreover, *Jsc* is determined by the molecular structure of dye and electrochemical properties of the mesoporous network in the electrolyte (Jose et al., 2008). Based on Equation (2.6), it was determined that higher *Pmax* at low intensity of light, *Pin* can produce higher solar conversion efficiency.

2.4 Material Selection of TiO_2-rGo in DSSCs

The DSSCs typically consists of photoelectrode, counter electrode, dye molecules, and organic electrolyte (Lin et al., 2011; Wei et al., 2011). Among these essential parts, the photoelectrode is the main factor in order to achieve the desired light PCE and maintain its stability. Taking into account of the processes involved in the photoactivity reaction under solar irradiation, the materials used as photoanode must satisfy several functional requirements with respect to high dye loading absorption, charge separation, and efficient in charge carriers such as Zinc Oxide (ZnO) (Giannouli, 2013), La^{3+} & Mg (Ako et al., 2016), Cu & Ag (Shakir and Abd-ur-Rehman, 2016), and rGO (Ding et al., 2015) etc. Among all of the available metal photoanode, rGO offers great promise for photovoltaic applications and it is perfectly suitable as a photoelectrode in DSSCs system, which has a positive impact on the photo-induced charge transport and suppress the charge recombination in DSSCs. Moreover, rGO also will lead rapid charge carrier mobility (holes and electrons) in DSSCs by the ultrafast extraction of photo-generated carriers. However, one of the major drawbacks of rGO in DSSCs is related to its structural defects.

For the further development, metal oxide is required to enhance its photocatalytic activity. Some metal oxides such as TiO_2, ZnO, and stannic oxide (SnO_2) have been used as photoanode in DSSCs. Among these metal oxide, TiO_2 nanocrystals gives the best PCE as compared to ZnO and SnO_2 due to the higher photocatalysis activity, abundance, and high quantum yield (Bauer et al., 2002; Bhattacharjee and Hung, 2013; Fukai et al., 2007; Han et al., 2009; Hoffmann et al., 1995; Hsu et al., 2014a; Seema et al., 2012; Zhuang et al., 2013). However, TiO_2 has limited solar light harvesting ability due to its wide band gap (3.0-3.2 eV) (He et al., 2013). Henceforth, the incorporation of TiO_2-rGO NC has become a promising strategy for the enhancement in terms of PCE in DSSCs application.

2.4.1 rGO

rGO term, according to International Union of Pure and Applied Chemistry (IUPAC), graphene is defined as a carbon monolayer of the graphite structure, described by analogy to a polycyclic aromatic hydrocarbon of quasi infinite size (Fitzer et al., 1995). The term “rGO” has been used loosely in the literature to represent pristine graphene. In the last two decades, rGO has attracted extensive interest as one of the promising candidates associated with its superior electrical conductivity, good thermal conductivity and better mechanical properties as compared to that of other types of materials (Liu et al., 2017; Luan et al., 2013; Zhang et al., 2017b). Nevertheless, rGO is not the first carbon material showing some exceptional properties in DSSCs. There are also over 100 papers published per year regarding the combining topics of rGO as photoelectrode and DSSCs, either freely suspended in solution or compacted to a robust photoelectrode. However, the drawbacks of such photoelectrode include the presence of defective sheets decorated with oxygenated groups (i.e. epoxides, hydroxyls, carbonyls), topological defects, and lattice vacancies between the reduction sheets. Nevertheless, rGO are dependent material and not sufficient to meet DSSCs demands.

2.4.1.1 rGO Structure

In 2004, single layer rGO was first discovered by Geim and Novoselov using “Scotch tape method” under ambient conditions. Accordingly, pristine graphene is an allotrope of carbon with honeycomb structure, the sp^2 hydridized carbon atoms are arranged in a basal plane of graphite lattice structure. However, pristine graphene remains a challenge where the aggregation or restacking occurred due to the van der Waals interactions. The interlayer spacing between graphite layers is around 0.34 nm (Chung, 2002). The graphene, either in single-layer nanosheet or few stacking-layer nanosheets, has attracted extensive attention attributed to its rapid electron transport and good conductivity properties. On top of that, rGO would be act as a conductive media, which is beneficial to the mechanism of the electrolyte liquid (Yuan et al., 2014). Additionally, rGO material is considered as a potential candidate to be introduced as photoanode in DSSCs due to its tunable bandgap and photon absorption, high visible light transparency, as well as ultra-fast charge carrier mobility. Figure 2.5 illustrates the carbon materials network, where single-layer of 2D rGO is considered to be the dominant material for 0D fullerene (wrapped up), 1D nanotube (rolled up), and 3D graphite (stacked up). Among them, the function of fullerene is significantly different from the CNT and rGO. CNT and rGO are only slightly different in terms of the chemical and electronic properties, while CNT and fullerene are not exactly sp^2-hybridized. The outstanding properties of electronic, thermal stability, and optical of rGO will be described in following section.

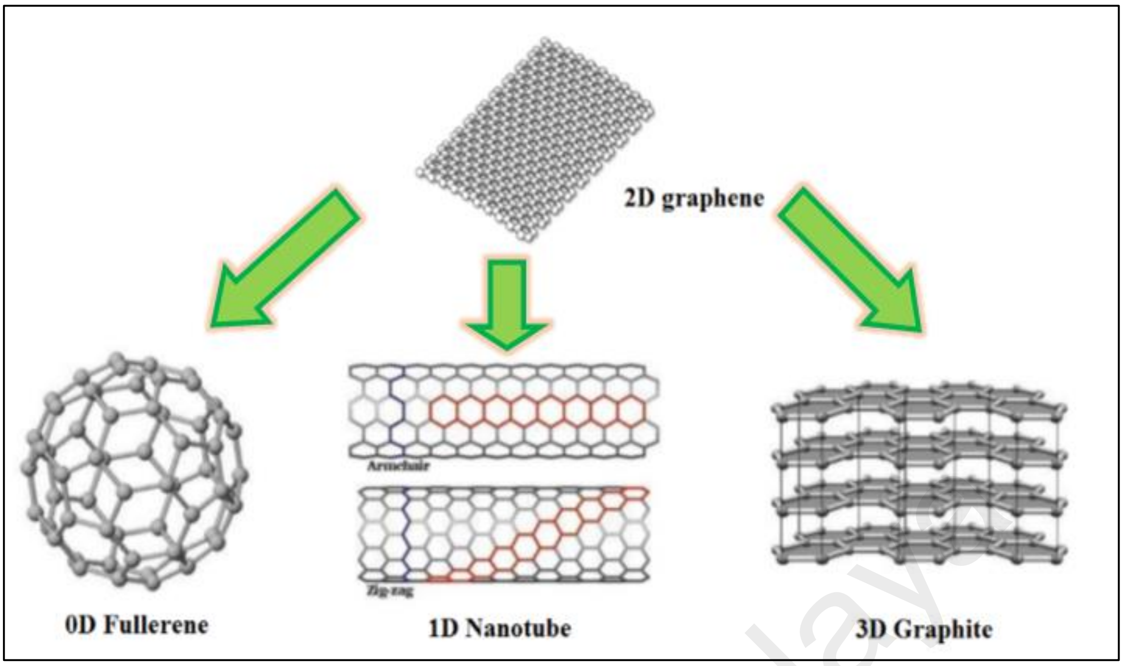

Figure 2.5: Carbon network family under 2D rGO material

2.4.1.2 Electronic Properties of rGO based Bilayer Systems

Generally, electronic properties of rGO provided high charge carrier concentrations and mobility, which promising candidate into DSSCs. In particular, pristine graphene is considered as zero band gap semiconductor due to its conduction and valance bands meet at the Dirac points. However, it is still difficult to produce one atom thick carbon layer of pristine graphene. In rGO synthesis, the bilayer system have 3 modifications called AA, AB or Bernal phase, and twisted bilayer. The AA bilayer where second carbon atom layer is stacked on the first carbon atom layer (Liu et al., 2009b). The twisted bilayer structure is where the top carbon layer rotated with the lower carbon layer by specific angle, θ. The AB or Bernal phase is the most stable among the bilayer system which half of the carbon atoms of top layer stacked on carbon atoms of lower layer whereas the remain is covered by different materials (Dos Santos et al., 2007).

The electronic properties of rGO bilayer systems are built from the electronic properties of graphene single layer system. In single layer of pristine graphene, the sp^2 hybridization (one *s* and two *p* obitals) capable to form σ bond between neighboring atoms. Carbon atoms have 6 electrons and its electron configuration is $1s^2\ 2s^2\ 2p^2$. In rGO, each carbon atom is bonded to three nearest neighbors of carbon atoms by strong covalent bonds. These σ bonds are formed from electrons in 2s, $2p_x$ and $2p_y$ valence orbitals and leaving one mobile electron in $2p_z$ orbital which aligned perpendicular to rGO sheet (Warner et al., 2012). The overlapping of $2p_z$ orbitals with neighbor atoms caused delocalization of valence (π) and conduction (π^*) bands. One electron from each carbon is donated to fill the valence band and leaving the conduction band empty.

For the AB bilayer configuration, the interlayer spacing, c_0 is estimated around 3.35 Å while AA and twisted bilayer are slightly different (McCann and Koshino, 2013). Furthermore, the sp^2 hybridization of bilayer is much heavier than monolayer of pristine graphene. As an addition, Dirac-like effective Hamiltonian described that the charge carriers of pristine graphene are massless chiral quasiparticles with a linear dispersion (Neto et al., 2009). Besides, the electronic spectrum of the bilayer of rGO maybe gapped or gapless and it could controlled by doping rate or other effective parameter. At last but not least, the electronic spectrum is depends on the interest of electronic application. Notably, bilayer of rGO is promising candidate than pristine graphene in DSSCs application due to the electronic properties are stacking-dependent and may change the electrodynamic features during hybridation process with other semiconductor materials (Rozhkov et al., 2016).

2.4.1.3 Thermal Conductivity of rGO

Thermal conductivity is the ability of the material to conduct heat over a wide range of temperature. In rGO, the heat conductivity is dictated by phonons transport rather than electrons. This is due to the concentration of free carriers in rGO is relatively low as compared to metals. Phonon transport can be divided into two types, namely diffusive and ballistic. Diffusive conduction only occurs at high temperature while ballistic conduction occurs at low temperature (Zhu et al., 2010). The investigation of thermal conductivity of rGO through conventional method is extremely difficult as it requires measuring the temperature drop over the thickness of examined film and the fact that pristine graphene is only one carbon atom thick. The nature of the rGO in terms of thermal conductivity properties respective with DSSCs was reported by some researchers (Fugallo et al., 2014; Guo et al., 2015; Pop et al., 2012). The rGO is a good heat conducting material with 5000 W/mK (Warner et al., 2012). High thermal conductivity of rGO could be advantageous when high current density is loading that generate significant amount of heat within DSSCs system.

2.4.1.4 Optical Properties of rGO

Due to its unique optical properties, rGO is able to capture ~2.3 % of visible light per sheet (Aghigh et al., 2015; Roy-Mayhew and Aksay, 2014a). The amount of visible light absorption is proportional to the number of rGO layers (Bonaccorso et al., 2010). Furthermore, a single layer of pristine graphene can only absorb 2.3% of light harvesting. This gives us a hint that the maximum light harvesting can go through ~5 sheets of pristine graphene or bilayer film provided the light transmittance is 90% (Bonaccorso et al., 2010). For this phenomenon, rGO sheet/film is a dependent material and a supporter to reduce the charge mobility rate in which the photoexcited electron transfers from VB to CB passing through the outer circuit of DSSCs. However, the absorption per unit electron mobility is low. When Fermi level is located at the Dirac point, the number of charge carriers will decrease while the resistivity will increase till its maximum ($V_g = 0V$). This is known as optical transition of rGO. The relaxation and recombination of photo-induced electron-hole pairs in rGO is highly dependent on the concentration of carrier in DSSCs (Zhu et al., 2010). Furthermore, rGO is also considered as a low-cost material and provides outstanding transparency properties to allow maximum light absorbance transfer along the FTO glass in DSSCs.

2.4.1.5 rGO Synthesis

In the past few decades, GO can be synthesized via synthetic approaches (Kovtyukhova et al., 1999) and several methods like Staudenmaier (Staudenmaier, 1898), Tour (Marcano et al., 2010), Hofmann (Hofmann and Holst, 1939), and Hummers (Hummers Jr and Offeman, 1958). Throughout these methods, GO are largely variable in terms of structural features (thickness/lateral size), colloidal dispersibility, and surface properties (oxygenated contain/ratio of sp^2 domains) due to the different reaction conditions, purification processing, and type of graphitic materials. Prior to rGO synthesis, structural and surface properties of GO production are primary stage and emphasized to determine their good electrical performance in DSSCs application. Besides, Hummers is the most widely used method for GO synthesis as compared to other synthesis methods (Jasim et al., 2016).

The rGO synthesis method is emphasized in this research in order to obtain high purity of rGO and affect a good PCE in DSSCs application (Ding et al., 2015; Hummers Jr and Offeman, 1958; Sellappan et al., 2013; Singh et al., 2011). Typically, GO and rGO is widely applied in DSSCs due to its compatible chemically and fabrication process after modification of functional groups. However, exfoliated graphite can be isolated from pristine graphene due to the topological defects, lattice vacancies, and high contained of oxygenated groups (epoxides, hydroxyls, carbonyls, etc.).

Several types of pristine graphene nanostructures can be found in powder form-based materials to develop large-area rGO, i.e., graphene oxide (GO), nanoribbons, nanoplatelets, as well as quantum dots. However, large-area production is one of the foremost challenges to produce the high-purity rGO sheets. As a short rGO preparation history flashback, Fernandez-Moran and co-researchers produced the millimeter-sized (as thin as 5nm) with around 15-layer rGO by micromechanical exfoliation from graphite in

1960 (Edwards; Li, 1961). After two years, Boehm and co-researchers (Boehm et al., 1994) observed the single layer and bilayers of colloidal graphite oxide using electron microscopy. In 1970s – 1980s, an increasing research attention has been focused on the chemical intercalation and exfoliation of oxidized graphite (Carr, 1970). In early 1990s, the fullerenes and nanotubes were discovered and attracted significant research attention on carbon materials including the rGO (Bethune et al., 1993). Consequently, atomic force microscopy (AFM) was employed to observe the topology of rGO and the highly oriented cleaved pyrolytic graphite (Soldano et al., 2010). In 1999, stacked graphite layers (with sub-10 nm) were obtained by rubbing micro fabricated graphite pillars on substrate, suggesting the possibilities in monolayer production (Mirkin and Tuominen, 2011). Also, Geim et al. reported the method of cleaving a graphite crystal with an adhesive tape to extract single layer graphene sheets in 2004. Next section will discuss the rGO synthesis using several techniques such as micromechanical exfoliation, colloidal suspension, epitaxial growth, chemical vapor deposition (CVD), and and chemical exfoliation. These rGO synthesis techniques are most famous approaches due to easy handling and low-cost as well as high-purity rGO production.

(a) *Micromechanical Exfoliation*

The first preparation of rGO by this method was reported by Novoselov and Gaim in 2004 (Novoselov et al., 2004). This technique peels off layers of rGO from a graphite crystal by using adhesive tape (Huc et al., 2008). The obtained flakes differ considerably in size and thickness, where the sizes range from nanometers to several tens of micrometers for single-layer rGO. However, it is difficult to obtain larger amounts of rGO and reproduce the same results by this method. This method has a low production cost as it uses only adhesive tapes and graphite crystal. The purity of the prepared rGO is very high with almost no defects.

(b) ***Colloidal Suspension***

rGO can be prepared in liquid-phase which is able to obtain a high amount of rGO. The easiest method would be to disperse the graphite in an organic solvent such as N-methylpyrrolidone (NMP), ethanol, dimethylsulfoxide (DMSO) and tetrahydrofuran (THF) with nearly the same surface energy as graphite (Lotya et al., 2010). The solution is then sonicated for long hours or a voltage is applied (Su et al., 2011). After the dispersion, the solution has to be centrifuged in order to dispose of the thicker flakes. The purity of the obtained rGO flakes is very much comparable to the micromechanical exfoliation. This method has a low production cost and produces large amounts of rGO but it is very time consuming.

(c) ***Epitaxial Growth***

Single- or bi-layer rGO can be formed on the Si face of the crystal by heating and cooling down SiC crystals, whereas few-layer rGO grows on the C face (Cambaz et al., 2008; Yang et al., 2013). The processing parameters such as temperature, heating rate, or pressure will greatly affect the results. When the temperature and pressure are too high, nanotubes will form instead of rGO. The conventional epitaxial growth method evaporates a thin Ni layer onto a SiC crystal. Carbon will diffuse through the Ni layer to form rGO or graphite layer on the surface depending on the heating rate. The resulting rGO is easy to detach from the surface as compared to the rGO produced by the growth on a simple SiC crystal without Ni (Enderlein, 2010).

The growth of rGO starts at several locations on the crystal and these rGO islands slowly grow together as shown in Figure 2.6. Therefore the rGO is not perfectly homogeneous, due to defects or grain boundaries. Its quality therefore is not as good as that of exfoliated rGO, except that the rGO would be grown on a perfect single crystal. However, the size of the homogeneous rGO layer is limited by the size of the crystal used.

The ability to produce large amounts of rGO by epitaxial growth is not as good as liquid-phase exfoliation but the results are reproducible.

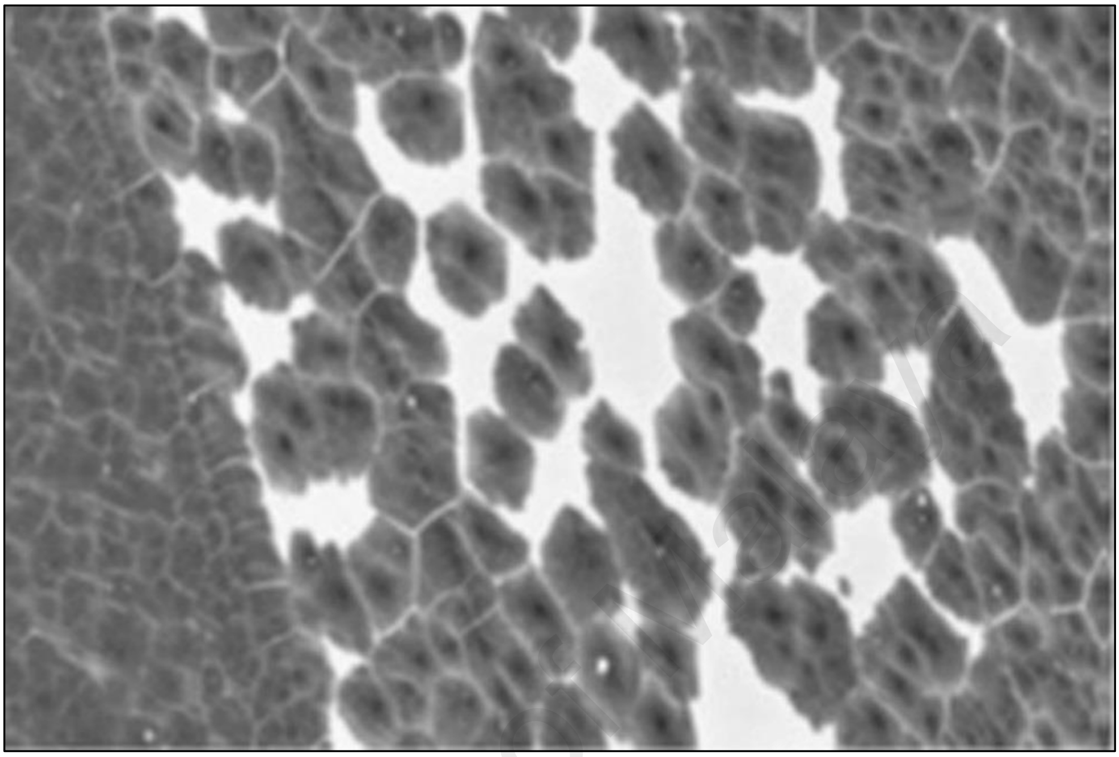

Figure 2.6: SEM image of rGO islands forming on copper foil and slowly growing close to each other (Robertson and Warner, 2011)

(d) *Chemical Vapor Deposition (CVD)*

Basically, in this technique, a substrate is exposed to gaseous compounds in high temperature. The gaseous compounds decomposes on the substrate surface to grow thin film. Among the rGO synthesis methods in Figure 2.7, CVD is the best technique to produce the pristine graphene in a large-scale production. In CVD method, rGO is grown directly on a transition metal substrate (Ni, Cu, SiO_2) via saturation of carbon source (methane) upon exposure to a H_2 gas at high temperature (~1000 ℃) to obtain mono-, bi- and tri-layer rGO (Kato et al., 2017; Zang and Lin, 2014; Zang et al., 2017). Based on the CVD concept, the solubility of carbon on the substrate will reduce once the substrate is cooled down and the carbon precipitates to form the single or multilayer rGO sheets on the substrate. However, CVD methods tend to suffer from shortcoming in terms of (i) controlling the thickness of film, (ii) secondary crystals could be formed easily, and (iii) high-cost fabrication processes (Juang et al., 2010). Among these rGO synthesis methods, the direct growth of CVD manufacturing technique has been classified as the most promising method for the bulk production of rGO material with less defects and electronic disorder (Ferreira et al., 2011).

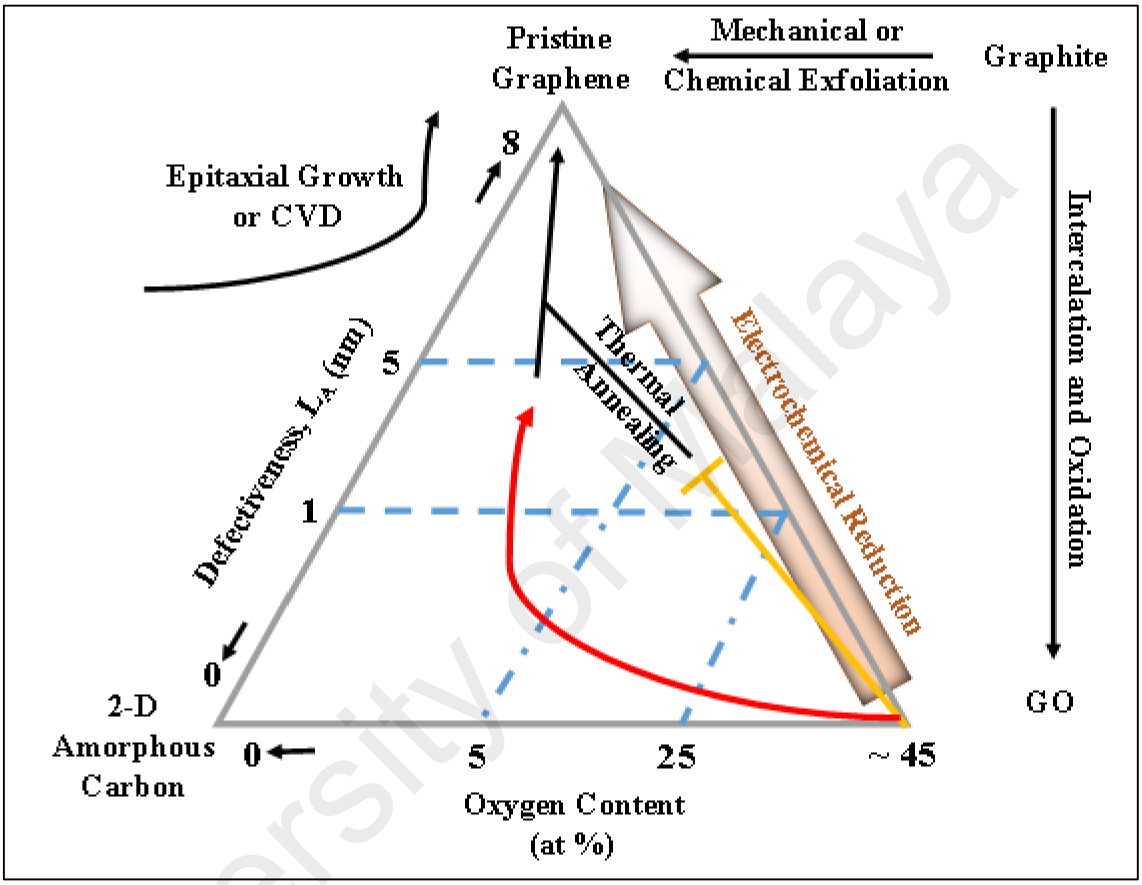

Figure 2.7: Overall hierarchy of rGO materials

(e) ***Chemical Exfoliation***

In order to produce large quantities of GO (a graphene-like nanosheets) in low-cost manner, the GO was commonly chemically exfoliated and reduced into rGO. (Hernandez et al., 2008; Parvez et al., 2014). Among these rGO synthesis methods, chemically exfoliated is the easiest way to form high purity of rGO. In general, the chemically exfoliation involves the sonication of organic compound solvent (*N*-methyl-pyrrolidone) in the graphite where the surface energy is close to the graphite structure. There are few commonly applied synthesis methods for GO production such as conventional Hummer's method (Hummers Jr and Offeman, 1958), modified Hummer's method (Shahriary and Athawale, 2014), simplified Hummer's method (Chong et al., 2015), and improved Hummer's method (Low et al., 2015a). In this project, Improved Hummer's method is chosen for GO synthesis due to the easy elimination of NO_2/N_2O_4 toxic gasses or inexistence of Na^+ and NO_3^- ions as compared with conventional Hummer's method where applied sodium nitrate ($NaNO_3$) as reactant (Chen et al., 2013a).

In this approach, graphite flakes will be oxidized via chemically oxidized to produce certain functional groups such as carbonyl, hydroxyl, and peroxyl in C-C bond (Ban et al., 2012). These functional groups indicate that rGO layers are peel off layer by layer from graphite after weakening the Van der Waals bonding between C-C bonds of graphite (Ban et al., 2012). As consequence, GO can be reduced by chemical, electrochemical and thermal approaches. Normally, thermal reduction or chemical reduction techniques are common apply in this reduction stage. In chemical reduction, the hydrazine solvent is a common reducing agent used by researchers to reduce the oxygen content and the size obtained normally in range of 1-10 µm (Bo et al., 2014). Ordinarily, reducing agents are poisonous chemical like hydrazine solvent and categorized as un-environmental friendly. Strong oxidants and intercalating compounds such as H_2SO_4, HNO_3, $KMnO_4$, $KClO_3$ and $NaClO_2$ were commonly used in order to oxidize the graphite. In this respect, GO could be reduced by chemical, electrochemical and thermal approaches. Accordingly, reducing agent (hydrazine solvent) will be used in chemical reduction reaction to reduce the oxygen content and the size of the rGO obtained is normally in the range of 1-10 µm.

Ordinarily, reducing agents such as hydrazine solvent are poisonous chemicals and have been categorized as un-environmentally friendly. In this respect, green and efficient reducing agents, i.e., caffeic acid (CA) have been used instead of those toxic chemical (Bo et al., 2014). However, CA as reducing agent has drawbacks such as cannot fully deoxygenate GO alone and dependent on hydrazine as supporting agent or surface modifier (Aunkor et al., 2016). Moreover, CA as reducing agent would formed additional functional groups on the rGO sheets and may lead the irreversible aggregation, rGO contamination, and lower electron conductivity in photovoltaic application (Aunkor et al., 2016). Eventually, chemically reduction technique with hydrazine as reducing agent is more preferable in order to fully hydrogenate GO sheets. In addition, Improved Hummer's method is less time consuming, low production cost, and produces high purity GO and rGO sheets.

2.4.2 Modification of rGO

Design and development of nanostructure of rGO has gained significant scientific interest and become the most studied material as it exhibits promising functional properties. However, an obvious hindrance to the widespread use of rGO as a photoelectrode in DSSCs due to its structural defects. In fact, rGO can only contain about 0.68% from our solar energy. Thus, utilization of visible light from our solar energy is essential that lead to the higher PCE in DSSCs application.

These drawbacks cannot be overcome by only optimizing the dimensions of rGO itself as described in previous section. Therefore, considerable efforts have been exerted to further improve the immigration of photo-induced charge carriers by minimize electron loss during excitation state, maximize photon absorption, improve the charge mobility and thus maximize the dye molecules loading by incorporating an optimum dopants of TiO_2 elements into rGO.

2.4.3 Titanium Dioxide (TiO_2)

Titanium dioxide (TiO_2) is a semiconductor material that exhibit transition metal oxide which is the naturally occurring oxide of titanium. Due to its outstanding electrical, optical, and magnetic properties, it has attracted extensive attention of numerous scientists since it demonstrates several unique characteristics such as low cost, non-toxicity, easy handling, strong photocatalytic activity, and stability against corrosion (Fan et al., 2012; Liang et al., 2010).

2.4.3.1 TiO_2 Structure

TiO_2 is an n-type semiconductor with three crystalline phases in nature, namely anatase, rutile and brookite (Gharavi and Mohammadi, 2015; Lee and Yang, 2011). These three crystalline phases are formed by TiO_6 octahedral structure linked with different corners and edges. Each octahedron in brookite is shared with three edges to form orthorhombic structure, whereas each octahedron in anatase and rutile is shared with four and two edges respectively to form tetragonal structure. Different structures of TiO_2 phase leads to different properties as shown in Table 2.2. The anatase has higher electric conductivity and proven as a remarkable material in solar energy conversion and catalytic applications such as solar cells and photocatalytic hydrogen production (Gong et al., 2012; Lee and Yang, 2011; Muniz et al., 2011). Due to its low constrained structure, the initial crystalline of TiO_2 is mostly in anatase phase in synthesis of TiO_2 (Hanaor and Sorrell, 2011).

Table 2.2: Properties of Anatase, Rutile and Brookite of TiO_2 (Gupta and Tripathi, 2011)

Properties	Crystal Structure	Band Gap (eV)	Space Group	Density (g/cm^3)	Refractive Index (η_D)	Geometry Structure

Rutile	Tetragonal	3.05	$P4_{2/mnm}$	4.27	2.609	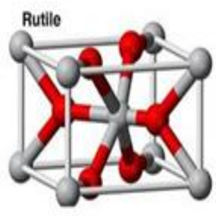
Anatase	Tetragonal	3.23	$14_{1/amd}$	3.89	2.488	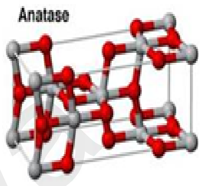
Brookite	Orthorho-mbic	3.26	Pbca	4.12	2.583	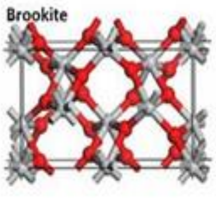

2.4.3.2 Optical Properties of TiO_2

TiO_2 is a wide band gap semiconductor with 3.05 eV in rutile phase, 3.23 eV in anatase phase and 3.26 eV in brookite phase (Lee and Yang, 2011). Based on the optical absorption measurement, rutile and anatase phases are transparent in visible region and its transparency ends when the adsorption-edge threshold photon energy is near to the direct interband gap E_0 (Zallen and Moret, 2006). Anatase of TiO_2 has only one indirect band gap of 3.23 eV, the electron transitions between the valence and conduction bands are restricted by crystal momentum. Whereas, rutile has one direct band gap of 3.05 eV and one indirect band gap of 3.10 eV as proven by many researchers (Valencia et al., 2010). Direct band gap is when an electron can be emitted from valence band to conduction band without any restriction. In addition, rutile is capable to scatter light owing to its high refractive index among other phases (Pessoa et al., 2015).

2.4.4 TiO_2 Synthesis – Hydrothermal Technique

The most commonly used chemical based or liquid-phase routes for TiO_2 synthesis techniques will be briefly reviewed (Carp et al., 2004; Chen and Mao, 2007; Ong et al., 2014). The advantages of solution-based TiO_2 synthesis are such as easy to obtain homogenous materials, easy formation of metal oxide chemically bonding with metal or even in complex organic structures, and better control over the stoichiometry (Gupta and Tripathi, 2012). To date, the hydrothermal technique is considered as “soft solution chemical processing” technique, which is an easier way to control the particles morphology, size, and their formation phase (Chang et al., 2012b; Li et al., 2011b). Tacchini and co-researchers work shows that TiO_2 nanotube configuration with large surface area and aspect ratio exhibited higher electrical contacts and charge carriers transport as compared to other configurations such as nanoparticles form (Tacchini et al., 2012). In 2008, Mogilevsky and co-researchers introduced that anatase inorganic nanotubes can be synthesized by using the hydrothermal technique (SharmilaDevi, 2014) whereas the side product titanate nanoribbons help to facilitate the photocatalytic activity. Through this technique, outer diameter of the tubes obtained is approximately 10-20 nm whereas the inner diameter of the tubes is around 5-8 nm with 1 μm length (Mogilevsky et al., 2008). Besides that, the hydrothermal process can be applied in the construction of bilayer photoanodes in solar cell with 3D-dendritic nanostructure and combine with 1D-nanowire in order to fasten the electron transport, high surface area, and pronounced light scattering effect (Mali et al., 2013).

2.5 TiO2-rGO NC

Based on literature review, rGO film is a potential candidate to improve the PCE of DSSCs, but it was normally studied and applied as a counter electrode (Ghasemi et al., 2017). Then, TiO_2 nanomaterials with superior photocatalytic activity have attracted great attention to be used in the DSSCs. However, photocatalysts suffer from drawbacks such as high electron-hole pair recombination resulting in a low PCE. Considering this fact, hybridization of TiO_2-rGO NC could enhance the photocatalysts activity by increasing the electron mobility and consequently reduce the charge recombination of the electron and hole. On top of that, agglomeration of TiO_2 can be overcome since the free electrons trapped at active area are fully occupied by C-C bonding of rGO. This provides electron-hole separation and facilitates the interfacial electron transfer (Bhanvase et al., 2017).

2.5.1 TiO_2-rGO NC Properties

Over the past few years, hybrid of TiO_2-rGO NC has gained much attention and has been intensively studied because of the unique features of enhancement in photocatalyst activity and accelerated electron mobility to suppress the charge recombination. Among the vast number of different dopants, TiO_2 is one of the most capable candidates to be coupled with rGO for enhancement in numerous diverse applications, such as DSSCs photovoltaic.

Several researchers have reported that the band gap of TiO_2 decreases with the tunable amount of rGO dopants in NC as shown in Table 2.3. This is due to the formation of Ti-O-C bond and the hybridization of C $2p^2$ orbitals and O $2p^4$ orbitals to form new valence band (Li et al., 2013; Zhang et al., 2009a).

Table 2.3: Band Gap Energy Values of TiO_2-rGO NC

Methods	Results (eV)	Reference
Thermal	Pure TiO_2 = 3.10 TiO_2-rGO = 2.95	(Zhang and Pan, 2011)
Hydrothermal	Pure TiO_2 = 3.20 1 wt% rGO-TiO_2 = 3.16	(Khalid et al., 2013)

	2 wt% rGO-TiO_2 = 3.13 5 wt% rGO-TiO_2 = 3.04 10 wt% rGO-TiO_2 = 3.00	
Solvothermal	Pure TiO_2 = 3.28 TiO_2-rGO = 2.72	(Wang et al., 2014b)
Hydrothermal	Pure TiO_2 = 3.03 TiO_2-rGO = 2.78	(Kumar et al., 2015)
Sonication	0.01 wt% rGO-TiO_2 = 2.95	(Kanta et al., 2017)

According to electrical properties of TiO_2-rGO NC, Zhang and co-researchers clarified that the photocatalytic performance can be improved with enhancement of carrier concentration and mobility between the rGO and TiO_2 materials (Jiang et al., 2011; Xiang et al., 2012a; Zhang et al., 2009a; Zhang et al., 2011c; Zhang et al., 2012b).

To enhance the photocatalytic activity of TiO_2-rGO NC, Khalid and co-researchers have shown that the function of TiO_2 can be easily enhanced in photocatalytic activity properties under visible light irradiation in terms of great absorptivity of dyes, extended light absorption range, and efficient charge separation with rGO (Geng et al., 2015; Khalid et al., 2013). Khalid and co-researchers (Khalid et al., 2013) demonstrated that the band gap energy is decreased from 3.20 eV of TiO_2 to 3.00 eV when incorporated with rGO. It is indicated that influence of rGO on the optical properties where increasing rGO amount will resulting the light absorption of TiO_2. Moreover, they claimed that presence of rGO in TiO_2 composite could be reduced the emission intensity in photoluminescence characterization and lead the enhancement of electron-hole pairs separation efficiency (Khalid et al., 2013).

2.5.2 Mechanism of TiO_2-rGO NC

Zhang and co-researchers (Zhang et al., 2011a) was formed the TiO_2-rGO NC under a simple liquid phase deposition method by utilized titanium tetrafluoride (TiF_4) and electron beam (EB) irradiation-pretreated rGO. They discovered that the preparation condition had significantly effect on structure and properties of TiO_2-rGO NC. Through this method, it can be synthesized more uniform, smaller in size of TiO_2 nanoparticles and exhibited higher photocatalytic activities with EB irradiation-pretreated rGO. Figure 2.8 was shown the mechanism of TiO_2-rGO NC undergo simple liquid phase deposition method.

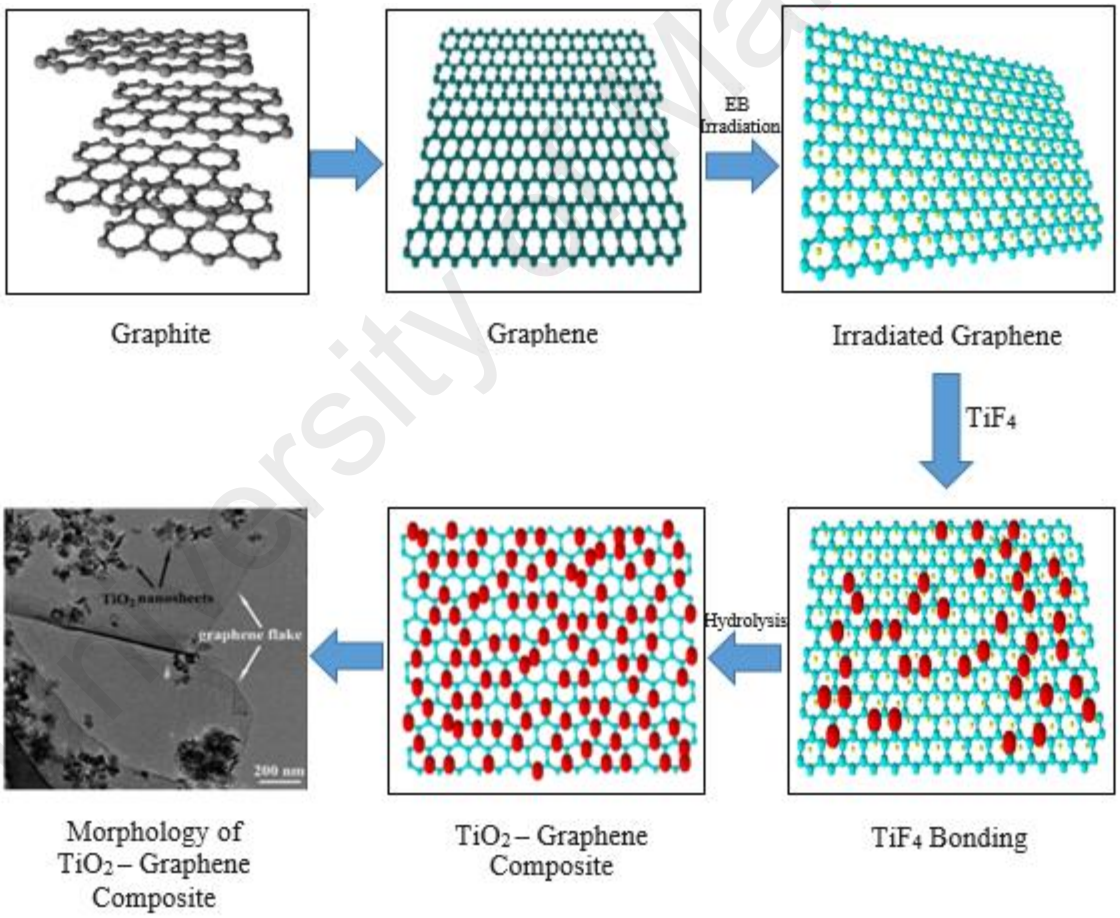

Type of Bond	Description
●	Carbon in graphite

	Carbon in rGO
	Irradiated Carbon
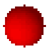	Titania Molecule
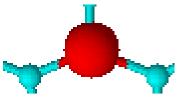	TiO_2-rGO NC

Figure 2.8: Mechanism of TiO_2-rGO NC

2.5.3 Mechanism of TiO_2-rGO NC in DSSCs

Figure 2.9 illustrates the electron flow when the rGO is loaded in between the TiO_2 molecules. The electron flow will be further enhanced if the rGO is well connected with TiO_2. This phenomena is caused by the suppression of back-transport electron from photoanode of FTO/ITO electrode to the I_3^- ions which subsequently increases the dye adsorption. Sung and co-researchers have mentioned that the presence of rGO oxide will reduce the back-transport in DSSCs and also assists in UV-reduction in TiO_2 (Khalid et al., 2013; Kim et al., 2009).

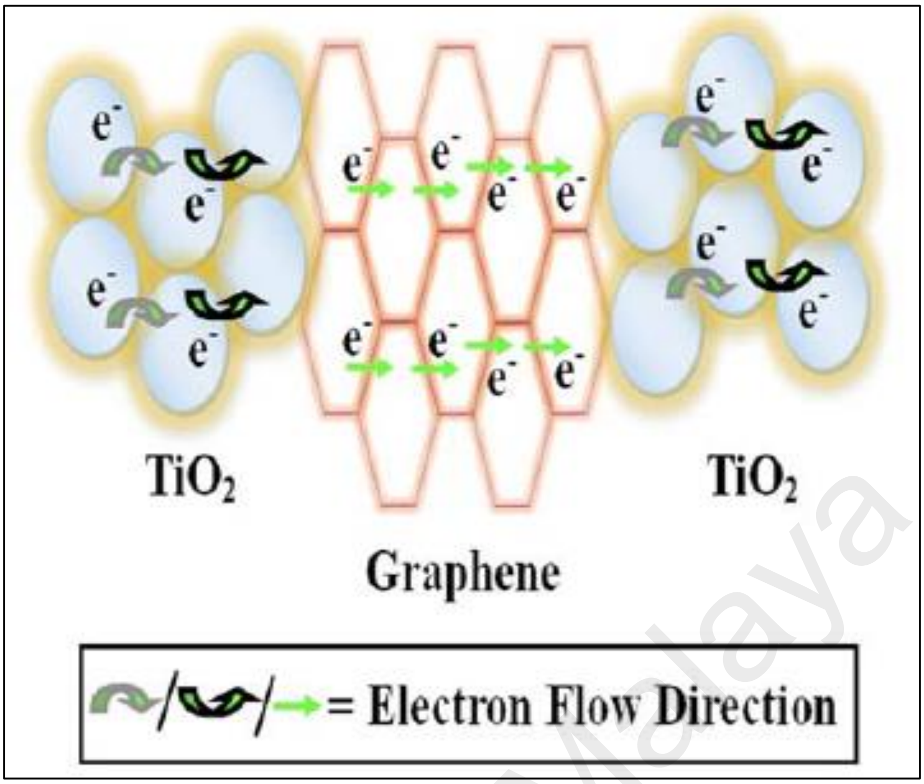

Figure 2.9: TiO_2-rGO NC bonding mechanism

2.5.4 TiO_2-rGO NC Synthesis

In this thin-film photovoltaic cell technologies, second generation solar cells are derived from the first generation solar cell by depositing one or more thin layers of semiconductors materials on the specified substrate such as metal, glass, or silicon wafer. According to Thien and co-researchers, a higher photocurrent density will attribute to a delayed recombination rate and longer electron lifetime (Thien et al., 2014). The photocurrent response of a solar cell is defined as the photo-generated electron-hole pairs interaction between the photoanode and photocathode electrode (Anandan, 2007; Khan et al., 2002; Park et al., 2006; Sellappan et al., 2013; Tryba et al., 2003; Wang et al., 2014a; Woan et al., 2009). The charge separation efficiency is increased due to the electronic interaction between rGO and photo-induced electrons of TiO_2 in the NC (Bell et al., 2011; Fan et al., 2011; Lee et al., 2012; Liang et al., 2012; Min et al., 2012; Ng et al., 2010; Wang et al., 2012b).

On top of low-cost and high reproducibility, TiO_2-rGO NC also show high interfacial contact and potential to enhance the photocatalytic activities of TiO_2. In these two decades, there are variety of techniques used to synthesize the TiO_2-rGO NC based materials to bright up photovoltaic technology especially in DSSCs application. For TiO_2-rGO NC, rGO could be easily synthesized from the graphite flakes through the intermediate product of GO (Marcano et al., 2010). This technique was beneficial to form the TiO_2 nanocrystals during the synthesis of TiO_2-rGO NC via the oxygenation of the functional groups from GO or rGO product (Liang et al., 2010). Kim and co-researchers reported that GO could be reduced via the UV-assisted photocatalytic reduction process using the 450W xenon arc lamp forming the TiO_2-rGO NC with low surface roughness and good adhesion at photoanode element (Kim et al., 2009). Dubey and co-researchers also reported that the GO could be reduced by the UV radiation in the presence of ethanol solvent and TiO_2 nanoparticles to form the TiO_2-rGO NC (Dubey et al., 2014). Another efficient technique to prepare the TiO_2-rGO NC is the direct growth process to enhance the photocatalytic activity. Recently, Xu and co-researchers (Xu et al., 2016) reported that rGO quantum dots could directly grow on 3D micropillar/microwave arrays of rutile TiO_2 nanorods forming the TiO_2-rGO NC. Additionally, the pathway for the large scale production of the TiO_2-rGO NC is the self-assembly approach of the in-situ grown nanocrystalline TiO_2 with stabilization of rGO in the aqueous solutions by the anionic sulfate surfactants (Wang et al., 2009a). Furthermore, Liu and co-researchers (Liu et al., 2016a) reported an accessible synthetic route of solvothermal approach to form the TiO_2-rGO NC with a better adsorption-photocatalytic activity than that of the pure TiO_2.

2.5.4.1 Sol-Gel Synthesis

Sol-gel technique is widely used in the synthesis of rGO-based semiconductor composites. This method depends on the phase transformation of a sol obtained from metallic alkoxides or organometallic precursors. For instance, tetrabutyl titanate dispersed in rGO-containing absolute ethanol solution will gradually form a sol with continuous magnetic stirring, and eventually change into TiO_2-rGO NC after drying and post heat treatment (Zhang et al., 2010c; Zhang and Cui, 2012).

The synthesis process is illustrated in Figure 2.10 (A) (Zhang et al., 2010c). The resulting TiO_2 nanoparticles closely dispersed on the surface of 2D rGO NS (Figure 2.10 (B)) (Zhang et al., 2010c). Wojtoniszak and co-researchers (Wojtoniszak et al., 2012b) was used a similar strategy to prepare the TiO_2-rGO NC via the hydrolysis of titanium (IV) butoxide in GO-containing ethanol solution. The reduction of GO to rGO was performed in the post heat treatment process. Meanwhile, Farhangi and co-researchers (Farhangi et al., 2011) was prepared Fe-doped TiO_2 nanowire arrays on the surface of functionalized rGO sheets using a sol-gel method in the green solvent of supercritical carbon dioxide. During the preparation, the rGO NS act as a template for nanowire growth through surface -COOH functionalities.

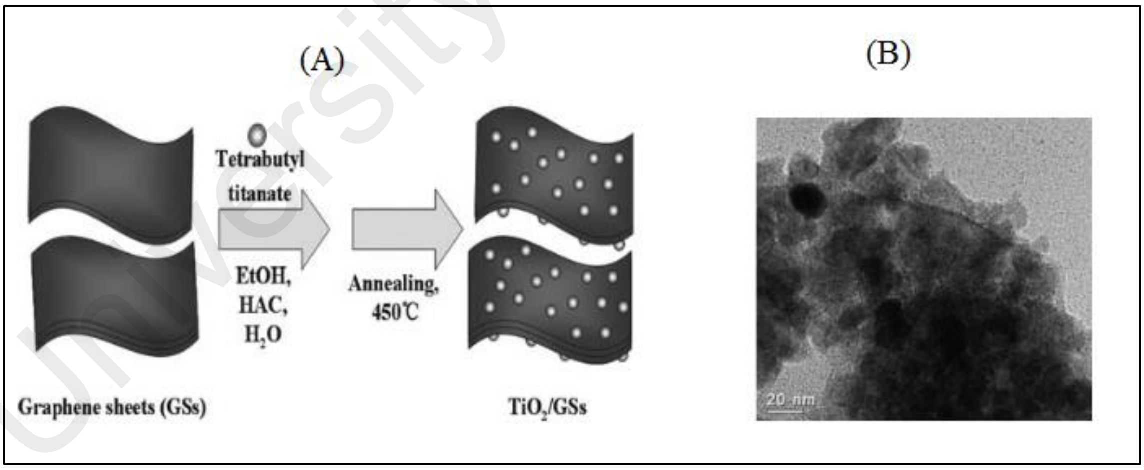

Figure 2.10: Schematic synthesis procedure (A) and typical TEM image of the TiO_2-rGO NC (B) (Zhang et al., 2010c)

2.5.4.2 Solution Mixing Synthesis

The solution mixing is a simple method used to fabricate rGO/semiconductor composite photocatalysts. The uniform distribution of photocatalysts is facilitated by the oxygenated functional groups on GO under vigorous stirring or ultrasonic agitation

(Zhang et al., 2011b). The rGO-based composites can be obtained after the reduction of GO in the composite. Bell and co-researchers (Bell et al., 2011) was fabricated TiO_2-rGO NC by ultrasonically mixing TiO_2 nanoparticles and GO colloids together, followed by ultraviolet (UV)-assisted photocatalytic reduction of GO to rGO. Similarly, GO dispersion and N-doped $Sr_2Ta_2O_7$ have been mixed together, followed by reduction of GO to yield $Sr_2Ta_2O_{7-x}N_x$-rGO composites under xenon lamp irradiation (Mukherji et al., 2011).

Paek and co-researchers (Paek et al., 2008) have prepared the SnO_2 sol by hydrolysis of $SnCl_4$ with NaOH and then mixed with the prepared rGO dispersion in ethylene glycol to form the SnO_2-rGO composite. On the other hand, Geng co-researchers have synthesized the CdSe-rGO quantum dots composites (Geng et al., 2010). In their work, pyridine-modified CdSe nanoparticles were mixed with GO sheets, where pyridine ligands provide π-π interactions for the assembly of CdSe nanoparticles on GO sheets.

2.5.4.3 In-Situ Growth Synthesis

The in-situ growth strategy provides efficient electron transfer between rGO and semiconductor nanoparticles through their intimate contact. The functional GO and metal salts are commonly used as precursors. The presence of epoxy and hydroxyl functional groups on rGO can act as the heterogeneous nucleation sites and anchor semiconductor nanoparticles avoiding the agglomeration of the small particles (Li et al., 2011c).

Lambert co-researchers have reported the in situ synthesis of petal-like TiO_2-GO by the hydrolysis of TiF_4 in the presence of aqueous dispersions of GO, followed by post thermal treatment to produce TiO_2-rGO NC (Lambert et al., 2009). With a high concentration of GO and stirring off, long-range ordered assemblies of TiO_2-GO sheets were self-assembled. Besides that, Guo co-researchers was synthesized TiO_2-rGO NC sonochemically from $TiCl_4$ and GO in ethanol-water system, followed by a hydrazine treatment to reduce GO into rGO (Guo et al., 2011). The average size of the TiO_2 nanoparticles were controlled at around 4-5 nm on the sheets, which is attributed to the pyrolysis and condensation of the dissolved $TiCl_4$ into TiO_2 by ultrasonic waves. Lastly, TiO_2-rGO were synthesized with various method not only apply in photovoltaic application but it is also in other useful application and summarized in Table 2.4.

Table 2.4: Summary of TiO_2-rGO synthesis in various application

Synthesis Method	Materials	Application	Reference
Sol-Gel	Ce-TiO_2-rGO	Photoelectrocatalytic	(Dubey et al., 2014; Hasan et al., 2014)
Sol-Gel	Anatase TiO_2-rGO	Photoelectrochemical water splitting	(Morais et al., 2016)
Solution Mixing	TiO_2-rGO	Photocatalytic selectivity	(Yu et al., 2016a)
Solution Mixing	TiO_2-rGO	Hydrogen production	(Chen et al., 2016c)
In-Situ Growth	TiO_2-rGO	Sodium/Lithium ion batteries	(Liu et al., 2015a)
In-Situ Growth	TiO_2-rGO	Photocatalytic activity	(Xing et al., 2016)

2.5.4.4 One-Step Hydrothermal Technique

Some of the semiconductor photocatalysts such as TiO_2 (Eder et al., 2009; Wang et al., 2008b; Xiang et al., 2012b; Yang et al., 2006; Yao et al., 2010), ZnO (Akhavan and Ghaderi, 2010; Li et al., 2011a; Williams and Kamat, 2009), Cu_2O (Xu et al., 2008), Fe_2O_3 (Morishige and Hamada, 2005), NiO (Wang et al., 2010), and WO_3 (Guo et al., 2012) have been explored in order to incorporation with rGO. Among these metal oxide, TiO_2 material is the most suitable candidate for further explore in this project due to its wide band gap (3.2 eV) and good in photocatalytic activity. Recently, TiO_2 has been widely explored in decoration with rGO as photoanode in DSSCs device (Chen et al., 2016b; Dobrzański et al., 2017; Ramamoorthy et al., 2017). With the low-cost and high reproducibility of TiO_2-rGO NC, it has high interfacial contact and potential to enhance the photocatalytic activity of TiO_2 and also charge carrier in DSSCs application.

As mentioned earlier in Section 2.4.3.1, TiO_2 structure consist of three phases namely brookite, anatase, and rutile. Among these phases, anatase TiO_2 is the most suitable phase for further incorporation with rGO due to good in photocatalytic activity for solar energy conversion (Pan et al., 2014). Table 2.5 contains a recent summary on the TiO_2-rGO film preparation as an efficient electrode by the distinct method to improve efficiency.

Table 2.5: Summary of TiO_2-rGO based photoanode in DSSCs

Materials	Optimized Parameter	Catalyst	Efficiency, η (%)	Method	References
TiO_2-graphene	0.25 wt% TiO_2	TiO_2	4.28	Heterogeneous Coagulation	(Sun et al., 2010a)
TiO_2-rGO	0.75 wt% TiO_2	TiO_2	5.50	Hydrothermal	(Shu et al., 2013b)
TiO_2-rGO	0.30 wt% TiO_2	TiO_2	6.26	HNO_3 Treatment	(Ko et al., 2013)
TiO_2-rGO	0.20 wt% TiO_2	TiO_2	7.19	Hydrothermal	(Xiang et al., 2014)
TiO_2-rGO	0.10 wt% TiO_2	TiO_2	6.29	Anodic Oxidation	(Song et al., 2014)

TiO_2-rGO	0.6 wt% rGO	rGO	8.24	Ultrasonic	(Ding et al., 2016)
TiO_2-rGO	1.0 ml rGO	rGO	6.69	Grätzel	(Wei et al., 2016)
TiO_2-rGO	6 h immersed in rGO	rGO	6.85	Hydrothermal	(Liu et al., 2017)

TiO_2-rGO NC based materials were synthesized via sol-gel, solution mixing, and in-situ growth method to bright up photovoltaic technology especially in DSSCs application. Among the synthesis of TiO_2-rGO NC method in Table 2.4, Hydrothermal process is an effective method to obtain TiO_2-rGO NC. Few years ago, Zhang et al. (Zhang et al., 2009a) synthesized TiO_2-rGO composite photocatalyst using hydrothermal treatment mixed GO sheets and commercial TiO_2 powders (Degussa P25) in an ethanol-water solvent to simultaneously achieve the reduction of GO and the deposition of P25 on the carbon substrate. In order to increase the interface contact and uniform distribution of TiO_2 nanoparticles on rGO sheets, a one-pot hydrothermal method was applied using GO and $TiCl_4$ in an aqueous system as the starting materials where the GO are reduced with reducing agent in the same time to form TiO_2-rGO NC (Zhang et al., 2012a). However, synthesis of TiO_2-rGO NC via conventional hydrothermal method are time consuming and complicity of the entire process.

Over the past few years, one-step hydrothermal method has been attracting much attention due to its simplest route to form TiO_2-rGO NC. In this process, TiO_2 are loaded on the GO sheets, where GO are reduced to rGO simultaneously without reducing agents. For example, Ding et al. (Ding et al., 2011) was reported rGO supported ultrathin TiO_2 nanosheets with exposed (001) high-energy facets by a simple hydrothermal method. However, the phase of TiO_2 are remain unknown in their study. Notably, one-step hydrothermal is a faster way to synthesis TiO_2 in changing phase whereas GO turn into rGO with a step during hydrothermal process. Furthermore, one-step hydrothermal method also contributed well TiO_2 particles in well crystalline formed without agglomeration on rGO sheets (Chang et al., 2012a).

Innovative approaches by using one-step hydrothermal technique to synthesis high-purity hybrid of TiO_2 with rGO as photoanode are crucial for developing efficient DSSCs system. In fact, the relationship between the Ti^{3+} ions on the rGO as well as their visible response of DSSCs performance was still a matter of debate and remains unclear. Thus, in the present study, the decoration of high purity and production of Ti-O-C bonding could be achieved by using a one-step hydrothermal technique.

2.5.4.5 Ion-Implantation Technique

In recent years, lots of efforts have been paid to enhance the photocatalytic activity of TiO_2-rGO NC as the photoanode in DSSCs using the conventional synthesis techniques such as molecular grafting, spray and dispersion. Many of researchers are explored their best to prepare an efficient approach on photoanode element to obtain a desired photocurrent density in order to obtain higher PCE for DSSCs application. However, there are still have drawbacks on photocurrent density resulting poor in PCE performance. Accordingly, the one-step hydrothermal method is one of the common approaches utilized to enhance the photocatalytic activity and reduce the lattice matter of the TiO_2-rGO NC hybrid materials (Chang et al., 2012c; Liang et al., 2014; Shen et al., 2011). Perhaps, this technique is the shortcut way and shorten fabrication time as compared with one-step hydrothermal technique. Previously, TiO_2-rGO NC as photoanode are attracted many researchers to explore and widely utilized in DSSCs. The PCE performance based TiO_2-rGO NC is shown in Table 2.6.

Table 2.6: Summaries of PCE based TiO_2-rGO NC photoanode in DSSCs

Photoanode materials	Preparation method	Reference Cell	Optimized content of rGO	Reference Cell of Photoanode				Improved of TiO_2-rGO NC Photoanode (under AM 1.5 condition)				Reference
				J_{sc}, (mA/cm^2)	V_{oc} (V)	*ff*	η (%)	J_{sc}, (mA/cm^2)	V_{oc} (V)	*ff*	η (%)	
TiO_2 with rGO (from GO)	Molecular grafting	$Ti(OBu)_4$	With/without rGO incorporation	1.95	0.52	0.31	0.32	6.67	0.56	0.45	1.68	(Tang et al., 2010)
P25-rGO	n/a	P25	0.05 wt.%	5.04	n/a	n/a	2.70	8.38	n/a	n/a	4.28	(Sun et al., 2010b)
TiO_2 with rGO (from GO)	Spray on TiO_2 film	TiO_2	Device comparison	16.40	0.60	0.52	5.09	18.20	0.58	0.58	6.06	(Song et al., 2011)
P25-rGO	n/a	P25	1 wt.%	18.83	0.69	0.46	5.98	19.92	0.70	0.49	6. 86	(Tsai et al., 2011)

TiO_2 with rGO (from GO)	Solvothermal	P25	ultra-small 2 nm TiO_2–rGO nanosheets	6.20	0.67	0.69	2.85	13.50	0.77	0.70	7.25	(He et al., 2011)
TiO_2 with rGO (from GO)	Dispersion	TiO_2 Nanosheets	0.75 wt.%	13.70	0.59	0.57	4.61	16.80	0.61	0.57	5.77	(Fan et al., 2012)
TiO_2-rGO	Hydrothermal	P25	1 wt.%	11.90	0.68	0.61	4.96	18.30	0.74	0.56	7.54	(Tang and Hu, 2012)
CdS- TiO_2-rGO	Hydrothermal	$Ti(OBu)_4$	8 mg	4.74	0.55	0.42	1.08	7.19	0.58	0.41	1.70	(Zhao et al., 2013)
TiO_2-rGO	Grätzel	P25	0.75 wt.%	10.75	0.69	0.57	4.20	12.16	0.67	0.68	5.50	(Shu et al., 2013a)
P25-rGO	Dispersion	P25	1 wt.%	11.90	0.69	0.61	4.96	15.40	0.67	0.64	6.58	(Tang et al., 2013)

TiO_2-rGO	CVD	TiO_2	Multilayer oxygenated rGO-TiO_2	12.70	0.70	n/a	5.60	16.0	0.73	n/a	6.70	(Shanmugam et al., 2013)
TiO_2-rGO inverse opal	Infiltrated	TiO_2 inverse opal	3 wt.%	12.39	0.66	0.60	4.86	17.10	0.72	0.61	7.52	(Kim et al., 2013)
TiO_2-rGO	Hydrothermal	$Ti(OBu)_4$	n/a	7.85	0.66	0.60	3.11	10.07	0.75	0.57	4.28	(Zhu et al., 2014)
TiO_2-rGO	n/a	TiO_2	0.005 wt.%	12.22	0.65	n/a	3.50	13.55	0.68	n/a	4.03	(Ha et al., 2016)
TiO_2-rGO	Hydrothermal	450 ˚C TiO_2-rGO	550 ˚C	13.65	0.69	0.51	4.85	14.17	0.74	0.51	5.34	(Chou et al., 2016)
Ti with rGO (from GO)	Hydrothermal	TTIP	Method comparison	15.26	0.68	0.59	5.82	18.46	0.73	0.69	8.62	(Nouri et al., 2016)
Ti-rGO	Sonication	TiO_2	0.01 wt.%	6.27	0.71	0.60	2.68	8.42	0.68	0.64	3.69	(Kanta et al., 2017)

TiO_2-rGO	Hydrothermal	TiO_2	0.5 mg/mL	6.93	0.62	0.65	2.82	12.13	0.65	0.64	5.08	(Raja et al., 2017)
rGO (from GO) with TiO_2	Thermal Reduction	TiO_2	n/a	10.14	0.68	0.67	4.60	11.06	0.67	0.74	5.50	(Zhang et al., 2017a)

To enhance the PCE performance, the continuous studies regarding ion implantation technique are explored as novelty technique for DSSCs application. Notable, there are no researches reported on Ti ion implanted on rGO as efficient photoanode for DSSCs application. This approach is trying to build out and endorsed as most effective routes to improve the DSSCs performance of TiO_2-rGO NC (photoanode) fabrication. Moreover, it is an enhanced approach which takes into consideration the photoinduced charge carrier, photogenerated electron-hole pairs, charge recombination and energy band gap of the TiO_2-rGO NC were proposed to bring the PCE to the satisfactory level. On top of that, this technique allows the incorporation of accelerated high-energy Ti^{3+} ion species into the raw surface under high applied power in a short period of time with less structural defect/low interfacial defect possibility and good optical properties as compared to the literature study (Chen et al., 2011).

Theoretically, Radio Frequency (RF) magnetron sputtering is considered as alternative way to overcome the DC magnetron sputtering by apply alternating current (AC) power source. This is a suitable method for the conductive and non-conductive target materials such as conductor, semiconductor, insulator and dielectric films (Figure 2.19). Generally, the frequency used in this technique is alternating voltages at a specific frequency of 13.56 MHz within the frequency range of 1 kHz-103 MHz. During positive electric field, the positive charged ions are accelerated to the surface of target and directly sputter the source on the FTO/ITO substrate while the negative field moment, the positive charged ions on the surface of target will be eliminated/neutralized by the electron bombardment force. However, high deposition rate of RF magnetron sputtering for FTO/ITO substrate deposition as compared to the DC sputtering magnetron sputtering accredited to the mobility difference of electrons and ions within plasma region. Therefore, high heating temperature is required to faster the sputtering process. Due to the major cost consideration of RF power supplies, RF magnetron sputtering deposition is generally limited to smaller substrate quantities and sizes.

2.6 Fabrication Technique of TiO_2-rGO NC based Photoanode in DSSCs Application

In this particular section, different preparations and various deposition technologies for the fabrication of TiO_2-rGO NC as the photoanode in DSSCs application will be highlighted and emphasized. Moreover, the schematic diagram/mechanism and PCE of DSSCs will be discussed as well. On top of that, different depositions of the TiO_2-rGO NC will be reviewed attributed to the very limited studies being reported on the physical methods. Physical method is defined as the physical spectacle for the preparation and deposition on the materials. Generally, there are two major sources/mediums have been applied under varieties of physical depositions such as liquid phase and gas phase. In this section, the PVD approach based liquid phase processes for TiO_2-rGO NC preparation such as spin coating, doctor blade printing, and eletrohydrodynamic deposition whereas the gas phase processes like thermal evaporation, electron beam evaporation, sputtering, pulsed DC sputtering, and DC magnetron sputtering & radio frequency magnetron sputtering will be briefly explained as well. At last, the recent studies for both liquid and gas phase processes as photoanode in DSSCs based materials instead of TiO_2-rGO NC were summarized in Table 2.7 & Table 2.8, respectively.

2.6.1 PVD Methods - TiO_2-rGO NC (Liquid Phase Processes)

2.6.1.1 Spin-Coating Technique

Spin coating method is a technique where the specified chemical/solvent/polymer drops on the center of substrate during the spinning at vigorous stirring. A uniform thin film will be formed and deposited on the substrate with low surface roughness. A simple schematic of spin coating including the deposition, spin up, spin off and evaporation is illustrated in Figure 2.11. In other words, the loaded solvent will be deposited uniformly on the substrate under high speed rotation and coating by centrifugal force.

The TiO_2-rGO NC prepared via spin coating method was widely utilized as photoanode assembly in DSSCs application. Tsai and co-researchers demonstrated that the TiO_2-rGO NC could be deposited on ITO substrates by spin coating method and used as an efficient electrode in DSSCs (Tsai et al., 2011). Accordingly, the presence of optimum rGO content (1 wt%) in TiO_2 could give the highest PCE of 6.86% under the light illumination of 100 $mWcm^{-2}$. This implies the reduction in photogenerated electrons loss and electron-hole pairs' recombination. Chen and co-researchers also investigated TiO_2/rGO-TiO_2 sandwich structure as working electrode via spin coating method. The ideal PCE of DSSCs was found to be 3.93% (Chen et al., 2014a). By using the spin coating method, Lee and co-researchers reported that the rGO quantum dots incorporated with the TiO_2 working electrode could give the PCE of 7.95% (Lee et al., 2013). Lately, Yao and co-researchers have established the hierarchical structures of TiO_2-rGO seed layer on FTO substrate by spin coating process, where the TiO_2 layer contains Er^{3+} and Yb^{3+} ions (Yao et al., 2016). The PCE of TiO_2:rGO-TiO_2:Er^{3+}, Yb^{3+} nanorods array was reported as 4.58% as compared to that of 3.38% for TiO_2 nanorods. The modification of TiO_2 with TiO_2:Er^{3+}, Yb^{3+} and Al_2O_3:Eu^{3+} represented the up conversion (UC) and down conversion (DC) materials, respectively. Also, the light scattering capabilities of DSSCs could be improved via the increase in light absorption, shorter charge transportation, and also faster charge carrier mobility when incorporated with rGO material. Apart from that, another advantage of utilizing the TiO_2 nanorods arrays is attributed to its one-dimensional nanostructure which can offer the direct pathway for photogenerated electrons.

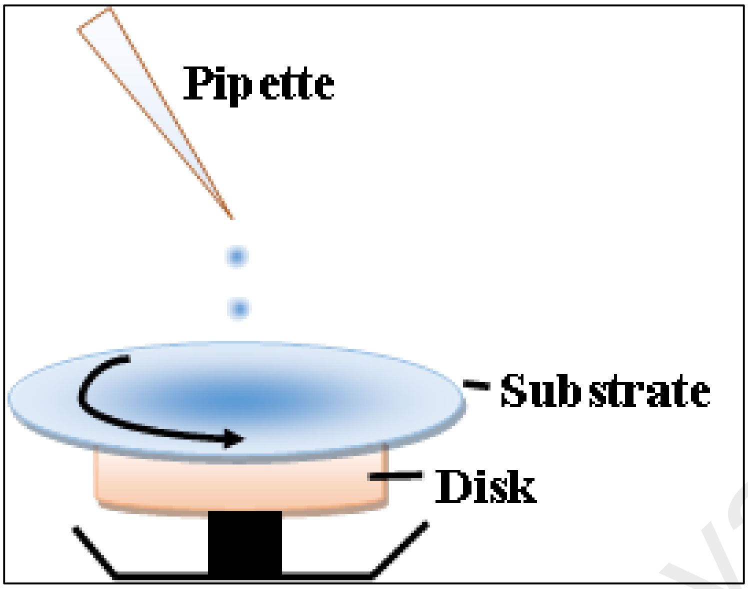

Figure 2.11: Spin coating diagram

2.6.1.2 Doctor-Blade Printing Technique

Generally, Doctor blade method is one of the alternative approaches to produce a large area thin film. Howatt and co-researchers are the first group reporting on the tape casting process producing the thin sheets of ceramic capacitors (Howatt et al., 1947). The doctor blade device to move plaster batts using aqueous and non-aqueous slurries was reported thereafter ("Method of producing high dielectric high insulation ceramic plates," 1952). Accordingly, Doctor blade or tape casting method are conducted by three simple steps, in which (i) TiO_2-rGO solution is applied along the glass substrate, (ii) a blade moving with a constant relative movement (pull and push) to spread the TiO_2-rGO along the surface active area, and (iii) TiO_2-rGO thin film formed uniformly in a gel-layer upon drying/annealing processes, as illustrated in Figure 2.12, respectively.

In DSSCs application, rGO quantum dots decorated TiO_2 nanofibers were coated onto FTO substrate by the doctor blade technique. The thickness was found to be approximately 10-12 µm thick and a high PCE of about 6.22% could be obtained (Salam et al., 2015). The strong interaction between rGO quantum dots and 1D TiO_2 nanofibers (without affecting the integrity) has consequently accelerated the photogenerated electron scan. Yoo and co-researchers (Yoo et al., 2004) have explored one-step process where the TiO_2 and rGO sheets were mixed to form the TiO_2-rGO paste. The paste was then deposited onto FTO substrate by doctor blade method (Eshaghi and Aghaei, 2015). However, a lower PCE of 0.7% was attained even if 1 wt% of rGO content was used.

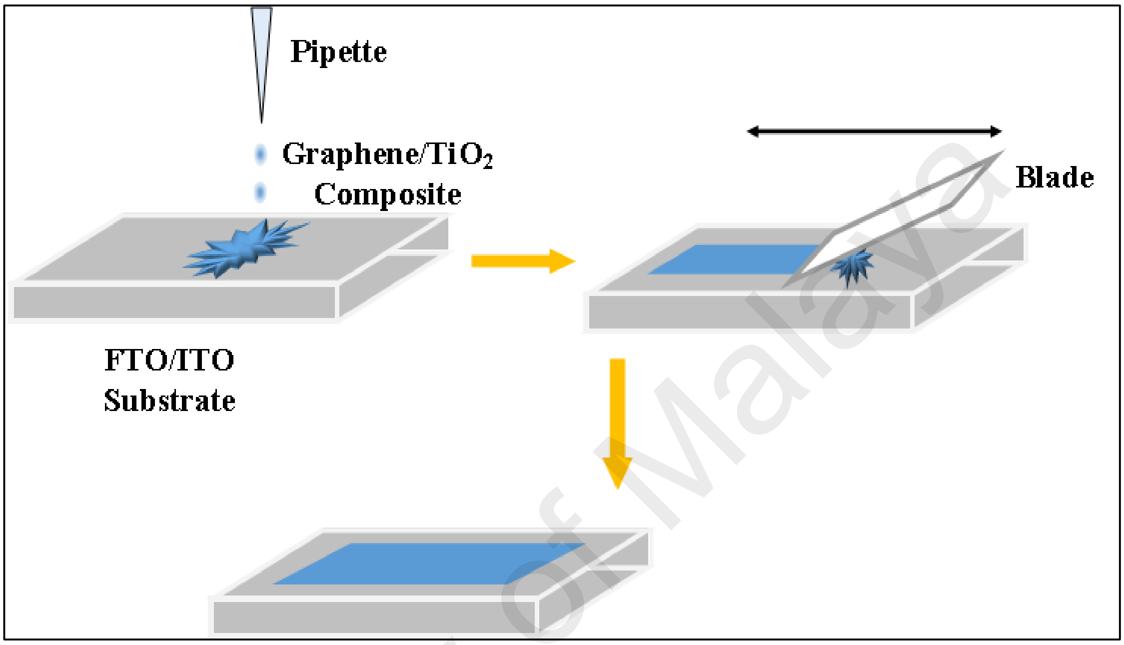

Figure 2.12: Doctor Blade technique for TiO_2-rGO as photoanode in DSSCs

2.6.1.3 Electrohydrodynamic Deposition Technique

Liquid phase of the electrohydrodynamic deposition is emphasized on the electrospray deposition, ESD (Figure 2.13). ESD method is mainly used for the fabrication of MEMS and NEMS in order to obtain thin films (< 10 µm). Normally, the nanoparticles source (liquid phase) will be converted into droplets form across the nozzle and spray to form a thin film on the FTO/ITO substrate. Among those aforementioned liquid phase deposition, ESD method has attracted the most attention and has the lowest cost merit for the large-area production (Liu et al., 2015b). The TiO_2-rGO NC thin films will be deposited uniformly by the evaporation or heating the solvent on FTO/ITO surface by sintering process.

Accordingly, polymer-TiO_2-rGO composite is able to be formed by using the ESD method in which the functionalized rGO was dissolved in *N*,*N*-dimethyl acetamide with polyvinyl acetate (PVAc) and titanium precursor. The PVAc-TiO_2-rGO composite fibers were formed as photoanode and potentially enhanced the PCE of DSSCs (Zhu et al., 2012). Recently, Liu and co-researchers (Liu et al., 2015b) studied the deposition time and the number of rGO layer deposition used as photo-anode in DSSCs by ESD method. Deposition duration for a single graphene layer was 1 min and the TiO_2-rGO NC of three layers could achieve the optimum PCE of 7.8% and 8.9%, respectively.

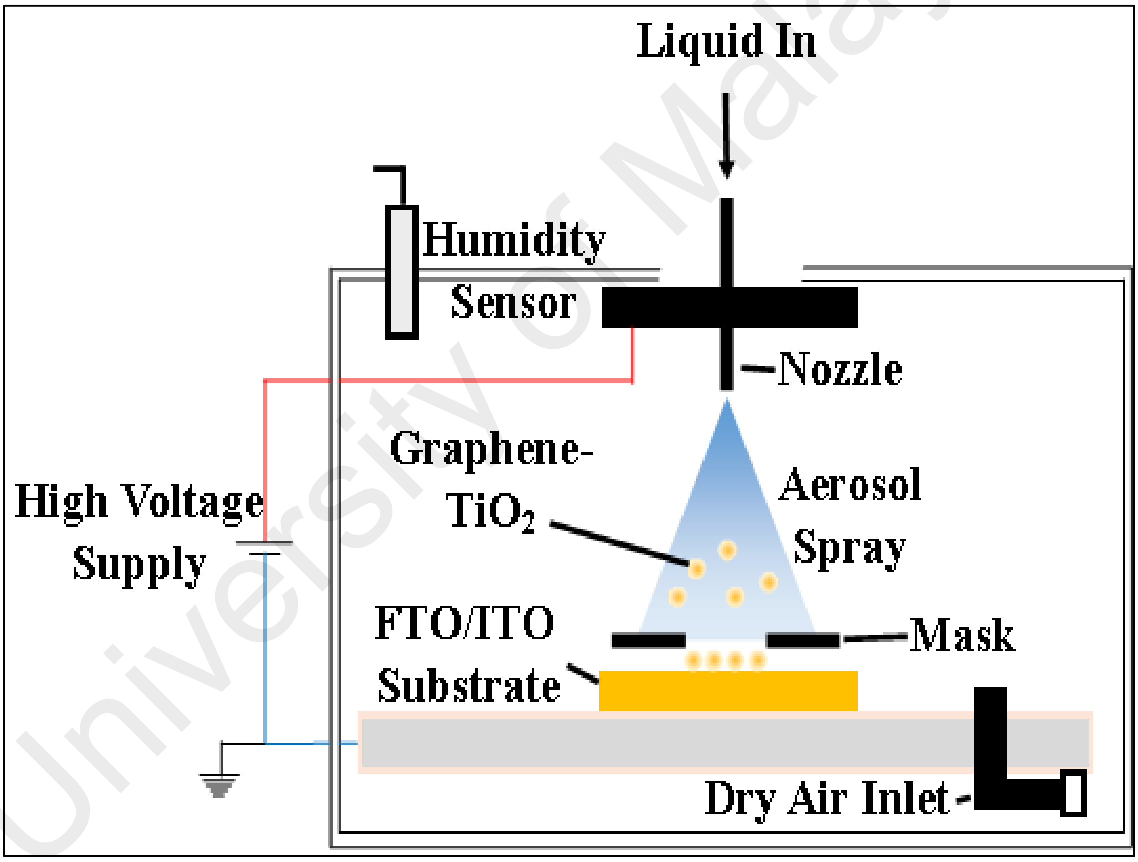

Figure 2.13: Schematic of electrospray deposition technique

Table 2.7: List of deposition techniques of liquid phase processes in DSSCs application

Deposition Method	Photoanode Materials	PCE, η (%)	Reference/Year
Spin-Coating	Luminescent Species-TiO_2	5.02	(Bella et al., 2015)/2015

Spin-Coating	Ga doped ZnO Seed	1.23	(Dou et al., 2015)/2015
Spin-Coating	Li-doped ZnO & SnO_2 nanocomposite	2.06	(Hung and Bhattacharjee, 2016)/2016
Spin-Coating	TiO_2	2.00	(Ghann et al., 2017)/2017
Doctor-Blade Printing	Mesoporous TiO_2	4.20	(Sahu et al., 2016)/2016
Doctor-Blade Printing	TiO_2	2.56	(Bernacka-Wojcik et al., 2016)/2016
Doctor-Blade Printing	TiO_2	1.14	(Kadachi et al., 2016)/2016
Doctor-Blade Printing	ZnO NS	2.00	(Patil et al., 2017)/2017
Electrospray Deposition	TiO_2 NPs	1.674	(Tang and Gomez, 2015)/2015

2.6.2 PVD Methods - TiO_2-rGO NC (Gas Phase Processes)

2.6.2.1 Physical Vapor Deposition (PVD) Technique

Generally, PVD technique is the deposition of thin film under the evaporation condition and sputtering under the vacuum chamber technology. Considering the particles tend to escape from the surface, TiO_2 particles with rGO material should be coated in closed environment. The particles moved in direct motion heading to the substrate when the TiO_2 was being heated (Figure 2.14). TiO_2 are physically coated onto rGO surface forming TiO_2-rGO NC thin films on the FTO/ITO substrate within a short deposition duration under closed chamber condition.

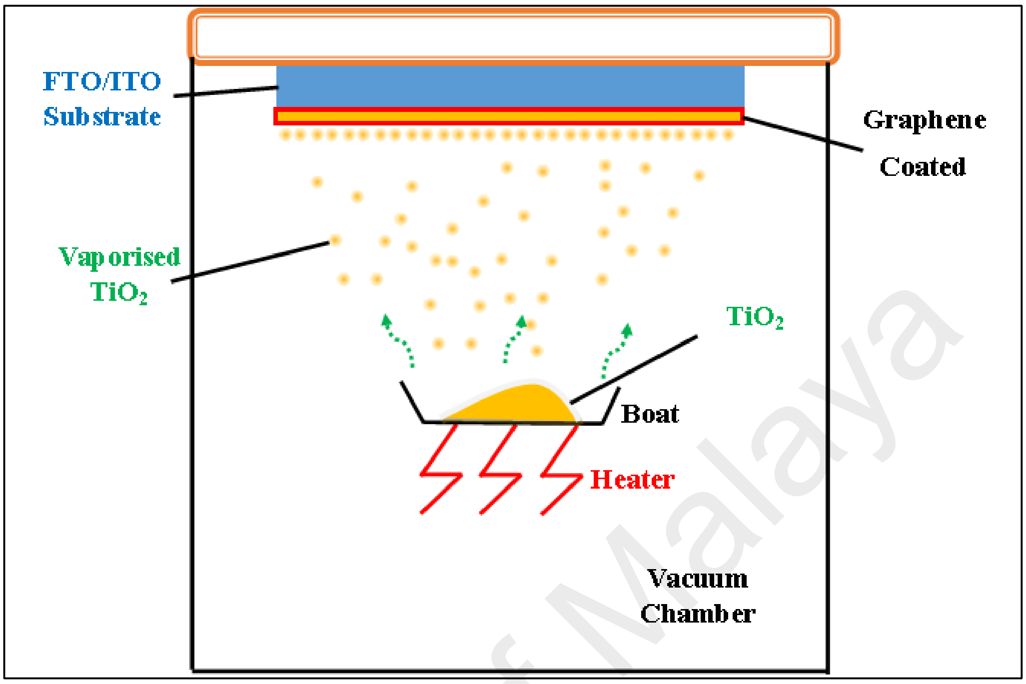

Figure 2.14: Schematic of physical vapor deposition method

2.6.2.2 Thermal Evaporation Technique

Several deposition techniques are under evaporation where the source particle material (TiO_2-rGO NC) needs to travel to the FTO/ITO substrate and being sintered into the thin film as photoanode. The evaporation techniques includes thermal evaporation, electron beam evaporation, sputtering, DC magnetron sputtering and radio frequency magnetron sputtering. This is a low cost and easy method to deposit a thin film. Upon source melting on a resistive heated boat via electrical heating, the source material is evaporated in the vacuum chamber and allows the vaporized particles directly transfer to the substrate (Figure 2.15). The high vacuum pressure is able to prevent the particles from scattering minimizing the residual gas impurities. However, an adhesive layer is needed to strengthen the thin film due to its poor adhesion properties. So far, no research work has been conducted on TiO_2-rGO thin film using this thermal evaporation method.

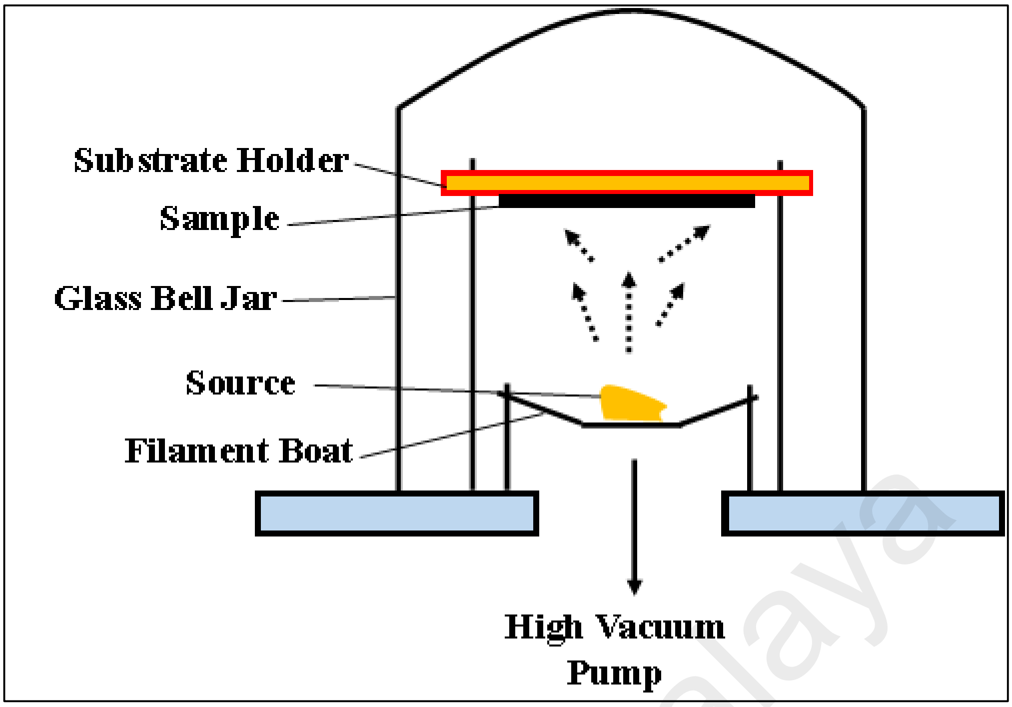

Figure 2.15: Schematic of thermal evaporation process

2.6.2.3 Electron Beam Evaporation (EBE) Technique

Electron Beam Evaporation (EBE) is one of the powerful deposition under PVD technique by applied high speed electron to bombard the target source (Figure 2.16). Kinetic energy of electron beam is produced from the electron gun by using electric and magnetic fields to shoot the target and vaporize surrounding vacuum area. Once the FTO/ITO substrate is heated by the radiation heating element, the surface atoms will have sufficient energy to leave the FTO/ITO substrate. In the same time, the FTO/ITO substrate will be coated when the thermal energy is less than 1 eV and the working distance are in the range of 300mm to the 1 meter.

Jin and co-researchers studied the reduction of back transfer electrons with the direct contact between electrolyte and the FTO glass substrate coated TiO_2 passivation layer (Jin and Choi, 2012). The preparation of the TiO_2 passivation layer was performed using EBE technique and has recorded PCE of 4.93% due to the reduction in electro-hole pairs charge recombination.

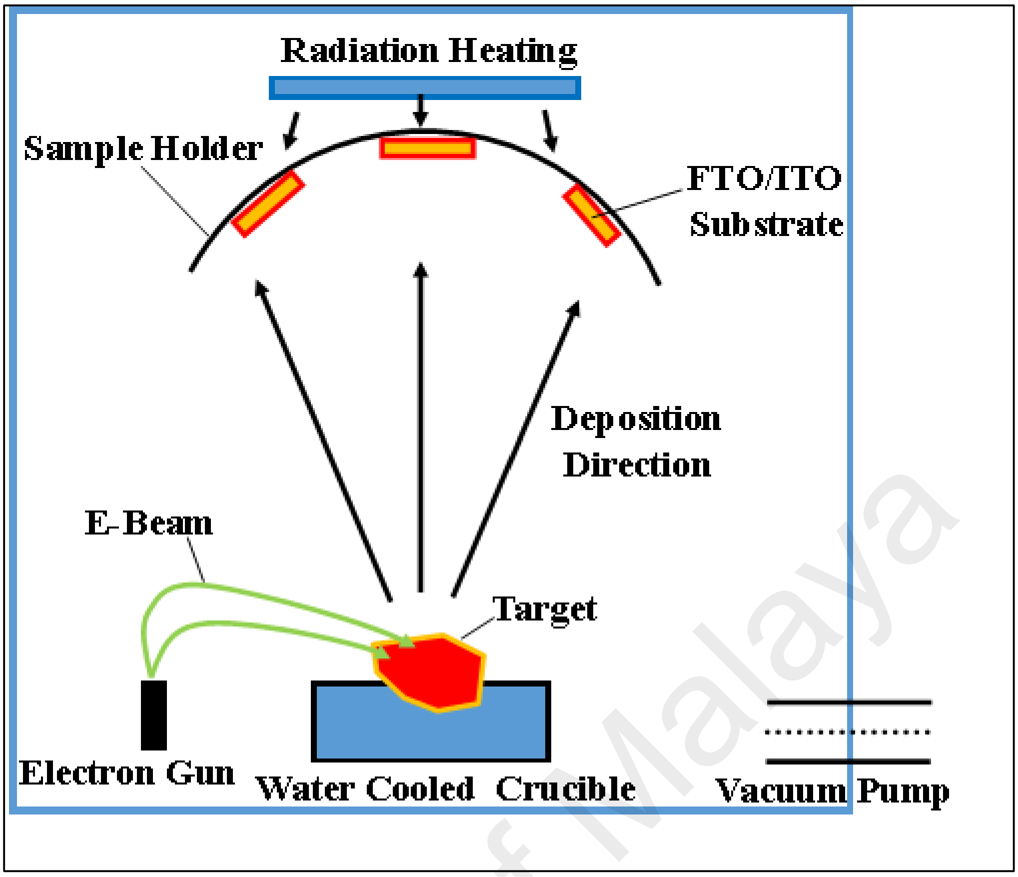

Figure 2.16: Schematic of electron beam evaporation process

2.6.2.4 Sputtering Technique

Sputtering is a useful deposition/modification technique whereby the accelerated ions are applied to expel the original particles on a target substrate via ions bombardment (Figure 2.17). In other words, sputtering method is considered as the momentum transfer process of ions that accelerated from the source to the collision of substrate particles. Apart from that, the electrical potential will cause the ions to accelerate and the ions will be reflected or absorbed to the FTO/ ITO substrate provided the kinetic energy is less than 5 eV. The substrate and lattice positions will be scratched once the kinetic energy is higher than that of the surface atom binding energy. Typically, there are two kinds of sputtering process utilizing the ions of an inert gas to eject atoms from the surface, such as (i) DC magnetron sputtering, and (ii) radio frequency (RF) magnetron sputtering. The advantage of using DC magnetron sputtering is its ability to increase the deposition rate with a minimal damage to the FTO/ITO substrate while the RF magnetron sputtering provides a direct pathway deposition of insulators. The common use of deposition materials by these two techniques are metal, alloy, and organic compound. In addition, there are also several sputtering with different deposition conditions like pulsed DC sputtering power (DCMSP), MF mid frequency AC sputtering power, high-power impulse magnetron sputtering (HIPIMS) etc.

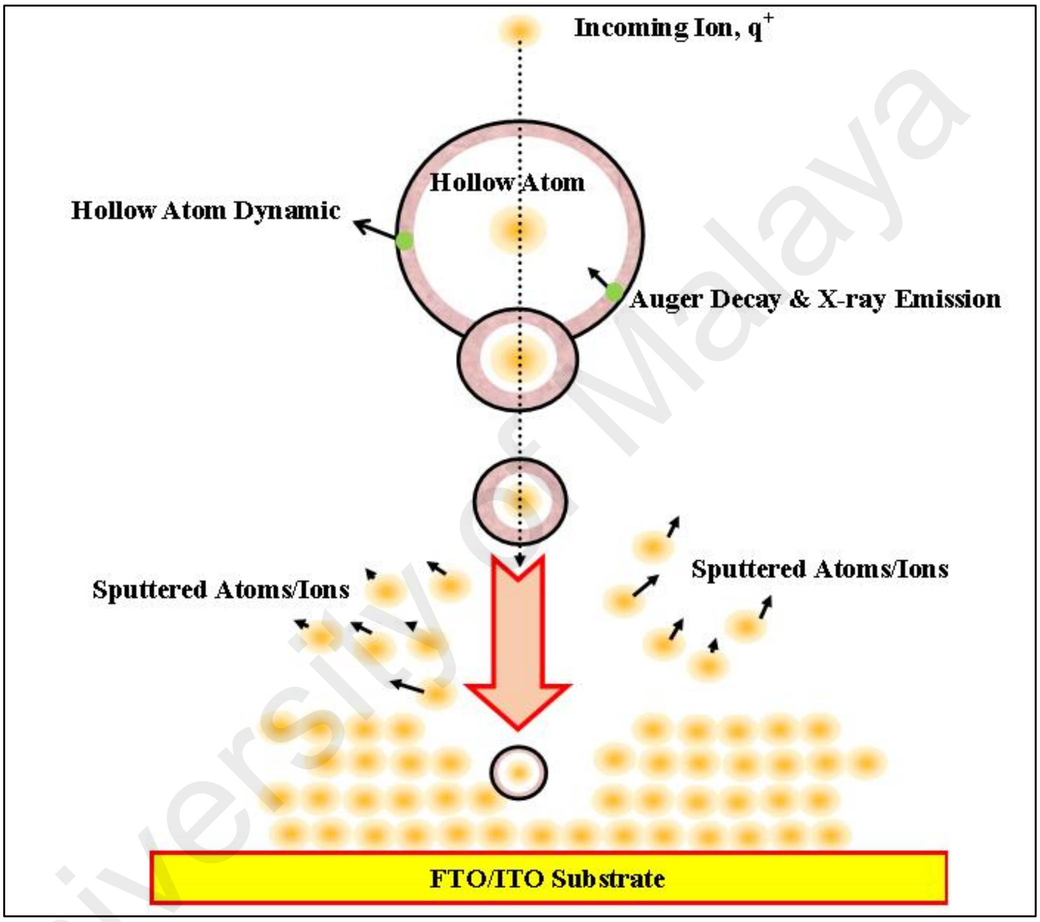

Figure 2.17: Schematic of sputtering process

(a) *Pulsed DC Sputtering Power Technique*

Pulsed DC sputtering technique is generally used for metals deposition and dielectrics coating so that the insulator materials are able to receive donator charge (Figure 2.18). This coating technology is widely used in industry sector such as semiconductor and optical for large area production. Also, this technique has been found broad application in reactive sputtering where the chemical reaction occurred in the plasma region between ionized gases and vaporized target materials. In reactive sputtering, the usage of oxygen, O_2 gas is to combine the target material within the plasma to form oxide molecules, while the argon, Ar gas is to convey kinetic energy upon impacting with the target materials.

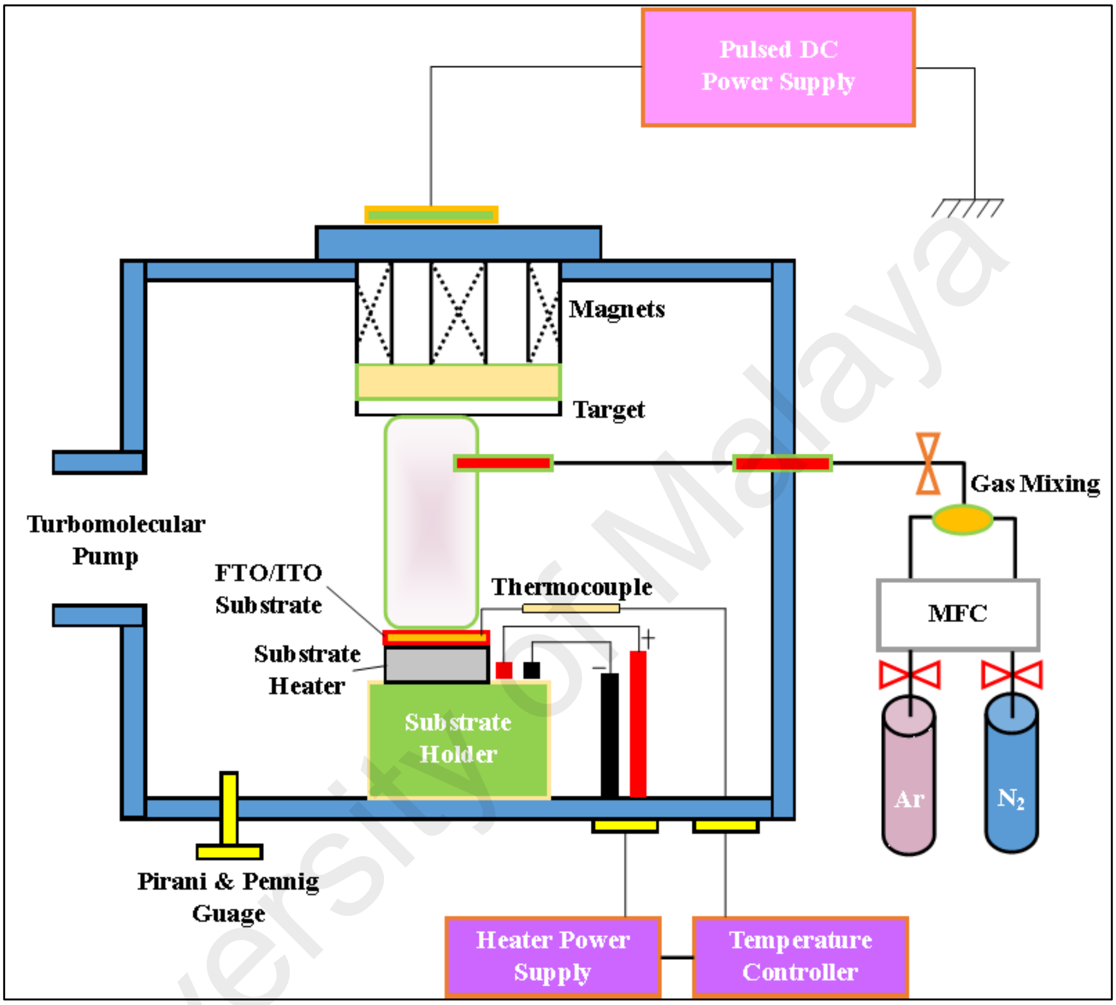

Figure 2.18: Schematic of pulsed DC magnetron sputtering power technique

(b) ***DC & RF Magnetron Sputtering Technique***

Direct current (DC) magnetron sputtering concept is the oldest deposition technique among the magnetron sputtering field. Accordingly, this particular method would compromise the ionization of the mixture of Argon, Ar and Nitrogen, N_2 gas while the positively charged sputtering gas could be easily accelerated towards the conductive target materials causing the ejected target atoms to deposit on the ITO/FTO substrate easier (Figure 2.19). It is a controllable and low cost sputter technique for relatively large substrate quantity and large scale production. Typically, the working DC sputtering technique is under 1000-3000V and the vacuum chamber is around 10^{-3} Pa with pressure around 0.075 to 0.12 torr. However, this technique can only be applicable for the conductive material but not for dielectric target. This is mainly attributed to the termination of the discharge of insulator materials during deposition process. In other words, the positive charge ions will be produced and accumulated on the surface of the dielectric or insulator films.

Radio Frequency (RF) magnetron sputtering can be considered as the alternative way to overcome the DC magnetron sputtering by applying alternating current (AC) power source. This approach is a suitable method for conductive and non-conductive target materials such as conductor, semiconductor, insulator, and dielectric film. Generally, the frequency used in this technique is an alternating voltage at a specific frequency of 13.56 MHz within the frequency range of 1 kHz-103 MHz. During the positive electric field, the positively charged ions would be accelerated to the surface of the target and directly sputtered the source on the FTO/ITO substrate. The positively charged ions on the surface of target will be eliminated/neutralized by the electron bombardment force during the negative field moment. However, high deposition rate of RF magnetron sputtering for FTO/ITO substrate deposition as compared to that of the DC sputtering magnetron sputtering has led to the mobility difference between the electrons and ions within plasma region. Therefore, high heating temperature is required to accelerate the sputtering process. RF magnetron sputtering deposition is generally only limited to smaller substrate quantities and sizes due to the cost consideration of RF power supplies.

Currently, Chen and co-researchers (Chen et al., 2014a) have deposited rGO film onto ITO substrate for 2 mins using the RF magnetron sputtering technique with the carbon target (99.99%) as the first photoanode layer under input power of 90 W and Ar gas flow rate of 90 sccm, while the TiO_2 film as second photoanode layer with spin-coating technique. The attained PCE was found to be 2.46%. Among these deposition based gas phase processes approach, the RF magnetron sputtering method is aimed to utilize in this project due to the Ti^{3+} ions might would simply accelerated with high energy under high applied power in a short period of time and implanted onto rGO surface or lattice.

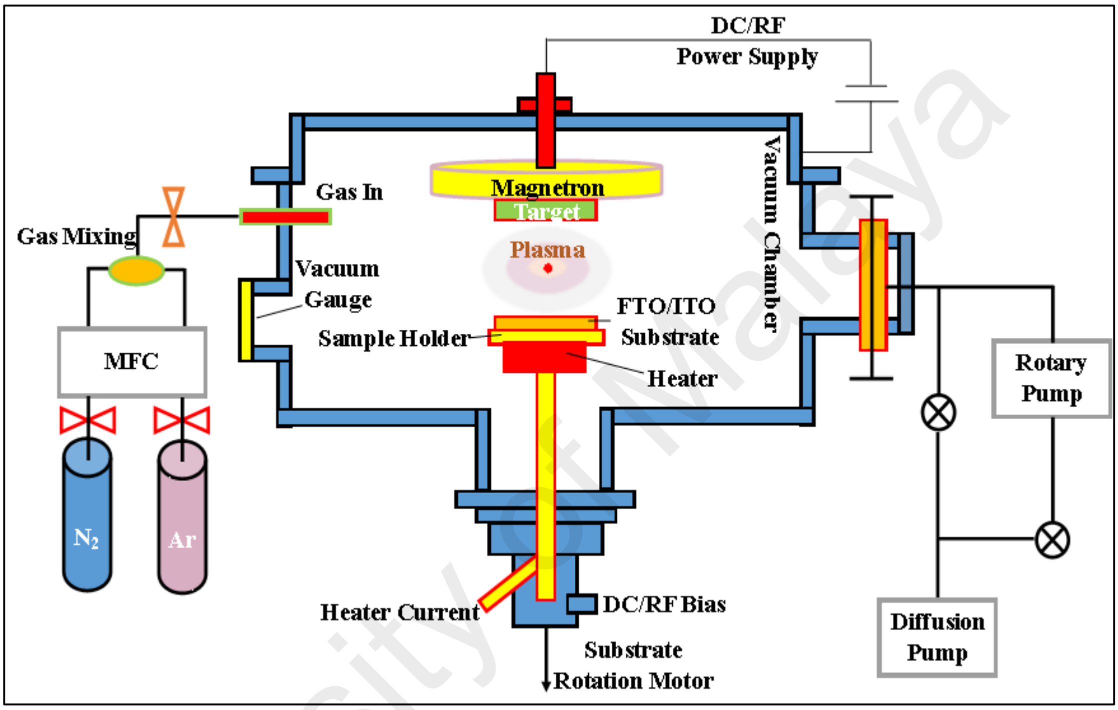

Figure 2.19: Schematic of DC/RF sputtering deposition technique

In term of deposition technique, all the best of authors' knowledge, there is less literature reporting on the gas phase processes to incorporate TiO_2 with rGO material. Table 2.6 shows the photoanode materials prepared using a variety of deposition methods to enhance the PCE of DSSCs. These gas phase processes included conductor and insulator materials coating other than that of the TiO_2-rGO NC materials for DSSCs application.

Table 2.8: List of deposition techniques based on gas phase processes in DSSCs application

Deposition Method	Photoanode Materials	PCE, η (%)	Reference/Year
PVD	GO-TiO_2	4.65	(Agarwal et al., 2015)/2015
PVD	Ag-TiO_2	4.80	(Noh et al., 2016)/2016
PVD	Mg^{2+}-TiO_2	5.90	(Cheng et al., 2016)/2016
Thermal Evaporation	rGO-TiO_2-P3HT-$PC_{61}BM$/PEDOT/PSS/Ag	2.32	(Morais et al., 2015)/2015
Thermal Evaporation	GO-ZnO	4.52	(Ahmed et al., 2016)/2016
EBE	Au-TiO_2	-	(Lee et al., 2016)/2016
Pulsed DC Sputtering	NiO_x-TiO_2	2.79	(Lin et al., 2013)/2013
DC Sputtering	TiO_2	4.00	(Waita et al., 2007)/2007
DC Sputtering	AZO/Ag/AZO	0.60	(Sutthana et al., 2010)/2010
DC Sputtering	TiO_2	2.07	(Meng and Li, 2011)/2011
RF Sputtering	TiO_2-rGO-TiO_2	3.93	(Chen et al., 2014a)/2014

RF Sputtering	Graphene/ZnO	3.98	(Hsu et al., 2014b)/2014
RF Sputtering	AZO/TiO_2/TiO_2 Porous Layer	5.69	(Huang et al., 2015)/2015

CHAPTER 3: METHODOLOGY

3.1 Introduction

This chapter presents experimental and characterization techniques which have been employed in this work. Herein, details of materials selection, methods, and flow of works are listed.

3.2 Materials and Chemicals

i. Graphite Flakes

Graphite flakes with <45 µm and ≥99.99% trace metals basis in powder form was purchased from Sigma Aldrich, Malaysia.

ii. Potassium Permanganate

Potassium Permanganate ($KMnO_4$) with 97% in crystalline powder form was purchased from Sigma Aldrich, Malaysia.

iii. Hydrazine Solution

Hydrazine solution with 35 wt. % in H_2O, 1.011 g/mL at 25 ℃, >1 (vs air), 5 mmHg (25 ℃) in solution form were purchased from Sigma Aldrich, Malaysia.

iv. Sulfuric Acid Solution

Sulfuric Acid (H_2SO_4) Solution with 0.5 M, 1 N in solution form were purchased from Merck Millipore, Malaysia.

v. Phosphoric Acid

Ortho-Phosphoric Acid (H_3PO_4) with 85% in solution form were purchased from Merck Millipore, Malaysia.

vi. Hydrogen Peroxide

Hydrogen Peroxide (H_2O_2) with 30% in solution form were purchased from Merck Millipore, Malaysia.

vii. Hydrochloric Acid

Hydrochloric Acid (HCl) with 37%, AR grade in solution form were purchased from Sigma Aldrich, Malaysia.

viii. Nitric Acid

Nitric Acid (HNO_3) for analysis EMSURE® Reag. Ph Eur,ISO with 65% in solution form were purchased from Merck Millipore, Malaysia.

ix. Acetonitrile

Acetonitrile with 99.8% and 41.05 g/mol in gel form were purchased from Sigma Aldrich, Malaysia.

x. Titanium (IV) Isopropoxide

Titanium (IV) Isopropoxide (TTIP) with 97% in liquid form were purchased from Sigma Aldrich, Malaysia.

xi. Triton X-100

Triton™ X-100 with laboratory grade in liquid form were purchased from Sigma Aldrich, Malaysia.

xii. Fluorine Doped Tin Oxide Coated Glass Slide

Fluorine Doped Tin Oxide Coated (FTO) Glass Slide with surface resistivity ~7 Ω/sq were purchased from Sigma Aldrich, Malaysia.

xiii. Di-tetrabutylammonium *cis*-bis(isothiocyanato) bis (2,2’-bipyridyl-4,4’-dicarboxylato)ruthenium(II)

Di-tetrabutylammonium *cis*-bis(isothiocyanato) bis (2,2’-bipyridyl-4,4’-dicarboxylato)ruthenium(II), N-719 with 95% in dye content were purchased from Dye-Sol Sdn. Bhd., Malaysia.

xiv. 2-propanol

2-propanol for analysis EMSURE® ACS,ISO,Reag. Ph Eur with 60.1 g/mol in solution were purchased from Merck, Malaysia.

xv. Acetic Acid

Acetic Acid with 60.05 g/mol in solution form were purchased from Sigma Aldrich, Malaysia.

xvi. Potassium Iodide

Potassium Iodide (KI) Emsure® ISO,Reag. Ph Eur in powder form were purchased from Merck Millipore, Malaysia.

3.3 Synthesis Method Procedure

3.3.1 GO Synthesis

In a typical procedure, GO was synthesized from graphite flakes by an Improved Hummer’s method. A H_2SO_4:H_3PO_4 (180:20 mL) solution was added to a mixture of graphite flakes (1.5 g) and $KMnO_4$ (9.0 g). The overall process was reacted in an ice–water bath condition (<20 ℃) (Marcano et al., 2010). Five reaction mixture samples were then stirred for 6, 12, 24, 48, and 72 h at constant speed (1200 rpm) to allow oxidation of graphite. In Figure 3.1, the color of the mixture changed from dark purplish green to dark brown color revealed that the oxidizing agent ($KMnO_4$) was fully mixed with the solutions (H_2SO_4, H_3PO_4, and graphite) (Lin et al., 2015). Then, the reaction mixture was cooled to room temperature and then poured into ice cube (~ 200 mL) with 3 mL of H_2O_2 to stop the oxidation process, and the color of the mixture changed to light brownish color, indicating a high oxidation level of graphite (Marcano et al., 2010). The GO was formed after centrifuged (7,000 rpm) for three times with HCl by using Eppendorf Centrifuge 5430 R [Capacity for 50 mL conical tubes (7800 rpm with 6 tubes)], and the supernatant was decanted away. The process was repeatedly done with deionized water (DI water) until a pH of 4-5 was achieved. Finally, the product known as GO powder was formed after the washing process and the GO experienced exfoliation. The GO was dried at 90 ℃ in a vacuum oven overnight to form the black color of GO.

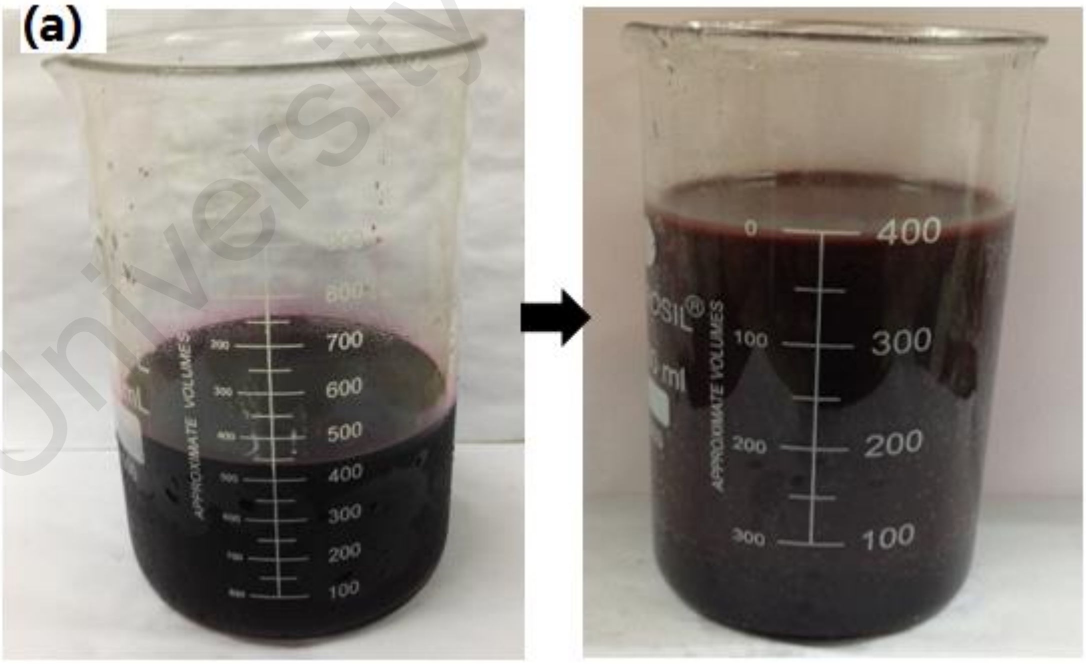

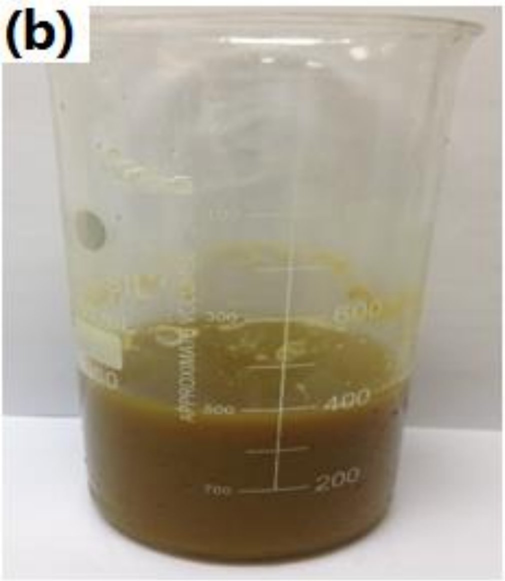

Figure 3.1: Color changes of (a) H_2SO_4, H_3PO_4, and Graphite to H_2SO_4, H_3PO_4, graphite, and $KMnO_4$ and (b) Mixture of (a) with H_2O_2

3.3.2 rGO Synthesis

GO was prepared according to the Improved Hummer’s Method in Figure 3.2 (a) which is obtained in Figure 3.1. The chemical reaction between oriented graphite multilayers and H_2SO_4/H_3PO_4 formed the GO, as shown in Figure 3.2 (b). The oxidation reaction in the graphite oxide solution was then terminated by the H_2O_2 solution (3 ml) after 72 hours forming the GO decorated with oxygenated functional groups (Figure 3.2 (c)) (Thakur and Karak, 2012). Finally, the GO was converted into a monolayer of rGO, via the chemically reduction method, by the addition of purified water (3 mg/mL) and hydrazine solution (1μL for 3 mg of GO) to prepare the high-yield nanoscale sheet (≈ 46 nm), as illustrated in Figure 3.2 (d). The process was repeated with stirring rates of 6, 12, 24, 48, and 72 h for each of the five samples of GO described above (6, 12, 24, 48, and 72 h). The rGO samples were dried in bench-tip air oven at 90 ℃ for 48 h.

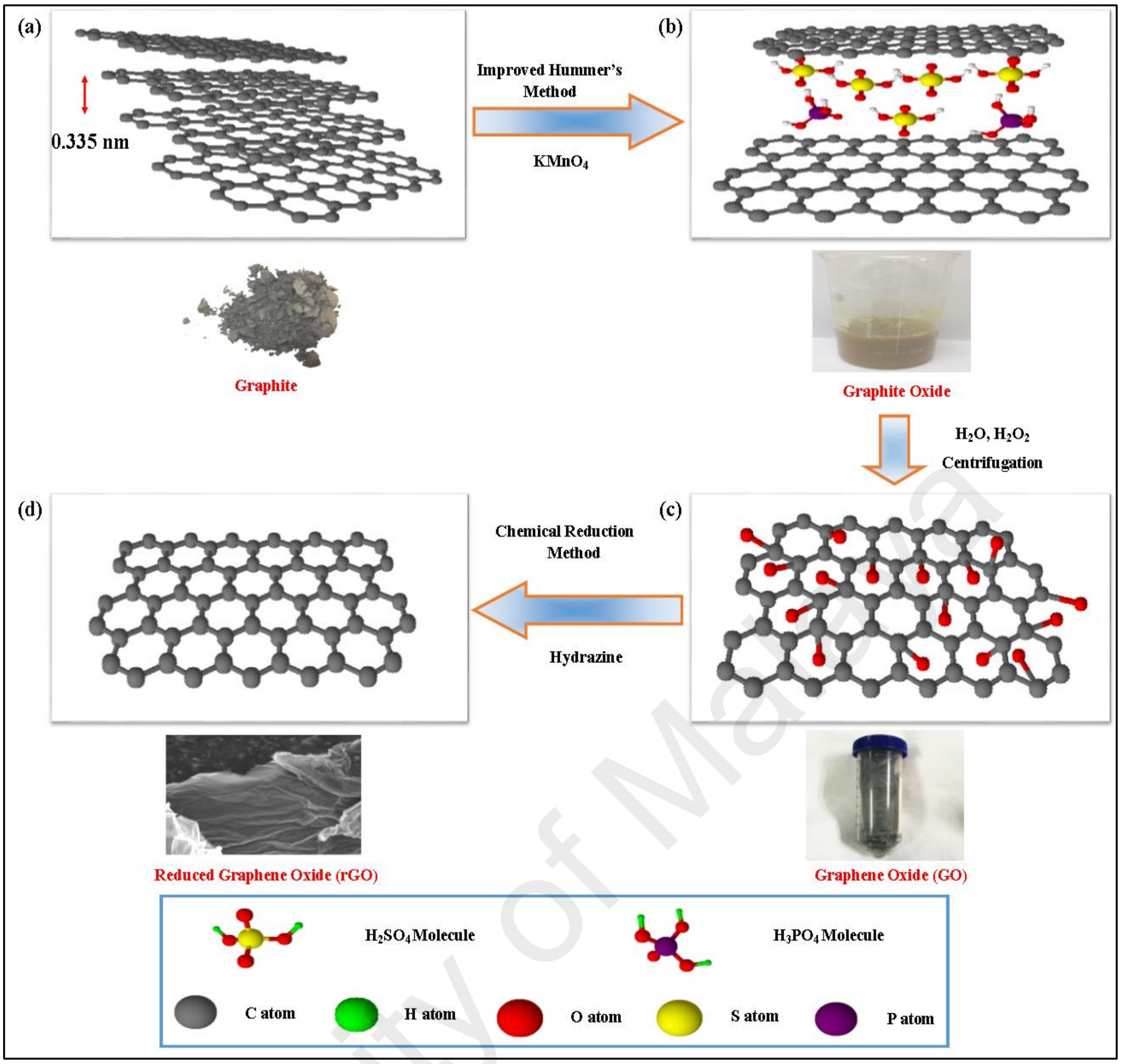

Figure 3.2: GO and rGO experimental synthesis mechanism

Figure 3.3 shows the three major steps comprises of the morphological image of graphite, one intermediate products (graphite oxidation reaction) and the final product of rGO. In the initial stage, the graphite flakes (solid black lines) in multi-layers formation. Then it reacted with H_2SO_4, $KMnO_4$, and HNO_3. The wide light green lines represent H_2SO_4/HSO_4^- intercalate during the oxidation process while the wide red lines represent a layer of mixture H_2SO_4/HSO_4^- intercalant with the oxidizing agent. Lastly, the GO was fully formed by the oxidizing agent which contained the H_2SO_4/HSO_4^- intercalant. Then GO will be further treated with hydrazine to form rGO.

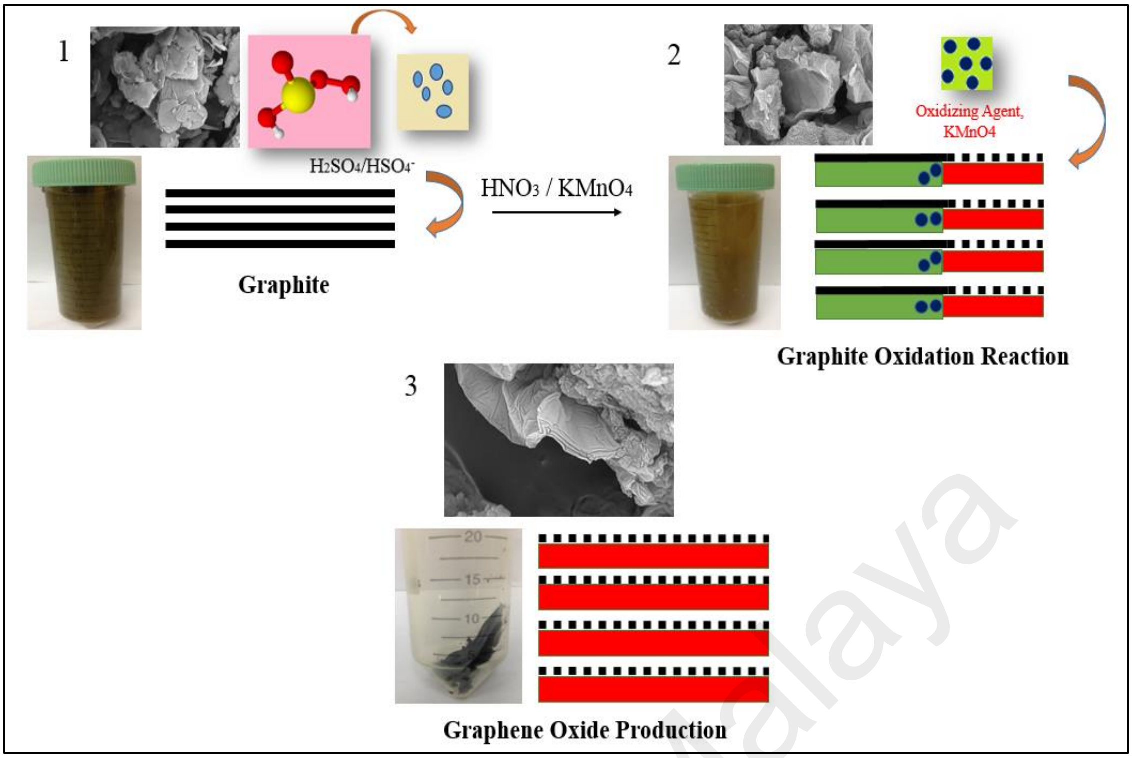

Figure 3.3: Schematic of GO synthesis from graphite flakes with corresponding images sample appearances at each stages

3.3.3 TiO_2 Synthesis

TiO_2 were prepared by the precipitation-peptization method by using TTIP as a precursor. At the beginning, the 10 mL of TTIP was added into the 40 mL of propanol solution. Then the transparent mixtures were performed after stirring continuously for 30 mins labelled as the first step mixture. Subsequently, a 5 mL of Acetic Acid, 10 mL of propanol, and a drop of Triton X-100 were poured into 10 mL of purified water, respectively. The mixture is stirred for 30 mins and labelled as the second step mixture. Next, the first step mixture was added slowly to the second step mixture with the rate of 1 mL/min. Finally, the mixture is stirred for 2 h and the homogenous of TiO_2 solution was obtained.

Regarding the NC process, the synthesized TiO_2 solution was poured slowly to the GO solution with 0.1 wt%, 0.2 wt%, 0.3 wt%, 0.4 wt%, and 0.5 wt% of TiO_2, respectively. The TiO_2-GO solution was stirred for 1 hour and then poured into a 50 ml Teflon-sealed autoclave. The TiO_2-GO solution was heated in a furnace at 180 ˚C for 9 hour. The GO was turned into rGO without reducing agent applied. Besides, the phase of TiO_2 was changed to anatase from brookite in order to narrow the band gap energy of DSSCs interfaces after incorporation with rGO (Yanagisawa and Ovenstone, 1999). At last, the anatase-TiO_2 were formed and incorporated with rGO. The molecular structure of TiO_2-rGO NC will be further discussed in Figure 5.12.

3.4 Preparation of Photoanode and Cathode in DSSCs – One-Step Hydrothermal Technique

Firstly, the FTO glass slide was cut in 1 cm^2 and rGO with and without the various amount of TiO_2 was pasted by the doctor-blade techniques, respectively. The active area of approximately 0.67 cm^2 was prepared as the photoanode part. The sintering process was carried out for each FTO glass by heating at 450 ℃ for 15 mins. Secondly, the sintered FTO containing rGO with and without the various amounts of TiO_2 as photoanode were soaked into a solution containing the anhydrous ethanol and 0.5 mM N-719 dye for overnight. Subsequently, the dyed-sensitized rGO with and without various amounts of TiO_2 were rinsed with acetonitrile in order to eliminate the physisorbed N-719 dye molecules. Thirdly, the cathode part was prepared by applying the 2B graphite pencil for 0.7 cm^2 as cathode side. Then, the photoanode was sandwiched together with the cathode and clipped with a normal paper clip. Finally, a few drops of KI electrolyte (0.5 M) were applied slowly and flowed between the photoanode and cathode. The diagram of DSSCs device of TiO_2-rGO NC based-DSSCs is shown in Figure 3.4.

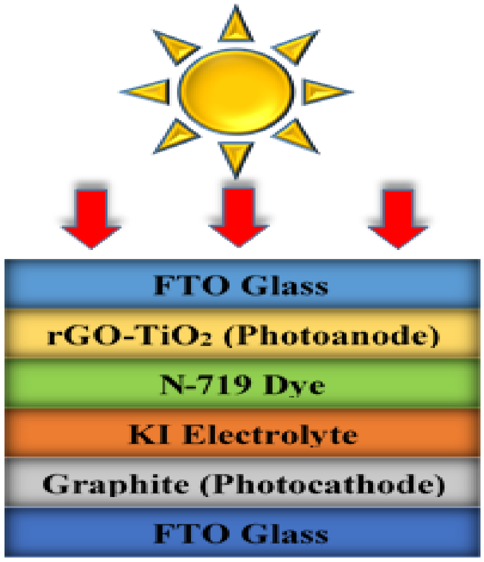

Figure 3.4: TiO_2-rGO NC Based-DSSCs Diagram

3.5 Preparation of Photoanode and Cathode in DSSCs – Ion Implantation Technique

The TiO_2-rGO NC based photoanode was prepared for the DSSCs device. Accordingly, the rGO NS was first deposited onto the FTO glass (2 cm x 2 cm) by the electrodeposition method as reported elsewhere (Low et al., 2015c). Deposited rGO NS was prepared for 10 samples in this study. 5 samples for Ti ions deposition based applied power with 50 W, 100 W, 150 W, 200 W, and 250 W whereas another 5 samples for sputtering duration study with 10 s, 20 s, 30 s, 40 s, and 60 s. Next, the rGO samples were sent to SIRIM, Malaysia for further Ti ion implantation using RF sputtering instrument. The purity of Ti target is 99.99%, diameter in 2 inch, and thickness in 0.25 inch. The target distance was fixed at 10 cm between Ti target with the sample while Ar gas flow rate at 15 sccm. In order to avoid surface contaminants, pre-sputtering was flow by pure Ar gas for 15 mins. Besides, the base pressure is 5 x 10^{-6} Torr and sputter process pressure at constant 2 x 10^{-3} Torr. These parameter were fixed for the applied power study set with constant deposition at time 40 s whereas sputtering duration study set with constant applied power at 150 W.

3.6 DSSCs Fabrication

In Figure 2.2, DSSCs have a sandwich configuration consisting of photoanode, cathode, N-719 dye and KI electrolyte. The active area of photoanode/counter electrode was fixed with 0.16 cm^2. To construct DSSCs, the N-719 dye that could absorb into the photoanode naturally was applied on the as-prepared TiO_2-rGO NC based photoanode. The remaining dye stained was then rinsed by ethanol followed by placed on the hotplate for the evaporate purpose. On the other hands, the electrodeposition process was conducted on the cathode in which the FTO glass slide was immersed into the solution containing 1.5 g of rGO, 100 ml distilled water and 4 ml of C_2H_3N for 30 mins. Finally, both electrodes were clipped together followed by applied 3 M of KI electrolyte.

3.7 Characterization

3.7.1 Synthesis of GO and rGO

The functional groups of GO and rGO samples were analyzed over a wave number range of 500–4000 cm^{-1} using a Bruker-IFS 66/S Fourier transform infrared (FTIR) spectroscopy by KBr pellet method in order to compare the changes in functional groups of carboxyl group (-COOH), carbonyl group (-C=O), and epoxide group (-O-). The spectra were recorded in 500–4000 cm^{-1} range. The phases of the GO and rGO were determined by X-Ray diffraction (XRD) using a D8 Advance X-Ray diffractometer-Bruker AXS by employing a scanning rate of 0.033 °s^{-1} in a 2θ range from 5 °to 60° with CuKα radiation (λ = 1.5418Å). Furthermore, Raman spectra were obtained using a Renishaw inVia microscope with HeCd laser source [laser excitation source (λ = 514.0 nm) at room temperature] for functional group and structural identification purpose. The band gaps of GO and rGO were calculated using Cary 60 UV–visible spectrophotometer from Agilent Technologies with 400 nm/s scan rate and 200–800 nm wavelength range. The surface morphologies of the samples were observed by scanning electron microscopy (SEM) using a TM3030 tabletop microscope at a working distance of approximately 2.0

mm at high vacuum mode with 5.0 kV and images were magnified into 30,000X times. The elemental analysis of the graphite flakes, GO, and rGO were determined using energy dispersion X-Ray (EDX microanalysis) equipped in the SEM. The morphologies for GO and rGO were further confirmed through high-resolution transmission electron microscopy (HRTEM) using a JEM 2100-F with 200 kV accelerating voltage.

For electrical characterization, an electrolysis method setup was employed for graphite, GO, and rGO deposition process. The overall process involved coating a very thin layer of graphite, GO, and rGO onto fluorine-doped tin oxide-coated glass slide (FTO, ~7 Ω/sq; Sigma-Aldrich). For deposition purpose, the two electrodes of FTO glass were immersed into a solution of 100 mL of DI water, 1 mL of acetonitrile, and 0.15 g of graphite. The two electrodes were then connected to a power supply with 60.0 V for 15 mins processing, which created a circuit through the graphite. The very thin layer of graphite, GO, or rGO will coated on anode side (-). The purpose of utilize FTO glass slide as both electrodes because of make easier to transfer the coated thin layer of graphite, GO, and rGO for anode side to tri-electrode system. Subsequently, the coated sample was connected in a tri-electrode system (red color) on an Autolab PGSTAT204 instrument and the samples were characterized under 300 W of solar illumination light source. Linear sweep voltammetry was carried out on the graphite in H_2SO_4 at various voltages; from -0.3 V reduction at the beginning, a maximum reduction was observed at 0.3 V. The process was repeated with dark condition, 0.15 g of GO, and rGO instead of graphite. The configuration system is shown in Figure 3.5.

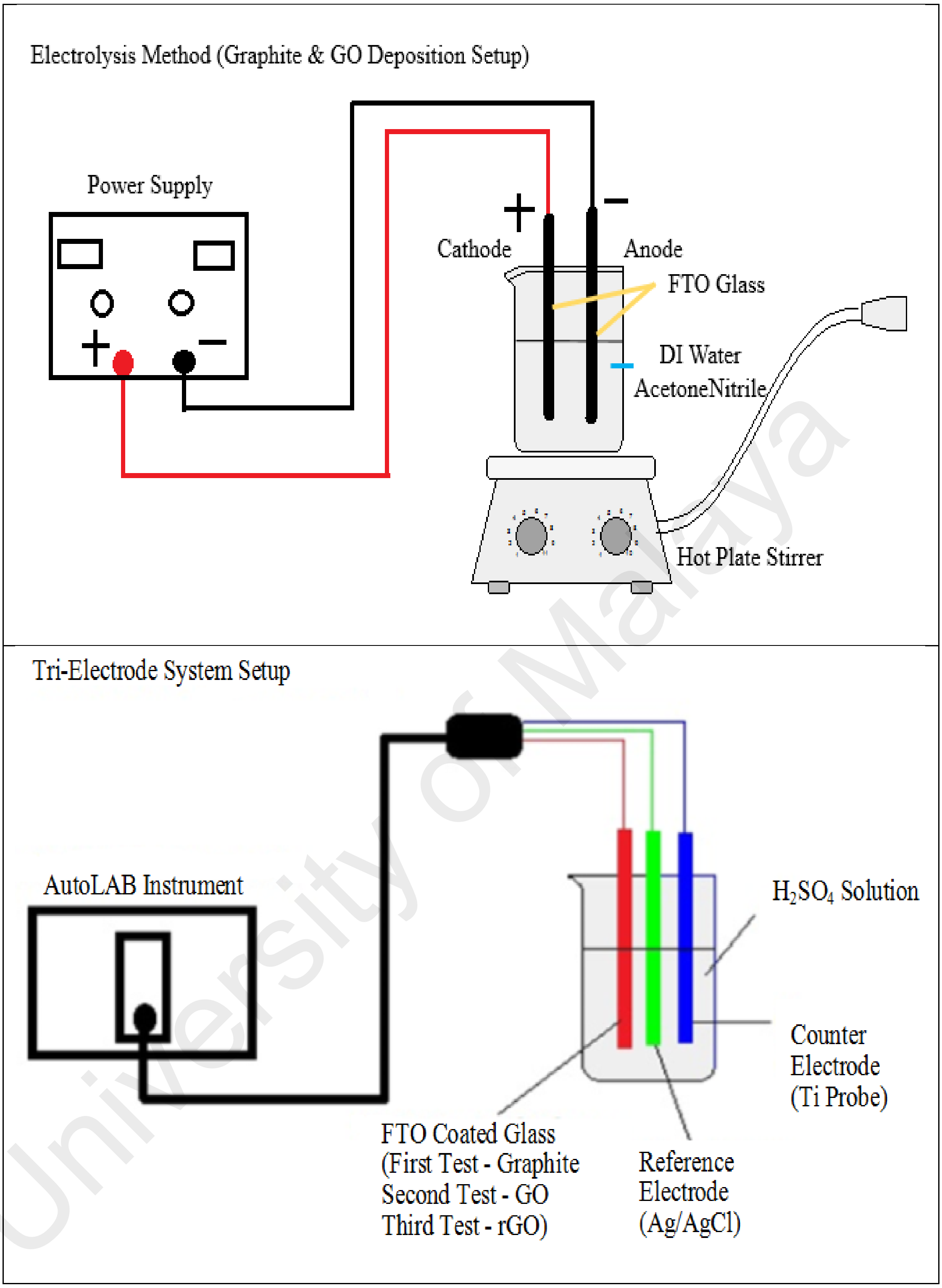

Figure 3.5: Electrolysis deposition and electrical characterization configuration setup

3.7.2 TiO_2-rGO NC based photoanode in DSSCs – One-Step Hydrothermal Technique

The sheet resistance of rGO thin film was measured using four point probe instrument. Several techniques were employed for the characterization of TiO_2-rGO NC. The phases of the rGO, TiO$_2$, and NC were determined by X-ray diffraction (XRD) using a D8 Advance X-ray diffractometer-Bruker AXS by employing a scanning rate of 0.033 $^\circ s^{-1}$ in a 2θ range from 10 ° to 90° with CuKα radiation (λ = 1.5418Å). Furthermore, the Raman spectra were obtained using a Renishaw inVia microscope with HeCd laser source [laser excitation source (λ = 514.0 nm) at room temperature] for the functional group and structural identification purpose. The band gaps of the NC samples were calculated using the Cary 60 UV–visible (UV-VIS) spectrophotometer from Agilent Technologies with 400 nm/s scan rate and 200–800 nm wavelength range. The topology, surface roughness, and height profile were carried out by using the atomic force microscopy (AFM) from the Bruker Multimode 8 instrument and the data were analysed by using the Nanoscope Analysis software. The particle size and morphology of the NC were observed by scanning the electron microscopy (SEM) using a TM3030 table top microscope at a working distance of approximately 2.0 mm at high vacuum mode with 5.0 kV and images were magnified into 30,000X times. Next, the elemental analysis of rGO and TiO$_2$-rGO was determined using the energy dispersion X-ray (EDX microanalysis) from the TM3030 table top microscope. For the photovoltaic performance test, the measurement of photocurrent density (*J*) versus the applied voltage (*V*) plotted data was obtained from the AUT 50284, Metrohm Autolab (PGSTAT204) under AM 1.5 condition (Input power, P$_{in}$ = 100 W) by using Mercury Xenon Lamp whereas the Nyquist plotted graph of electrochemical impedance spectroscopy (EIS) was performed from Metrohm Autolab (PGSTAT100N). Both characterizations were measured under the illumination of AM 1.5 condition (Newport 91160, 300W xenon lamp, USA).

3.7.3 TiO$_2$-rGO NC based photoanode in DSSCs – Ion Implantation Technique

The crystal structure and degree of crystallinity of rGO and TiO$_2$-rGO NC were studied using X-ray diffraction (XRD). The XRD were performed using D8 Advance X-ray diffractometer-Bruker AXS by employing scanning rate of 0.033 deg/s in a 2θ range from

10˚ to 90˚ with CuKα radiation (λ=1.5418 Å) at 40 kV and 30 mA. The morphology and lattice structures of rGO, rGO NS and TiO_2-rGO NC were characterized by field emission scanning electron microscopy (FESEM, FEI Quanta 200 FEG), HITACHI UHR Cold-Emission FE-SEM SU 8000 and JEM 2100-F (HRTEM, Accelerating voltage: 200kV). Raman and Photoluminescence spectroscopy (PL) spectral analysis were performed using Renishaw inVia microscope (HeCd laser source, λ = 514.0 nm) for functional group and structural identification purposes. The band gaps energy of TiO_2-rGO photoanode (prepared with different of applied powers) were measured by UV-2600 [UV-Visible-diffuse reflectance spectrophotometer (UV DRS), Shimadzu Co., Japan] under 400nm/s-scan rate and 200-800-nm wavelength. The functional groups of TiO_2-rGO based photoanode were recorded in range of 500-4000 cm^{-1} using attenuated total reflectance Fourier transform infrared (ATR-FTIR) spectroscopy. Furthermore, elemental analyses were carried out with energy dispersive X-ray (EDX microanalysis) equipped with FE-SEM SU 8000, while the wide scan (100-1200 eV) and narrow scan of X-Ray Photoelectron Spectroscopy (XPS) were measured and performed using PHI Quantera II instrument (MIMOS Berhad, Malaysia). All binding energy values correction was conducted on 284.6 eV which refer to C1s peak. Ti ion implantation was carried out using RF Sputtering equipment (SIRIM Berhad, Malaysia). The *J-V* curves of DSSCs were determined by Autolab PGSTAT204 under the solar irradiation with the input power of 100 W (Mercury Xenon Lamp-based Newport 66902 instrument).

CHAPTER 4: SYNTHESIS AND CHARACTERIZATION OF GO AND rGO

4.1 Introduction

The rGO consists of sp^2-bonded carbon atoms that are densely packed in a honeycomb crystal lattice and it is basic structural element of other carbon allotropes, like graphite, charcoal, carbon nanotubes, and fullerenes (Boehm et al., 1994). This material has attracted much scientific interest in global research because of its exceptional physical properties, such as high electronic conductivity, good thermal stability, and excellent optical properties as discussed in previous chapter (Fugallo et al., 2014; Guo et al., 2015; Rozhkov et al., 2016). An increasing number of rGO material research studies have been devoted because of its 2D honeycomb-structured lattice that improves the movement of charge carriers. These charge carriers are able to travel sub-micrometer distances without scattering because of their high electrical conductivity. Fundamentally, the high electrical conductivity of pristine graphene is dictated by several form variations, such as wrapped up-fullerene form, rolled up-carbon nanotube form, or stacked up-graphite form. Sythesis of GO material can generally be produced by several disruptive technologies such as micromechanical exfoliation (Huc et al., 2008), colloidal suspension (Su et al., 2011), epitaxial growth (Yang et al., 2013), CVD (Kato et al., 2017), and chemical exfoliation (Hummers Jr and Offeman, 1958). All of these approaches could be adapted for the synthesis GO material; however, micromechanical approach is considered the most promising method to achieve the high purity of GO due to its low-cost manner (Geim, 2009).

Crystals with high structural and electronic quality are produced using the micromechanical approach. Unfortunately, this method is still far from being an effective and efficient technology because of low production scale and time consumption issues (Geim, 2009). Thus, continuous efforts have been exerted to search for alternative way to mass produce GO material that can be adopted for large-scale industrial production.

Previously, Park and Ruoff (Park and Ruoff, 2009) indicated that chemical oxidation of graphite is a feasible method for the preparation of GO. This method involves oxidation of graphite to GO using highly oxidizing agent ($KMnO_4$) and subsequently reducing GO to rGO using hydrazine solvent. The main advantage of this synthesis method over other methods is scalability and low production cost of GO in large quantity. Furthermore, rGO could be dispersed in both polar and non-polar solvents by functionalizing the surface of rGO, which contains =O stretching, C–O–C stretching, C–O stretching, and broad band for hydroxyl functional group (Thakur and Karak, 2012). As a matter of fact, these electron-donating functional groups could be used as a media for the complete exfoliation of GO from graphite flakes.

Theoretically, chemical exfoliation of graphite flakes caused weak van der Waals interaction bond between the carbon layers (Zhu et al., 2011). By contrast, reduction of GO caused all of the oxygen-containing groups to disappear during the chemical reduction stage (Kuila et al., 2012). The chemical exfoliation process such as Conventional Hummer's method, Modified Hummer's method, and Improved Hummer's method are invented to produce GO with large size or aspect ratio, high yield, and less toxic gasses (Zheng et al., 2014). Among these Hummer's methods, Improved Hummer's method is the higher reaction efficiency and less toxic gas emission (Lin et al., 2015). Based on literature review, most of the rGO reported previously possessed small lateral dimensions of about few hundred nanometers to a few microns. The large lateral dimension with high degree of oxidation is necessary in this research as a complete oxidation and to be exfoliated easily especially in large sheets (Huang et al., 2011). Table 4.1 presents the experiments conducted by several authors regarding the lateral size studies with different synthesis of GO. Much literature summarized that large-area GO sheets were difficult to synthesize because of unavoidable tearing of GO sheets during the extreme oxidation with $KMnO_4$ and reduction with hydrazine condition in an Improved Hummer's method of chemical exfoliation process.

Table 4.1: Summary of GO lateral dimensions

Lateral Dimension (nm)	Synthesis technique	References
~500	Hummer's Method	(Zhang et al., 2009c)
~2000	Modified Hummer's Method	(Yang et al., 2011)
~1 000	Modified Hummer's Method	(Su et al., 2009)
~5 000	Modified Hummer's Method	(Gurunathan et al., 2013)
~150 000	Simplified Hummer's Method	(Ban et al., 2012)
~200 000	Hummer's Method	(Zhou and Liu, 2010)
~ 500 000	Hummer's Method	(Kim et al., 2015a)
> 1,000 000	Hummer's Method	(Cai et al., 2017)

Besides the effect of stirring speed, stirring duration is also one of the essential factor in the synthesis of GO and rGO in this research in order to obtain high purity of rGO in order to obtain high yield production. Furthermore, the synthesis process for GO or rGO needs to be simple and cost effective for possible adoption to large industrial production scale and gasses toxic reduction. Based on literature (Table 4.2), most of the researchers who synthesized GO or rGO which are focused on stirring duration but not in stirring speed study.

Table 4.2: Summary of GO synthesis based stirring duration

Stirring Duration (h)	Synthesis Technique	References
1	Modified Hummer's	(Loryuenyong et al., 2013)

1	Modified Hummer’s	(Zhang et al., 2013)
2.5	Modified Hummer’s	(Moo et al., 2014)
6	Modified Hummer’s	(Chen et al., 2014b)
2.5	Hummer’s	(Cao and Zhang, 2015)
3	Modified Hummer’s	(Rahmanian et al., 2015)
1	Modified Hummer’s	(Jasim et al., 2016)
4.5	Improved Hummer’s	(Yu et al., 2016b)
6	Modified Hummer’s	(Alam et al., 2017)
6	Modified Hummer’s	(Zaaba et al., 2017)

To the best of our knowledge, detailed studies on the formation of ultralarge or ultrathin nanoscale GO and rGO sheets at a high stirring speed are lacking. Therefore, in this study the effect of the stirring duration and speed was discussed.

At the last stage of this chapter, physicochemical properties and electrical characterization based synthesized GO and rGO were carried. Through this chapter, the objectives of this chapter were covered:

1. To understand the effect of stirring speed and stirring duration on the preparation of GO and rGO to obtain ultrathin or ultralarge rGO sheets during chemical exfoliation process.

To study the integral properties (e.g., functional groups, aspect ratio, crystal structure, optical properties, and morphology) of GO and rGO nanosheet based electrical characteristic.

4.2 Research Findings

4.2.1 Physical Properties of Graphite, GO, and rGO

In the present study, the effect of stirring duration at a high speed of 1200 rpm on the formation of nanoscale rGO sheets was discussed. The present study aims to determine the optimum duration at high stirring speed that would achieve the desired rGO with highly efficient electrochemical properties.

The morphology of the graphite, GO, and rGO samples were illustrated using SEM as presented in Figure 4.1. As illustrated in Figure 4.1 (a), graphite particles are in a platelet-like crystalline form of carbon (Loryuenyong et al., 2013). The layer of graphite sheet has a thickness of 154 nm. Interestingly, the thickness of GO sheets became small with a thickness of 89.2 nm [Figure 4.1 (b)]. The main reason was that the consecutive carbon basal planes (d-spacing) were increased and the distance between carbon layers increased simultaneously. The morphology of the rGO sample [Figure 4.1 (c)] has a similar appearance to the graphite and GO samples, but the average wall thickness of the sheet layer was further reduced to ≈46 nm. This result suggests that the oxygenated molecules were removed from the rGO orbital. When oxidation was reduced by hydrazine, the rGO sheets fully obtained a monolayer structure with 46 nm [Figure 4.1 (c)].

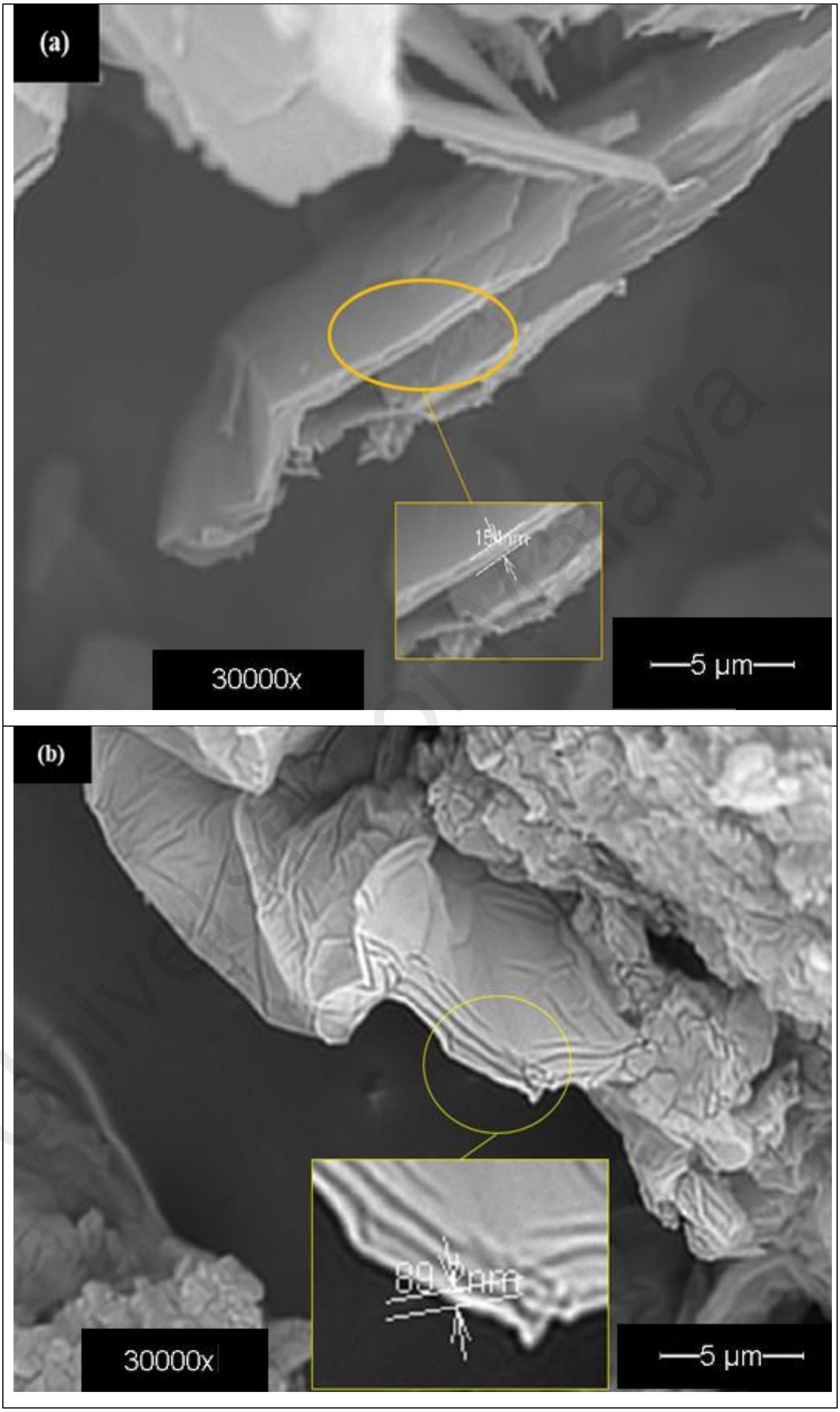
(a)
154nm
30000x
5 µm
(b)
89.2nm
30000x
5 µm

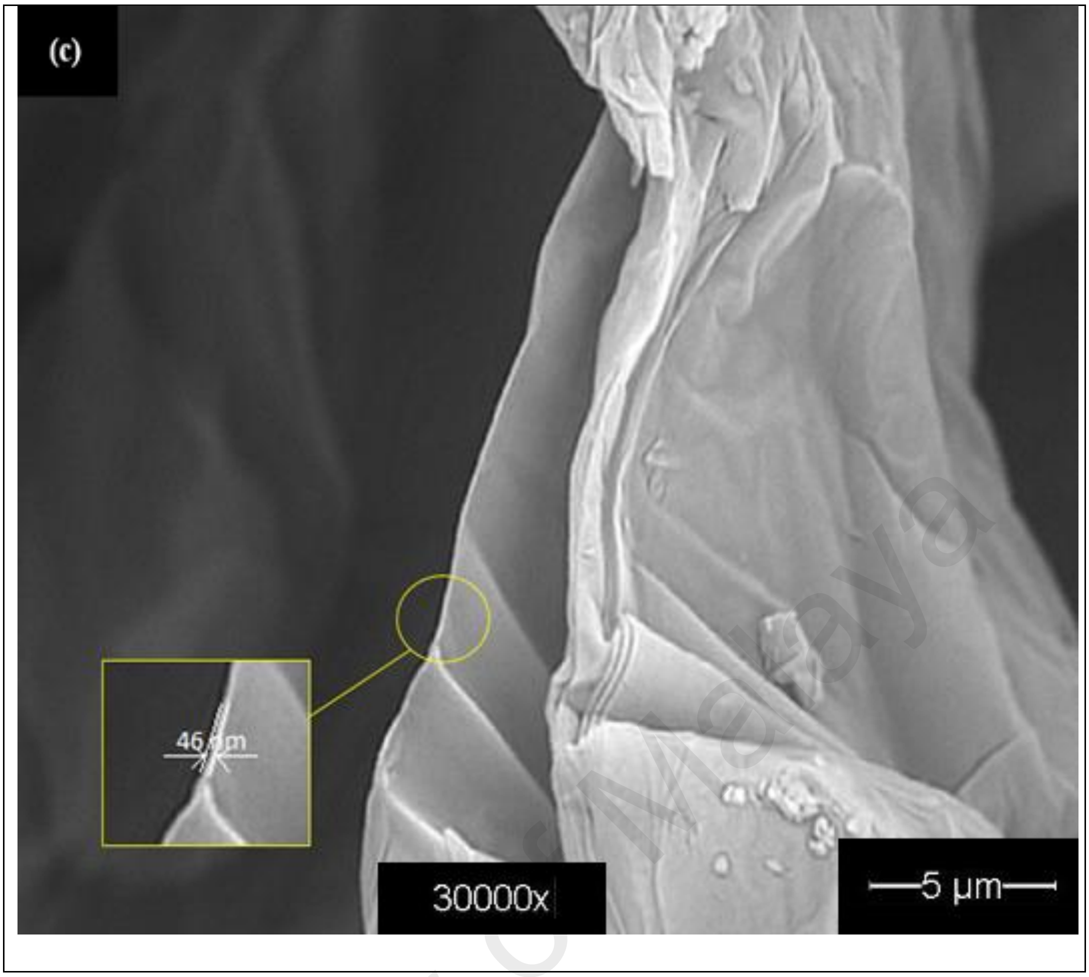

Figure 4.1: SEM images of (a) graphite, (b) GO, and (c) rGO samples

Subsequently, corresponding EDX analysis were conducted to determine the average atomic percent (at.%) of the elements present in graphite, GO, and rGO samples. The results from EDX spectra are presented in Table 4.3. For the pristine graphite sample, the peaks of C and O were detected, which indicate the existence of C (96.30 at.%) and O (3.70 at.%) elements. For the GO sample, the intensity of the C peak from the EDX spectrum decreased significantly from 96.30 at.% to 65.41 at.%, whereas the O element increased tremendously from 3.70% to 34.59%. This result was understandable because of the presence of oxygenated molecules from $KMnO_4$ during the oxidation process. A high C peak was found from the rGO sample (88.01 at.%), but the O peak decreased to 11.99%. The result was attributed to the strong reduction reactions involved using hydrazine agent. The value of O peak still exist notified that the rGO is formed and detectable in bilayer system and not in single layer of pristine graphene. Besides, carbon content significantly increased in rGO material, and carbon–carbon atoms well bonded with each other.

Table 4.3: EDX results of graphite, GO, and rGO samples

Materials	Carbon, C (Atomic %)	Oxygen, O (Atomic %)	Total (Atomic %)
Graphite	96.30	3.70	100.00
GO	65.41	34.59	100.00
rGO	88.01	11.99	100.00

An atomic scale morphological study was carried out to examine the structural layers of GO and rGO using the HRTEM analysis as exhibited in Figure 4.2. Figure 4.2 (a) shows the HRTEM image of the GO sample after high-speed stirring of 1200 rpm. The image shows that large amount of white spots were deposited on the surface of the GO sample. This observation indicates the presence of a bonding network between the oxygenated functional groups (-O-, -OH, and -COOH) and the carbon planes and would help in stability in terms of electron transportation in DSSCs (Karim et al., 2013). The HRTEM image for rGO sample is exhibited in Figure 4.2 (b). The silk-like appearance of rGO after the reduction process was clearly observed.

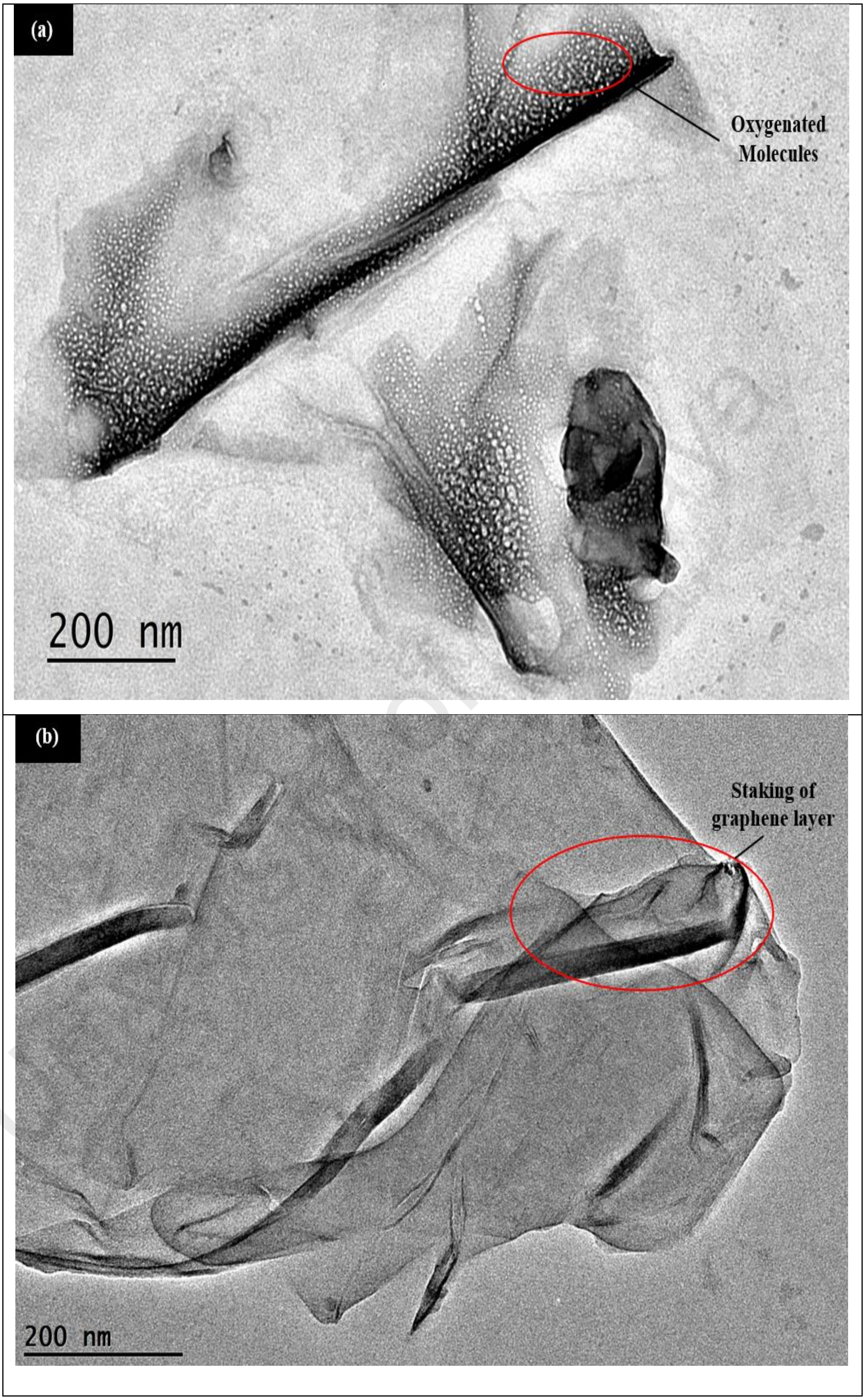

Figure 4.2: HRTEM images of (a) GO and (b) rGO samples

A simple three-dimensional schematic of a monolayer rGO sample is shown in Figure 4.3. This image manifests that ultrathin layer of rGO can be formed using a stirrer at a high stirring speed to assure that oxygenated molecules and agglomeration of small particles were reduced.

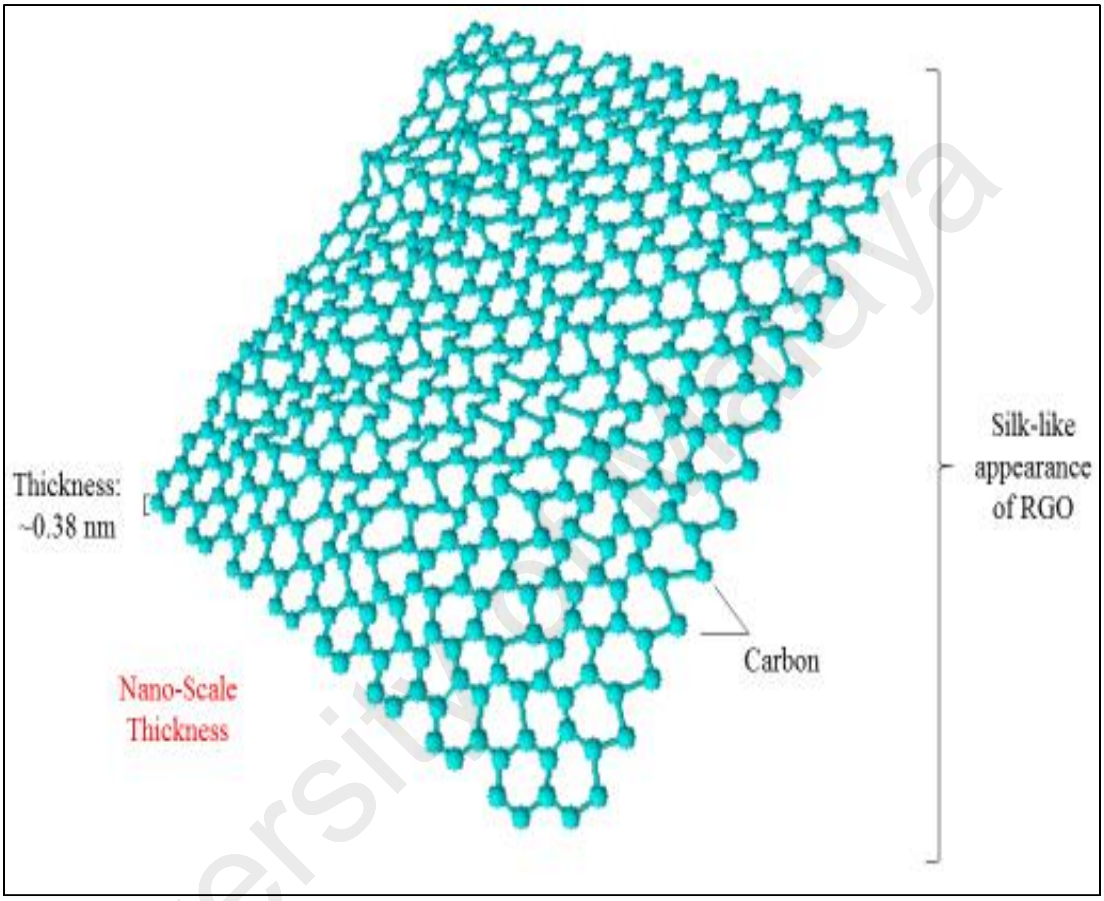

Figure 4.3: A schematic of the silk-like, three-dimensional appearance of rGO monolayer

The XRD analysis was used to investigate the crystal structure, orientation and average spacing. Thus, representative samples were selected for the XRD analysis. Figure 4.4 (a) shows pristine graphite exhbited a sharp and intense peak at $2\theta = 26.58°$ (FWHM = 0.3600), which corresponds to the well-arranged layer structure with d-spacing of 0.335 nm along the (002) orientation (Titelman et al., 2005; Zeng et al., 2011). In addition, a small Bragg reflection of graphite phase (004) was also detected at 2θ value of 54.73 ° with d-spacing of 0.17 nm (FWHM = 0.2952). The presence of graphite phase was identified by ICDD file 9012230 (Reference Pattern = 01-075-2078). The XRD pattern for GO at a high stirring speed (after the pristine graphite undergo oxidation process) is shown in Figure 4.4 (b). The peak (002) shifted to a low angle at 2θ = 8.59° with FWHM = 0.6000 (Reference Pattern = 01-074-2329), but the distance between consecutive carbon layers (d-spacing) increased from 0.335 nm to 0.703 nm because of the introduction of oxide functional groups to the carbon basal plane by chemical oxidation reaction. This phonomena inferred that the interlayer distance (d-spacing) between consecutive carbon layers were weakened by the intercalation of GO formation, which have epoxy, hydroxyl, carbonyl, and carboxyl groups located between the edges of consecutive carbon basal planes (Titelman et al., 2005; Wojtoniszak et al., 2012a; Zeng et al., 2011). The rGO sample exhibited a wide peak at 2θ = 24.3 °with d-spacing of 0.38 nm (FWHM = 0.5904) as presented in Figure 4.4 (c). This result may be attributed to the assembly of rGO layers and indicated that poor arrangement of rGO sheets along the stacking direction, which implied this rGO sample was comprised mainly from single or only a few layers of rGO with d-spacing of 0.38 nm (Thakur and Karak, 2012). Furthermore, the disappearance of the peak at 2θ = 8.59° from the XRD pattern also indicated that the oxygen functional groups or the oxygenated molecules were mostly removed from the rGO sample (Thakur and Karak, 2012). A less intense peak with (001) orientation of rGO were observed at 2θ = 42.7 ° (FWHM = 0.2952) and 2θ = 44.5 ° (FWHM = 0.2952) indicated the turbostratic band of disordered carbon materials (Reference Pattern = 96-210-1125).

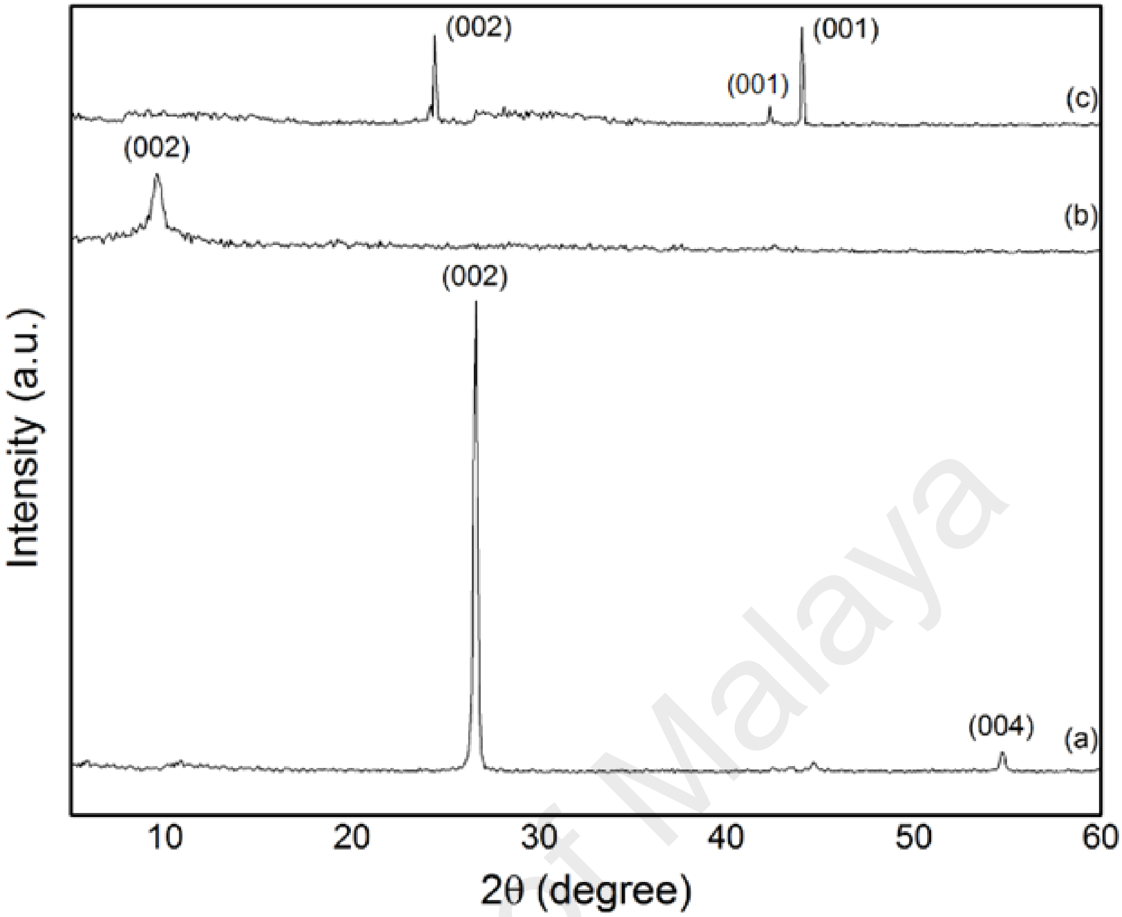

Figure 4.4: XRD patterns of (a) graphite, (b) GO, and (c) rGO samples

Ultraviolet–visible spectroscopy (UV–Vis) measurement was carried out to monitor the degree of oxidation of the GO and rGO samples. In addition, the absorption of GO and rGO transition from the ground state to excited state were determined. The result was strongly based on its reflectance in the visible range depending on the color of the GO and rGO samples involved. As shown in Figure 4.5, GO and rGO samples shown absorption peaks at 272 and 284 nm, respectively. Based on the absorbance spectra of GO, the main absorption peak at 272 nm indicated the π–π* transition of the aromatic C–C ring, whereas the weak absorption at 319 nm was due to the n–π* transition of C=O bonds (Thakur and Karak, 2012). When GO was reduced to rGO, a red shift within the UV region was observed at 284 nm; the decrease in oxygenated functional groups and the increase of aromatic C–C bonds facilited the electrons to be easily excited at low energy (Thema et al., 2012). In addition, the energy band gap of rGO (4.37 eV) is much lower than that of GO (4.56 eV), which proved that the energy required to free an outer shell electron from its orbit shell to become mobile charge carrier is much better for rGO than for GO. Besides, the data obtained around the sharp peak were rough because high concentrations of GO and rGO were detected during the UV–Vis test. The band gap measurement of GO and rGO is shown below:

$$E_g = \frac{1240}{\lambda}$$ **Equation (4.1)**

Light brownish GO solution and light black rGO solution were used for the UV–Vis test (as shown in the inset of Figure 4.5). The optical absorption of rGO was expected to be higher than that of GO. In this case, rGO solution was taken in lesser concentration than GO to obtain a stable dispersion of rGO in absolute ethanol. In fact, UV–Vis spectra totally depend on the concentration of the solution involved; therefore, rGO exhibited higher optical absorption than GO.

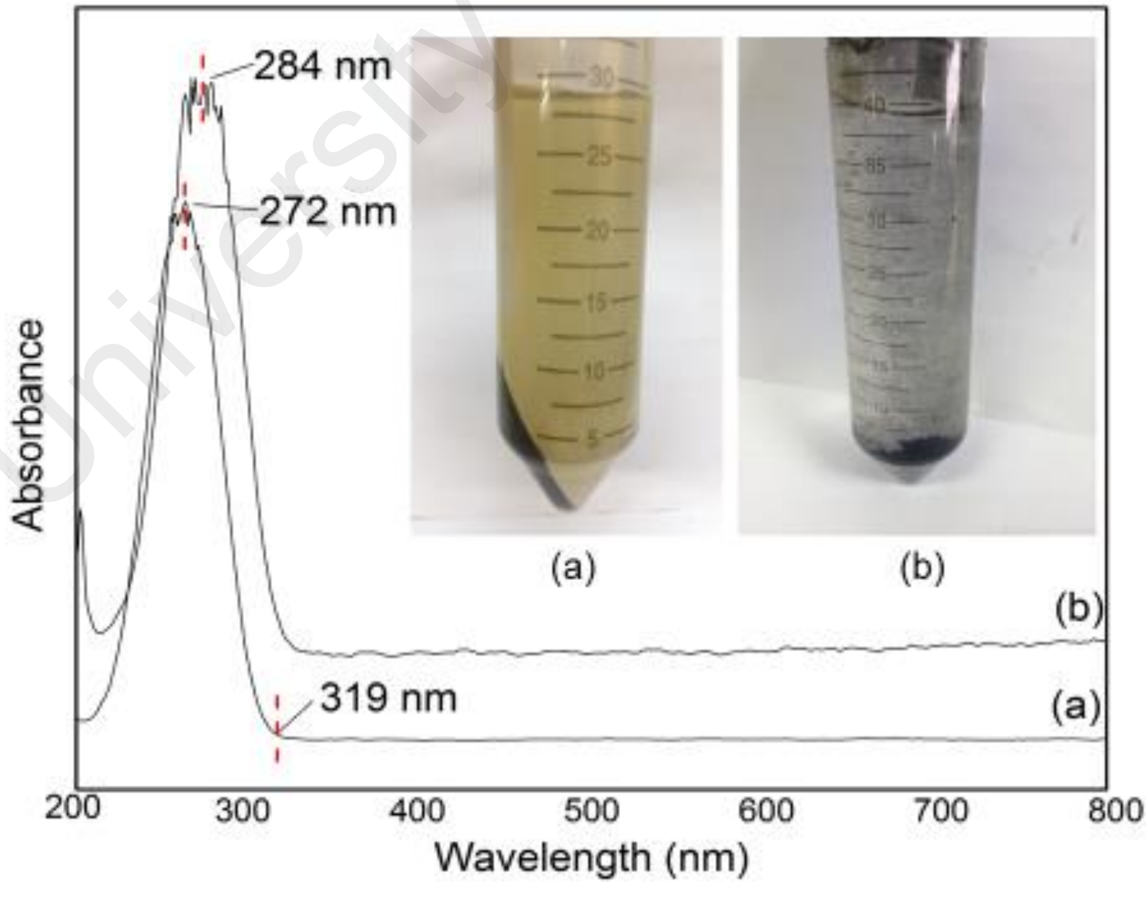

Figure 4.5: UV–Vis spectra of (a) GO and (b) rGO samples

4.2.2 Chemical Properties of Graphite, GO, and rGO

The variation in the transmittance value of the functional group for rGO sheet synthesis based on different stirring durations was studied using the FTIR instrument. Theoretically, GO has several essential acute peaks detected by FTIR patterns such as C=O stretching at 1720 cm^{-1}, C–O–C stretching at 1204 cm^{-1}, and C–O stretching at 1049 cm^{-1}. These results confirmed that the oxygen molecules (O) were occupied greatly during the GO synthesis step. Furthermore, a broad and intense band of hydroxyl group (–OH) at 3400 cm^{-1} was observed from the FTIR pattern (Figure 4.6). Interestingly, the transmittance value (intensity) broadened with increased high-speed stirring duration, indicating the increased diffusion rate of oxygen molecules into the graphite flakes to form carbonyl group, carboxylic group, and epoxy group in GO (Thakur and Karak, 2012). Based on basic chemistry knowledge, it might be obtained high-yield large-area GO of desired result could be expected when 72 h of high-speed stirring at 1200 rpm because of the significant appearance of oxygenated bonds during oxidation process (Thakur and Karak, 2012). Thus, large amount of oxygenated molecules participate in the reaction and weaken the van der Waals interaction between the graphite oxide layers to facilitate their exfoliation (Zeng et al., 2011). Hence, a high stirring speed (1200 rpm) for 72 h was used as optimum parameter for the rest of the experiments in the beginning stage of GO sheet preparation. As an addition, functional group of C=O stretching at 1720 cm^{-1} for 24 h sample was slightly shifted to the lower value might due to the defect occurred during GO synthesis.

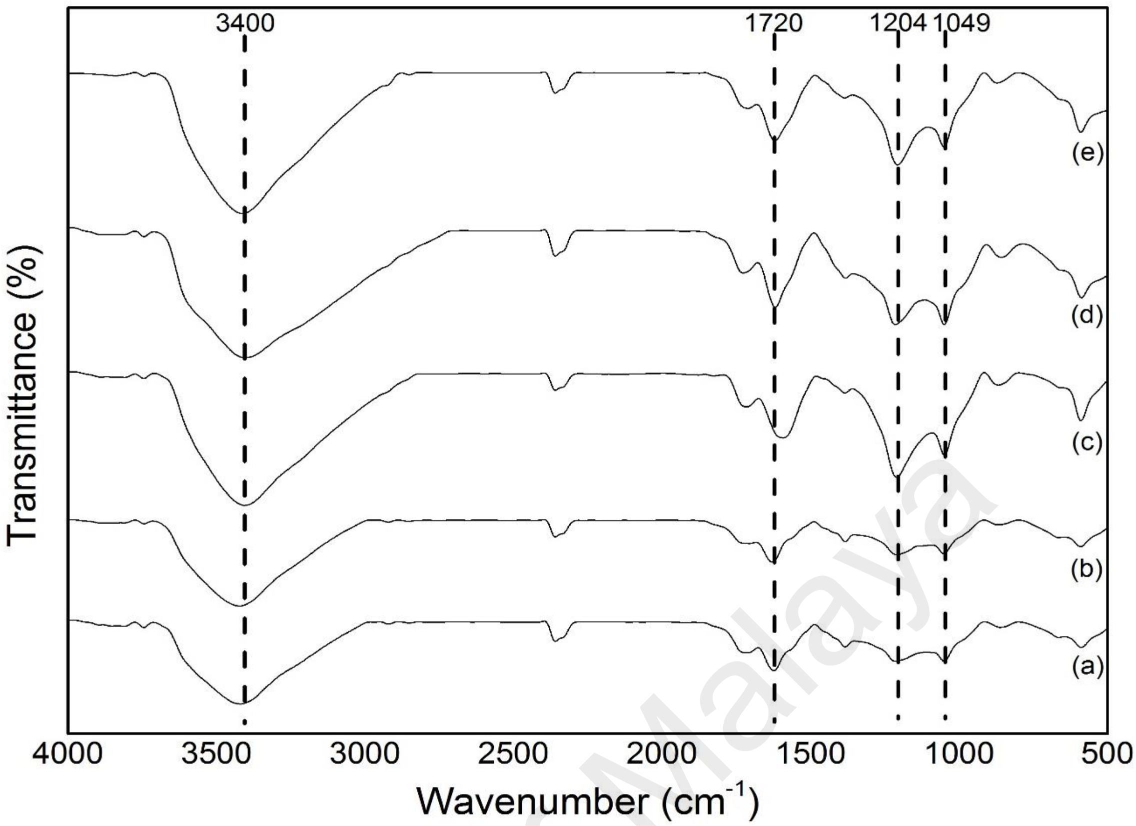

Figure 4.6: FTIR spectra of GO based on different stirring durations: (a) 6, (b) 12, (c) 24, (d) 48, and (e) 72 h

Figure 4.7 presents the FTIR results for graphite, GO sample that underwent 72 h stirring, and 72 h GO sample chosen for rGO production with 6, 12, 24, 48, and 72 h stirring duration. The reason for comparing the variation of rGO stirring duration is to observe the fluctuation of functional groups during the chemical reduction process. All of the essential peaks of the rGO samples at 1720, 1204, 1049, and 3400 cm^{-1} significantly dropped compared with either graphite or GO samples. These phenomena clearly illustrated that oxygen functional groups such as C=O stretching, C–O–C stretching, C–O stretching, and hydroxyl groups were mostly removed and became rGO during the chemical reduction process. Given that the rGO results at 3400 cm^{-1} peak from 6 h to 72 h stirring duration slowly decreased, the 72 h rGO formation process was implemented for easy elimination of hydroxyl groups from the carbon basal plane and simple transformation to rGO. Lastly, a disappearance of C=C bonds at 1720 cm^{-1} along the rGO samples caused by strong oxidation agent such as $KMnO_4$ was observed (Titelman et al., 2005).

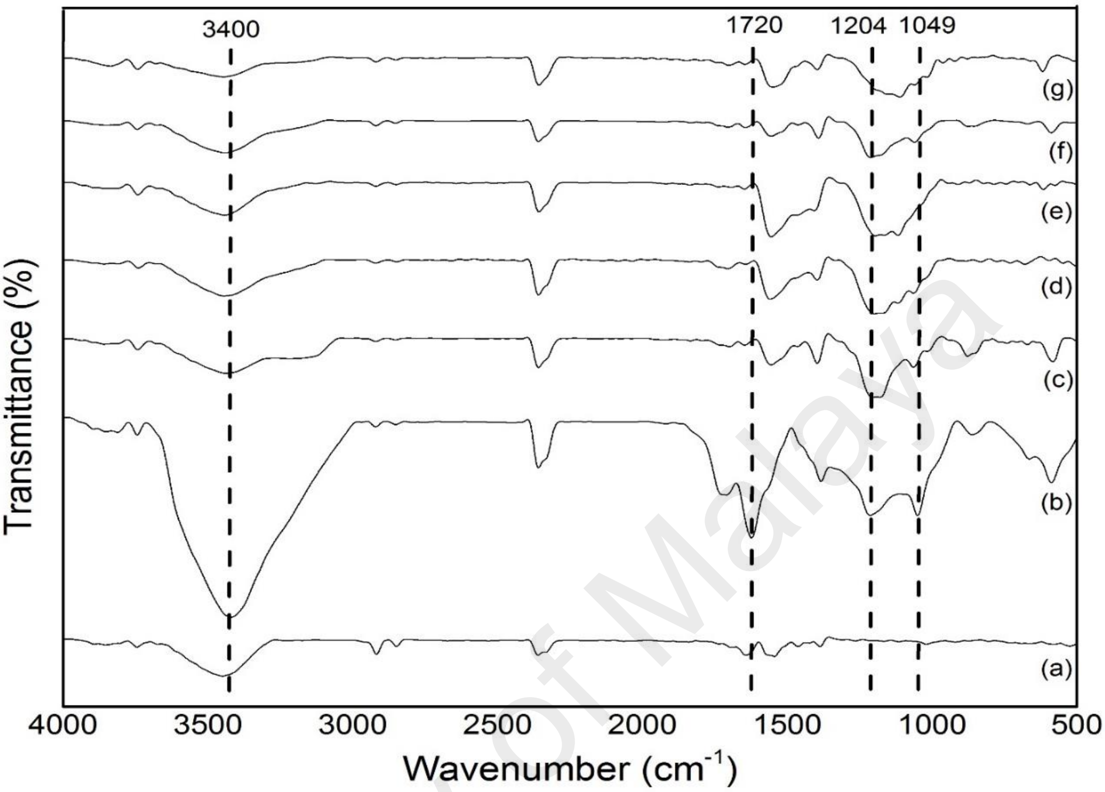

Figure 4.7: FTIR spectra of (a) graphite, (b) GO with 72 h stirring, and rGO produced from sample (b) with stirring duration of (c) 6, (d) 12, (e) 24, (f) 48, and (g) 72 h

Raman analysis was applied to determine and understand the number and orientation of layer, quality, and types of edge of the GO sample that underwent 72 h stirring duration and rGO sample with 72 h which reduced from 72 h GO. For the GO sample, the major band position in the Raman spectra was significantly changed after treating with a reducing agent (hydrazine solvent) because of elastically scattering charge carriers (Cancado et al., 2004). From the spectra of GO and rGO in Figure 4.8, two major vibration bands in the range between 1100 and 1700 cm^{-1} were detected. The D vibration bands of GO and rGO were recorded at 1353.85 and 1349.25 cm^{-1}, respectively, with the breathing mode of κ-point photons of A_{1g} symmetry (Thakur and Karak, 2012). On the contrary, the G vibration bands of GO and rGO were observed at 1588.40 and 1603.31

cm^{-1} to comply with first-order scattering of E_{2g} phonons by their sp^2-hybridized carbon (Thakur and Karak, 2012). Generally, the intensity ratio of the D band to the G band (I_D/I_G) increased the intensity vibration band by more than double after the reduction of GO. The D vibration band of rGO increased mainly because of the sp^2 carbon orientation. The high intensity of G vibration band also indicated that rGO obtained more isolated domains in rGO than in GO (Wang et al., 2011c). The G vibration band of rGO increased because of their removal of oxygen moieties from GO (Cui et al., 2011). To verify the monolayer or multilayer stacking of rGO layers, the two-phonon (2D) Raman scattering of rGO-based materials is an essential. The significant peak that appeared at 2711.76 cm^{-1} determined that rGO is a Lorentzian peak of the 2D vibration of monolayer pristine graphene compared with GO with a smaller peak at 2669.00 cm^{-1}. Consequently, the 2D bands of both GO and rGO peaks were shifted to a high wave number, and the peaks indicated multilayer rGO. The 2D vibration bands of GO and rGO were recorded at 2943.27 and 2945.77 cm^{-1}, respectively. The 2D peaks of both GO and rGO indicated that they have multilayer structures. The incident occurred may be because GO consists of oxygenated molecules that have the ability to prevent rGO layers from stacking with one another. Conversely, the intensity of rGO slightly increased may be because of the absence of functional groups, and only a few rGO layers stack with one another to form a multilayer rGO (Thakur and Karak, 2012).

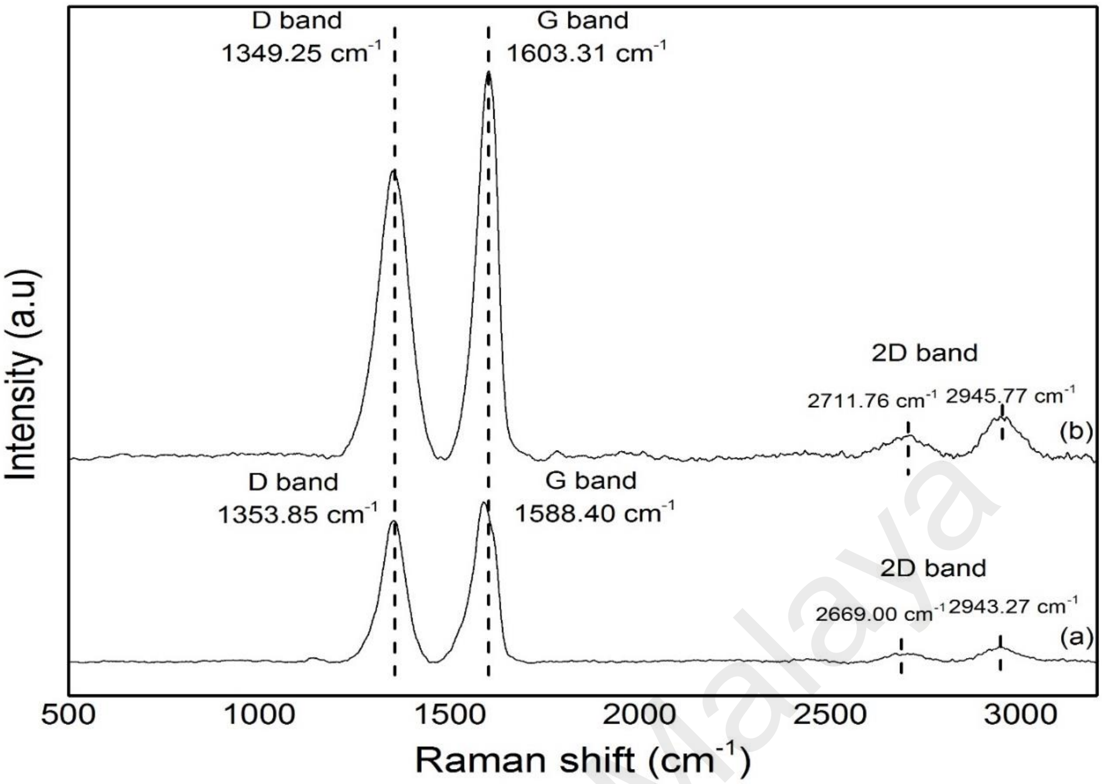

Figure 4.8: Raman spectra of (a) 72 h GO and (b) 72 h rGO from 72 h GO sample

4.2.3 Electrical Characteristics of Graphite, GO, and rGO

A scanning potentiostat was used to measure current under an applied potential (*I*–*V*) characteristic curves for the graphite, GO, rGO samples (Figure 4.9). Under dark conditions, all samples exhibited non-significant current of less than 10 mA. However, the current increased under solar illumination. This is because of graphite, GO, and rGO exhibit a good conductor properties under irradiation. A maximum current of 7.6 mA was observed for the rGO sample, which is relatively higher than those of GO (6.6 mA) and graphite (1.9 mA). These results are consistent with this study, which suggested that the ultrathin rGO sample could enhance the transportation of photo-induced charge carriers rapidly. This result reveals that the rGO sample exhibited better electrical properties than GO and graphite samples. In the same way, current (*I*) exhibited an increasing trend from rGO (7.6 mA) > GO (6.6 mA) > graphite (1.9 mA). This dramatically increasing trend proved that electrochemical rGO showed a much higher carbon to oxygen ratio than GO.

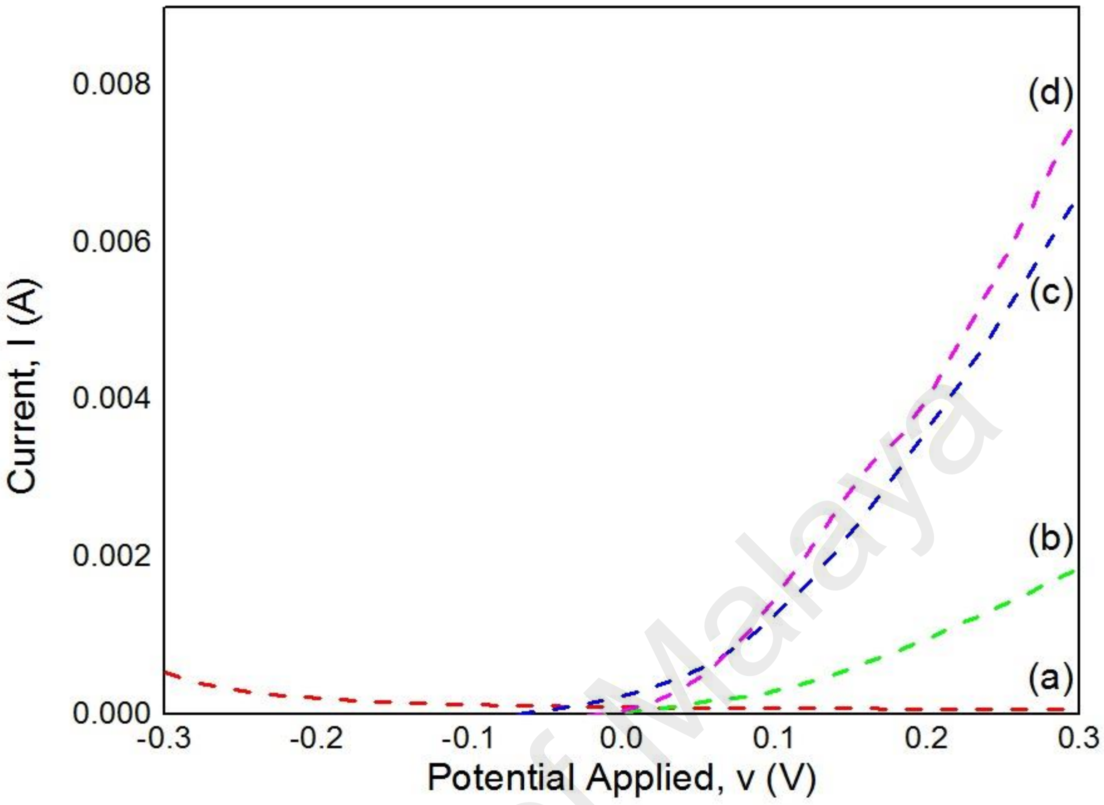

Figure 4.9: ***I–V*** **characteristic curves of (a) FTO default glass, (b) graphite, (c) GO with 72 h stirring duration, and (d) rGO with 72 h stirring duration**

4.3 Discussion

Overall, a schematic diagram illustrating the formation of graphene-like materials (rGO) through exfoliation and reduction of GO sample is presented in Figure 4.10. In brief, the efficient production of GO could be realized by an Improved Hummer's method, whereas the exfoliation of GO to form rGO could be performed by chemical reduction. Based on an Improved Hummer's method, the new material of H_3PO_4 was introduced instead of $NaNO_3$ to overcome toxic gasses issue and difficulty removal of residual formed from the waste water (Chen et al., 2013a). As addition, the advantages to apply this method is due to the increasing reaction yield and reducing toxic gas evolution while doubled the amount of $KMnO_4$ as oxidizing agent in GO synthesis. Subsequently, the synthesized GO sample created functionalized oxygenated bonds with carbon atoms. When GO was formed, the crystalline structure of d-spacing was increased compared with the graphite flake structure. Lastly, GO was reduced with hydrazine solvent to form rGO sample with ultrathin crystalline structure. The oxygenated bonds was fully expelled or reduced from GO orientation.

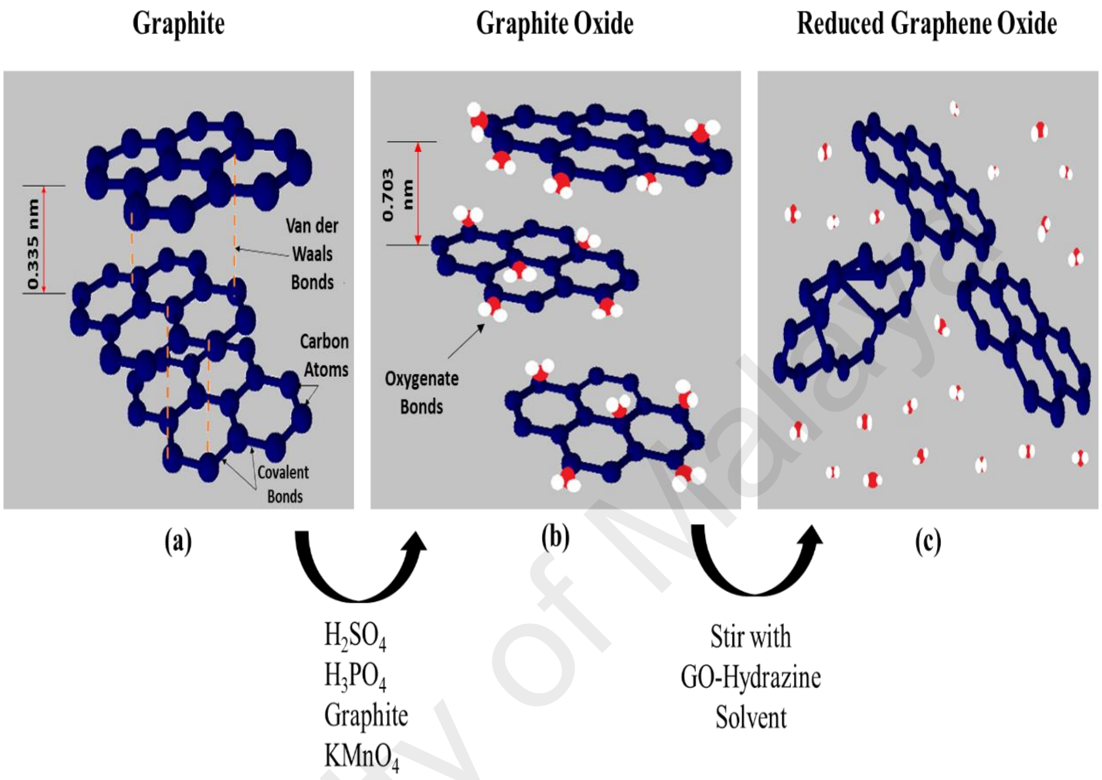

Figure 4.10: Mechanism of rGO formation: (a) graphite undergoing oxidation process to (b) GO and exfoliation of GO to (c) rGO under chemical reduction process

4.4 Conclusion

In this chapter, a constant high stirring speed at 1200 rpm for 72 h GO was successfully synthesized by Improved Hummer's method to eliminate the toxic gasses evolution and aimed for high yield production. Next, GO underwent reaction for another 72 h stirring duration and added hydrazine solvent as reducing agent finally formed an ultrathin rGO with an average thickness of 46 nm. The optimized speed of 1200 rpm is fixed in this experimental in order to ensure that balance between interface tension and shearing stress of GO and rGO sheets. Furthermore, the high speed at 1200 rpm is used to improve the system stability and reduce the agglomeration of small carbon particles rate. Moreover, high-yield large-area GO was obtained after 72 h of high-speed stirring speed at 1200 rpm because of the significant appearance of oxygenated bonds (C=O stretching, C–O–C stretching, C–O stretching, and hydroxyl groups). Based on the FTIR analysis, the decline of hydroxyl groups from the carbon basal plane was achieved significantly to form few layers of rGO sheets after high-speed stirring for 72 h. The ultrathin monolayer rGO sample could enhance the transportation of photo-induced charge carriers rapidly based on the *I*–*V* characteristic curves as compared to GO and graphite samples. Such a mechanistic understanding is very important for the controlled growth of ultrathin rGO sheets, which may be used in many socio-economic applications, such as solar cells, touch sensors, light-emitting diodes (LEDs), ultrafast transistors, and others.

CHAPTER 5: ONE-STEP HYDROTHERMAL TECHNIQUE OF TiO_2-rGO NANOCOMPOSITE IN DSSCS

5.1 Introduction

Nowadays, the public concern about the environment, climate change, and limited fossil fuel resources have given rise to the urgent need of fostering development in the area of renewable energies which are inexhaustible and non-polluting. The renewable energy is one of the technologies to generate clean and green sources of energy to overcome the greenhouse gasses and global carbon emissions issues. The renewable energy was performed as the alternative energy sources which provide us energy in a sustainable manner.

Recently, the photovoltaic solar era such as the DSSCs was aroused instead of the conventional solar cell due to the large availability and low-cost of the ingredient material as well as easy processing (Ding et al., 2015; Luan et al., 2013). This renewable energy technology enables the conversion of sunlight energy into useful electricity by generating electron and hole pairs (EHPs) in order to overcome the global warming issue.

During the past few years, significant efforts have been established by utilizing the rGO in order to decrease the light harvest of dye molecules and improve the PCE of DSSCs (Chang et al., 2014; Yin et al., 2014). However, pristine graphene as photoelectrode conducted in DSSCs device can only absorb 2.3% of visible light from the solar illumination (Huang et al., 2012a; Machado and Serp, 2012). Furthermore, synthesized rGO will contains point defects (Cançado et al., 2017), cluster defects (e.g. structural defect) (Stubrov et al., 2017), and boundaries or edges (Liu et al., 2016b). Defects normally known as detrimental the properties of materials, but also can beneficial to materials in providing dopants to control their carrier concentration (Araujo et al., 2012).

In order to further improve the immigration of photo-induced charge carriers and cluster defect, considerable efforts have to be exerted on the rGO as photoanode by introducing a metal oxide material. This combination aimed to enhance the photocatalytic activity under visible light illumination and decrease the structural defect. The doped Ti^{3+} ions can occupy interstitial positions into rGO sheets forming Ti-O-C bonds. Lately, interesting and unique features of the photocatalyst system have gained much attention and become a favourite research matter among various groups of scientists. Among the vast number of different metal oxides, TiO_2 is one of the most capable candidates to be coupled with rGO photoelectrodes for enhancement in numerous diverse applications such as energy storage (Wang et al., 2009b), photochemical (Wang et al., 2009b), photovoltaics (Wang et al., 2008a), and photocatalytic (Zhang et al., 2009b) based hydrogen fuel generation and degradation of organic contaminations. The reasons are mainly attributed to the enhancement of EHPs separation, prolonged visible light absorption (400-700 nm), and consequently enhanced PCE of DSSCs (Pan et al., 2012b).

The TiO_2-rGO Nanocomposite (NC) was noted that properties of this binary nanocomposite primarily depend on the nature of the preparation method and role of optimum TiO_2 species incorporated into the rGO and formed the Ti-O-C bonding. The Ti-O-C bonds helped in shifting up of valence band and hence reduce the band gap. Furthermore, these bonds also facilitated the conductive pathway of charge carries between TiO_2 to rGO, resulting in reduced of charge recombination and enhanced the PCE of DSSCs. It could be understood that an optimum content of TiO_2 and possible formation of well-distribution of TiO_2-rGO NC are important issues to be addressed in order to form an ideal photoelectrode for the DSSCs system and continue to move towards a sustainable renewable solar cell system.

In this chapter, it will covered the few objectives correspond to this project.

1. To study the formation of TiO_2-rGO NC via One-Step Hydrothermal Technique.
2. To determine the optimum loading content of TiO_2 species on the rGO as photoanode in DSSCs for improving their conductivity as well as PCE.
3. To understanding the working mechanism of TiO_2-rGO NC as photoanode in DSSCs.

5.2 Research Findings

5.2.1 Physical Properties of TiO_2-rGO NC

The morphology of the rGO and 0.1-0.5 wt% of TiO_2-rGO NC are shown in Figure 5.1. In our previous study (Chapter 4), the thickness of synthesized rGO nanosheet was 46 nm with the removal of oxygenated molecules from the exfoliated GO (Low et al., 2015c). Besides, it can be clearly observed that a single platelet of TiO_2 particles was fully coated with the aggregated TiO_2 particles on rGO nanosheets as shown in Figure 5.1 (b)-(f). From Figure 5.1 (b)-(f), it seems that the amount of TiO_2 is increasing from 0.1 wt% to 0.3 wt%.

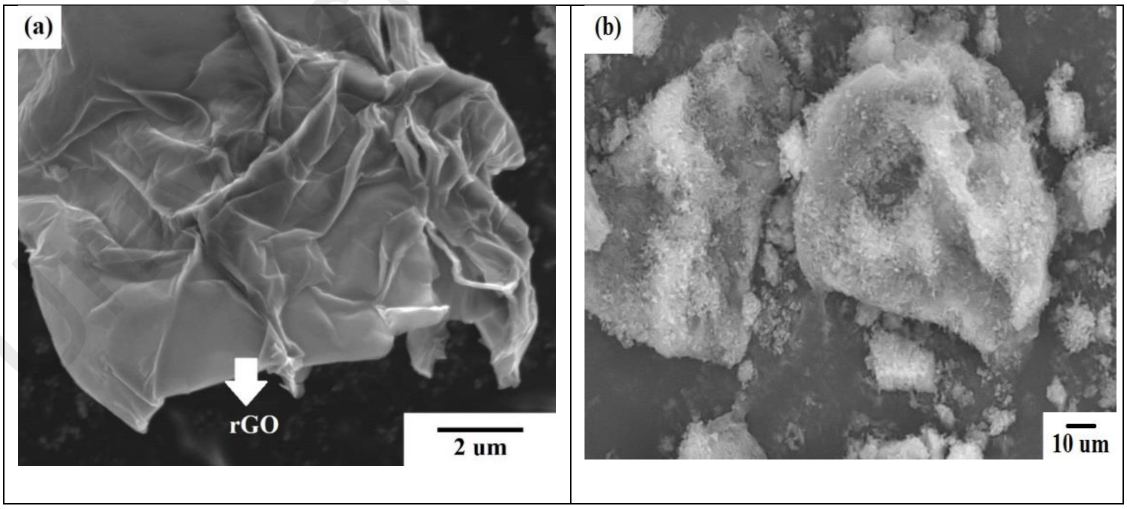

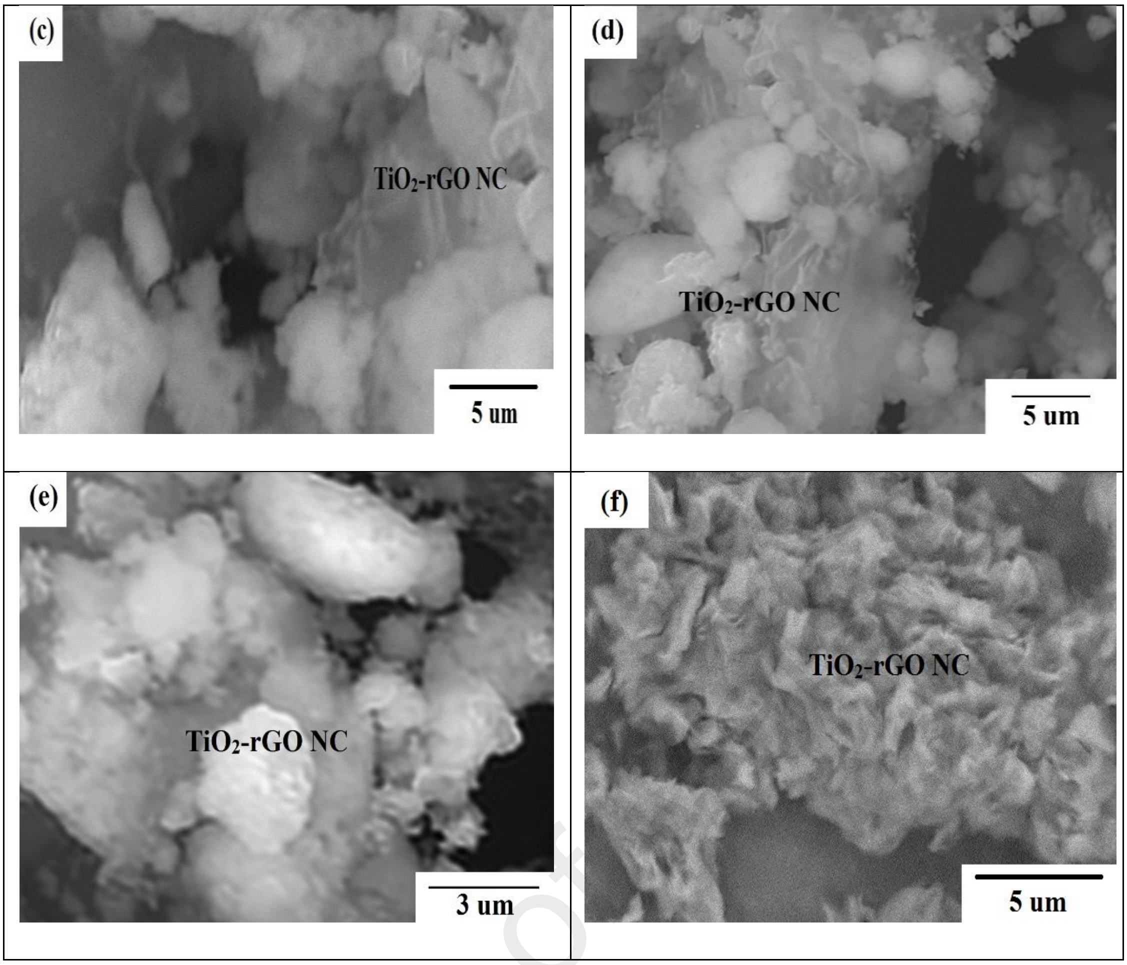

Figure 5.1: SEM images of (a) rGO and TiO$_2$-rGO NC of (b) 0.1 wt%, (c) 0.2 wt%, (d) 0.3 wt%, (e) 0.4 wt%, (f) 0.5 wt%

The EDX analysis for the elements of rGO and 0.1-0.5 wt% of TiO$_2$-rGO NC are summarized in Table 5.1. The recorded data was based on our previous study (Chapter 3, Section 3.4.1) with the appearance peaks of C and O 88.01 at% and 11.99 at%, respectively. This indicated that O was reduced from GO by Improved Hummer's method (Low et al., 2015c). On the other hand, the amount of Ti and O element in TiO$_2$-rGO NC increased with the loading amount. It was noticed that a significant decline of C element from 88.01 at% to 18.34 at% whereas the O element is increased from 11.99 at% to 58.32 at% upon addition of TiO$_2$ from 0.1 to 0.5 wt.%. This was attributed to the formation of Ti-O-C bonds after the hydrothermal process.

Table 5.1: EDX result of rGO and 0.1-0.5 wt% of TiO_2-rGO NC

Materials	Carbon, C (Atomic %)	Oxygen, O (Atomic %)	Titanium, Ti (Atomic %)	Total (Atomic %)
rGO	88.01	11.99	-	100.00
0.1 wt% of TiO_2-rGO NC	49.01	37.65	13.34	100.00
0.2 wt% of TiO_2-rGO NC	43.75	39.78	16.47	100.00
0.3 wt% of TiO_2-rGO NC	34.16	45.84	20.00	100.00
0.4 wt% of TiO_2-rGO NC	24.23	54.31	21.46	100.00
0.5 wt% of TiO_2-rGO NC	18.34	58.32	23.34	100.00

XRD was used to determine the crystallographic structure of synthesized rGO, TiO_2, and TiO_2-rGO NC. Figure 5.2 shows the XRD patterns of rGO, TiO_2, and TiO_2-rGO subjected to annealing at 450 ℃ for 120 mins. The XRD pattern for rGO in Figure 5.2 (a) have the appearance of an intense diffraction peak with (002) orientation of rGO at 2θ = 24.3 ° with d-spacing of 0.38 nm (FWHM = 0.5904) and the other two negligible peaks with (001) orientations that occurred at 42.7 ° (FWHM = 0.2952) and 44.5 ° (FWHM = 0.2952), respectively (Low et al., 2015c). It is worth noting that an obvious anatase TiO_2 phase was observed in the XRD patterns as presented in Figure 5.2 (b). Meanwhile, the XRD patterns for the sample TiO_2-rGO NC are shown in Figure 5.2 (c) - (g). The sharp crystallize peaks at 25.3 °, 37.9 °, 47.9 °, 54.0 °, 55.3 °, 62.5 °, 68.9 °, 70.5 °, 75.3 °, and 84.5 ° were implemented to (101), (004), (200), (105), (211), (204), (116), (220), (215), and (303) orientation of anatase TiO_2 (JCPDS 21-1272) (Figure 5.2 (b)), respectively (Hamid et al., 2014a). Furthermore, the peaks of anatase TiO_2 still remains at the same position after the TiO_2 coated with the rGO. The reason for utilizing the anatase TiO_2 rather than rutile TiO_2 during the DSSCs assembly is mainly due to its wider energy band gap (Hagfeldt et al., 2010a). The band gap of anatase TiO_2 (~3.2 eV), which was larger than

TiO_2 rutile phase with ~3 eV (Hagfeldt et al., 2010a). The wider band gap of TiO_2 anatase phase will provide more stability either in photo-catalytic or photovoltaic performance than that of TiO_2 rutile phase. Moreover, charge carrier recombination in anatase is slower than rutile by factor of 10 which is due to smaller grain-sizes in anatase phase (Hanaor and Sorrell, 2011). The average crystallize size was calculated using Scherrer equation corresponding to the (101) orientation phase from the ranging of 0.1 - 0.5 wt% of TiO_2-rGO NC, which was 33.29 nm, 25.60 nm, 22.19 nm, 55.50 nm, and 37.00 nm, respectively. As an addition, 0.3 wt% of TiO_2-rGO NC was the smallest crystallize size, relatively to the highest crystallinity due to its highest intensity at (101) orientation as compared to other samples (Liu, 2014; Norrish and Taylor, 1962). This is due to the optimum content of TiO_2 incorporated with rGO. Besides, the TiO_2 peaks from Figure 5.2 (c) - (g) were fully covered neither (002) nor (001) peaks of rGO from Figure 5.2 (a), it might be due to the lower diffraction intensity and crystallinity of the rGO nanosheets as compared to the anatase TiO_2 nanoparticles (Zhang et al., 2009b).

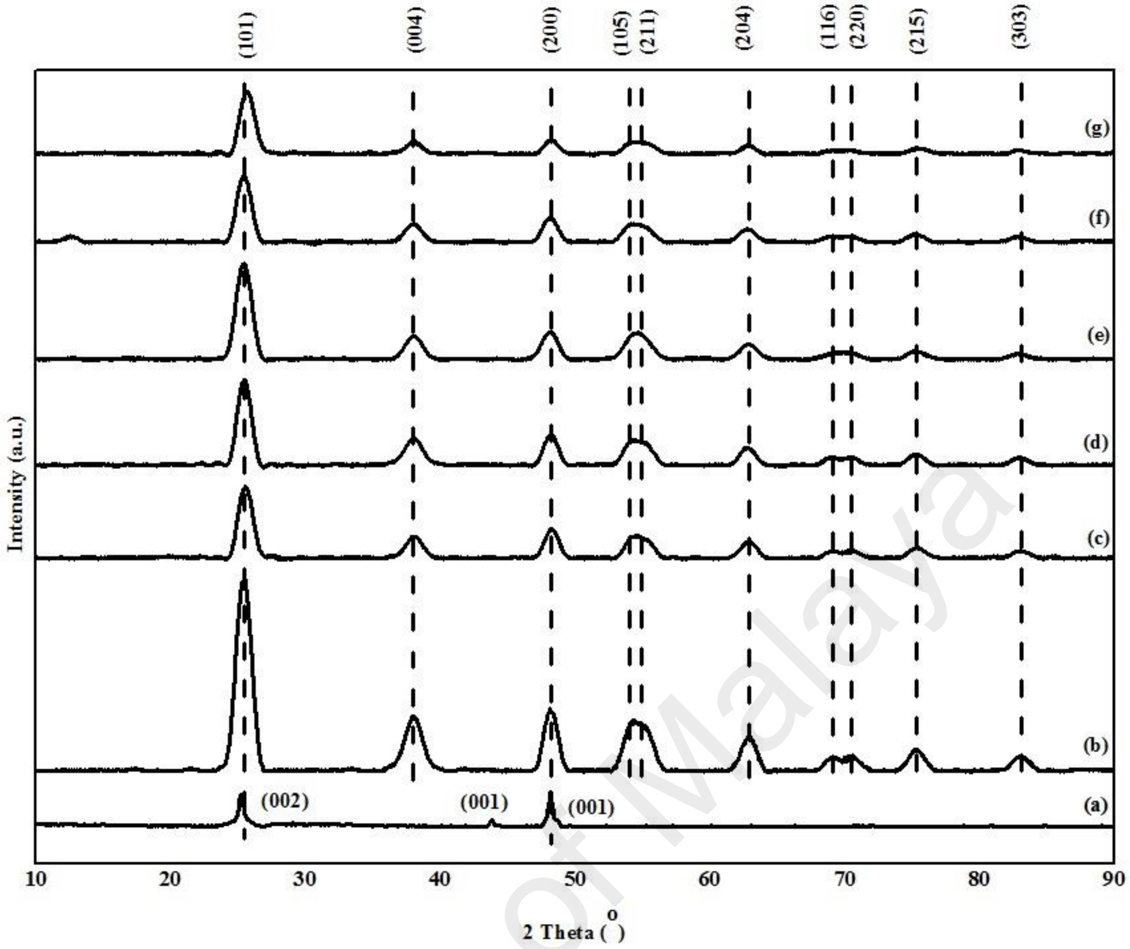

Figure 5.2: XRD patterns of (a) rGO, (b) Anatase TiO_2, TiO_2-rGO NC of (c) 0.1 wt%, (d) 0.2 wt%, (e) 0.3 wt%, (f) 0.4 wt%, and (g) 0.5 wt%

Furthermore, the UV-VIS spectroscopy absorption spectra of rGO and 0.1-0.3 wt% of TiO_2-rGO NC are shown in Figure 5.3. The UV-Vis spectra was often used to prove the optical characteristic and comprehend the conjugation of the TiO_2-rGO NC. The UV-Vis results showed the 0.3 wt% of TiO_2-rGO NC formed is having highest absorbance intensity among the other concentration of TiO_2 included rGO. It is indicating a strong absorption by the anatase TiO_2 nanoparticle coated well with rGO nanosheets (Wang et al., 2011a). For the rGO sample, there was a broad intensity peak at 263 nm and weak absorption peak at around 318 nm. The absorption peak at 263 nm was indicated by the π→π* transition of aromatic C-C bonds, whereas the weak absorption peak at 318 nm was assigned by the n→π* transition of C=O bonds (Thakur and Karak, 2012).

Based on Figure 5.3, the absorption edge of 0.1-0.5 wt% of TiO_2-rGO NC were within 270-290 nm. It was shifted into the visible region, attributed to the presence of rGO and obeyed the quantum size effect, which a larger size offered lower energy and resulting red shifted obtained by extrapolating the linear portion of the curve to zero and positioned into the visible light range as compared to the rGO (Dai et al., 2010). In addition, the role of rGO in NC is also attributed to the surface electric charge increased and the hybrid of the electron-hole pair was formed during the irradiation process (Liu et al., 2011a). On the contrary, the intrinsic of TiO_2 in NC assigned to the electron transitions from the valence band O_2p will be moved to the conduction band, Ti_{3d} (Tan et al., 2013c). This phenomenon had the tendency to narrow the band gap of TiO_2 due to the presence of rGO (Zhang et al., 2010b). Besides, there was also a weak absorption edge at around 300-430 nm. The intensification of the wavelength is mainly due to the arrangement of Ti-O-C chemical bonds which were formed and expected to benefit the efficiency of solar energy in terms of fastening the rate of electron flow in DSSCs application (Lim et al., 2015a).

In the meantime, the calculated band gap energy, E_g of rGO decreased from 4.71 eV to ~3.76-3.84 eV of 0.1-0.5 wt% of TiO_2-rGO NC by applying Equation (4.1), resulting the energy required for TiO_2-rGO NC to free an outer shell electron from the orbit shell to mobile charge carrier much easier than rGO (Low et al., 2015c). The calculated E_g value of rGO (4.71 eV) was approximately closer to the theoretical value (4.40 eV) (Velasco-Soto et al., 2015). It is well known that the band gap energy, E_g is inversely proportional to the absorption band edge, λ as shown below (Dai et al., 2010):

On the basis of the above analysis, the synergistic effects of the few factors (red-shifted wavelength, Ti-O-C bonds formed, and Eg decreased) can be concluded that the photocurrent density, J_{sc} will be achieved at the maximum value.

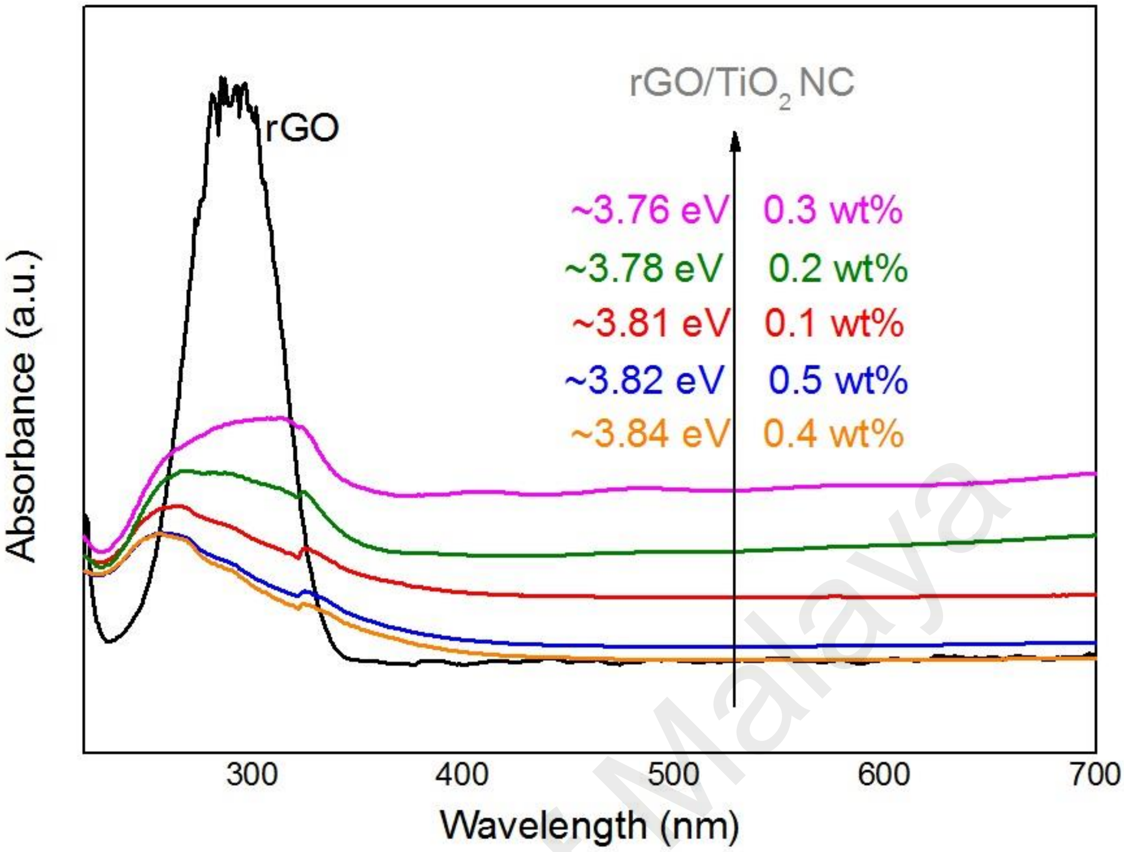

Figure 5.3: UV-Vis Spectra of rGO, and TiO_2-rGO NC with 0.1 wt%, 0.2 wt%, 0.3 wt%, 0.4 wt%, and 0.5 wt%

The surface morphologies of the rGO nanosheets, the TiO_2 nanoparticles in anatase phase, and the 0.3 wt% of rGO-TiO_2 NC were further observed using an FESEM instrument. These images were captured under extremely low-voltage (2.0 kV) in order to prevent penetration of light emission through the rGO nanosheets and 0.3 wt% of TiO_2-rGO NC. From Figure 5.4 (a), it can be observed that the rGO has a silk like appearance after the reduction process. In a previous study, the lateral size of rGO was measured to be approximately 46 nm and it was determined that only few layers of rGO nanosheets were stacked together (Low et al., 2015c). The anatase phase of TiO_2 nanoparticles with high crystallinity is shown in Figure 5.4 (b). The lattice parameters were discussed later in the HRTEM analysis section. In Figure 5.4 (c), the white color particles correspond to the TiO_2 nanoparticles, which were deposited and distributed across the surface. The average particle size of TiO_2 were determined using ImageJ software and obtained around 22.7 nm. The inset image in Figure 5.4 (c) demonstrated that the measurement of particles dimension while the scan area, mean size, and particle size are summarized in Table 5.2, respectively.

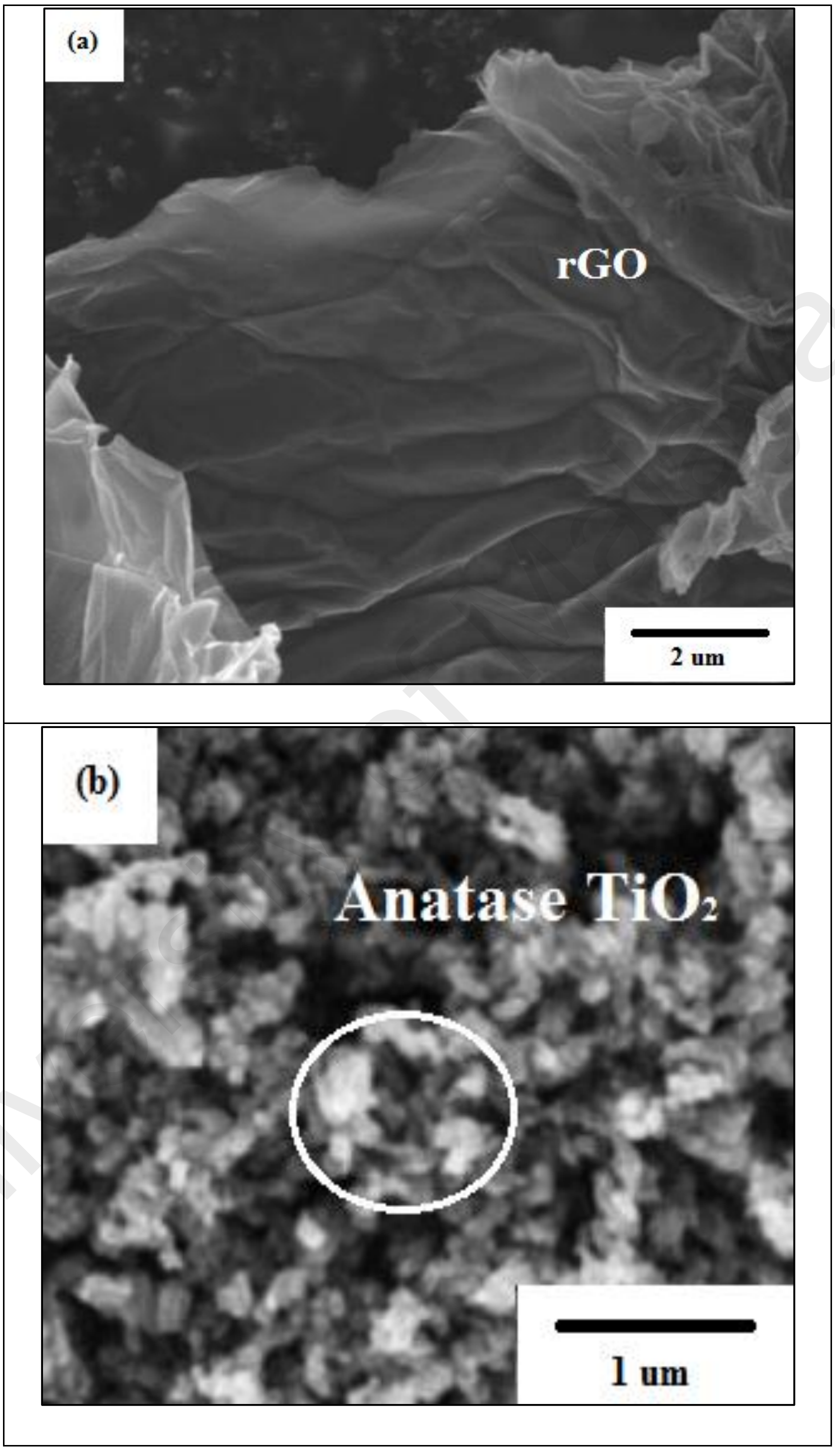

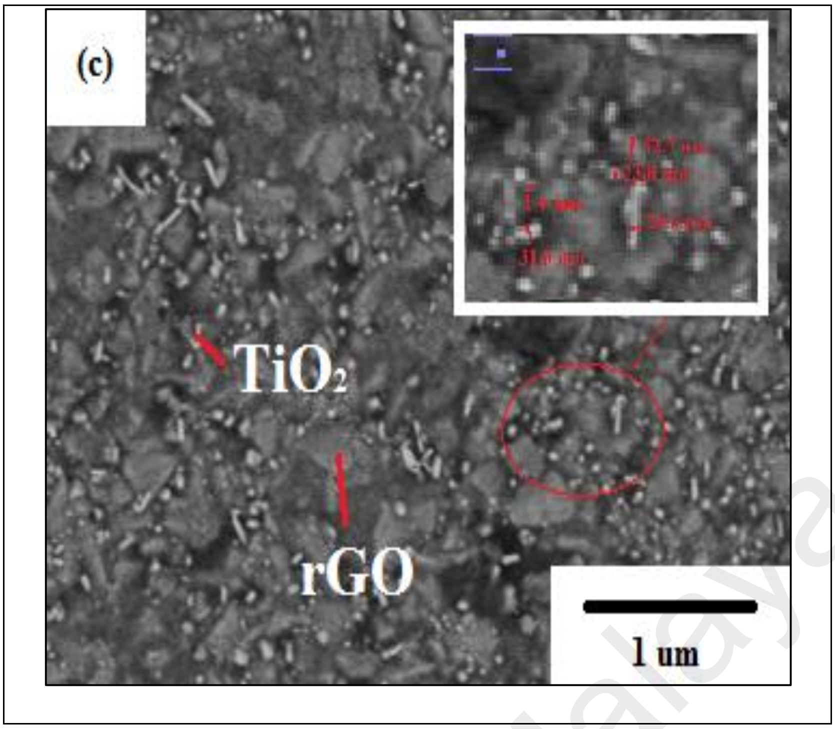

Figure 5.4: FESEM images of (a) rGO nanosheets, (b) anatase TiO_2 nanoparticles, and (c) 0.3 wt% of TiO_2-rGO NC

Table 5.2: Average particle size of TiO_2-rGO NC

Point	Area (μm^2)	Mean (μm)	Length (nm)
1	3.9×10^{-4}	151.6	32.7 ±0.1
2	2.9×10^{-4}	111.8	23.8 ±0.1
3	3.9×10^{-4}	150.9	31.0 ±0.1
4	2.9×10^{-4}	123.7	24.6 ±0.1
5	2.9×10^{-4}	131.7	1.6 ±0.1
Average Particle			22.7 ±0.1

HRTEM images of 0.3 wt% of TiO_2-rGO NC are shown in Figure 5.5 (left side). The rGO nanosheet are shown like semi-transparent with round shape appearance whereas the bright black color shapes on top of rGO nanosheet are TiO_2 nanoparticles. It is clearly seen that the TiO_2 nanoparticles were deposited on rGO nanosheet. Furthermore, Figure 5.5 (a) shows the thickness of rGO was estimated to be around 5.2 nm corresponded to

14 layers within the lattice region (Thakur and Karak, 2012). Besides, the interlayer distance, *d* is approximately 0.37 nm and is in agreement with the XRD results along (002) orientation. Interestingly, the lattice distance of TiO_2 nanoparticles was measured to be 0.33 nm, very close to the XRD results along (101) orientation with *d*-spacing of 0.35 nm in Figure 5.5 (b).

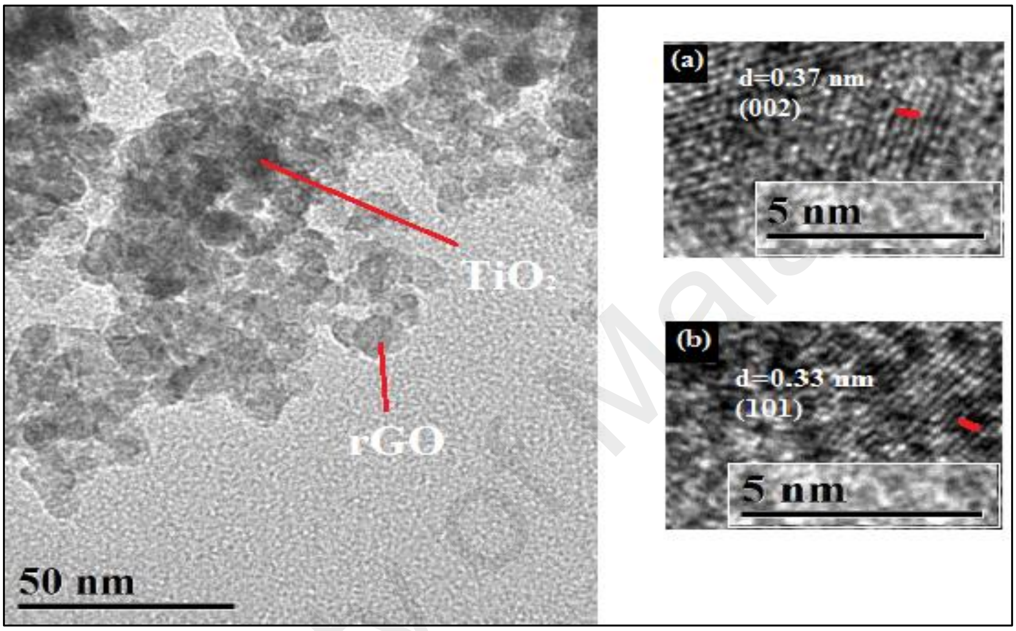

Figure 5.5: HRTEM images of 0.3 wt% of TiO_2-rGO NC at different resolution (a) 50 nm and (b) 5 nm

The Atomic Force Microscopy (AFM) is a useful tool to study the surface topology and height profiles of rGO and 0.3 wt% of TiO_2-rGO NC (Cao et al., 2014). The AFM topology images and its two-dimensional (2D), three-dimensional (3D), and height profiles of the rGO and 0.3 wt% of TiO_2-rGO NC were shown in Figure 5.6 (a) and (b), respectively. In these 2D and 3D images, the brightest and dark pink colour represents the highest point of the sample surface whereas the dark and orange colour represents the valley or sample pores (Safarpour et al., 2015). It was observed that both of the lateral dimension of rGO and 0.3 wt% of TiO_2-rGO NC were enlarged in nanometers (nm) scale. The surface analysis of rGO and 0.3 wt% of TiO_2-rGO NC were summarized in Table 5.3. As compared to Figure 5.6 a (ii) and b (ii), it was clearly observed that the surface roughness, R_a of 0.3 wt% of TiO_2-rGO NC (132.00 nm) was much higher than the rGO (9.86 nm) indicated that the TiO_2 was coated on the rGO. It was assigned to the greater dye adsorption in DSSCs as compared with rGO (Jeng et al., 2013). Subsequently, the efficiency of DSSCs will also exponentially increase due to the R_{max} and line profile of 0.3 wt% of TiO_2-rGO NC with 950.00 nm and 778.10 nm corresponding with 84.40 nm and 13.94 nm, respectively.

Table 5.3: Surface analysis of rGO and 0.3 wt% of TiO_2-rGO NC

Sample	Roughness Parameters			
	Thickness (Mean), nm	Roughness (R_{max}), nm	Line Profile, nm	Surface Roughness (R_a), nm
rGO	1.35	84.40	13.94	9.86
0.3 wt% of TiO_2-rGO NC	11.25	950.00	778.10	132.00

Based on Figure 5.6 (a), the mean value of rGO thickness was ~ 1.35 nm, which proved that the synthesized rGO sheet was approximately categorized as the mono carbon atom layer. Furthermore, the ~ 1.35 nm measured thickness was divided to the theoretical single layer rGO sheet of ~ 0.78 nm whereas ~ 0.57 nm was contributed to the functional groups such as bulky carbonyl, epoxy, and carboxyl groups on the surface when the rGO was formed (Liu et al., 2011a). The mean thickness was obtained for the desired value of 11.25 nm after TiO_2 was coated with the thickness of rGO. Herein, the thickness of TiO_2 can be considered as nanoparticles with ~ 9.9 nm as shown in Figure 5.6 (b). Thus, the 0.3 wt% of TiO_2-rGO was categorized as NC in terms of height profile after being well examined by AFM instrument.

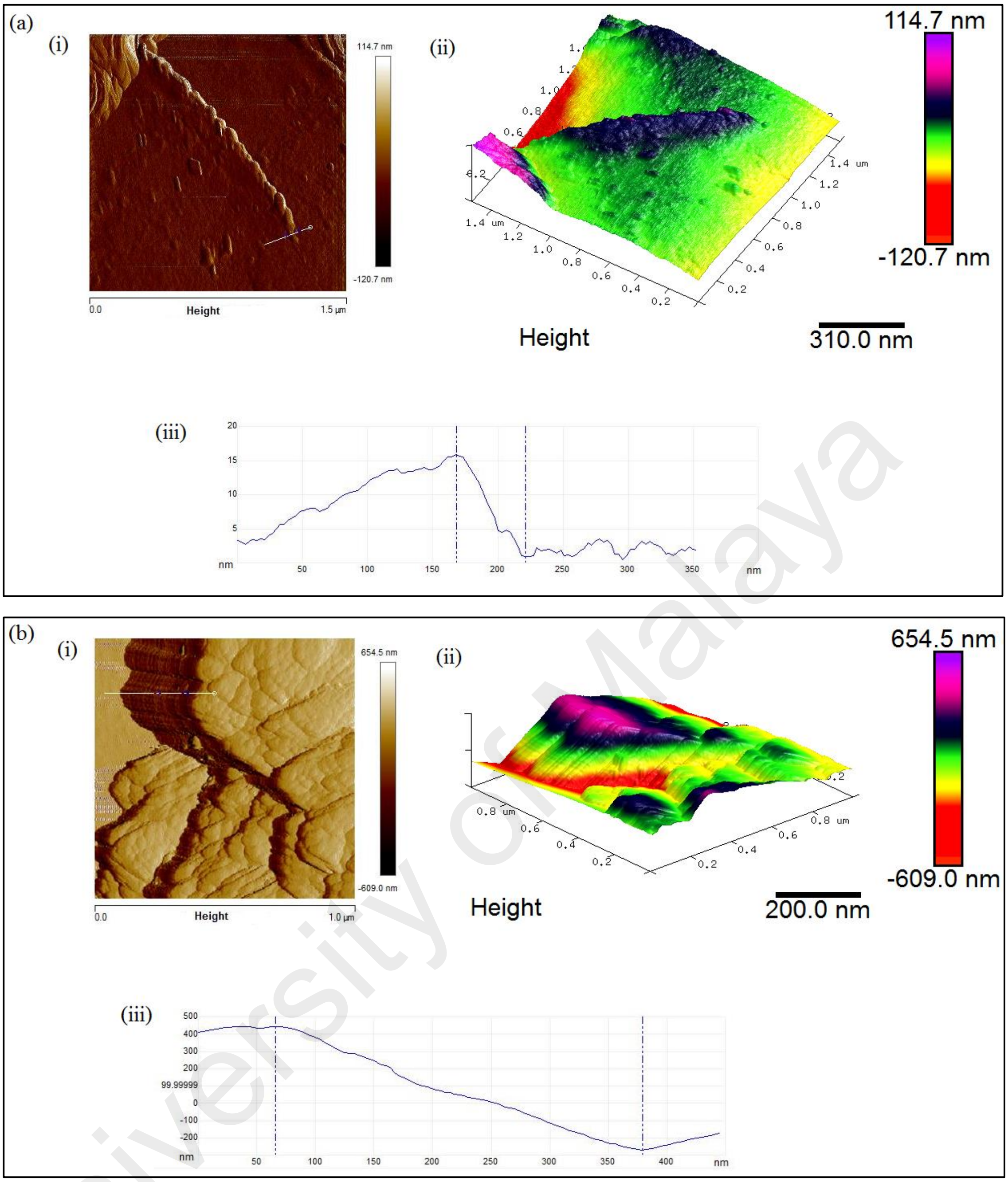

Figure 5.6: AFM topology of (i) 2D height, (ii) 3D height, and (iii) their line profile corresponding with (i) for (a) rGO and (b) 0.3 wt% of TiO_2-rGO NC

The sheet resistance (R_s) of the thin films was measured to study the uniformity resistance of rGO. The R_s values of rGO thin film were summarized in Table 5.4. In addition, the five points were measured on surrounding of the rGO thin film coated on top of FTO glass and average R_s of rGO thin films was 0.51 Ω/sq. The average R_s values were almost similar due to the uniform cotion of rGO thin film on FTO glass.

Table 5.4: Sheet resistance of rGO thin films

Point	Sheet Resistance, R_s (Ω/sq)
1	0.51
2	0.53
3	0.53
4	0.49
5	0.50

5.2.2 Chemical Properties of TiO_2-rGO NC

The Raman spectroscopy is a powerful, fast and non-destructive technique to elucidate the vibration band and particle size of TiO_2-rGO NC film. Figure 5.7 presents the Raman scattering spectra of the rGO, synthesized anatase phase of TiO_2, and the comparison of TiO_2 nanocrystals loaded on the rGO in the range of 0.1 wt% to 0.5 wt%. Based on our preliminary results, the synthesized rGO was only a few layers with 46 nm/layer (Low et al., 2015c). In this Raman spectra for rGO recorded that there were two broadbands corresponding to the D vibration bands (1349.25 cm^{-1}) and G vibration bands (1603.31 cm^{-1}), respectively (Low et al., 2015c). The D bands indicated that the breathing mode of the κ-point photons of A_{1g} symmetry whereas the G bands obeyed the first-order scattering of E_{2g} phonons by their sp^2-hybridized carbon (Thakur and Karak, 2012). Obviously, the integrated intensity ratio of the D band corresponding to the G band (I_D/I_G) for rGO with 1.202 was lower than the TiO_2-rGO NC ranging from 0.1 wt% - 0.5 wt%, which was 1.338, 1.349, 1.526, 1.203, and 1.209, respectively. These are mainly due to the disorder in the graphitic nature increased after the incorporation of the TiO_2 nanoparticles, decreasing aspect in terms of sp^2 carbon orientation with the TiO_2 nanoparticles, and isolation rate domains in the rGO when the NC reaction is taken (Wang et al., 2011b). Based on the I_D/I_G for the TiO_2-rGO NC results, 0.3 wt% of TiO_2-rGO NC gained the highest intensity ratio and best sample among the other NC with 1.526. These observations may be attributed to the disorder of rGO that increased in terms of the photo-thermal after TiO_2 was loaded (Umrao et al., 2014b). While the particle size of rGO (La) was indirectly proportional to the intensity ratio, I_D/I_G as shown below (Ferrari and Robertson, 2000):

$$I(D)/I(G) = \frac{C(\lambda)}{La} \qquad \textbf{Equation (5.1)}$$

where the $C(\lambda)$ is 514.0 nm. The average particle size, La of rGO and 0.1 wt% - 0.5 wt% TiO_2-rGO NC can be identified by applying Equation (5.1) with 427.6 nm, 384.2 nm, 381.0 nm, 336.8 nm, 427.3 nm, and 425.1 nm, respectively. This indicates that the rGO of 0.3 wt% TiO_2-rGO NC was performed on the smallest particle upon the attachment of TiO_2 nanoparticles (Shu et al., 2013b). This occurrence may be one of the factors affecting the photocurrent density of DSSCs. Meanwhile, this scenario is also justifiable in the sense of the smallest particle size where the higher photocurrent density was performed. Furthermore, it was clearly showed that the 2D vibration peaks of TiO_2-rGO NC from Figure 5.7 (c) to (g) mostly disappeared as compared to rGO mainly due to the existing of specified functional group such as growths of oxygenated molecules during the hydrothermal process (Thakur and Karak, 2012).

Regarding to the Raman spectra results, even on the anatase TiO_2 or TiO_2 itself to form NC, it was proven that the precision of the synthesized TiO_2 was at the anatase phase and enabled to collaborate with the rGO material based on their Raman shift frequency, the covalency correlations and bond length calculation as compared with the theoretical aspect. The thermodynamically stable anatase phase consists of four major peaks at 141.85, 396.53, 517.12, and 641.86 cm^{-1} whereas a minor peak was at 197.00 cm^{-1} (Hamid et al., 2014a). Based on the assumption of the site symmetries for the Ti and O atoms within the unit cell (D_{2d} for Ti; C_{2v} for O) defined from theoretical space group

D_{4h}^{19} for anatase TiO_2 phase, it is consists of six Raman-active “lattice vibrations” allocated as: E_g (147 cm^{-1}), E_g (197 cm^{-1}), B_{1g} (397 cm^{-1}), A_{1g} (517 cm^{-1}), B_{1g} (640 cm^{-1}), and E_g (640 cm^{-1}) while a weak lattice vibration as the first overtone as B_{1g} (796 cm^{-1}) (Balachandran and Eror, 1982). Besides, the calculation of Ti-O bond lengths, $V_{ti\text{-}o}$ (Hardcastle and Wachs, 1991) is shown below:

$$V_{ti\text{-}o} = 21349exp^{(-1.9176R)}$$ **Equation (5.2)**

where $V_{ti\text{-}o}$ is the Raman frequency (cm^{-1}) and R is the bond length (Å). The purpose of analyzing the Ti-O bond lengths is to determine the actual phase composition of the TiO_2 to further improve our photoactivity performance.

Based on the Raman spectra for the synthesized anatase TiO_2 and TiO_2-rGO NC shown in Figure 5.7 within the range of 140-650 cm^{-1}, it is recorded that the three major peaks were at 394.39, 508.64, and 633.15 cm^{-1}; one minor peak at 201.75 cm^{-1}; as well as an intense peak at 147.21 cm^{-1}. These lattice vibration peaks were gained for every synthesized TiO_2-rGO NC sample very close to the theoretical anatase phase value. Consequently, the site symmetry modes can be assigned as E_g (147.21 cm^{-1}), E_g (201.75 cm^{-1}), B_{1g} (394.37 cm^{-1}), A_{1g} (508.64 cm^{-1}), and E_g (633.15 cm^{-1}). Subsequently, the range within 246.00-351.00 cm^{-1} is attributed to the O-O covalent interaction bonding (Hardcastle, 2011) whereas the sharp peaks of 147.21 cm^{-1} were endorsed to the Ti-Ti bonding in the octahedral chains with the bond length of 4.16 Å. Meanwhile, the broadband peaks for 201.75, 394.37, 508.64, and 633.15 cm^{-1} are moderately distorted TiO_6^{8-} octahedron in anatase which was categorized as the Ti-O bonding (Calculated Ti-O bond lengths: 2.43, 2.08, 1.95, and 1.83 Å by Equation (5.2)) (Hardcastle, 2011). Hence, the Raman spectra proved that the anatase of TiO_2 was fully incorporated with the rGO due to the appearance of lattice vibration peaks, symmetry modes, and the Ti-O bond lengths (Hardcastle, 2011).

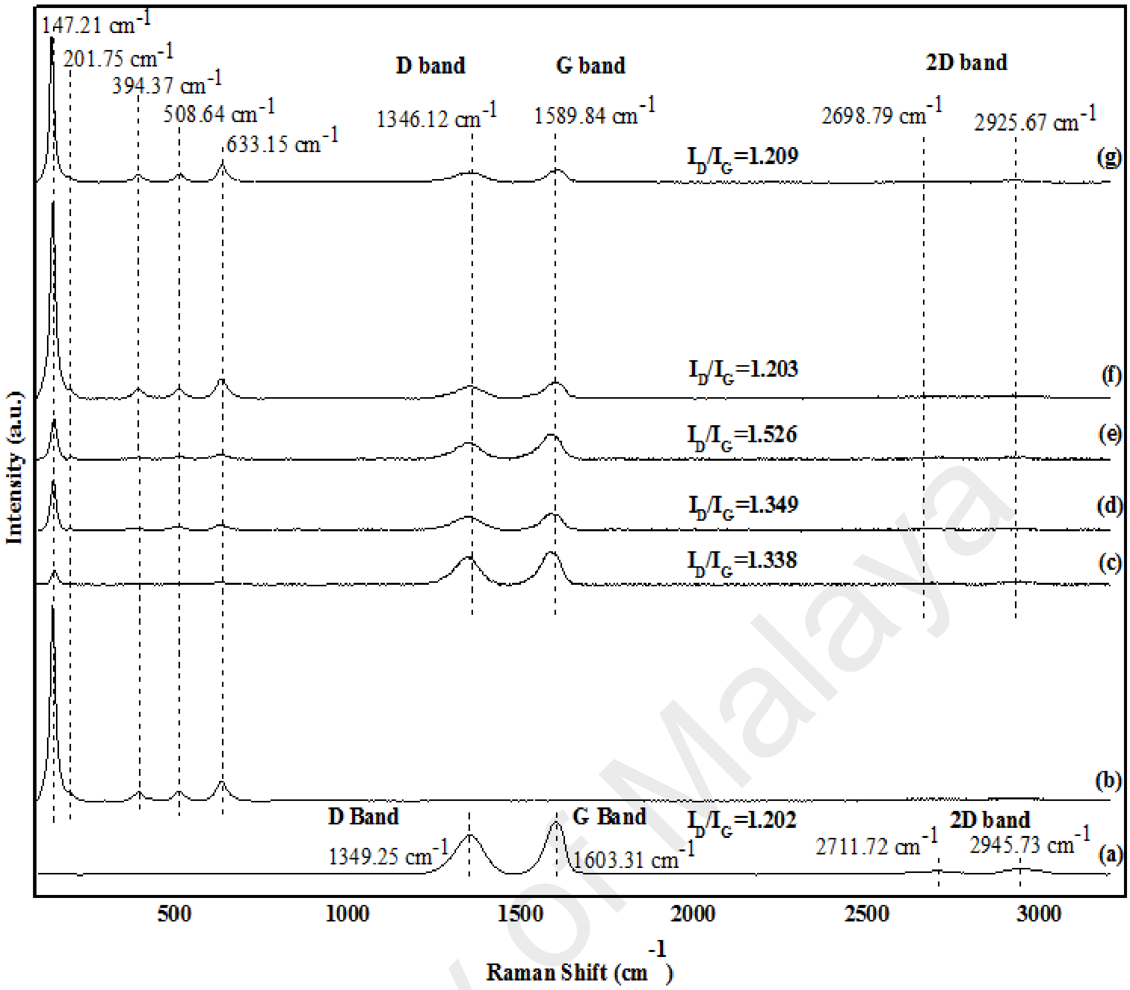

Figure 5.7: Raman scattering spectra of (a) rGO, (b) Anatase TiO_2, (c) 0.1 wt% of TiO_2-rGO NC, (d) 0.2 wt% of TiO_2-rGO NC, (e) 0.3 wt% of TiO_2-rGO NC, (f) 0.4 wt% of TiO_2-rGO NC, and (g) 0.5 wt% of TiO_2-rGO NC

5.2.3 Effect of TiO_2-rGO NC in DSSCs Application

5.2.3.1 Electron Mobility Characterization of TiO_2-rGO NC

The DSSCs devices were assembled based on various photoanodes, i.e. rGO nanosheets, anatase TiO_2 nanoparticles, and 0.3 wt% of TiO_2-rGO NC. The average values of conductivity and electron mobility of rGO nanosheets-based DSSCs, anatase TiO_2 nanoparticles-based DSSCs, and 0.3 wt% of TiO_2-rGO NC-based DSSCs were measured under room temperature using a Zeta potentiometer. From the results in Table 5.5, the anatase TiO_2 nanoparticles-based DSSCs sample obtained the lowest conductivity with 11.2 µS/cm and electron mobility with 0.5 µm.cm/Vs. This might be due to the larger band gap energy of 3.2 eV as compared with rGO nanosheets-based

DSSCs and 0.3 wt% of TiO_2-rGO NC-based DSSCs (2.90 eV) (Dette et al., 2014; Tan et al., 2013a). From the best of our knowledge, TiO_2 nanoparticles have good photocatalytic activity properties under ultra-violet (UV) and absorb UV light more easily. However, the charge carrier of TiO_2 nanoparticles will be lower in terms of rate of electron movement under visible light condition resulting in a lower conductivity as compared with rGO nanosheets or even 0.3 wt% of TiO_2-rGO NC. On the other hand, rGO nanosheets-based DSSCs recorded an intermediate level with a higher conductivity of 25.9 μS/cm and electron mobility of 0.7 μm.cm/Vs than anastase TiO_2 nanoparticles-based DSSCs. Theoretically, the rGO material is a good conductor, with smaller energy band gap, and faster charge carrier or electron movement (Chong et al., 2016). However, rGO nanosheets-based DSSCs are a weak photo-absorbent medium during electrical testing. Hence, the best candidate for photoanode-based DSSCs was 0.3 wt% of TiO_2-rGO NC which achieved a conductivity of 29.1 μS/cm and a mobility of around 1.0 μm.cm/Vs. Thus, 0.3 wt% of TiO_2-rGO NC-based DSSCs was the corporation of rGO nanosheets and TiO_2 nanoparticles neither good conductor nor good photocatalytic activity in order to enhance the PCE of DSSCs.

Table 5.5: Average values of conductivity and electron mobility of DSSCs based-rGO nanosheets, DSSCs based-anatase TiO_2 nanoparticles, and DSSCs based-0.3 wt% ofTiO_2-rGO NC

Materials	Conductivity, μS/cm	Electron Mobility (μmcm/Vs)
rGO Nanosheets	25.9	0.7
Anatase TiO_2 Nanoparticles	11.2	0.5
0.3 wt% of TiO_2-rGO NC	29.1	1.0

Figure 5.8 show the conductivity reading of DSSCs based-TiO_2-rGO NC using conductivity under was 28.9 μS/cm which matched the previous electrical testing.

Figure 5.8: Conductivity reading of TiO_2-rGO NC

5.2.3.2 DSSCs Analysis

The TiO_2 nanoparticle treatment was carried out in this study in order to enhance the efficiency of rGO. Furthermore, the enhancement of efficiency also depends on the type of dye sensitized to complete the DSSCs system. Herein, N-719 dye was integrated to fasten the excited electron from the dye that would transfer into the conduction band (CB) of TiO_2-rGO photoanode during the irradiation reaction (Song et al., 2014). The photovoltaic characteristics of rGO, TiO_2, and TiO_2-rGO NC (Figure 5.9) were analyzed and summarized in Table 5.6 with corresponding to the photocurrent density (J_{sc}), open-circuit voltage (V_{oc}), as well as maximum power point (J_{mp} and V_{mp}), fill factor (ff), maximum power (P_{max}), and the overall conversion efficiency, PCE (η).

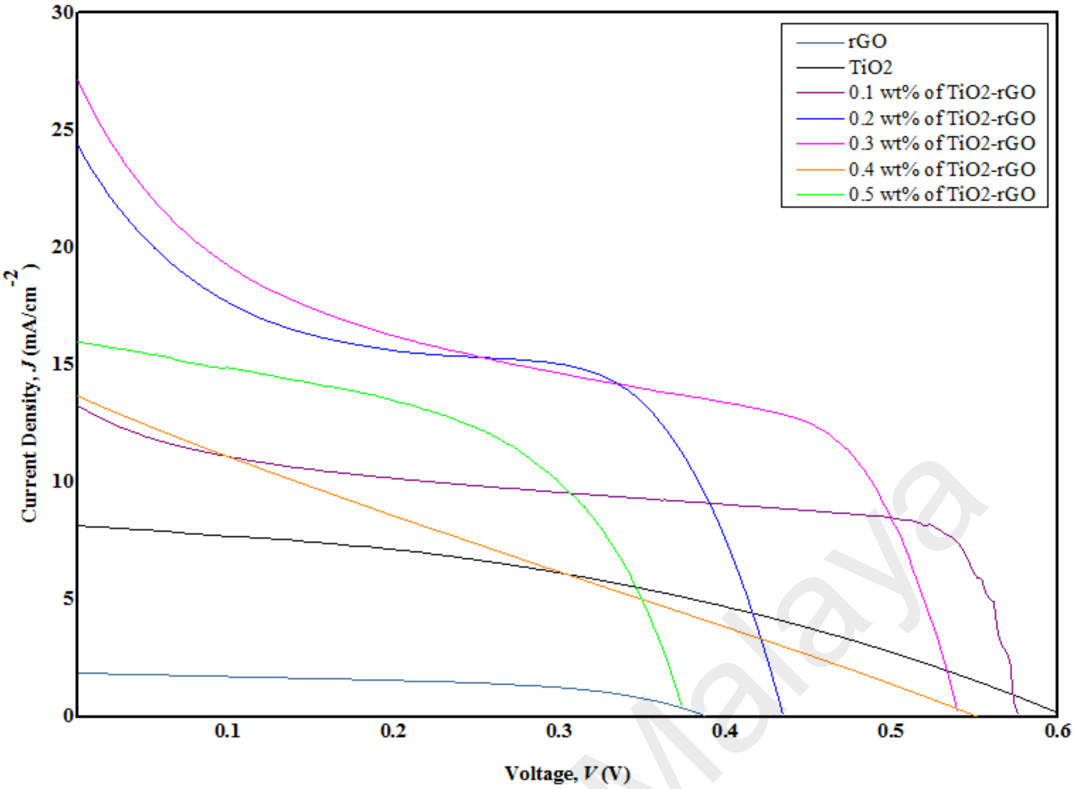

Figure 5.9: *J-V* Curves of DSSCs under AM 1.5 condition with rGO, TiO_2, and various amount of TiO_2-rGO

Moreover, the ff, P_{max}, and PCE were calculated from Equation (2.5) and Equation (2.6), respectively. Herein, the formula of ff was the maximum power area over the actual output area (Green, 1981). Meanwhile, the P_{max} formula was obtained from Equation (2.6) multiple with the actual V_{oc}-J_{sc} value (Hussein et al., 1995).

Table 5.6: Typical photovoltaic performances of DSSCs with rGO, TiO_2, and various NC photoanode

Photoanode Materials	J_{sc} (mA/cm^2)	V_{oc} (V)	J_{mp} (mA/cm^2)	V_{mp} (V)	ff (%)	P_{max} (mW/cm^2)	PCE, η (%)
rGO	1.92	0.39	1.90	0.35	0.89	0.67	0.67
TiO_2	8.19	0.61	6.50	0.42	0.55	2.75	2.75
0.1 wt% TiO_2-rGO NC	13.59	0.58	10.67	0.55	0.74	5.83	5.83

0.2 wt% TiO_2-rGO NC	25.40	0.43	17.10	0.35	0.55	6.01	6.01
0.3 wt% TiO_2-rGO NC	28.36	0.54	14.89	0.48	0.47	7.20	7.20
0.4 wt% TiO_2-rGO NC	13.92	0.55	5.45	0.40	0.28	2.14	2.14
0.5 wt% TiO_2-rGO NC	16.09	0.37	13.86	0.28	0.65	3.87	3.87

The summarized performance of the DSSCs based on the J_{sc} and V_{oc} was interpreted in Figure 5.10. These data were generated from Figure 5.9 as an easier or alternative way to determine the efficiency of DSSCs. The rGO-based DSSCs possess the below performance parameters: J_{sc} = 1.92 mA/cm^2, V_{oc} = 0.39 V, J_{mp} = 1.90 mA/cm^2, V_{mp} = 0.35 V, ff = 0.89 %, P_{max} = 0.67 mW/cm^2, and η = 0.67 % whereas the TiO_2-based DSSCs with J_{sc} = 8.19 mA/cm^2, V_{oc} = 0.61 V, J_{mp} = 6.50 mA/cm^2, V_{mp} = 0.42 V, ff = 0.55 %, P_{max} = 2.75 mW/cm^2, and η = 2.75 %. The photovoltaic performance of TiO_2 was higher than rGO due to the high photocatalyic activity during the irradiation (Pavasupree et al., 2006b).

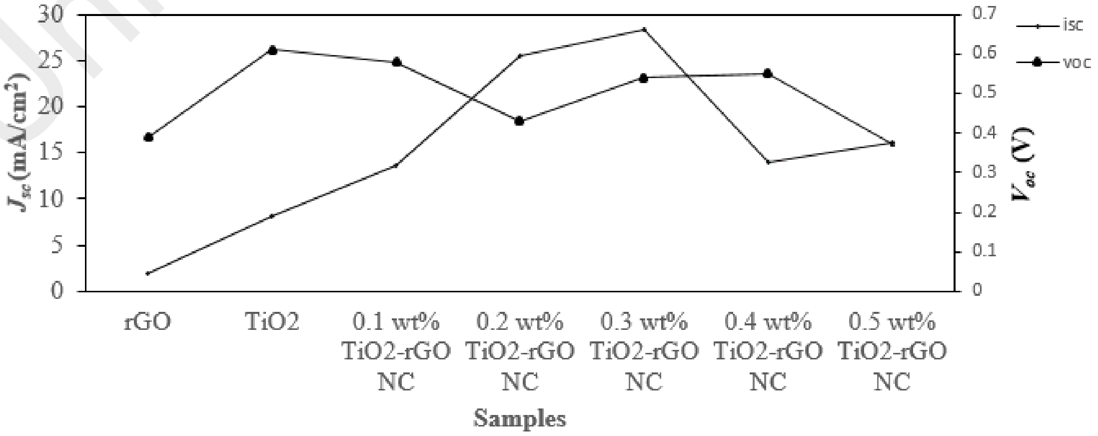

Figure 5.10: Typical output trends of J_{sc}, V_{oc} with based-samples and different contents of TiO_2 incorporated with rGO

For the best of understanding, the criteria to gain a desired short-circuit current (I_{sc}) are mostly established by good charge injection from the excited state of dye into the TiO_2-rGO photoanode and great charge transport (Wang et al., 2013). Notwithstanding, the I_{sc} was considerable as J_{sc} when the charge collection and transportation efficiency of the injected electrons from N-719 dye molecules were formed. From Figure 5.10, it was clearly seen that J_{sc} was a great dependent factor of the loading amount of TiO_2 as compared to either rGO or TiO_2-based of DSSCs. The J_{sc} of TiO_2-rGO NC from 0.1 wt%-0.5 wt% was recorded as 13.59 mA/cm^2, 25.40 mA/cm^2, 28.36 mA/cm^2, 13.92 mA/cm^2, and 16.09 mA/cm^2, respectively. Interestingly, among the J_{sc} of NC obtained in Figure 5.10, 0.3 wt% of TiO_2-rGO NC was the highest J_{sc} compared to the 0.1 wt% of TiO_2-rGO NC with the lowest J_{sc}, which increased at 108.7%. It is mainly due to the higher probability to capture and transport the electrons from CB or photoanode electrode in a high conductivity condition (Ding et al., 2015). Obviously, all of the NC obtained higher J_{sc} as compared with the rGO-based and TiO_2-based due to the formation between rGO and TiO_2 consequential maximizes the conductivity since the rGO has good conductivity and TiO_2 has high photocatalytic characteristic (Liu et al., 2013a).

According to the principle of DSSCs, V_{oc} values are associated with the difference between the Fermi level in TiO_2 under the illumination and Nernst potential from the redox couple reaction in the KI electrolyte (Wang et al., 2006a). Thus, the stable point of V_{oc} should be less than 0.7 V due to the rGO has exceptional electrical conductivity and resulting the reduction of the number of recombination between TiO_2 and KI electrolyte (Figure 5.10) (Ding et al., 2015). In contrast, the V_{oc} of NC from 0.1 wt% to 0.5 wt% was listed with 0.58 V, 0.43 V, 0.54 V, 0.55 V, and 0.37V, respectively. As a result, the V_{oc} was facing the unstable condition due to the recombination in TiO_2 when incorporated with rGO. However, these were not a big issue for the NC samples as long as they still work well in more electron density generated resulting the shifted of Fermi level (Tan and Wu, 2006), leading to less than 0.7 V (Figure 5.10). Moreover, the V_{oc} from 0.1 wt% - 0.4 wt% of TiO_2-rGO NC was verified within the range of rGO and TiO_2 which the TiO_2 was the highest V_{oc} among these NC-based DSSCs. It was related to the surface charge and charge recombination case. Meanwhile, the more recombination of TiO_2 as well as the V_{oc} in NC-based DSSCs decreased and thus the electron density in TiO_2 will be reduced (Shu et al., 2013a). However, the 0.5 wt% of TiO_2-rGO NC was considered to be a neglected sample due to the lower V_{oc} as compared with rGO-based DSSCs.

From Table 5.6, the ff value from 0.1 wt% - 0.5 wt% of TiO_2-rGO NC was achieved as 0.74 %, 0.55 %, 0.47 %, 0.28 %, and 0.65 %, respectively. The data was calculated from Equation (2.5). Theoretically, the fill factor of the DSSCs will be higher once the interior resistance of the DSSCs is lower (Ding et al., 2015).

$$ff = \frac{1}{R_s} \qquad \textbf{Equation (5.3)}$$

where R_s = Total series resistance.

After the interpretation of ff for these NC, it was noticed that 0.3 wt% and 0.4 wt% TiO_2-rGO NC were recorded as the second lowest and lowest value, respectively. It was allocated to the higher amount of TiO_2 which was present in the NC resulting the decline conductivity of rGO (Ding et al., 2015). Meanwhile, the lower conductivity gained will achieve higher interior resistance and finally obtain lower fill factor values. Furthermore, the electron mobility of rGO is only 0.1-10 $cm^2V^{-1}s^{-1}$ (Eda et al., 2011) as slow as TiO_2 with 0.1-4 $cm^2V^{-1}s^{-1}$ (Tang et al., 1994). Thus, the existence of TiO_2 will affect the fill factor of NC due to the interaction between TiO_2 and rGO then the interior resistance is increased (Ding et al., 2015). At last but not least, the ff of rGO and TiO_2-based DSSCs were acquired to higher values as compared to 0.3 wt% and 0.4 wt% TiO_2-rGO NC ascribed to the lower interior resistance since the rGO behaviour is an excellent conductivity (Yeh et al., 2014) while TiO_2 has good photocatalytic activity (Sedghi and Miankushki, 2012) in DSSCs.

Nonetheless, the efficiency, η is the destination point to determine the photovoltaic performance of DSSCs. Herein, the η from 0.1 wt% to 0.5 wt% was listed as 5.83 %, 6.01 %, 7.20 %, 2.14 %, and 3.87 %, respectively. From the listed results, it can be concluded with 0.3 wt% that TiO_2-rGO NC is the best perform and most suitable content amount for TiO_2 incorporated with rGO. The conversion efficiency of 7.20% corresponding to the rGO and TiO_2 by the increment of 974.6 % and 161.8 % was achieved. Additionally, 0.3 wt% of TiO_2-rGO NC accomplished the highest photovoltaic performance by the major affected factor of J_{sc}, which addressed the good electron transfer efficiency, high light scattering, and greatest in the dye absorption (Xiang et al., 2014). At last, these DSSCs samples rely on more than three times electron flow lifetime since the monolayer of rGO was a considerable similar structure with nanotubes (Ohsaki et al., 2005).

5.2.3.3 EIS Analysis

The electrochemical impedance spectrum (EIS) is widely used to characterize the interfacial electrical properties in DSSCs. The EIS results of DSSCs based on the Nyquist plot in Figure 5.11 (a) comprised two main semicircles which are one smaller curve appeared in the range of 36 - 40 Ω and a bigger curve from 40 - 98 Ω to complete the overall DSSCs circuit related to transfer and recombine processes regarding the photo-excited electrons in the DSSCs. In a short summary, the first smaller semicircle (high-frequency region) was attributed to the charge transfer at photoanode whereas the second semicircle (intermediate frequency region) was accredited to the electron recombination at the TiO_2-rGO/N-719 dye/KI electrolyte interface. After fitted the EIS data, an equivalent circuit of the DSSCs will be generated with the specified electronic component values in Figure 5.11 (b). The fitted equivalent circuit of DSSCs was categorized into three parts. The first part was the series resistance, *Rs*, which represents the transfer resistance of the FTO glass and KI electrolyte. The second part was connected in the parallel circuit by the charge recombination resistance, *Rct* whereas the chemical capacitance, *Cμ* was considered as the chemical capacitance of N-719 dye/TiO_2-rGO/KI electrolyte interface. The final parts of the parallel connected circuit categorized as the low-frequency region were $R_{graphite}$ and $C_{graphite}$; both of these components reproduced the electron diffusion of the KI electrolyte. The charge transfer resistance, $R_{graphite}$ stands for the interface of KI electrolyte/graphite/FTO glass while the $C_{graphite}$ addressed the interfacial capacitance of these interfaces (Van de Lagemaat et al., 2000).

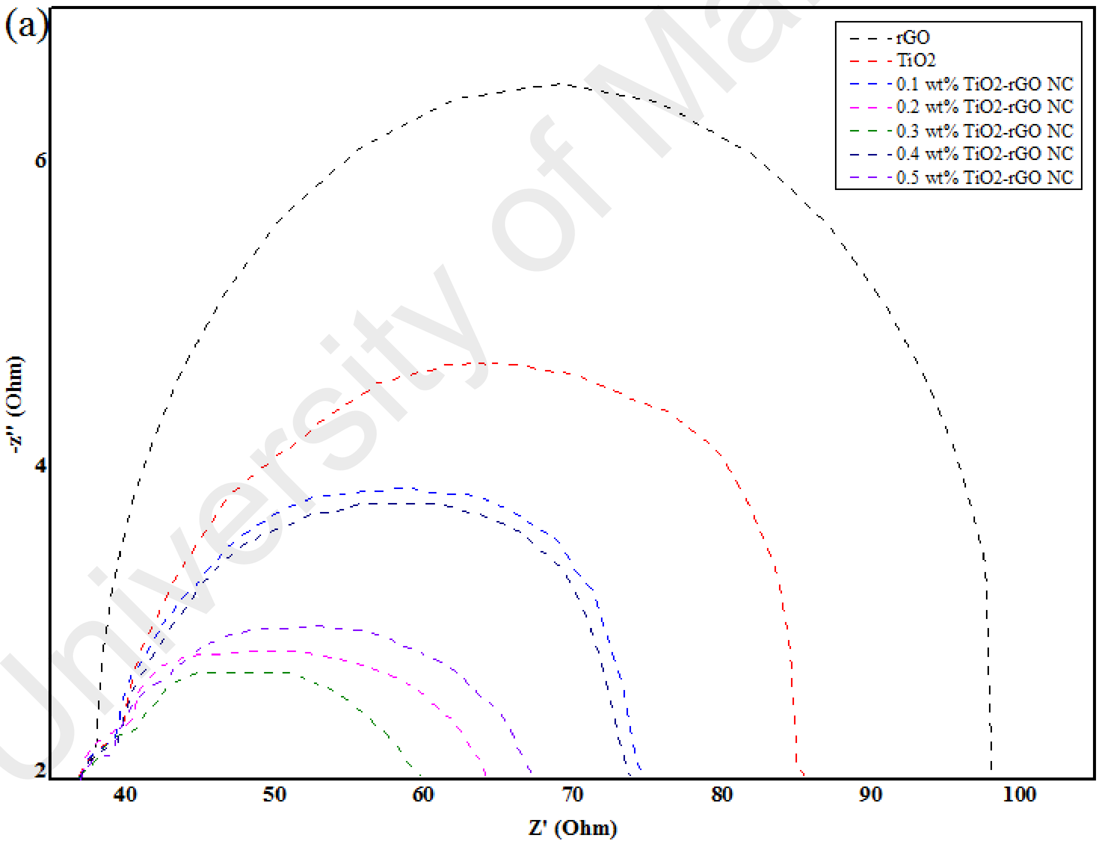

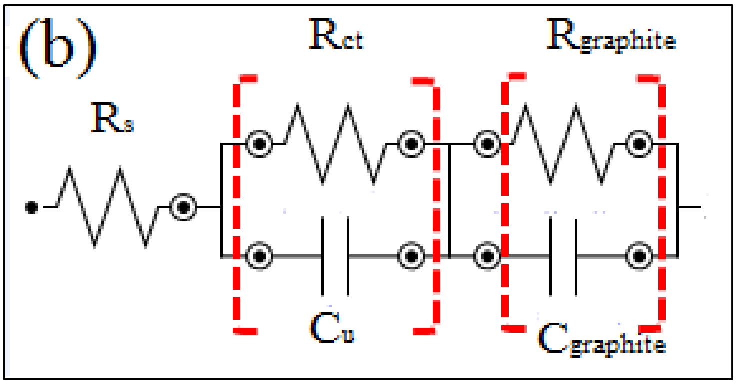

Figure 5.11: EIS measurements of Nyquist Plot (a) and equivalent circuit (b) of DSSCs with rGO, TiO_2, and various TiO_2-rGO NC

In Figure 5.11 (a), the significant values occurred with and without being loaded with TiO_2. The curves of the rGO-based photoanode film and TiO_2-based photoanode film were higher than the NC film due to the number of any catalyst chemical reaction performed on these films. Thus, the rGO and TiO_2-based photoanode films acquired a higher charge recombination resistivity and led to lower energy conversion efficiency performance as compared to the NC film. Apart from without TiO_2 loaded materials, the 0.3 wt% TiO_2-rGO NC has the most lowest curve among other NC film materials which was due to the more TiO_2 successfully formed with the rGO and enhanced the photocatalytic activity, and consequential rapidly injected the photo-excited electrons from the exited dye (S^*) into the CB of TiO_2-rGO film.

From Table 5.7, the R_{ct} of rGO loaded with the various amount of TiO_2 NC photoanode films has smaller values as compared to without the loaded samples. This phenomenon indicated that TiO_2 enhanced the photocatalytic activity between the rGO film and dye/I_3^- electrolyte, performing a higher efficiency since the rGO and TiO_2 are good mobility of the charge carriers and good photocatalytic activity, respectively (Pavasupree et al., 2006a; Roy-Mayhew and Aksay, 2014b). In addition, the electron life-time (τ) was also considered a vital parameter for DSSCs (Wang et al., 2006b), which derived from the C_μ and R_{ct} by the Nyquist plot of EIS fitted curve as below:

$$\tau = C_\mu R_{ct} \qquad \textbf{Equation (5.4)}$$

In the comparison of τ value in Table 5.7, 0.1, 0.2, and 0.3 wt% of TiO_2-rGO NC have longer life-time performance as compared to the without loaded samples. The 0.3 wt% of TiO_2-rGO NC has the longest life-time with 29.3 ms and this indicates the reliable samples in terms of energy conversion efficiency among the NC samples. Meanwhile, the presence of TiO_2 in the rGO formed TiO_2-rGO NC as a photoanode film in DSSCs definitely has an intelligence to improve the photoelectric performance by the intrinsic and photocatalytic activities, and the decreasing of R_{ct} values of NC photoanode film leads to the higher life-time of electrons.

Table 5.7: Summaries of charge combination resistance, chemical capacitance, and its electron life time of photoanode materials

Photoanode Materials	R_{ct} (Ω)	C_μ (μF)	τ (ms)
rGO	18.2	315	5.7
TiO_2	13.8	1105	15.2
0.1 wt% TiO_2-rGO NC	10.6	2085	22.1
0.2 wt% TiO_2-rGO NC	7.8	3567	27.8
0.3 wt% TiO_2-rGO NC	7.6	3854	29.3
0.4 wt% TiO_2-rGO NC	9.8	967	9.5
0.5 wt% TiO_2-rGO NC	8.9	1057	9.4

5.3 Discussion

Figure 5.12 reveals the molecular structure of rGO, anatase TiO_2, and Ru sensitizer complexes: N-719 dye; Di-tetrabutylammonium cis-bis(isothiocyanato)bis(2,2'-bipyridyl-4,4'-dicarboxylato)ruthenium(II). The molecular formula of the rGO always depends on the production value but the existence of linear formula is $C_xH_yO_z$. On the other hand, the molecular formula of the anatase is TiO_2 whereas the molecular formula of N-719 dye is $C_{58}H_{86}N_8O_8RuS_2$.

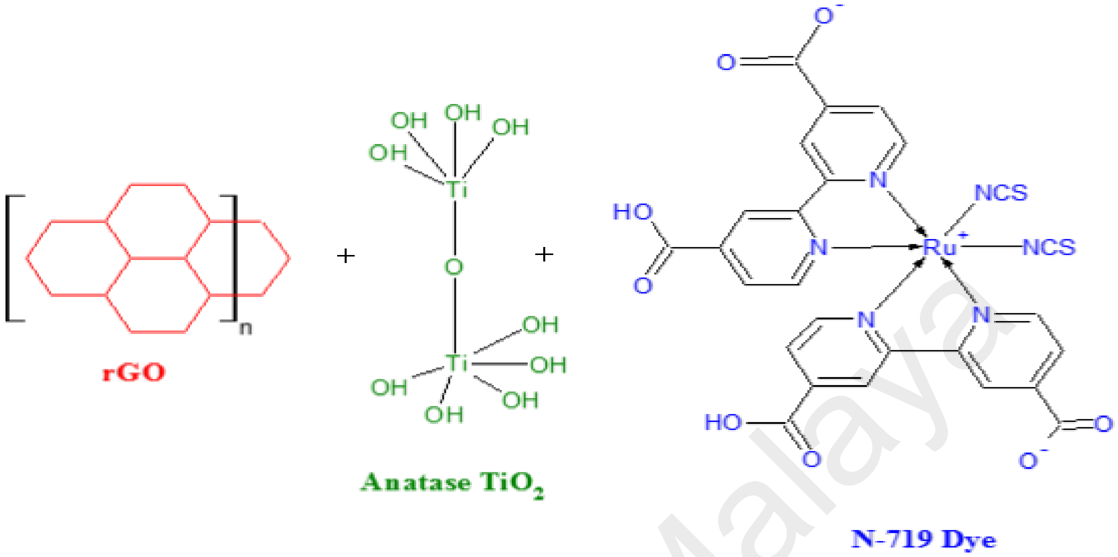

Figure 5.12: Molecular Structure of rGO, Anatase TiO_2, and N-719 Dye

There are three main reasons that the promising of rGO coated with TiO_2 to form TiO_2-rGO NC in order to enhance the performance of DSSCs. First, the TiO_2 have the ability to improve the separation between the electron and hole since rGO has high electron mobility (Adán-Más and Wei, 2013). Second, the corporation between TiO_2 and rGO can enlarge the absorption range of the visible region after the Ti-O-C was bonded. Third, the TiO_2-rGO NC can increase the interaction area and adsorption and result the N-719 dye to have the ability to create π-π interaction (Tan et al., 2012). In terms of the electron transfer, TiO_2 have good attraction with the epoxy and carboxylate groups of rGO (Williams et al., 2008). For the Fermi levels, rGO could be chosen as the electron shuttle in TiO_2 since the rGO has a higher value (-4.4 eV) as compared to the TiO_2 (-4.2 eV) at the conduction band (CB) (Figure 2.4). The possible reaction between TiO_2 and rGO is shown by the following equation:

$$TiO_2(e^-) + rGO \rightarrow TiO_2 + rGO(e^-) \qquad \textbf{Equation (5.5)}$$

Through this reaction, after the TiO_2 was coated with the rGO formed NC, it has the possibility to improve the performance of DSSCs in terms of good conductivity, charge mobility, adsorption, and etc.

Nevertheless, the rGO by TiO_2 as catalyst materials, good anchoring of COO^- and COOH to N-719 dye is compulsory since the TiO_2 is a hydroxyl-rich material (Lee et al., 2010a). Furthermore, it also assisted the preference of Ti-O, Ti-OH, and Ti-OH_2 from TiO_2 during the attachment of N-719 dye (Charbonneau et al., 2010).

The molecular structures of TiO_2-rGO-Ru sensitizer complexes (N-719 dye) for the dried condition and overall chemical bonding were shown in Figure 5.13 (a) and (b), respectively. Both of the illustrations show that the C bond of rGO was connected well with the Ti bond after the hydrothermal process. The polymer symbol ($[\ ]_n$) represents that several bondings occurred in between the rGO and TiO_2 after the hydrothermal process was carried out. The dotted retangle box represented as R_1 was distributed as the same loop for other chains. It was determined by the occurence of specified peaks of the rGO and TiO_2 in the Raman results and discussed in Figure 5.7. As seen in the Figure 5.13 (a) and (b), the bonding of the two neighbouring carboxylic acid/carboxylate groups of N-719 dye was bonded with the anatase TiO_2, namely bidentate-bridging whereas the negligible H_2O was the remover after the H-bonding donating group from N-719 dye and –OH group from TiO_2 (Lee et al., 2010a).

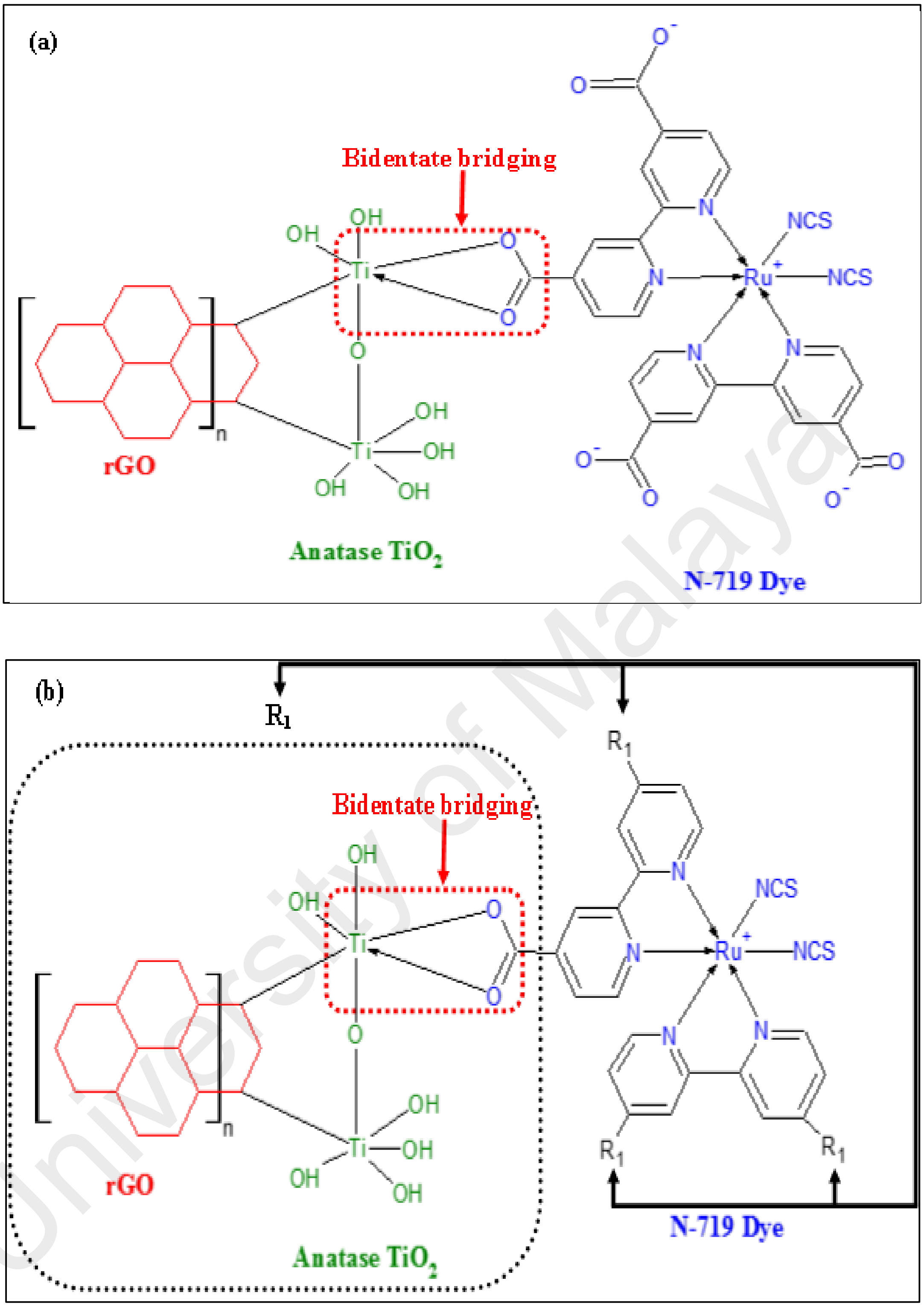

Figure 5.13: Chemical bonding of (a) N-719 dye absorbed and dried and (b) DSSCs complete structure

Among variety of TiO_2 content, the 0.3 wt% of TiO_2 content performed the best PCE of DSSCs due to the photogenerated electrons transferred from CB of TiO_2, passthrough the rGO NS and then transport quickly to FTO glass without recombination (Figure 2.4).

5.4 Conclusion

The rGO nanosheets by chemical reduction method, TiO_2 by precipitation-peptization method, and performed TiO_2-rGO NC by the hydrothermal process have been synthesized. The effects of rGO coated with a different amount of TiO_2 as photoanode in DSSCs were studied. The optimum loading content of 0.3 wt% of TiO_2-rGO NC possesses the highest conversion efficiency of 7.20% due to the NC acquired lower charge combination resistance, which leads to a higher electron mobility, improves photoelectron transfer and enhances the photoconversion efficiency energy of DSSCs. However, the excess TiO_2 species of 0.4 wt% and 0.5 wt% resulted in poor photoconversion efficiency performance attributed to the over photocatalytic reaction occurred leaving extra holes on the counter electrode.

CHAPTER 6: ION-IMPLANTATION TECHNIQUE OF TiO_2-rGO NANOCOMPOSITE IN DSSCS

6.1 Introduction

Recently, strong interest has been aroused in the third generation of photovoltaic solar cell technology, particularly the DSSCs device, attributed to their rational energy conversion efficiency, flexibility, low production cost and ease fabrication process as compared to that of the silicon-based solar cells (Chang et al., 2016; Freitag et al., 2017). Typically, DSSCs have a sandwich configuration consisting of three main elements, i.e., rGO photoanode, electrolyte containing I^-/I_3^- redox couple and Pt-layered cathode with four essential interfaces of FTO/rGO (photoanode), rGO/dye, dye/electrolyte and electrolyte/FTO (cathode) (Jin et al., 2012; Sheng et al., 2011). In order to acquire a higher PCE performance for the DSSCs, the materials and the fabrication technique of photoanode had been identified to be the major factors which needed to be taken into account to achieve an increased access rate of the photogenerated electrons from dye to the photoanode (Song et al., 2014). In fact, photoanode is one of the main platform to facilitate electrons flow with controllable rate with dependent material used.

In the past few decades, rGO was widely used as photoanode due to its outstanding photoelectric properties such as rapid charge carrier mobility and electron transfer (Kim et al., 2015b). In addition, rGO photoanode can be easily fabricated with large surface area and host with different types of semiconducting layers like TiO_2, ZnO, SnO_2 etc (Guo et al., 2015). However, synthesized of rGO sheets are lowered the mechanical strength properties which contained defects may resulting easy cracking. Somehow, the PCE of DSSCs based rGO photoanode without any modification was not an efficient working electrode (Low et al., 2017a). Apart of that, continuous explored have been exerted in order to enhance efficient charge carrier transport, semiconducting layer should have a wide bandgap, stability, high surface area, and appropriate photocatalytic support to maximize dye sensitizer loading. Among semiconducting materials, TiO_2 is the best candidate to be explored due to its good potential in UV light absorbance. As example, TiO_2 can serves as protector for organic dyes where the dyes are unstable under UV range (Hagfeldt et al., 2010b). In the past few decades, anatase TiO_2 was found to be the most common used material to induce photocatalytic properties on photoanodes attributed to its long-term thermodynamic stability, low-cost and relative non-toxicity (Fujishima et al., 2008; Hashimoto et al., 2005). However, anatase TiO_2 tended to suffer from high recombination center of electrons and holes coupled with wide band gap (i.e., 3.2 eV) (Tan et al., 2013a).

In order to improve the PCE of DSSCs, it is a must to explore and engineer the modification rGO material with supporting substance (semiconducting material) as efficient photoanode. To the best of our knowledge, hybrid of rGO NS with TiO_2 was one of the promising approach in order to gain both of the unique properties such as fast charge carrier mobility, more dye loading, and good photocatalytic properties (Chen et al., 2016a; Lim et al., 2015b; Tang et al., 2010). In fact, comprehensive fabrication techniques to prepare TiO_2-rGO NC as efficient photoanode was also one of the critical factor in order to control purity and minimizes defect of its rGO sheets which are indirectly influence the PCE performance of DSSCs (Guo et al., 2015). As aforementioned, the recent development of synthesis TiO_2-rGO NC methods were briefly discussed in Chapter 2. However, there are still facing some challenges although comprehensive works on DSSCs application has been accomplished. As example, the effect of TiO_2-rGO NC synthesis and mechanism in terms of photogenerated electron enhancement still remain unclear.

In this chapter, the modification of rGO Nanosheet (NS) via Ti ion implantation technique were studied under various applied power and sputtering duration.

1. To study the effect and formation of TiO_2-rGO NC by Ion Implantation Technique by different applied power and sputtering duration.
2. To explore the physical and chemical properties of TiO_2-rGO NC as photoanode in DSSCs.

To determine the PCE of DSSCs based applied power and sputtering duration parameter.

6.2 Research Findings

6.2.1 Effect of Applied Power of Ti Ions Implanted on rGO NS

The XRD patterns of rGO, anatase TiO_2, and variation of Ti ion sputtering applied power (50 W, 100 W, 150 W, 200 W, and 250 W) onto rGO NS are shown in Figure 6.1. For the rGO sample, three peaks were interpreted in Chapters 3 and 4. For the anatase TiO_2, there are some broad band crystalline peaks at $2\theta = 25.4^\circ$, 54.3°, 61.9°, 62.8°, and 70.4° were assignable to the along orientation of (101), (105), (116), (220), and (215) planes, respectively, which can be indexed to pure anatase phase of TiO_2 (Liu et al., 2011b). For the best of our knowledge, the determination of crystalline TiO_2 is based on the (101) peak at 25.4°. For the Ti ion sputtered onto rGO NS samples, there were clearly showed that increases in applied power with increases of intensity peaks along 25.4°. In other words, it is indicated that the presence of Ti ion occupied onto rGO NS with increases of intensity peak while the applied power were increased. As addition, the increment broad band peak at 45.6° along (200) plane was correspond with rGO plane. Besides, the two peaks along 28.2° and 32.3° relatively represented the presence of Ti^{3+} species onto the rGO NS.

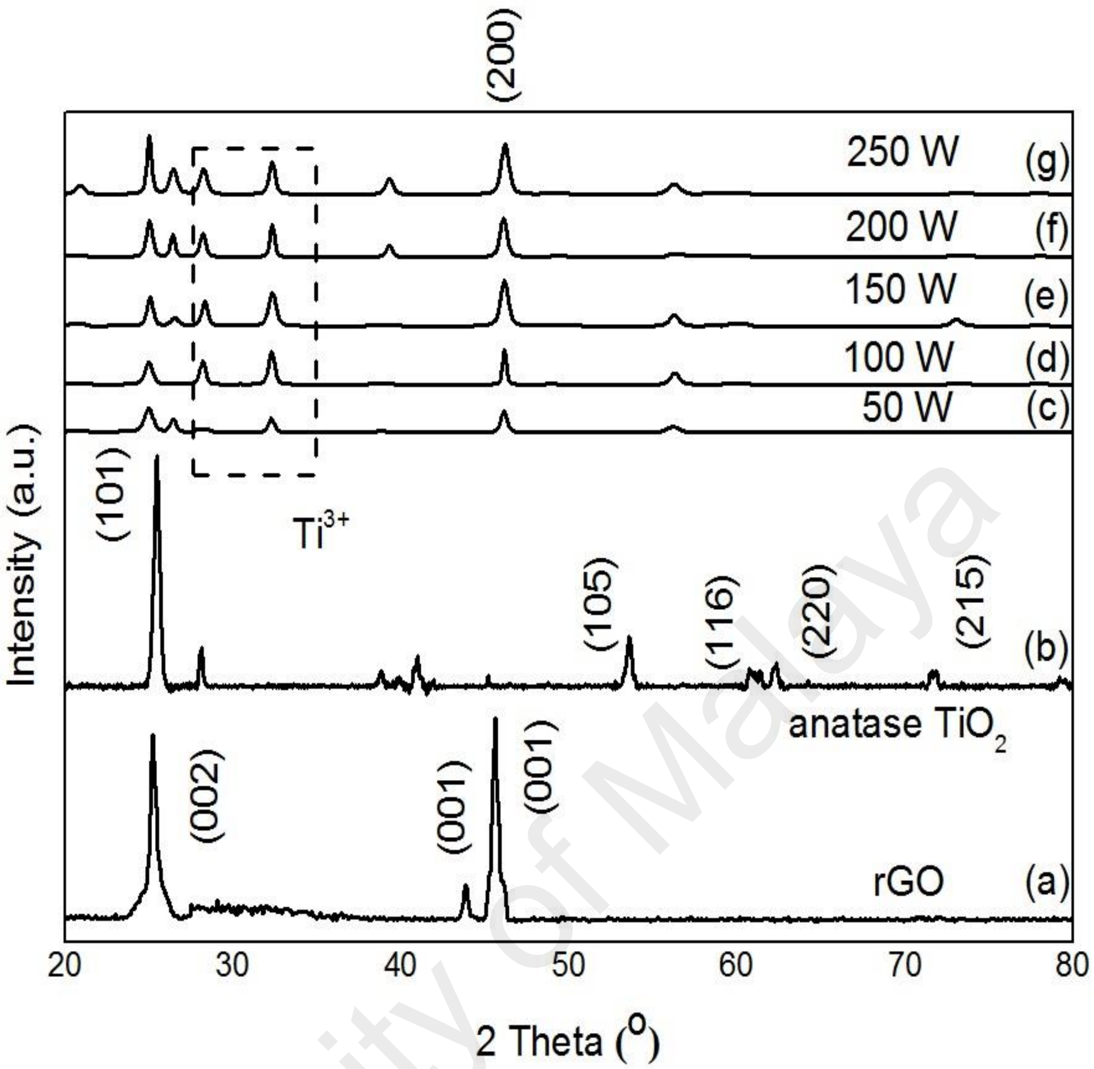

Figure 6.1: XRD patterns of (a) rGO, (b) anatase TiO_2, and (c)-(g) variation of Ti^{3+} ion sputtering applied power

UV-DRS was performed to study the optical properties of rGO after implanted with the Ti^{3+} ion using various applied powers. Figure 6.2 showed the UV-DRS spectra mode and the Tauc plots of TiO_2-rGO NC. It is clearly illustrated in Figure 6.2 (a) that the absorption edges from the 50W to 250 W, estimated band gap energy were ~2.89 eV (150 W), ~3.08 eV (50 W, 100 W, 200 W), and ~3.10 eV (250 W). Generally, these typical absorptions with an intense transition in the UV region were used to measure the intrinsic band gap absorption of Ti ion implantation where the electron transited from the valence band (VB) into conduction band (CB) ($O_{2p} – Ti_{3d}$). Specifically, both of the E_g values were calculated using Equation (4.1) based on the absorbance plot. The reflectance spectra can then be transformed into Tauc plot (Figure 6.2 (b)) by applying the Kubelka-Munk (K-M) expression Equation (6.2). Based on the experimental results, the red-shifted absorption edge (Figure 6.2 (a)) coupled with the lowest Eg (i.e., ~2.89eV) of the 150 W Ti ion-based material as compared to those implanted using 250 W (i.e., ~3.10 eV) indicated that the 150 W TiO_2-rGO NC possessed the highest absorbance in the visible-light range (300-350 nm) due to the closer CB and VB to the Fermi level. Considering these facts, it could be concluded that 150W was the optimum applied power to implant the Ti ion onto the rGO NS associated to the fastest rate of the photogenerated electron-hole pairs which would eventually enhance the efficiency performance in DSSCs system.

$$F(R) = \frac{(1-R)^2}{2R} \qquad \textbf{Equation (6.1)}$$

$$F(R) * hv = A(hv - E_g)^2 \qquad \textbf{Equation (6.2)}$$

where; λ = wavelength; $F(R) = K - M\ function$; R = reflectance; ; $h = Planck's constant; v = \frac{c}{\lambda}; c = speed\ of\ light; and\ A = constant$

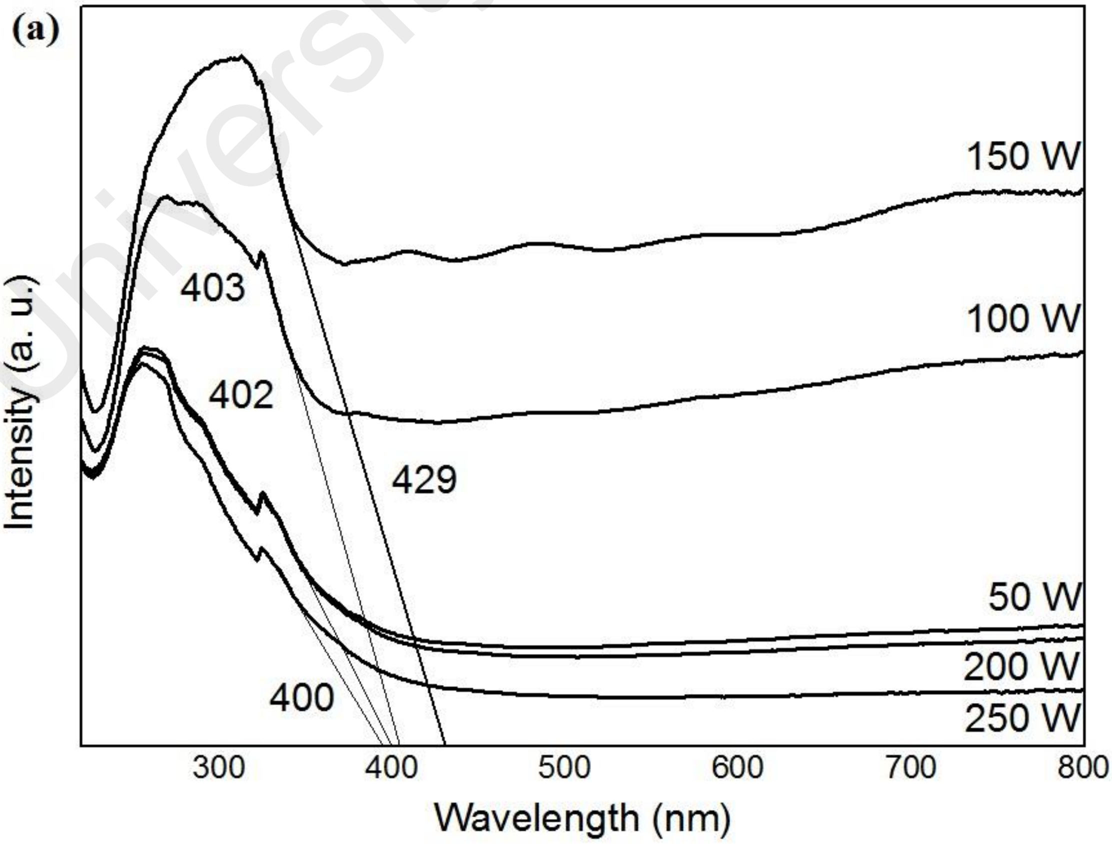

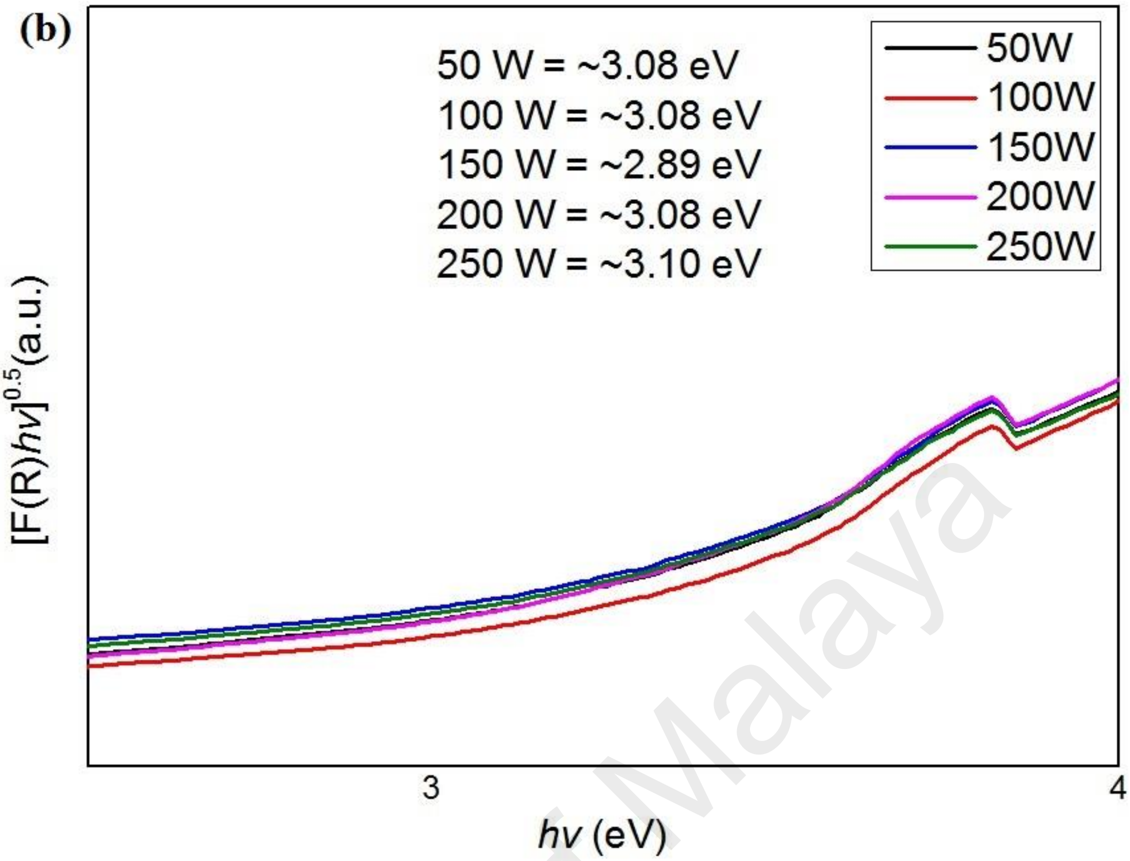

Figure 6.2: (a) UV-DRS absorbance spectra and (b) Tauc plots of difference watts

Raman spectroscopy is a useful tool to observe the vibrational peaks and to study the surface microstructure of the rGO and Ti ion-based materials. Figure 6.3 (a) and (b) illustrated the Raman spectra for both pristine rGO and anatase TiO_2, respectively. Accordingly, rGO showed two broad vibration bands within 1200-1700 cm^{-1}, in which the D vibration band appeared at 1350.95 cm^{-1} and G vibration band at 1604.96 cm^{-1}. Specifically, the D vibration mode arose from the breathing mode of κ-point photons of A_{1g} symmetry, while the G vibration band was ascribed to the first-order scattering of E_{2g} phonons by the sp^2 carbon network in rGO (Low et al., 2015c; Thakur and Karak, 2012). As shown in Figure 6.3 (b), the anatase phase of TiO_2 consisted of five major vibration peaks at 126.26, 205.51, 375.71, 495.32 and 616.67 cm^{-1}, which were assignable to the $E_{g(1)}$, E_g, $B_{1g(1)}$, A_{1g} and $E_{g(2)}$ modes, respectively (Hamid et al., 2014b; Šćepanović et al., 2009). Apart from that, Figure 6.3 (c)-(g) showed the Raman spectra of the Ti ion-based materials post Ti-ion implantation with various applied powers from 50 to 250W. The Raman spectra revealed the presence of the characteristic group frequencies associated to the presence of anatase TiO_2 and rGO. Some broad peaks around 100-700 cm^{-1} corresponded to typical anatase TiO_2, while the two broad bands within 1200-1700 cm^{-1} were assignable to rGO. In addition, among the five applied powers for Ti ion implantation, 150 W was found to be the most stable and optimized condition to prepare the photoanode for DSSCs associated to the appearance of significant peaks of rGO (D and G bands) as compared with other applied powers coupled with the reduced point defects of rGO vacancy during the Ti-ion implantation process (Wulff et al., 1967). On top of that, the G vibration band of 150 W Ti ion-based materials (1621.32 cm^{-1}) possessed the highest intensity peak which corresponded to the sp^2 hybridized carbon network. It is worth to mention that there was a slight distinction between the pristine rGO peaks at 1350.95 (D band) and 1604.96 cm^{-1} (G band) after the Ti ion implantation peaks at 1349.41 (D band) and 1621.32 cm^{-1} (G band). The I_D/I_G ratio for 50, 100, 150, 200, and 250 W were 0.68, 0.54, 0.73, 0.29, and 0.62 respectively. This demonstrated that 150 W applied power is the best parameter to incorporate with rGO. Besides, this observation gave us a hint that the surface amorphization modification on rGO NS by the Ti ion implantation had taken place (Chen et al., 2011).

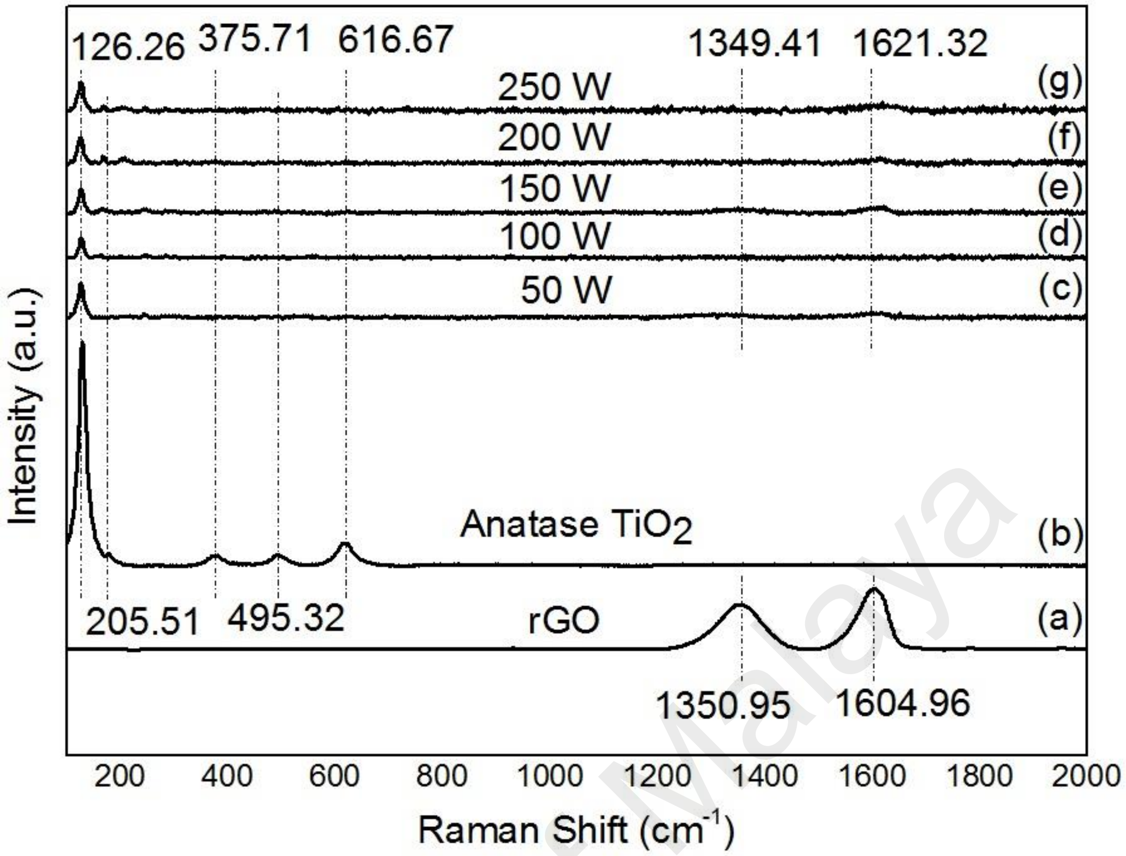

Figure 6.3: Raman spectra of rGO-NS before and after Ti ion implantation with different watts

Photoluminescence spectroscopy (PL) was used in the present research work to study the recombination and efficiency of the charge carrier trapping in the rGO surface after the Ti ion implantation. Figure 6.4 showed the PL spectra of rGO post implanted with Ti^{3+} with different applied power falling in the range of 350-600 nm. Accordingly, three major peaks located at 438, 471 and 494 nm, namely the photocatalyst regions, were commonly used to differentiate the formation and/or separation of the photoinduced electron-hole pairs (Babu et al., 2015). To the best of our knowledge, the peaks located at 438 and 471 nm were ascribed to the band edge free excitons (Liu et al., 2009a), while the excitonic PL peak at 494 nm was attributed to the surface oxygen vacancies or defects in the catalysts (JING and FU HG, 2005). Accordingly, it was discovered that the charge recombination of TiO_2-rGO photocatalysts using the applied powers of 100 and 150 W were lower than that of those 50, 200 and 250 W. In other words, lower recombination of TiO_2-rGO NC will obtain high PCE performance. Furthermore, the rGO in TiO_2

photocatalysts tended to reduce the electron-hole pair recombination due to its good electrical properties (W Lai et al., 2015). Specifically, 150 W was found to be the optimum applied power resulting the lowest PL intensity attributed to the lowest recombination rate of the electrons and holes under light irradiation. On top of that, this phenomenon inferred the high efficiency in the electron-hole separation and thereby enhanced the PCE. In contrast, the applied powers of 50, 200 and 250 W to implant the Ti ion onto rGO NS were found contributing to the higher PL intensities and thereby the higher recombination rate of electron-hole pair. In this respect, these three applied powers were not as applicable as 150 W considering these shortcomings might slow down the carrier mobility in TiO_2-rGO NC and eventually decrease the photocatalytic activity.

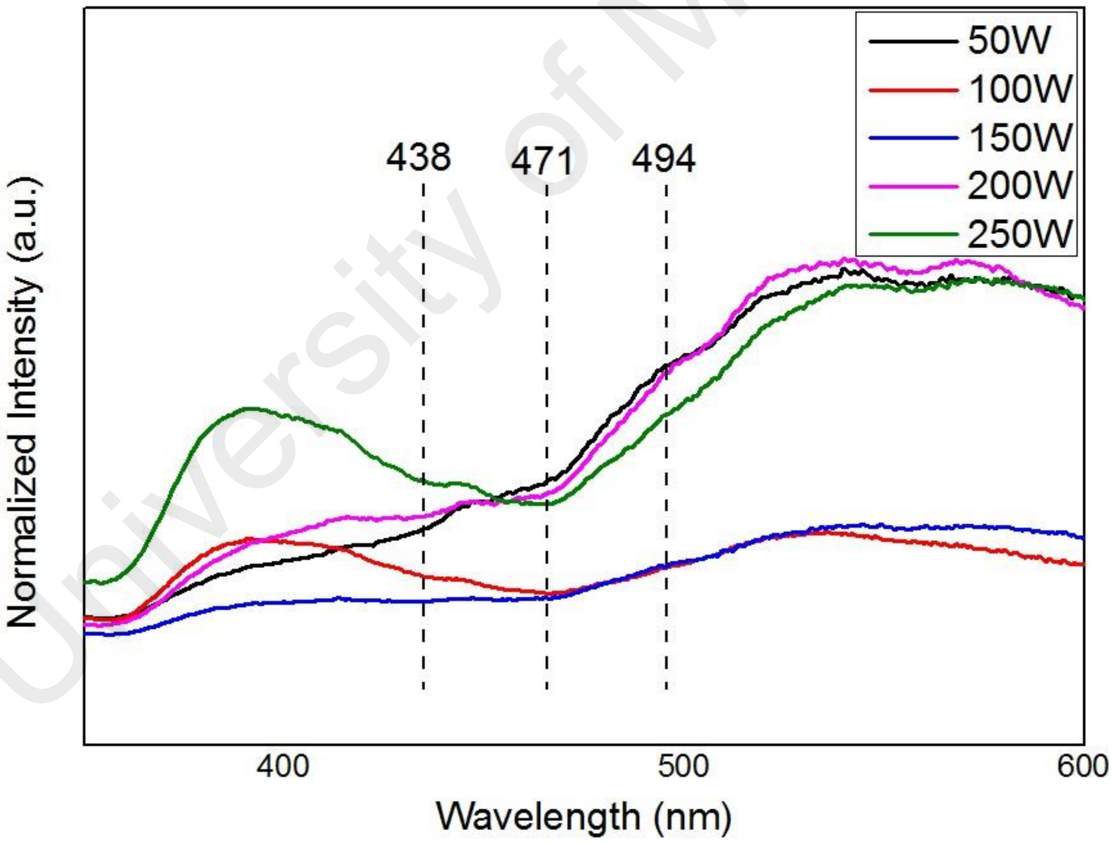

Figure 6.4: PL spectra of rGO by Ti ion implantation with different watts

The ATR-FTIR was carried out to identify the existing functional groups present in the rGO and TiO_2-rGO NC. Figure 6.5 showed the FTIR spectra of rGO and Ti ion implanted rGO NS (at various applied powers ranging from 50 to 250 W). Accordingly, the rGO exhibited some insignificant absorption peaks after the chemically reduction process which could be assigned to the hydroxyl group (O-H, 3425 cm^{-1}), the carboxyl moieties (C=O, 1720 cm^{-1}), the unoxidized graphitic domains or stretching deformation vibration of intercalated water for C=C skeletal (1520 cm^{-1}), the carboxyl group (C-O, 1400 cm^{-1}), the epoxide C-O-C or the phenolic C-O-H stretching vibrations (1220 cm^{-1}) and the epoxy or alkoxy groups of C-O stretching vibrations (1030 cm^{-1}) (Low et al., 2015c; Sim et al., 2014). It was clearly shown in Figure 6.5 that the peak intensity of the O-H group in rGO decreased and approached zero after the Ti ion implantation process. This gave us a hint that the Ti ion was fully loaded onto the rGO NS leading to higher interactions with the O-H functional group in NC (Sher Shah et al., 2012). Based on these facts, 150 W was found to be the optimum applied power considering all the rGO absorption peaks were eliminated. On top of that, it was also discovered that the Ti could react with the epoxide or phenolic groups in rGO forming the Ti-O-C/Ti-O-Ti absorption peak at 800 cm^{-1} (Sakthivel and Kisch, 2003).

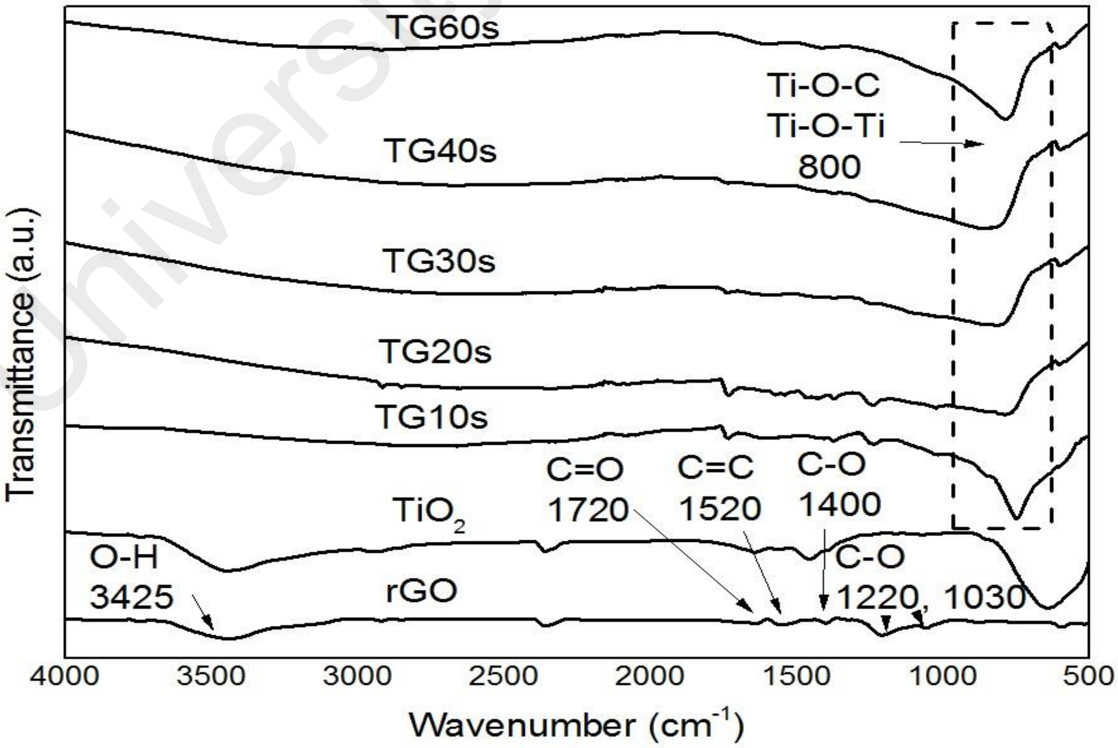

Figure 6.5: FTIR spectra of rGO and rGO by Ti ion implantation with different watts

Figure 6.6 (a)-(c) showed the surface morphologies of the rGO before and after the Ti ion implantation to form NC, while, Figure 6.6 (d) illustrated the lattice dimension of the TiO_2-rGO NC. Accordingly, as illustrated in Figure 6.6 (a), the synthesized rGO NS showed a tissue-like monolayer structure. From our previous report, the thickness of the synthesized rGO was estimated to be ~46 nm by controlling the synthesis time of GO (Low et al., 2015b). Figure 6.6 (b) showed the surface morphology of rGO NS post Ti ion implantation using the ion implantation technique, while the inset in Figure 6.6 (b) corresponded to the zoom-in morphology under higher magnification and EDX spectrum. It is noteworthy that the Ti ions scattered around the surface of the rGO and most of them were implanted onto the rGO. The EDX spectrum of 150 W sample indicated the presence of C, O, and Ti elements in TiO_2-rGO NC. On top of that, the EDX data also suggested the formation of Ti-O-C bonding post Ti ion implantation. This will be discussed further in the FTIR section. As shown in Figure 6.6 (c), the average size of Ti nanoparticles were found to be 70-80 nm after Ti ion implantation. Figure 6.6 (d) showed the lattice fringes of the synthesized rGO and Ti ion-based materials. Based on the HRTEM images captured under 2 nm magnification, the brighter color with 0.34 nm spacing (i.e., 3.4 nm with 10 lattice lines) corresponded to the carbon network of rGO attributed to (002) orientation (Chong et al., 2016; Chong et al., 2015; Low et al., 2015a). Furthermore, the darker color with 0.35 nm spacing (corresponding to 3.5 nm with 10 lattice lines) represented the anatase TiO_2 ascribed to (101) orientation plane (Babu et al., 2015). The mixed color could be denoted as the combination of Ti-O-C (Umrao et al., 2014a). Besides, the 0.19 nm (i.e., 1.9 nm of 10 lattice spacing) signified the thinnest region of Ti-O-C NC and implied the suitability of TiO_2-rGO NC as an efficient photoanode to enhance the photogenerated electron in DSSCs.

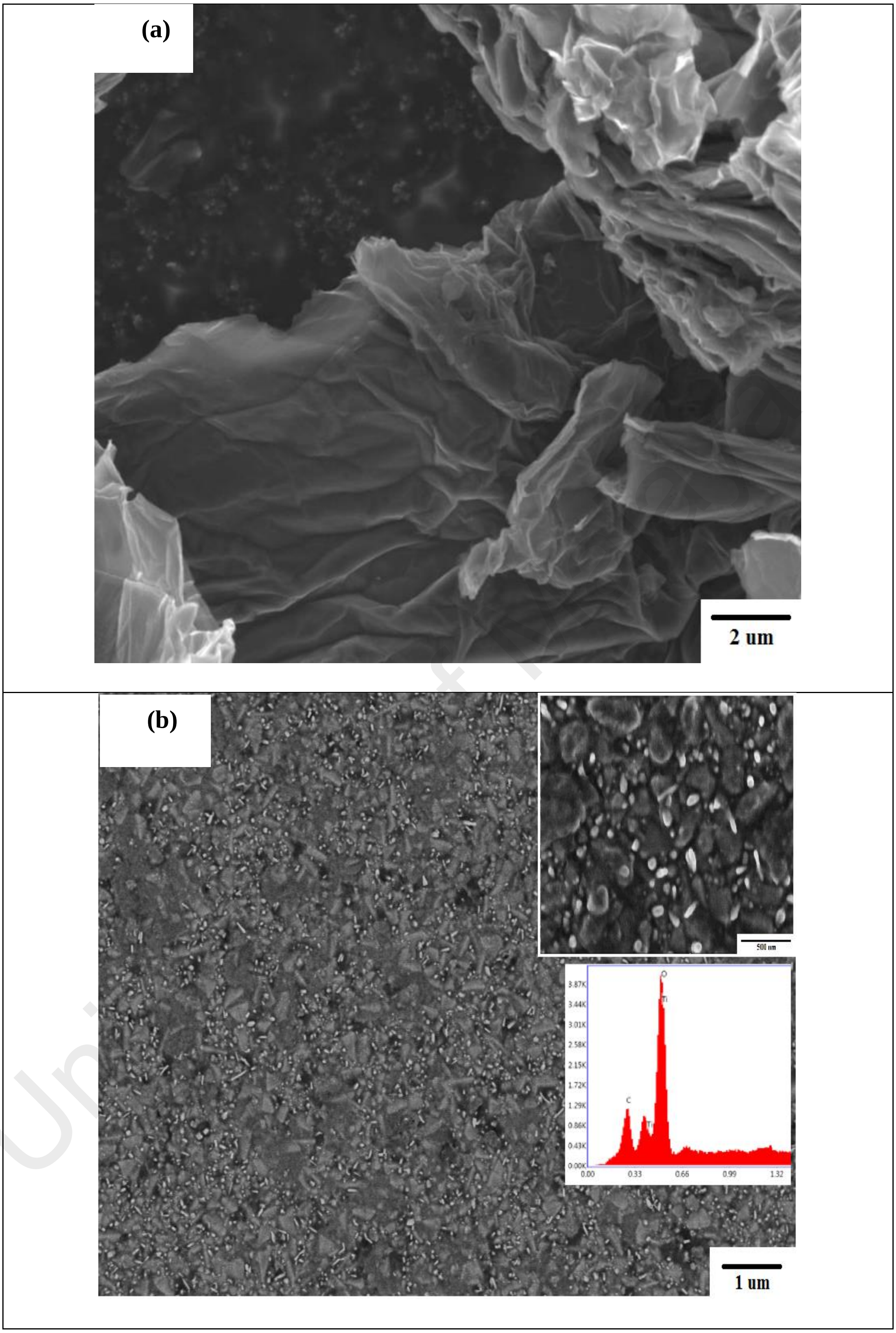
(a)
2 um
(b)
500 nm
3.87K
3.44K
3.01K
2.58K
2.15K
1.72K
1.29K
0.86K
0.43K
0.00K
0.00
0.33
0.66
0.99
1.32
O
Ti
C
Ti
1 um

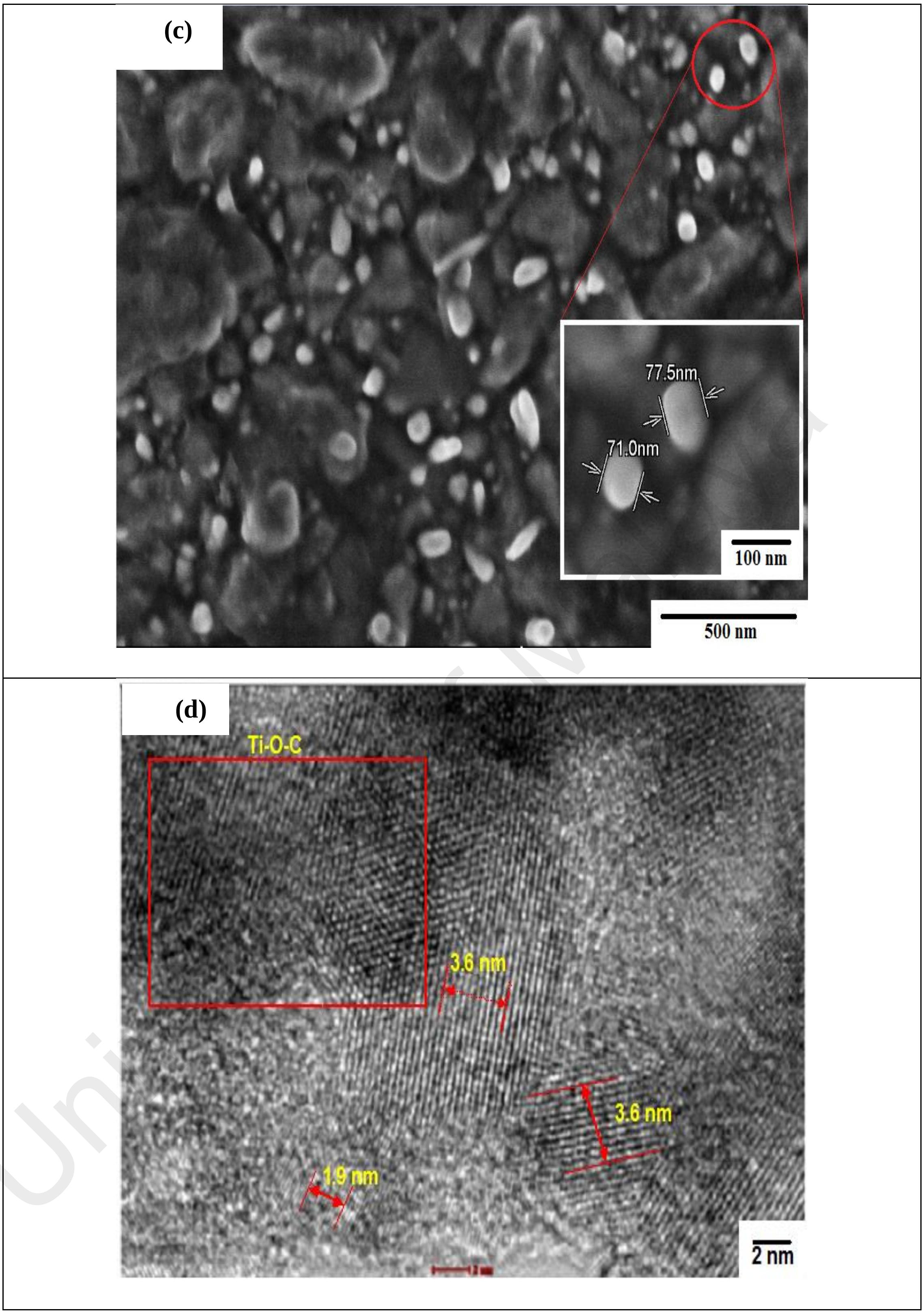

Figure 6.6: FESEM images of the (a) rGO NS, (b) Top view of rGO-Ti ion implanted with the inset of EDX for 150 W sample, (c) Size measurement of the Ti ion implanted, and (d) HRTEM images of rGO-Ti ion implanted

XPS was used in the present study to detect the element compositions (i.e., C, Ti, O) and the chemical state of rGO before and after the Ti ion implantation process (Singhbabu et al., 2014). Figure 6.7 (a) and (b) showed the survey spectra of the rGO and 150 W Ti ion implanted rGO, respectively. It was clearly illustrated in Figure 6.7 (a) that the rGO possessed two major peaks: C 1s peak and O 1s peak. Figure 6.7 (b) showed that few essential peaks (i.e., C 1s, O 1s, Ti $2p_3$, Ti $2p_1$, and Ti 2s) emerged after the Ti ion implantation process using the applied power of 150 W. Based on the XPS survey spectra data, it was found that the C 1s peak reduced while the O 1s increased post Ti ion implantation as compared to that of rGO. This finding was attributed to the introduction of Ti ion onto rGO NS by the substitutional technique. Specifically, the introduction of Ti ion resulted in stronger O 1s but weaker C 1s could be explained by the contribution of oxygenated group from the TiO_2 and the joint distribution surface area with the Ti functional group (Bell et al., 2011). Furthermore, it was found that the O 1s and C 1s peaks in both rGO and Ti ion implanted rGO located at the same binding energy indicating that same specimen of rGO was deposited on the FTO glass and underwent the Ti ion implantation process.

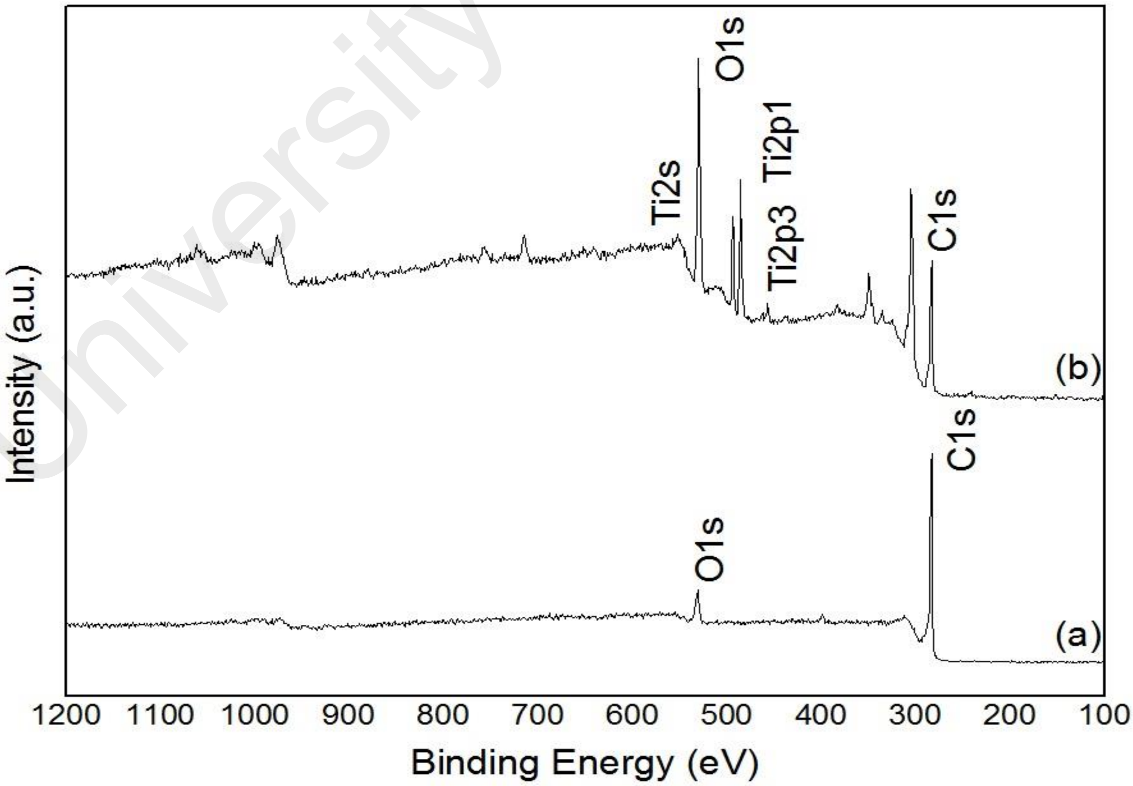

Figure 6.7: XPS survey spectra of the photoanode (a) rGO and (b) rGO with 150 W of Ti ion implantation

Figure 6.8 (a) and (b) illustrated the high resolution XPS data of C 1s peaks of rGO and TiO_2-rGO NC, respectively. Based on the C 1s XPS spectra of the rGO and TiO_2-rGO NC, the peaks located at the binding energies of 284.8 eV and 284.7 eV were mainly attributed to the C-C (aromatic) and the reduced binding energy detected indicated that the Ti ion was implanted successfully onto rGO and thereby weakened the C-C bonds. The increased intensity of the C-O peaks in rGO and TiO_2-rGO NC positioned at 285.6 eV and 285.8 eV, respectively. This is indicated that, the O that dispelled from Ti bonded well with the C element (Wang and Zhang, 2011). Under the same condition, the intensity peaks of COOH for TiO_2-rGO NC located at 288.5 eV was found to be wider than the rGO that located at 288.6 eV. This suggested the strengthening of the carboxylic functional groups after the Ti ion implantation process forming the Ti-O-C bond (Zhang et al., 2010a; Zhao et al., 2010). In addition, the intensity peak at 288.6 eV, which represented the Ti-O-C structure, revealed that the Ti atoms replaced some of the C atoms successfully via the substitution approach onto the lattice of rGO NS during the Ti ion implantation process (Liu, 2014). Figure 6.8 (c) and (d) showed the O 1s peaks for both rGO and TiO_2-rGO, respectively. It is clearly illustrated in Figure 6.8 (c) that the O 1s spectra peaks for rGO consisted of the C=O with the binding energy of 531.6 eV and C-O of 533.3 eV. As illustrated in Figure 6.8 (d), these C=O and C-O peaks disappeared after the Ti ion implantation process. However, the intensity peaks located at 529.9 eV, 531.5 eV and 532.8 eV, representing the TiO_2, OH and H_2O emerged post Ti ion implantation process. This suggested the formation of Ti-O and Ti-O-C bonds in TiO_2-rGO NC (Zeng et al., 2015). Figure 6.8 (e) displayed the Ti 2p XPS spectra of TiO_2-rGO NC. The Ti 2p of TiO_2 showed a distribution of the spin-orbital ($2p_{3/2}$ and $2p_{1/2}$) and these peaks were found shifted to higher binding energies of 458.4 eV and 464.0 eV as compared to that of the Ti ion source from pure anatase phase (i.e., 457.9 eV and 463.8 eV). This is in a good agreement with the pure anatase phase of Ti(IV) tetragonal structure, Ti^{3+}) (Li et al., 2014; Song et al., 2005). The shift is mainly due to the presence of C element in rGO NS granted onto the TiO_2 lattice forming the Ti-C and/or Ti-O-C bonds (Liu, 2014; Zeng et al., 2015).

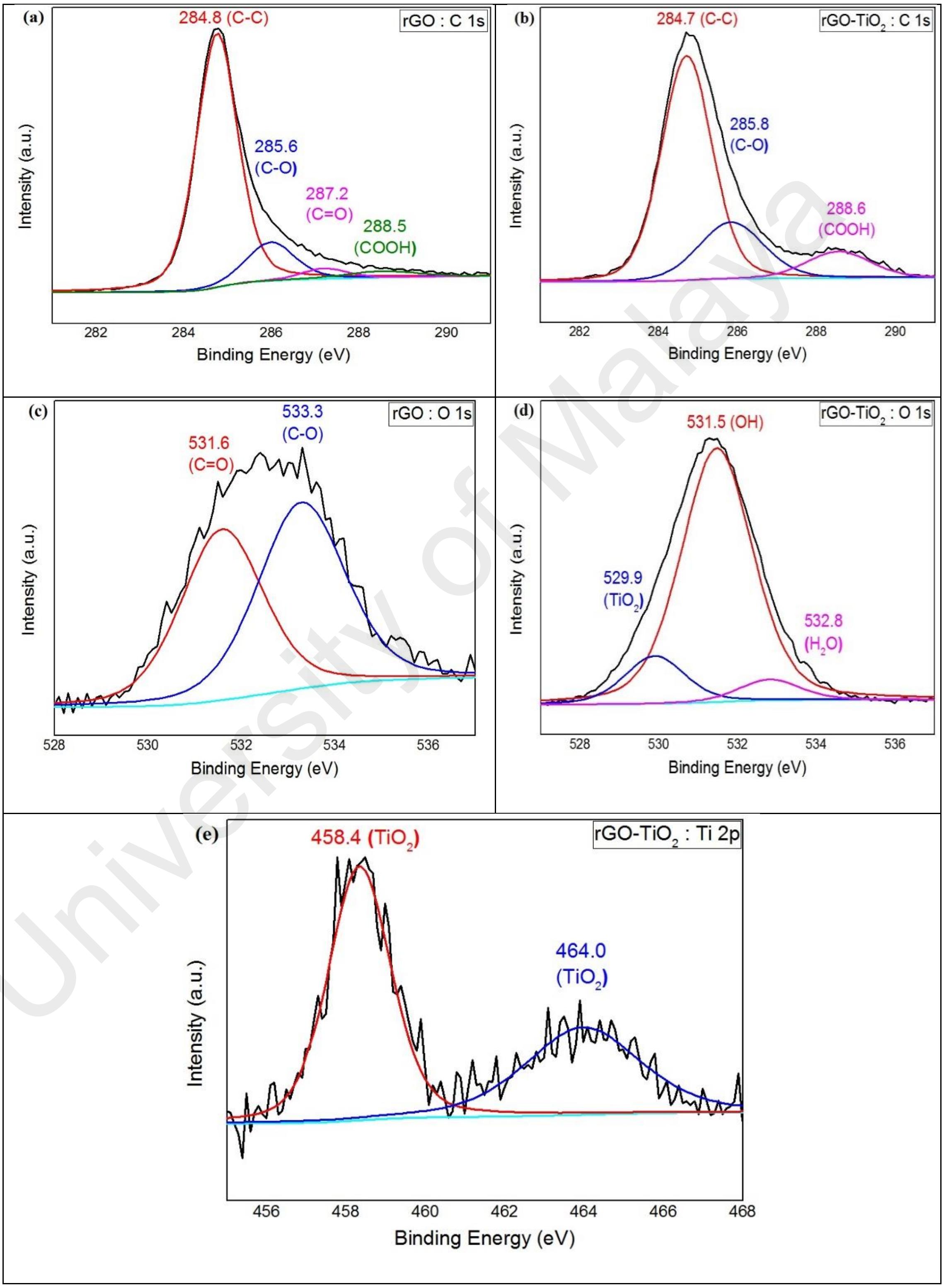

Figure 6.8: XPS spectra of C 1s peaks of (a) rGO (b) TiO_2-rGO NC (150 W of Ti ion implantation); O 1s peaks of (c) rGO (d) TiO_2-rGO NC (150 W of Ti ion implantation) and (e) Ti 2p of TiO_2-rGO NC (150 W of Ti ion implantation)

6.2.2 PCE of DSSCs Performance – Applied Power

Figure 6.9 showed the density current against voltage curves, *J-V* characteristics of DSSCs based on rGO (before and after the Ti ion implantation process), while, Table 6.1 tabulated the DSSCs performances based on the J-V curves. It was found that the raw rGO had a short circuit current density, J_{sc} of 4.34 mA/cm^2, an open circuit potential, V_{oc} of 0.39 V and the PCE, η of 0.68% prior to the Ti ion implantation process. A significant increase in the value of η from 0.68% to 8.51% was observed post Ti ion implantation process implying the presence of Ti^{3+} at the photoanode promoting the photogenerated electrons (Pradhan et al., 2007). The desired power applied to implant the Ti ion onto rGO NS was found to be 150 W due to the highest *Jsc* value of 25.02 mA/cm^2 obtained. This was in good agreement with the aforementioned narrowing band gap energy which discussed earlier. However, a decrease in η was detected by using relatively high applied power (i.e., >150W) to implant the Ti ion onto rGO NS. This was mainly attributed to the over photocatalytic activity generated among the N719 dye/rGO/TiO_2 interfaces and the increased charge transport resistance at the KI electrolyte/N719 dye/rGO/TiO_2 interfaces (Figure 2.3) (Huang et al., 2012b). The reduction in the rate of photogenerated electrons eventually led to the decrease in η.

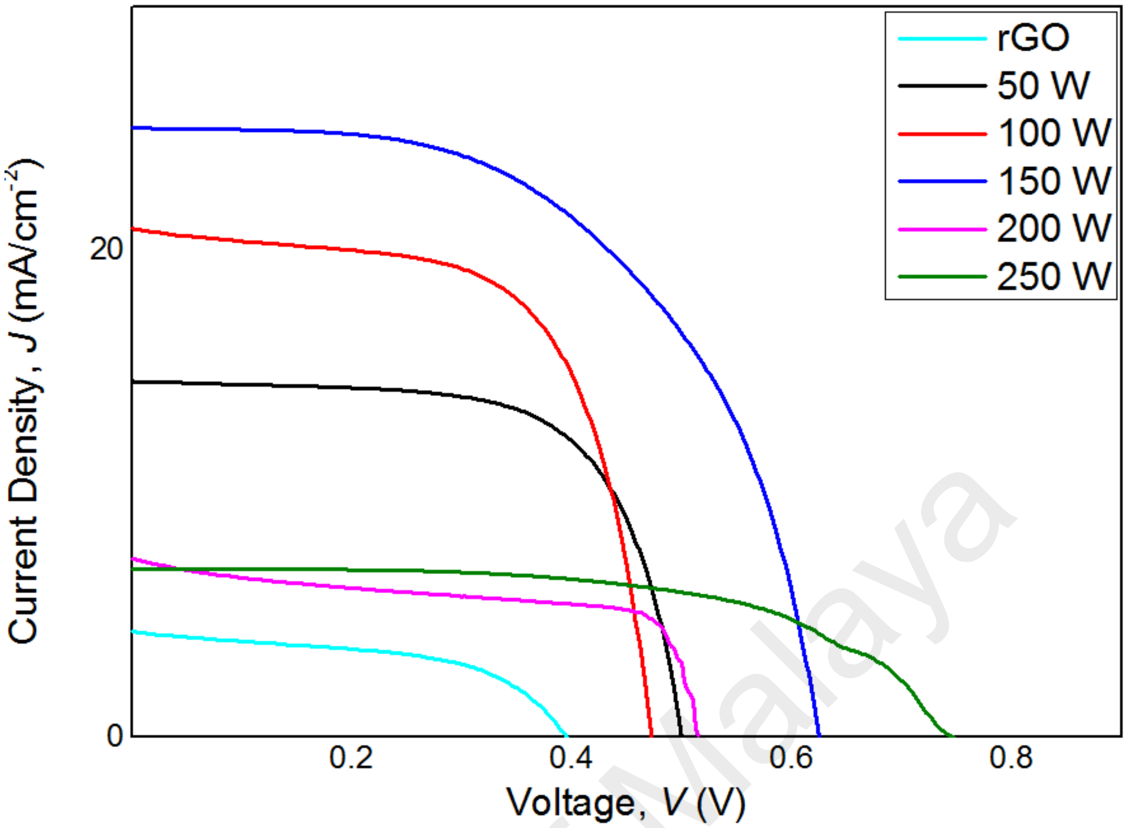

Figure 6.9: *J-V* Curves of DSSCs under AM 1.5 condition (power density, P_s = 100 mW/cm^2) with rGO and rGO implanted by various applied powers

Table 6.1: Typical photovoltaic performances of DSSCs with rGO before and after Ti ion implantation

Applied Power, W (W)	Short Circuit Current Density, J_{sc} (mA/cm^2)	Open Circuit Voltage, V_{oc} (V)	Maximum Current Density, J_{mp} (mA/cm^2)	Maximum Voltage, V_{mp} (V)	Fill Factor, ff, %	Maximum Power, P_{max}, (mW/cm^2)	PCE, η (%)
0	4.34	0.39	1.91	0.35	0.40	0.68	0.68
50	14.61	0.50	11.74	0.41	0.66	4.82	4.82
100	20.88	0.47	16.41	0.38	0.64	6.28	6.28
150	25.02	0.63	17.29	0.49	0.54	8.51	8.51
200	7.35	0.52	4.84	0.47	0.60	2.29	2.29

250	6.90	0.75	4.92	0.59	0.56	2.90	2.90

6.2.3 Effect of Sputtering Time of Ti Ions Implanted on rGO NS

Figure 6.10 shows the XRD patterns of rGO, anatase TiO_2, and variation of sputtering time of Ti ion access onto rGO NS with 10s, 20s, 30s, 40s, and 60s, respectively. rGO were discussed in Chapters 4 and 5 whereas anatase TiO_2 was clearly illustrated in Figure 6.1. The XRD analysis further presented that main peak of TG10s-TG60s at 25.4˚ along (101) are increases correspond with the increases of sputtering time. It is indicated that the increases of Ti ion implanted onto rGO NS in longer sputtering time. Furthermore, the appearance of two peaks at 28.2˚ and 32.3˚ also proved that the presence of Ti^{3+} species onto rGO NS.

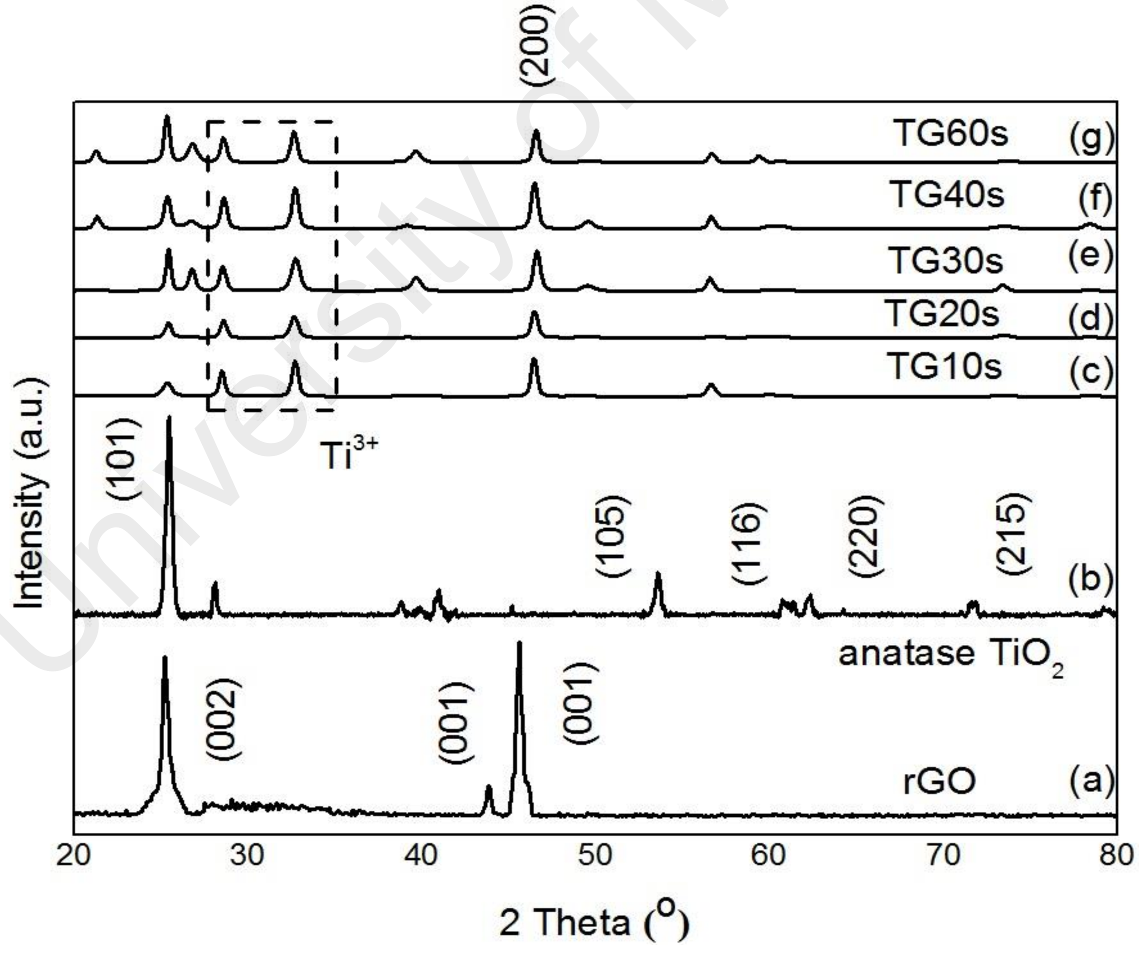

Figure 6.10: XRD spectra of (a) rGO, (b) anatase TiO_2, and variation of sputtering time of Ti ion onto rGO NS (c) TG10s, (d) TG20s, (e) TG30s, (f) TG40s, and (g) TG60s

UV-VIS spectroscopy was applied to study the optical properties of TiO_2-rGO NC (Pan et al., 2012a). Figure 6.11 (a) and (b) shows absorbance and Tauc plot of rGO NS implanted by Ti ion with variation of time (10s, 20s, 30s, 40s, 60s) and denoted as TG10s, TG20s, TG30s, TG40s, and TG60s, respectively. In comparison between implantation duration in Figure 6.11 (a), TG40s remarkably substantial red shifted to the higher wavelength in the absorption edge as compared to the TG60s. It is indicated that narrowing band gap after implanted by Ti ion. On the other hand, the optical band gaps of TiO_2-rGO NC with TG10s, TG20s, TG30s, TG40s, and TG60s were determined using Tauc plot of the Kubelka-Munk (KM) function in Figure 6.11 (b). The estimated band gaps of TG10s – TG60s were 3.06, 3.09, 2.82, 2.76 and 3.15 eV, respectively. From the optical band gap observation, TG40s shows the optimize Ti implantation duration as it was the smallest band gap obtained as compared among others implantation duration. The smallest band gap of TG40s (2.76 eV) could be ascribed to the more O=C-O-Ti bonds were formed between Ti ion with rGO during implantation process (Tan et al., 2013b). It is remarkable that TG40s obtained smaller band gap (2.76 eV) as compared with 150W with 2.89 eV indicated that faster charge carrier transportation rate in TG40s and hence efficient in PCE performance. In addition, duration study of TG40s sample is the most optimized samples as compared with power applied of 150W sample via ion implantation technique due to the more Ti ions access in duration study.

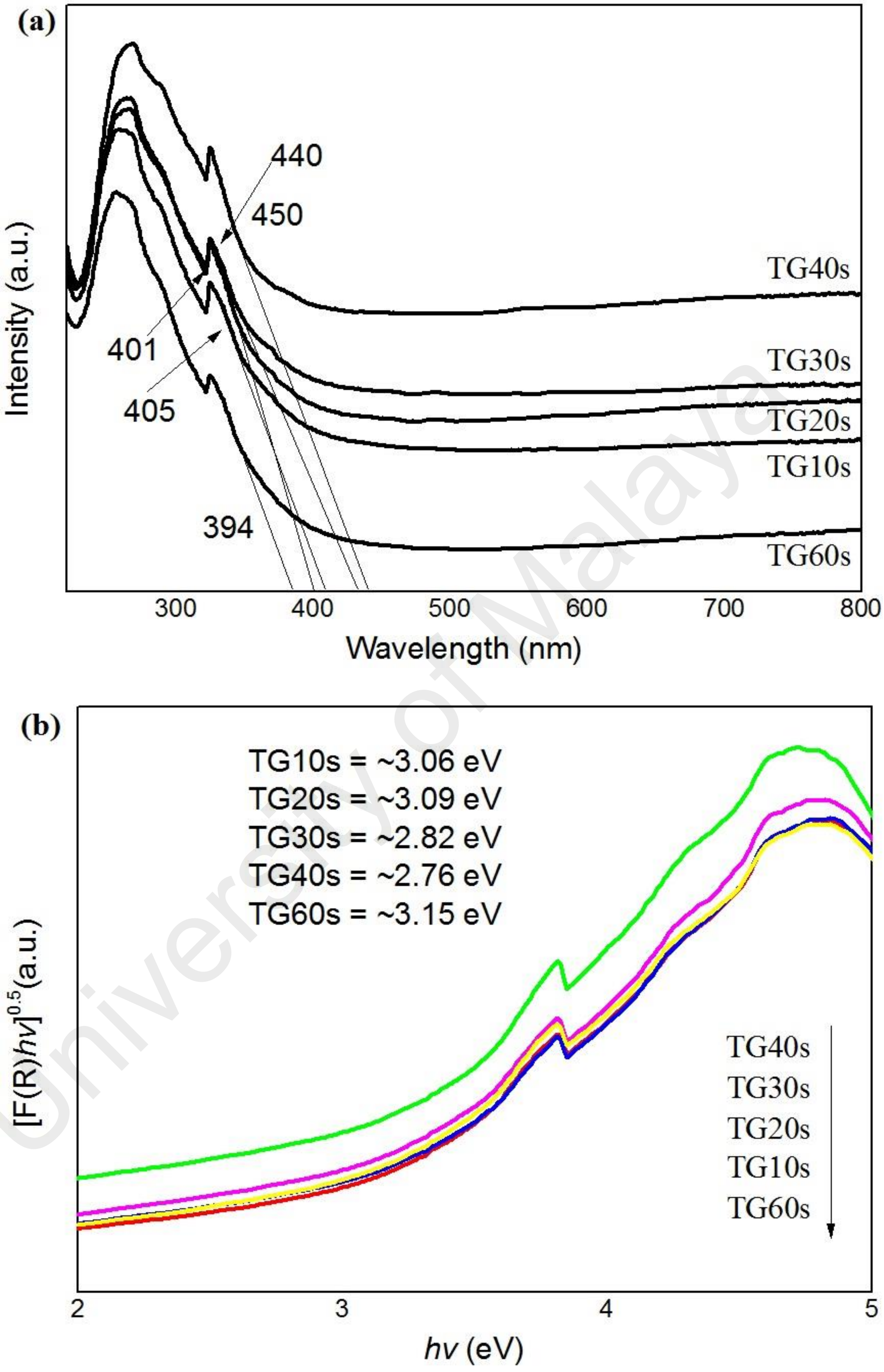

Figure 6.11: Variation of implantation time of UV-DRS (a) absorbance spectra and (b) Tauc plot

The structural characteristics and phase composition of rGO, anatase TiO_2, and rGO implanted by Ti ions based sputtering time were investigated by Raman spectroscopy. In Figure 6.12, 7 Raman spectras were shown regarding rGO, anatase TiO_2, and Ti ions implanted onto rGO NS via ion implantation technique with different sputtering times of 10s, 20s, 30, 40s, and 60s. The main characteristic peak of rGO appears at 1350.95 and 1604.96 cm^{-1} which attributed to the D and G vibration mode, respectively. The D vibration mode represented the defects, edges, and disordered carbon (A_{1g} symmetry) whereas G is first-order scattering of phonons by the sp^2-bonded carbon network (E_{2g} symmetry) (Thakur and Karak, 2012). Besides, the main broad peak of anatase TiO_2 at 126.26 cm^{-1} which is attributed to the main anatase vibration mode, $E_{g(1)}$. Moreover, the presence of crystalline TiO_2 is confirmed by the vibration peaks at 207.27 cm^{-1} for E_g, 372.27 cm^{-1} for $B_{1g(1)}$, 493.62 cm^{-1} for A_{1g}, and 611.65 cm^{-1} for $E_{g(2)}$ (Wang et al., 2015). The presence of vibration peaks of anatase TiO_2 in TiO_2 decorated rGO NS (126.26 cm^{-1}) is in agreement with the strong interaction between TiO_2 and rGO NS of TG10s – TG60s. In addition, the decreasing intensity at 126.26 cm^{-1} of TG60s as compared with TG40s indicated that excess Ti ions implanted onto rGO NS. The disappearance of D (1341.73 cm^{-1}) and G (1596.06 cm^{-1}) vibration peaks in TG10s – TG60s due to the huge intensity peaks of anatase TiO_2 (126.26 cm^{-1}). Among the sputtering time comparison, TG40 is the best sample due to the insignificant appearance of D and G vibration peaks although participated by the Ti ion implanted. In addition, I_D/I_G ratio of TG10s-TG60s were 0.65, 0.55, 0.34, 0.76, and 0.58, respectively. It is clearly shown that intensity ratio of I_D/I_G of TG40s is higher than 0.3 wt% TiO_2-rGO NC.

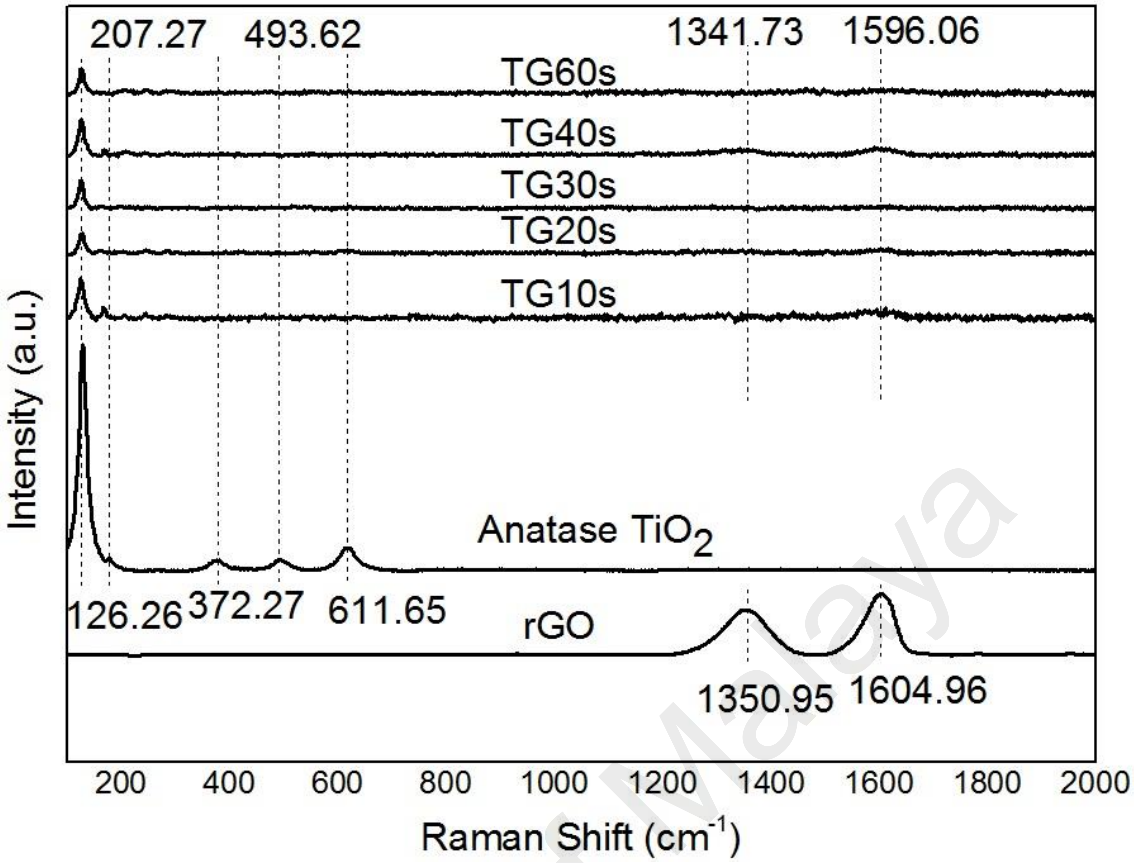

Figure 6.12: Raman Spectra of rGO, anatase TiO_2, and TiO_2-rGO NC based TG10s, TG20s, TG30s, TG40s, and TG60s

Photoluminescence spectroscopy (PL) was used to analyze the recombination of TiO_2-rGO NC within visible light region (400-700 cm^{-1}). In Figure 6.13, PL spectra of TiO_2-rGO NC were distributed into three main peaks located at 438, 471, and 494 nm, respectively. The part of regions were discussed at Figure 6.4. Interestingly, TG40s was established as lowest intensity PL peak under light irradiation and it is attributed to the enhancement of charge separation of electron-hole pairs. Since rGO is good conductor, it was assisted TiO_2 to overcome electron-holes pairs recombination and thus resulting a good photocatalytic activity as compared to other sputtering time. Besides, TG60s obtained highest intensity PL peak and assigned as high recombination rate of electron-hole pairs and slower the electrolyte redox reaction. The PL intensity decreases with increases of sputtering time (TG10s-TG30s) indicated that presence of Ti^{3+} ions to the rGO NS and consequently enhanced the photocatalytic of sample.

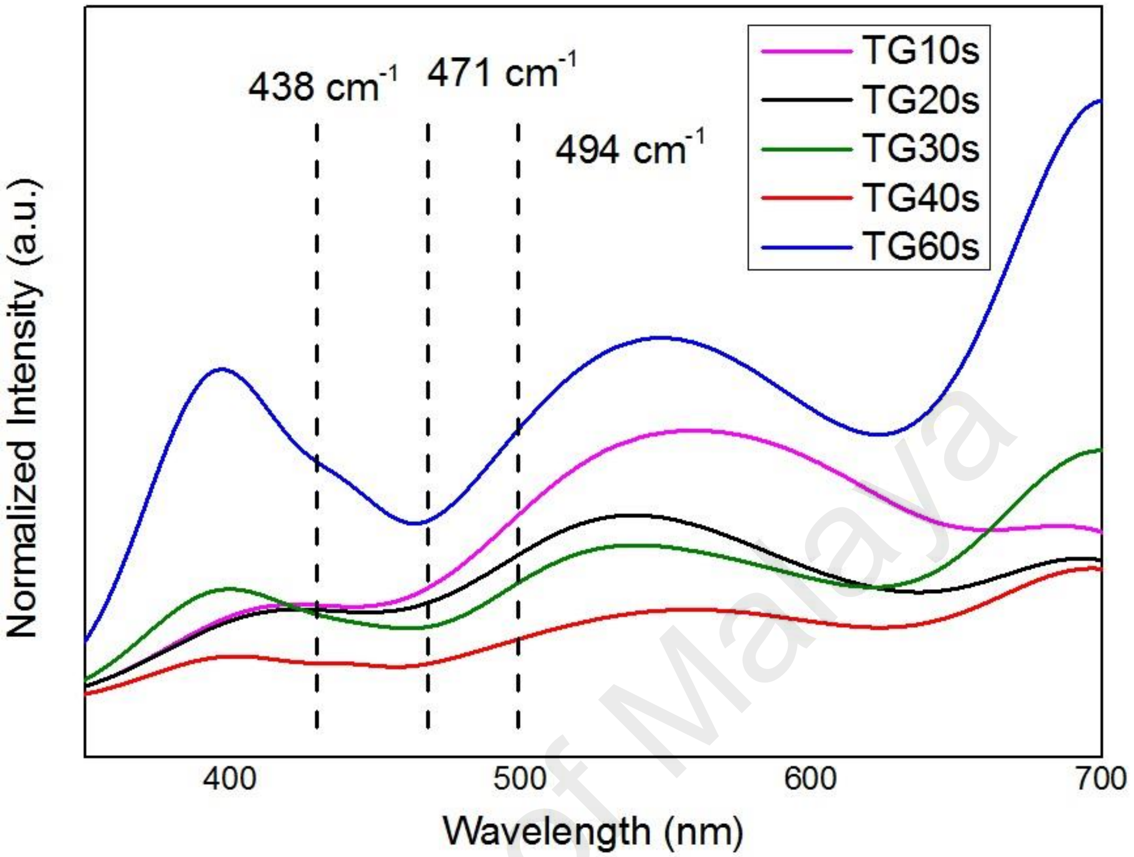

Figure 6.13: PL Spectra of Ti ion sputtering time onto rGO NS with 10s, 20s, 30s, 40s, 60s

The functional groups study were further analysed by using ATR-FTIR. Figure 6.14 shows the FTIR spectra of rGO and TiO_2-rGO NC based on sputtering time of 10s, 20s, 30s, 40s, and 60s. The TiO_2-rGO NC with variation of Ti ion implantation sputtering time implanting on rGO NS denoted as TG10s, TG20s, TG30s, TG40s, and TG60s. The FTIR spectra of rGO was obtained from the applied power study and briefly discussed in Figure 6.5. In the spectrum of rGO, the peaks at 3425 cm^{-1} and 1520 cm^{-1} are assigned to the stretching vibration of hydroxyl groups (-OH) and the skeletal vibration groups (C=C). The other peaks at 1720, 1400, 1220, and 1030 cm^{-1} are ascribed to the vibrations of oxygenated groups carboxyl C=O, carboxyl C-O, epoxide C-O-C or phenolic C-O-H, and alkoxy C-O, respectively. The FTIR spectrums shows that most of the oxygenated contained functional groups in TG10s – TG60s were eliminated but contributed to formed

Ti-O-C or Ti-O-Ti bonds absorption peak within 800 – 900 cm^{-1}. TG60s mostly will form Ti-O-Ti rather than Ti-O-C due to the excess of Ti ion implanted on the rGO NS. This phenomena attributed to the oxygen-containing at 1220 cm^{-1} and 3425 cm^{-1} decrease dramatically as Ti ion was implanted onto rGO NS from TG10s to TG60s samples. Among sputtering time of Ti ions, TG40s is the most significant in disappearance of oxygen-containing absorption peak (1030, 1220, 1400, 1720, and 3425 cm^{-1}) accredited that Ti ion with 40 s is a suitable coating duration for rGO NS.

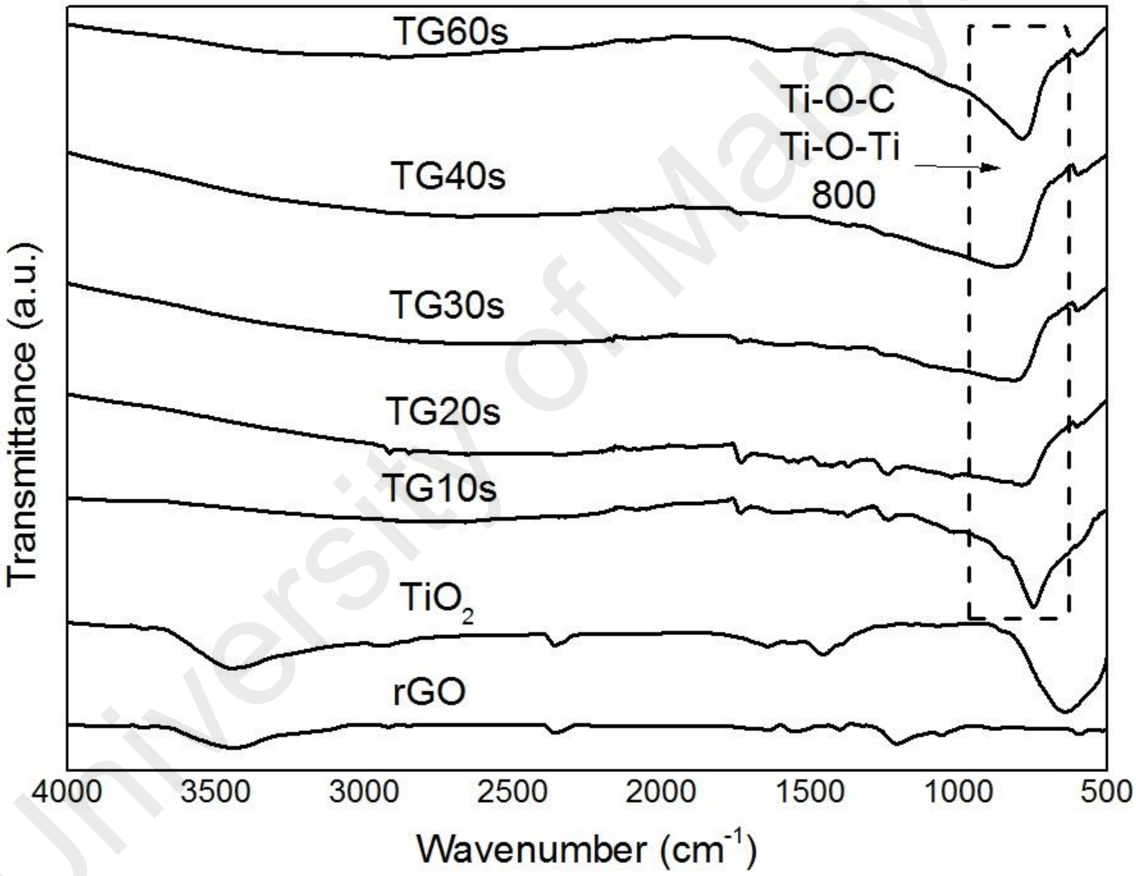

Figure 6.14: FTIR spectra of rGO NS and rGO NS incorporated with Ti ion implantation with variation of sputtering time

Structural morphology of the rGO and TiO_2-rGO NC photoanodes were observed using FESEM instrument as shown in Figure 6.15 (a) – (c). The Figure 6.15 (a) show the rGO exhibits in multilayers or binary layer system. After Ti ions implanted onto rGO NS, it was show in Figure 6.15 (b). The inset of EDX results in Figure 6.15 (b) shows amount of C, Ti, and O were recorded as 20.88 at%, 28.14 at%, and 46.24 at%, respectively.

Besides, the desertion compounds with 4.74 at% like F, Mg, and Si are insignificant in this correspond sample. In these irrelevant compound detected, F compound was obtained from the FTO glass, Mg compound are get from RF sputtering instrument, whereas Si compound was obtained from the conductive tape during observation process. Furthermore, the particle size of Ti ion is estimated ~61.6 nm as shown in Figure 6.15 (c). Next, the lattice of TiO_2-rGO NC of TG40s was captured using HRTEM instrument under 2 nm magnification in Figure 6.15 (d). The darker color (grey) represented anatase TiO_2 agreement with (101) orientation while lattice was measured ~0.35 nm corresponded with 10 lines whereas brighter color (white) ascribed to the ~0.34 nm/10 lines was assigned as graphitic sp^2 carbon network of rGO (Babu et al., 2015). Besides, the mixed color (white and grey) denoted as TiO_2-rGO where TiO_2 were incorporated with rGO and formed Ti-O-C bonding (Low et al., 2017b).

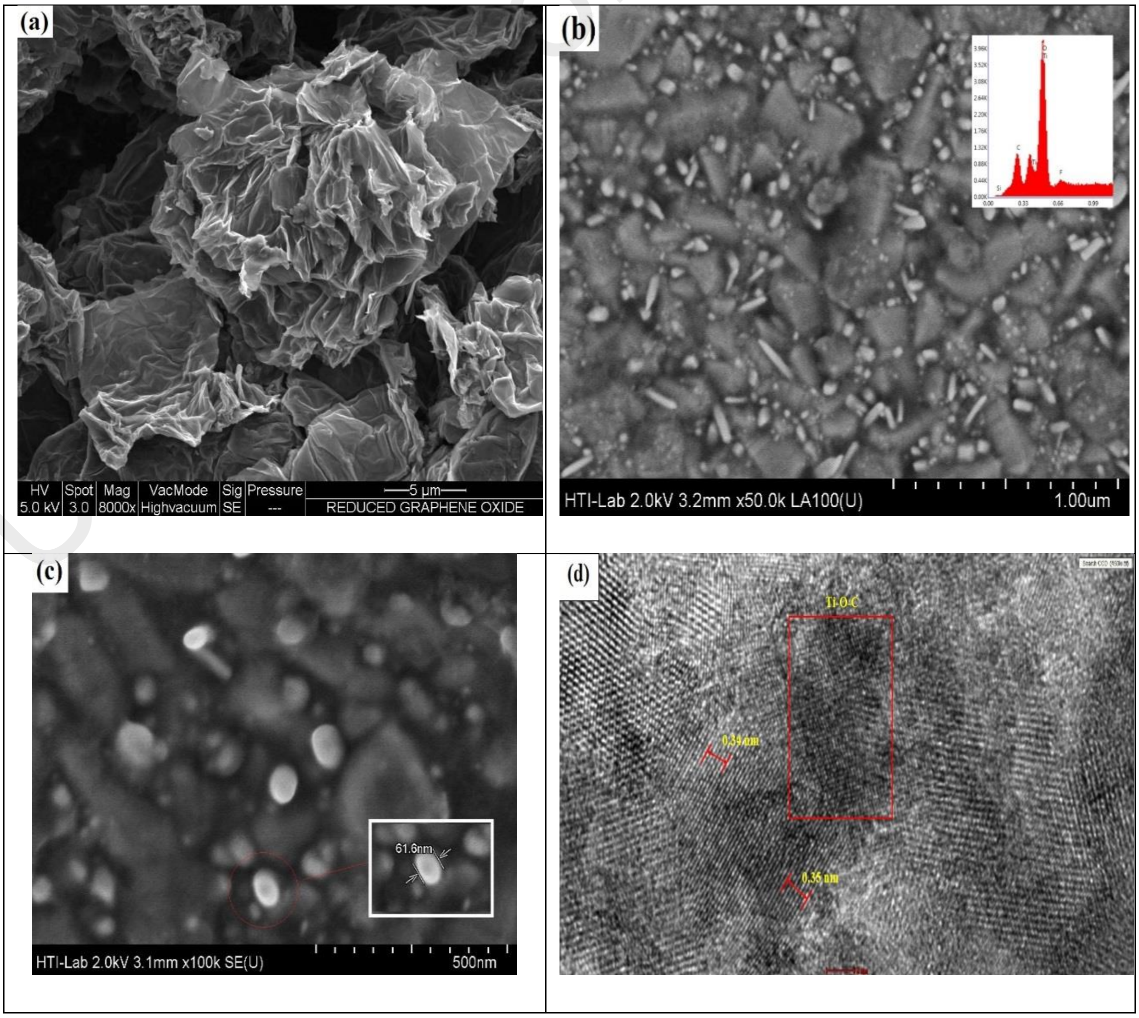

Figure 6.15: FESEM images of (a) rGO, TiO_2-rGO NC of (b) TG40s with inset EDX results, (c) measurement of Ti ion particle in TG40s, and (d) HRTEM images of TG40s

The XPS analysis was studied to investigate the chemical state C, Ti, O elements in rGO and modified rGO photoanodes (TG40s). Figure 6.16 (a) shows the survey speatras of rGO and Figure 6.16 (b) shows rGO incorporated with TiO_2 NC (TG40s). The rGO spectrum consists of C1s and O1s at 283 eV and 531 eV, respectively (Figure 6.16 (a)). Furthermore, TG40s shows of four main peaks which were C1s, Ti2p, O1s, and Ti2s located at 283, 458, 529, and 564 eV, respectively. The presence of Ti2p and Ti2s attributed to the TiO_2 was implanted onto rGO NS. Besides, the decreased of C1s intensity clearly proved that most of the carbon network of rGO structure were broke by Ti ions with high accelerated energy and successfully formed Ti-O-C bonding. In addition, the O1s intensity of TG40s was increased as compared with rGO due to the more oxygen contributed by the TiO_2 bonded with rGO. In this survey spectrum, TG40s considered better in structural form as compared with 150W applied power due to the less residual/noise obtained within 288 eV and 455 eV.

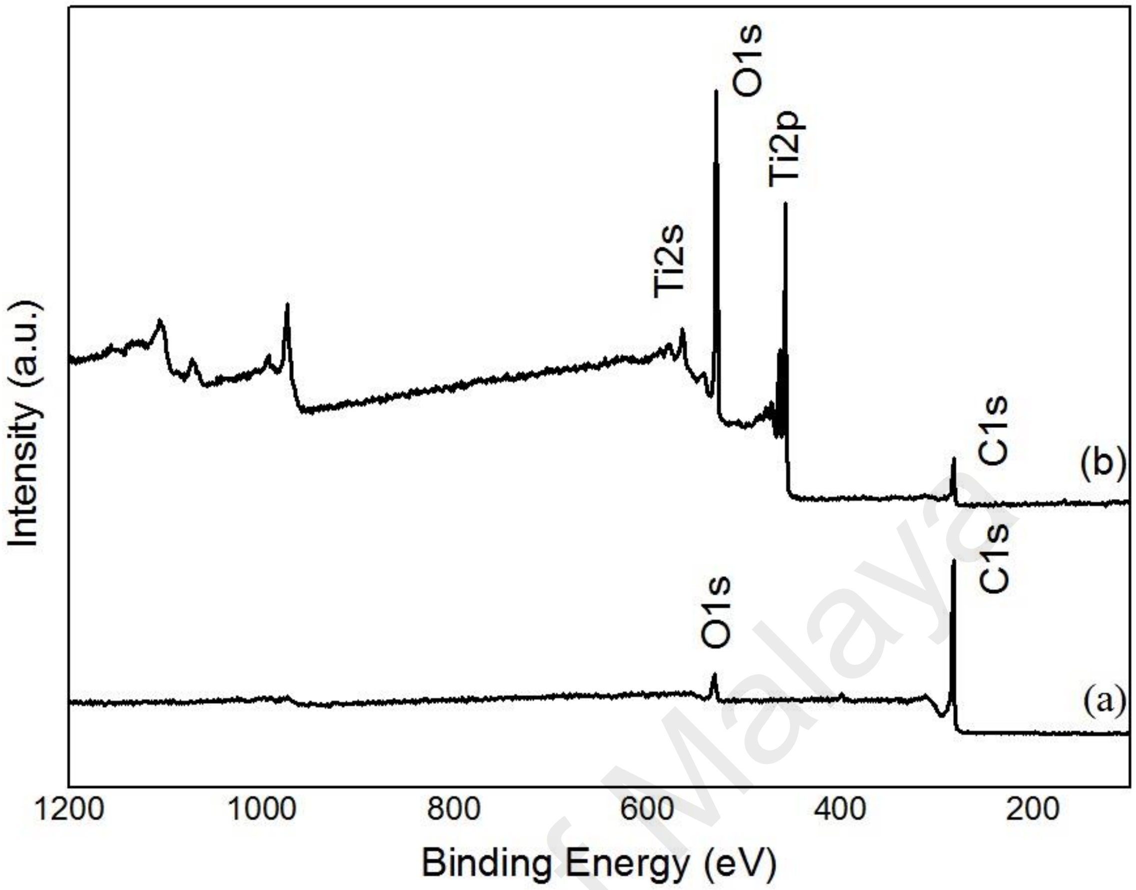

Figure 6.16: XPS wide scan spectra of (a) rGO and (b) TG40s

Figure 6.17 displays the C1s XPS spectras of rGO and modified rGO by Ti ions via ion implantation process with 40s. For rGO (Figure 6.17 (a)), one typical peak of C-C located at ~284.7 eV is attributed to the graphitic sp^2 carbon atoms and the other three peaks at ~285.9, ~287.2, and ~288.5 eV are assigned to the carbon atoms bonding with oxygenated functional groups such as C-O (epoxy and hydroxyl), C=O (carboxylate), and COOH, respectively (Xiang et al., 2011b). These oxygenated functional groups of rGO could act as active sites for directly bonding with Ti ions to form TiO_2-rGO NC (Cheng et al., 2013). The C1s XPS spectra of the TG40s shows binding energies at 284.5, 285.7, and 288.6 eV. The C1s broad peak located at ~284.5 eV is assigned to graphitic sp^2 carbon atoms peak whereas ~285.7 eV attributed to the defect-containing sp^2 hybridized carbons (Xiang et al., 2011a). Moreover, the weak peak located at ~288.6 eV is assigned to the carboxyl carbon functional group (O-C=O), which revealed that O=C-O-Ti bonds were formed. The –OH groups from the COOH were eliminated during Ti ion implantation process and formed Ti-O-C bonding (Xiang et al., 2011a). For the C1s of TG40s, the C-C and C-O were shifted to the lower binding energies at 284.5 eV and 285.7 eV as shown in Figure 6.17 (b). The negative shifts of C-C and C-O are associated weaken the carbon network bond (C-C) and consequently presence of TiO_2 species onto the rGO NS and replaced some of the carbon network with Ti-O-C bond (Haldorai et al., 2014). Additionally, the disappearance of C=O in TG40s attributed that the region were fully covered by O=C-O and formed O=C-O-Ti bonding.

Likewise, the O1s spectrum rGO and TG40s were shown in the Figure 6.17 (c) and (d), respectively. In the O1s of rGO, the peak at 531.6 eV assigned to the C=O bond whereas peak at 533.3 eV ascribed to the C-O bond. After Ti ion implantation process, the disappearance of C=O and C-O bond while presence of TiO_2, OH, and H_2O at 530.5, 531.1, and 532.4eV, respectively. This phenomena were attributed to the attendance of Ti-O-C bond in TG40s (Zeng et al., 2015). This results implemented that TiO_2 was fully implanted onto rGO NS and thus proved that the interaction between C, O, and Ti after ion implantation process.

For the Ti2p spectrum of TG40s, it can be divided into several contributions corresponding to the different oxidation states of Ti. In Figure 6.17 (e), the $Ti2p_{3/2}$ and $Ti2p_{1/2}$ peaks have binding energies of 458.3 and 464.1 eV, respectively. Moreover, the presence of Ti^{3+} peak at binding energy of 459.4 eV attributed to the recognition of Ti ions implanted was Ti^{3+} species. Besides, the chemical state shift of $Ti2p_{3/2}$ to $Ti2p_{1/2}$ peak was 5.8 eV. The position of Ti2p peak of TG40s attributed that no Ti-C bonding formed between rGO and TiO_2-rGO NC (Haldorai et al., 2014).

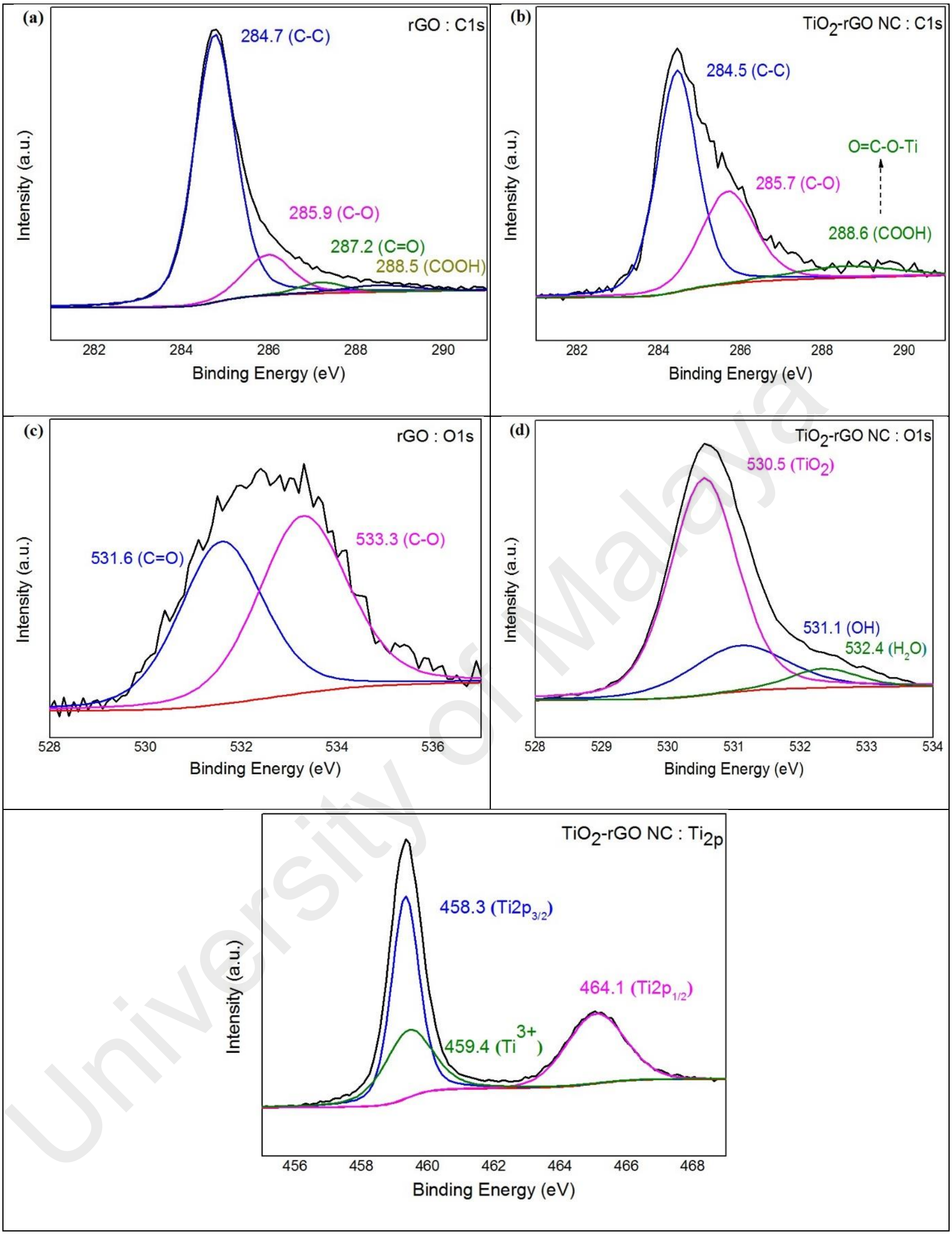

Figure 6.17: High resolution XPS spectra of C1s for (a) rGO and (b) TG40s; O1s for (c) rGO and (d) TG40s; and Ti2p for (e) TG40s

6.2.4 PCE of DSSCs Performance – Sputtering Time

A *J-V* characteristics of DSSCs based on rGO and rGO implanted by Ti ions with variation of sputtering time from 10s to 60s denoted as TG10s, TG20s, TG30s, TG40s, and TG60s whereas the summarized DSSCs performance is shown in Figure 6.18 and

Table 6.2, respectively. The calculated values were obtained from Equations (2.5) and (2.6) based on *J-V* characteristics graph.

As seen, the η values are increased from 6.05 % to 8.78 % with the increases of sputtering Ti ions duration. It is indicated that incorporated of Ti ions onto rGO NS can enhance the photocatalytic properties. However, the excess duration of Ti ions (TG60s) will affect the PCE decreases with 5.39 %. This is due to the over charge recombination generated by Ti ions on the rGO NS and resulting higher resistance at the photoanode component. At last but not least, the η values determined the working DSSCs performance. In other words, the η obtained by TG40s with 8.78 % was higher than 150 W with 8.51 %. This results implied that the effect of duration study is much more reliable and stable than the power applied study, as discussed above. Aforementioned, sputtering time could permit Ti ion implanted homogenously onto rGO NS than power applied study.

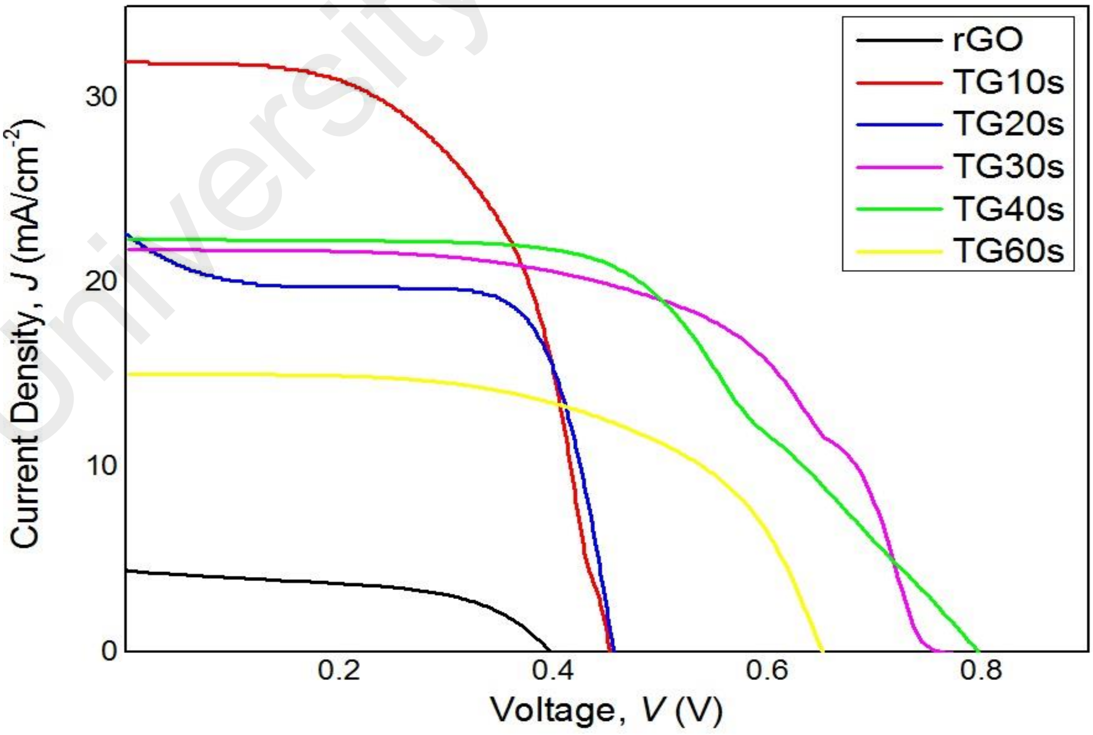

Figure 6.18: ***J-V*** **curve of DSSCs based rGO and rGO with implantation time from TG10s to TG60s**

Table 6.2: Typical photovoltaic performance of DSSCs with rGO and effect of Ti ion implantation duration

Sample	Short circuit current density, *Jsc* (mA/cm^2)	Open circuit voltage, *Voc* (V)	Maximum current density, *Jmp* (mA/cm^2)	Maximum voltage, *Vmp* (V)	Fill factor, *ff* (%)	Maximum power, *Pmax* (mW/cm^2)	PCE, η (%)
rGO	4.34	0.39	1.91	0.35	0.40	0.68	0.68
TG10s	32.00	0.45	0.40	15.20	0.42	6.05	6.05
TG20s	22.70	0.46	0.40	15.35	0.59	6.17	6.17
TG30s	21.81	0.76	0.40	20.62	0.50	8.29	8.29
TG40s	22.39	0.80	0.40	21.81	0.49	8.78	8.78
TG60s	15.08	0.65	0.40	13.48	0.55	5.39	5.39

6.3 Discussion

Figure 6.19 (a) illustrated the lattice arrangement of rGO. The prepared rGO NS was then modified by the Ti ion implantation technique with two different parameters which were applied powers (50, 100, 150, 200 and 250 W) and sputtering duration (10, 20, 30, 40, and 60 s). The duration of implantation was fixed at 40 s for applied power study samples whereas applied power was fixed at 150 W for sputtering time study samples to ensure that the Ti ions maximized and efficiently implanted onto rGO NS (Figure 6.19 (b). It is noteworthy to mention that the fabrication of TiO_2-rGO NC as the photoanodes using this ion implantation technique could deal with a higher PCE in DSSCs as compared to others deposition/incorporation technique (Yen et al., 2011). Furthermore, the Ti ions could accelerated with high energy (1 MeV) and implanted onto the rGO NS in a short time while some of the Ti ions could penetrated into the lattice of rGO to form

TiO_2-rGO NC (Figure 6.19 (c)). In addition, the 1 Mev energy was set to minimize the interfacial defects of rGO NS with small collusion process.

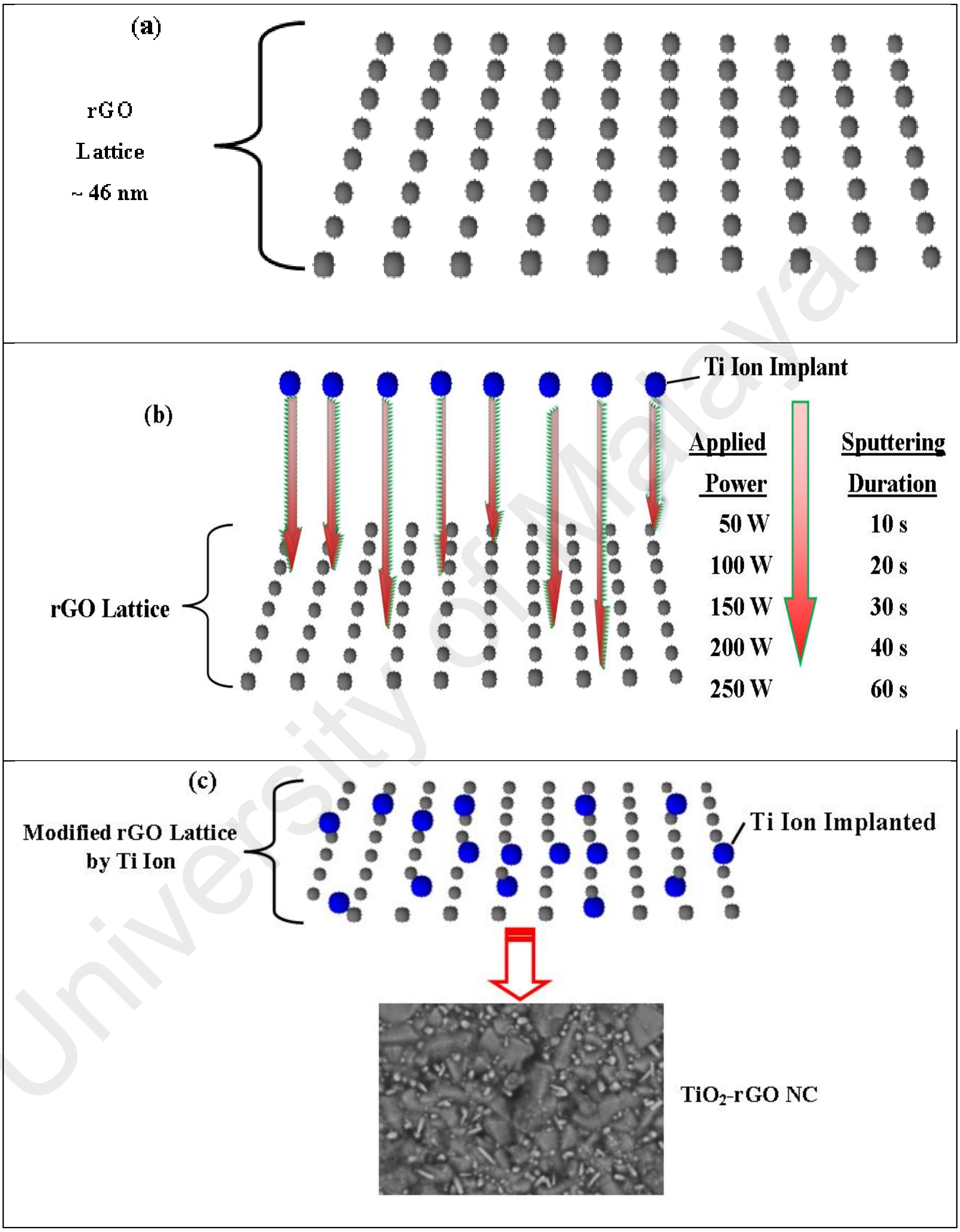

Figure 6.19: Surface Modification of rGO by Ti Ion Implantation Technique

6.4 Conclusion

In this chapter, the use of Ti ion implantation method to modify the rGO NS followed by preparing the TiO_2-rGO NC as the photoanodes in DSSCs. The effect of various applied powers and sputtering duration to implant the Ti ion onto rGO NS with high energy within a short time and hence the PCE of DSSCs were investigated. The thickness of rGO was found to be ~46 nm, while the size of Ti ion implanted was detected to be ~70-80 nm. Under UV-Vis results, the estimated bandgap of the 150 W TiO_2-rGO NC was found with 2.89 eV whereas TG40 s denoted the lowest estimated bandgap with 2.76 eV. It was indicated the formation of stronger Ti-O-C bonds associated to the closer conduction band between rGO with FTO glass. Moreover, FTIR and XPS spectra confirmed the presence of elements such as Ti, O and C and the formation of Ti-O-C bonds in TiO_2-rGO NC. The desired power applied to implant the Ti ion onto rGO NS was found to be 150 W and 40 s in order to give 8.78 % PCE. The highest PCE attained as a result of the efficient separation coupled with prolonged recombination charge carrier probability, the higher photogenerated electron-hole pairs and the reduced band gap.

CHAPTER 7: CONCLUSION

7.1 Preamble

In this research project, comprehensive research works were conducted in aspect of literature study, methodology, and data collection for TiO_2-rGO NC and PCE performance of DSSCs findings. In summary, the preparations of TiO_2-rGO NC as photoanode via one-step hydrothermal and ion implantation technique for comparison technique purpose in order to obtain desired PCE. The objectives are required to accomplish as following:

1. To study the integral properties (e.g., functional groups, aspect ratio, crystal structure, optical properties, and morphology) of pure rGO NS based electrical characteristic.
2. To study the formation of TiO_2-rGO NC using one-step hydrothermal technique and ion implantation technique.
3. To study the DSSCs photovoltaic characteristics (e.g., photocurrent density, fill factor, PCE, and EIS) of TiO_2-rGO NC based photoanode in DSSCs application.

Objectives 1: To study the integral properties (e.g., functional groups, aspect ratio, crystal structure, optical properties, and morphology) of pure rGO NS based electrical characteristic.

- Improved Hummer's method and chemically reduction process was chosen for GO and rGO synthesis due to high purity, ultrathin layer could be obtained.
- The synthesized GO under 72 h at high stirring speed is the optimized results due to the comparison of oxygenated group and it was observed that 72 h of GO has the broad peak of hydroxyl group at 3400 cm^{-1}. However, less than 72 h stirring will resulted in shorter intensity.

- The presence of D and G bands in rGO was higher than GO attributed to the increased of sp^2-hybridized carbon and removed of oxygenated moieties, respectively.
- 72 h of rGO was obtained highest current performance as compared with 72 h of GO and graphite. This phenomena proved that rGO NS has highest charge carriers transport as compared to the GO and rGO.

Objective 2: To study the formation of TiO_2-rGO NC using one-step hydrothermal technique and ion implantation technique.

- Two effective route of rGO NS incorporated with TiO_2 as photoanode were successfully conducted via one-step hydrothermal and Ti ion implantation techniques in order to simplify the process and attempted to bombard Ti^{3+} ions into rGO NS. The purpose of conduct these two approaches are study the bonding composition and comparison the DSSCs performance based on TiO_2-rGO NC photoanode samples.
- In one-step hydrothermal process, 0.3 wt% of TiO_2-rGO NC achieved a maximum conductivity of 29.1 µS/cm with electron mobility of 1.0 µmcm/Vs. Electron mobility of rGO incorporated with TiO_2 was approximately 30% higher than rGO NS whereas obtained a 50% increments as compared with anatase TiO_2. The presence of 0.3 wt% of TiO_2 in rGO NS resulting the increase of photo-induced electrons transportation rate and minimize the recombination losses within the TiO_2 lattice in this binary hybrid photoelectrode.
- For the Ti ion implantation technique, FTIR spectra coupled with the elemental/chemical states in XPS analysis revealed the presence of Ti-O-C functional groups. The formation of Ti-O-C bonding from TiO_2-rGO NC could

fasten electron charge mobility transfer from the CB to VB with minimize the electron-holes pairs recombination. Moreover, the average size of Ti ion was found to be 70-80 nm as incorporated with rGO NS whereas the spacing of anatase TiO_2 onto rGO NS were formed ~0.34 nm under HRTEM analysis.

- In Ti ion implantation technique, bandgap energy of optimized sample via Ti ions sputtering duration (TG40s) obtained lower value with ~2.60 eV than optimized sample of 150W applied power with ~2.89 eV, it is indicated that efficient Ti^{3+} species formed with rGO and hence improved the photocatalytic activity.

Objective 3: To study the DSSCs photovoltaic characteristics (e.g., photocurrent density, fill factor, PCE, and EIS) of TiO_2-rGO NC based photoanode in DSSCs application.

- In one-step hydrothermal process, 0.3 wt% of TiO_2 incorporated with rGO NS showed η of 7.20 %. An improvement of the η in Ti ions implantation technique with 8.51 % and 8.78% on applied power parameter (150 W) and sputtering duration parameter (TG40s), which acted as efficient of electron transport at the photoanode to the outer circuit of DSSCs. However, excessive Ti^{3+} species that incorporated with rGO reached a saturation condition and started accumulate on the rGO surface (>0.4 wt%, >150 W, and >40 s of Ti). This phenomena resulting recombination of electron-hole pairs increased and increased the interior resistance of electron flow during light illumination process and eventually reduced the DSSCs performance.
- rGO-TiO_2 NC prepared as photoanode using Ti ion implantation technique demonstrated better PCE performance than one-step hydrothermal. The results manifested that effective incorporation of Ti^{3+} species onto rGO lattice which

could be achieved by lattice substitutional via high kinetic energy process during implantation process.

As an overall remarks of this research work, it is concluded that the amount of Ti^{3+} species loaded onto rGO nanosheets play an important role in developing an efficient photoelectrode in order to further improve the photogenerated electrons charge carrier mobility and photocatalytic activity of DSSCs.

7.2 Limitations of the Study

The preparation technique was not able to demonstrate conclusively that TiO_2-rGO NC as efficient photoelectrode in DSSCs: A well-prepared of TiO_2-rGO NC via ion implantation technique was conducted and shown better PCE performance. This technique could be more consistent as compared with one-step hydrothermal technique in term of PCE performance for DSSCs application. However, Ti ions were not fully penetrate into rGO NS but majority retained on the rGO surface. Apart from a rationale preparation technique, the assembled TiO_2-rGO NC as photoanode also facing difficulty in receiving maximize the solar irradiation of 100W, and minimize the risk of electron losses. Besides, the maximum dye loading (reduction of charge recombination) with large internal surface area of TiO_2-rGO NC remains to be further explored. As addition, the effectively controllable of well-formation of Ti-O-C bonding by either one-step hydrothermal or ion implantation technique is a difficult task in this study.

Simple DSSCs device assembly and harvested under normal solar simulator light source. Firstly, the DSSCs were assembled by sandwiched configuration by normal paper clips without sealed process and protection foil within the active area. This simple DSSCs application might affected the overall PCE performance where the device was not probably constructed and thus increased charge carrier motion resistance within devices.

Secondly, the only utilized of solar simulator under conventional AM 1.5 condition without source tuning into bigger input power might restrict the performance of DSSCs.

7.3 Recommendations for Further Research

DSSCs is a key target for the development of alternative, sustainable, renewable, and clean resources for future energy system. In this work, the use of TiO_2-rGO NC as efficient photoanode was found to achieve 8.78 % of PCE. This value is still far from the initial starting point for practical application of about 7.20 %. Hence, the development of rGO with TiO_2 materials is still a challenge. Several suggestions and recommendations should be noteworthy for further developments were proposed as follows:

- Enhancing the photocurrent density by highly conductive rGO material with controllable nanostructures
- Fabrication of an ideal graphene-based catalysts of photoanode and avoid stacking of graphene sheets.
- Development of novel photocatalysts materials incorporation with rGO
- Modification of TiO_2-rGO nanostructures by adding potential conductor support to increase the dye loading and photocatalytic activity
- Precise approaches of composite catalysts with uniform morphologies and controllable nanoparticle

For the highly conductive rGO synthesis, it should produce via chemical vapor deposition (CVD) method to obtain large-scale of monolayer graphene sheets with high quality which is close to pristine graphene. Since graphene have several unique properties, graphene should attempt to incorporate with metal-free catalysts such as active sites in order to functionalize graphene structure and minimize some defects. Furthermore, metal/metal oxide nanohybrids like Pd, Au, Ru,CoO_x, Au-Pd, and MnCoO should be introduce to the TiO_2-rGO to perform better PCE performance. Lastly, graphene could be form a ternary composite particle (raspberry-like composite particles) like polystyrene/rGO/Au nanoparticles; which is not only obtain high catalytic activity but also able to produce uniform size and controllable surface morphology.

REFERENCES

Adán-Más, A., and Wei, D. (2013). Photoelectrochemical properties of graphene and its derivatives. *Nanomaterials, 3*(3): 325-356.

Agarwal, R., Sahoo, S., Resto, O., and Katiyar, R. S. (2015). Plasmon Enhanced Photovoltaic Performance in TiO$_2$-Graphene Oxide Composite Based Dye-Sensitized Solar Cells. *ECS Journal of Solid State Science and Technology, 4*(9): M64-M68.

Aghigh, A., Alizadeh, V., Wong, H., Islam, M. S., Amin, N., and Zaman, M. (2015). Recent advances in utilization of graphene for filtration and desalination of water: A review. *Desalination, 365*: 389-397.

Ahmed, M. I., Hussain, Z., Mujahid, M., Khan, A. N., Javaid, S. S., and Habib, A. (2016). Low resistivity ZnO-GO electron transport layer based CH3NH3PbI3 solar cells. *AIP Advances, 6*(6): 065303.

Akhavan, O., and Ghaderi, E. (2010). Toxicity of graphene and graphene oxide nanowalls against bacteria. *ACS nano, 4*(10): 5731-5736.

Ako, R. T., Ekanayake, P., Tan, A. L., and Young, D. J. (2016). La modified TiO$_2$ photoanode and its effect on DSSC performance: A comparative study of doping and surface treatment on deep and surface charge trapping. *Materials Chemistry and Physics, 172*: 105-112.

Alam, S. N., Sharma, N., and Kumar, L. (2017). Synthesis of Graphene Oxide (GO) by Modified Hummers Method and Its Thermal Reduction to Obtain Reduced Graphene Oxide (rGO). *Graphene, 6*(01): 1.

Anandan, S. (2007). Recent improvements and arising challenges in dye-sensitized solar cells. *Solar energy materials and solar cells, 91*(9): 843-846.

Araújo, G. L., and Martí, A. (1994). Absolute limiting efficiencies for photovoltaic energy conversion. *Solar Energy Materials and Solar Cells, 33*(2): 213-240.

Araujo, P. T., Terrones, M., and Dresselhaus, M. S. (2012). Defects and impurities in graphene-like materials. *Materials Today, 15*(3): 98-109.

Armaroli, N., and Balzani, V. (2007). The future of energy supply: challenges and opportunities. *Angewandte Chemie International Edition, 46*(1‐2): 52-66.

Asif, M., and Muneer, T. (2007). Energy supply, its demand and security issues for developed and emerging economies. *Renewable and Sustainable Energy Reviews, 11*(7): 1388-1413.

Aunkor, M., Mahbubul, I., Saidur, R., and Metselaar, H. (2016). The green reduction of graphene oxide. *Rsc Advances, 6*(33): 27807-27828.

Babu, S. G., Vinoth, R., Kumar, D. P., Shankar, M. V., Chou, H.-L., Vinodgopal, K., and Neppolian, B. (2015). Influence of electron storing, transferring and shuttling assets of reduced graphene oxide at the interfacial copper doped TiO$_2$ p–n heterojunction for increased hydrogen production. *Nanoscale, 7*(17): 7849-7857.

Balachandran, U., and Eror, N. (1982). Raman spectra of titanium dioxide. *J. Solid State Chem., 42*(3): 276-282.

Ban, F. Y., Majid, S. R., Huang, N. M., and Lim, H. N. (2012). Graphene oxide and its electrochemical performance. *International Journal of Electrochemical Science, 7*(5): 4345-4351.

Bauer, C., Boschloo, G., Mukhtar, E., and Hagfeldt, A. (2002). Ultrafast studies of electron injection in Ru dye sensitized SnO 2 nanocrystalline thin film. *International Journal of Photoenergy, 4*(1): 17-20.

Bell, N. J., Ng, Y. H., Du, A., Coster, H., Smith, S. C., and Amal, R. (2011). Understanding the enhancement in photoelectrochemical properties of photocatalytically prepared TiO_2-reduced graphene oxide composite. *The Journal of Physical Chemistry C, 115*(13): 6004-6009.

Bella, F., Griffini, G., Gerosa, M., Turri, S., and Bongiovanni, R. (2015). Performance and stability improvements for dye-sensitized solar cells in the presence of luminescent coatings. *Journal of Power Sources, 283*: 195-203.

Benson, J., Xu, Q., Wang, P., Shen, Y., Sun, L., Wang, T., Li, M., and Papakonstantinou, P. (2014). Tuning the catalytic activity of graphene nanosheets for oxygen reduction reaction via size and thickness reduction. *arXiv preprint arXiv:1411.4056*.

Bernacka-Wojcik, I., Wojcik, P., Aguas, H., Fortunato, E., and Martins, R. (2016). Inkjet printed highly porous TiO_2 films for improved electrical properties of photoanode. *Journal of colloid and interface science, 465*: 208-214.

Bethune, D., Klang, C., De Vries, M., Gorman, G., Savoy, R., Vazquez, J., and Beyers, R. (1993). Cobalt-catalysed growth of carbon nanotubes with single-atomic-layer walls. *Nature, 363*(6430): 605-607.

Bhanvase, B., Shende, T., and Sonawane, S. (2017). A review on graphene–TiO_2 and doped graphene–TiO_2 nanocomposite photocatalyst for water and wastewater treatment. *Environmental Technology Reviews, 6*(1): 1-14.

Bhattacharjee, R., and Hung, I.-M. (2013). A SnO2 and ZnO Nanocomposite Photoanodes in Dye-Sensitized Solar Cells. *ECS Solid State Letters, 2*(11): Q101-Q104.

Blanita, G., and Lazar, M. D. (2013). Review of graphene-supported metal nanoparticles as new and efficient heterogeneous catalysts. *Micro and Nanosystems, 5*(2): 138-146.

Bo, Z., Shuai, X., Mao, S., Yang, H., Qian, J., Chen, J., Yan, J., and Cen, K. (2014). Green preparation of reduced graphene oxide for sensing and energy storage applications. *Scientific reports, 4*: 4684.

Bo, Z., Wen, Z., Kim, H., Lu, G., Yu, K., and Chen, J. (2012). One-step fabrication and capacitive behavior of electrochemical double layer capacitor electrodes using vertically-oriented graphene directly grown on metal. *Carbon, 50*(12): 4379-4387.

Boehm, H. P., Setton, R., and Stumpp, E. (1994). Nomenclature and terminology of graphite intercalation compounds (IUPAC Recommendations 1994). *Pure and Applied Chemistry, 66*(9): 1893-1901.

Bonaccorso, F., Sun, Z., Hasan, T., and Ferrari, A. (2010). Graphene photonics and optoelectronics. *Nature photonics, 4*(9): 611-622.

Bridge, G., Bouzarovski, S., Bradshaw, M., and Eyre, N. (2013). Geographies of energy transition: Space, place and the low-carbon economy. *Energy Policy, 53*: 331-340.

Cai, C., Sang, N., Shen, Z., and Zhao, X. (2017). Facile and size-controllable preparation of graphene oxide nanosheets using high shear method and ultrasonic method. *Journal of Experimental Nanoscience*: 1-16.

Cai, W., Borlace, S., Lengaigne, M., Van Rensch, P., Collins, M., Vecchi, G., Timmermann, A., Santoso, A., McPhaden, M. J., and Wu, L. (2014). Increasing frequency of extreme El Niño events due to greenhouse warming. *Nature climate change, 4*(2): 111-116.

Cambaz, Z. G., Yushin, G., Osswald, S., Mochalin, V., and Gogotsi, Y. (2008). Noncatalytic synthesis of carbon nanotubes, graphene and graphite on SiC. *Carbon, 46*(6): 841-849.

Cancado, L., Pimenta, M., Neves, B., Dantas, M., and Jorio, A. (2004). Influence of the atomic structure on the Raman spectra of graphite edges. *Physical review letters, 93*(24): 247401.

Cançado, L. G., da Silva, M. G., Ferreira, E. H. M., Hof, F., Kampioti, K., Huang, K., Pénicaud, A., Achete, C. A., Capaz, R. B., and Jorio, A. (2017). Disentangling contributions of point and line defects in the Raman spectra of graphene-related materials. *2D Materials, 4*(2): 025039.

Cao, N., and Zhang, Y. (2015). Study of reduced graphene oxide preparation by Hummers' method and related characterization. *Journal of Nanomaterials, 2015*: 2.

Cao, X., Tian, G., Chen, Y., Zhou, J., Zhou, W., Tian, C., and Fu, H. (2014). Hierarchical composites of TiO_2 nanowire arrays on reduced graphene oxide nanosheets with enhanced photocatalytic hydrogen evolution performance. *J. Mater. Chem. A, 2*(12): 4366-4374.

Carp, O., Huisman, C. L., and Reller, A. (2004). Photoinduced reactivity of titanium dioxide. *Progress in solid state chemistry, 32*(1): 33-177.

Carr, K. (1970). Intercalation and oxidation effects on graphite of a mixture of sulphuric and nitric acids. *Carbon, 8*(2): 155IN11159-11158IN16166.

Chang, B., Huang, N. M., An'amt, M. N., Marlinda, A. R., Norazriena, Y., Muhamad, M. R., Harrison, I., Lim, H. N., and Chia, C. H. (2012a). Facile hydrothermal preparation of titanium dioxide decorated reduced graphene oxide nanocomposite. *International journal of nanomedicine*.

Chang, B. Y. S., Huang, N. M., An'amt, M. N., Marlinda, A. R., Norazriena, Y., Muhamad, M. R., Harrison, I., Lim, H. N., and Chia, C. H. (2012b). Facile hydrothermal preparation of titanium dioxide decorated reduced graphene oxide nanocomposite. *International journal of nanomedicine, 7*: 3379.

Chang, B. Y. S., Huang, N. M., An'amt, M. N., Marlinda, A. R., Norazriena, Y., Muhamad, M. R., Harrison, I., Lim, H. N., and Chia, C. H. (2012c). Facile hydrothermal preparation of titanium dioxide decorated reduced graphene oxide nanocomposite. *International journal of nanomedicine, 7*(1): 3379-3387.

Chang, C. H., Lin, H. H., Chen, C. C., and Hong, F. C. N. (2016). Fabrication of High‐Efficiency (11%) Dye‐Sensitized Solar Cells in Backside Illumination Mode with Microstructures. *Advanced Materials Interfaces, 3*(14).

Chang, D. W., Choi, H.-J., Filer, A., and Baek, J.-B. (2014). Graphene in photovoltaic applications: organic photovoltaic cells (OPVs) and dye-sensitized solar cells (DSSCs). *J. Mater. Chem. A, 2*(31): 12136-12149.

Charbonneau, C., Lee, K., Shan, G., Gomez, M., Gauvin, R., and Demopoulos, G. (2010). Preparation and DSSC performance of mesoporous film photoanodes based on aqueous-synthesized anatase nanocrystallites. *Electrochem. Solid St. Lett., 13*(8): H257-H260.

Chen, B., Sha, J., Li, W., He, F., Liu, E., Shi, C., He, C., Li, J., and Zhao, N. (2016a). Graphene oxide-assisted synthesis of micro-sized ultrathin single-crystalline anatase TiO_2 nanosheets and their application in dye-sensitized solar cells. *ACS applied materials & interfaces*.

Chen, B., Sha, J., Li, W., He, F., Liu, E., Shi, C., He, C., Li, J., and Zhao, N. (2016b). Graphene oxide-assisted synthesis of microsized ultrathin single-crystalline anatase TiO_2 nanosheets and their application in dye-sensitized solar cells. *ACS applied materials & interfaces, 8*(4): 2495-2504.

Chen, D., Zou, L., Li, S., and Zheng, F. (2016c). Nanospherical like reduced graphene oxide decorated TiO_2 nanoparticles: an advanced catalyst for the hydrogen evolution reaction. *Scientific reports, 6*.

Chen, J., Yao, B., Li, C., and Shi, G. (2013a). An improved Hummers method for eco-friendly synthesis of graphene oxide. *Carbon, 64*: 225-229.

Chen, J., Zhang, G., Luo, B., Sun, D., Yan, X., and Xue, Q. (2011). Surface amorphization and deoxygenation of graphene oxide paper by Ti ion implantation. *Carbon, 49*(9): 3141-3147.

Chen, L.-C., Hsu, C.-H., Chan, P.-S., Zhang, X., and Huang, C.-J. (2014a). Improving the performance of dye-sensitized solar cells with TiO_2/graphene/TiO_2 sandwich structure. *Nanoscale research letters, 9*(1): 1-7.

Chen, L., Zhou, Y., Tu, W., Li, Z., Bao, C., Dai, H., Yu, T., Liu, J., and Zou, Z. (2013b). Enhanced photovoltaic performance of a dye-sensitized solar cell using graphene–TiO_2 photoanode prepared by a novel in situ simultaneous reduction-hydrolysis technique. *Nanoscale, 5*(8): 3481-3485.

Chen, T., Hu, W., Song, J., Guai, G. H., and Li, C. M. (2012). Interface functionalization of photoelectrodes with graphene for high performance dye‐sensitized solar cells. *Advanced Functional Materials, 22*(24): 5245-5250.

Chen, X., and Mao, S. S. (2007). Titanium dioxide nanomaterials: synthesis, properties, modifications, and applications. *Chemical reviews, 107*(7): 2891-2959.

Chen, Y., Song, B., Chen, R. M., Lu, L., and Xue, J. (2014b). A study of the superior electrochemical performance of 3 nm SnO 2 nanoparticles supported by graphene. *Journal of Materials Chemistry A, 2*(16): 5688-5695.

Cheng, G., Akhtar, M. S., Yang, O.-B., and Stadler, F. J. (2013). Novel preparation of anatase TiO_2@ reduced graphene oxide hybrids for high-performance dye-sensitized solar cells. *ACS applied materials & interfaces, 5*(14): 6635-6642.

Cheng, G., Shaheer Akhtar, M., Yang, O., and Stadler, F. J. (2016). Nanoprecursor-Mediated Synthesis of Mg2+-Doped TiO_2 Nanoparticles and Their Application for Dye-Sensitized Solar Cells. *Journal of Nanoscience and Nanotechnology, 16*(1): 744-752.

Chong, S. W., Lai, C. W., and Abd Hamid, S. B. (2016). Controllable electrochemical synthesis of reduced graphene oxide thin-film constructed as efficient photoanode in dye-sensitized solar cells. *Materials, 9*(2): 69.

Chong, S. W., Lai, C. W., and Hamid, S. B. A. (2015). Green preparation of reduced graphene oxide using a natural reducing agent. *Ceramics International, 41*(8): 9505-9513.

Chou, J.-C., Huang, C.-H., Lin, Y.-J., Chu, C.-M., Liao, Y.-H., Tai, L.-H., and Nien, Y.-H. (2016). The Influence of Different Annealing Temperatures on Graphene-Modified TiO_2 for Dye-Sensitized Solar Cell. *IEEE Transactions on Nanotechnology, 15*(2): 164-170.

Chung, D. D. (2002). Review graphite. *Journal of materials science, 37*(8): 1475-1489.

Corporation, K. (2016, 25 October 2016). World's Highest Conversion Efficiency of 26.33% Achieved in a Crystalline Silicon Solar Cell - A World First in a Practical Cell Size -. Retrieved from http://www.kaneka.co.jp/kaneka-e/images/topics/1473811995/1473811995_101.pdf

Coumou, D., and Rahmstorf, S. (2012). A decade of weather extremes. *Nature climate change, 2*(7): 491-496.

Cui, P., Lee, J., Hwang, E., and Lee, H. (2011). One-pot reduction of graphene oxide at subzero temperatures. *Chemical Communications, 47*(45): 12370-12372.

Dai, S., Wu, Y., Sakai, T., Du, Z., Sakai, H., and Abe, M. (2010). Preparation of highly crystalline TiO_2 nanostructures by acid-assisted hydrothermal treatment of hexagonal-structured nanocrystalline titania/cetyltrimethyammonium bromide nanoskeleton. *Nanoscale Res. Lett., 5*(11): 1829-1835.

De Angelis, F., Fantacci, S., Selloni, A., Grätzel, M., and Nazeeruddin, M. K. (2007). Influence of the sensitizer adsorption mode on the open-circuit potential of dye-sensitized solar cells. *Nano letters, 7*(10): 3189-3195.

Dette, C., Perez-Osorio, M. A., Kley, C. S., Punke, P., Patrick, C. E., Jacobson, P., Giustino, F., Jung, S. J., and Kern, K. (2014). TiO_2 Anatase with a Bandgap in the Visible Region. *Nano letters, 14*(11): 6533-6538.

Ding, H., Zhang, S., Chen, J.-T., Hu, X.-P., Du, Z.-F., Qiu, Y.-X., and Zhao, D.-L. (2015). Reduction of graphene oxide at room temperature with vitamin C for RGO–TiO_2 photoanodes in dye-sensitized solar cell. *Thin Solid Films, 584*: 29-36.

Ding, H., Zhang, S., Juan, P.-C., Liu, T.-Y., Du, Z.-F., and Zhao, D.-L. (2016). Enhancing the photovoltaic performance of dye-sensitized solar cells by modifying TiO_2 photoanodes with exfoliated graphene sheets. *RSC Advances, 6*(47): 41092-41102.

Ding, S., Luan, D., Boey, F. Y. C., Chen, J. S., and Lou, X. W. D. (2011). SnO 2 nanosheets grown on graphene sheets with enhanced lithium storage properties. *Chemical Communications, 47*(25): 7155-7157.

Dobrzański, L. A., vel Prokopowicz, M. P., Palček, P., Drygała, A., Lukaszkowicz, K., and Król, M. (2017). PHOTOANODE OF DYE-SENSITIZED SOLAR CELLS BASED ON TITANIUM DIOXIDE WITH REDUCED GRAPHENE OXIDE. *Materials Engineering-Materiálové inžinierstvo (MEMI), 24*(1): 1-10.

Dos Santos, J. L., Peres, N., and Neto, A. C. (2007). Graphene bilayer with a twist: electronic structure. *Physical review letters, 99*(25): 256802.

Dou, Y., Wu, F., Mao, C., Fang, L., Guo, S., and Zhou, M. (2015). Enhanced photovoltaic performance of ZnO nanorod-based dye-sensitized solar cells by using Ga doped ZnO seed layer. *Journal of Alloys and Compounds, 633*: 408-414.

Dubey, P. K., Tripathi, P., Tiwari, R., Sinha, A., and Srivastava, O. (2014). Synthesis of reduced graphene oxide–TiO_2 nanoparticle composite systems and its application in hydrogen production. *International Journal of Hydrogen Energy, 39*(29): 16282-16292.

Durantini, J., Boix, P. P., Gervaldo, M., Morales, G. M., Otero, L., Bisquert, J., and Barea, E. M. (2012). Photocurrent enhancement in dye-sensitized photovoltaic devices with titania–graphene composite electrodes. *Journal of Electroanalytical Chemistry, 683*: 43-46.

Eda, G., Ball, J., Mattevi, C., Acik, M., Artiglia, L., Granozzi, G., Chabal, Y., Anthopoulos, T. D., and Chhowalla, M. (2011). Partially oxidized graphene as a precursor to graphene. *J. Mater. Chem., 21*(30): 11217-11223.

Eder, D., Motta, M., and Windle, A. (2009). Iron-doped Pt–TiO_2 nanotubes for photo-catalytic water splitting. *Nanotechnology, 20*(5): 055602.

Edwards, F. Session BI, Intracellular Morphology.

Enderlein, C. (2010). *Graphene and its interaction with different substrates studied by angular-resolved photoemission spectroscopy.* Freie Universität Berlin, Germany.

Eshaghi, A., and Aghaei, A. A. (2015). Effect of TiO_2–graphene nanocomposite photoanode on dye-sensitized solar cell performance. *Bulletin of Materials Science, 38*(5): 1177-1182.

Fan, J., Liu, S., and Yu, J. (2012). Enhanced photovoltaic performance of dye-sensitized solar cells based on TiO_2 nanosheets/graphene composite films. *Journal of Materials Chemistry, 22*(33): 17027-17036.

Fan, W., Lai, Q., Zhang, Q., and Wang, Y. (2011). Nanocomposites of TiO_2 and reduced graphene oxide as efficient photocatalysts for hydrogen evolution. *The Journal of Physical Chemistry C, 115*(21): 10694-10701.

Farhangi, N., Chowdhury, R. R., Medina-Gonzalez, Y., Ray, M. B., and Charpentier, P. A. (2011). Visible light active Fe doped TiO_2 nanowires grown on graphene using supercritical CO2. *Applied Catalysis B: Environmental, 110*: 25-32.

Ferrari, A. C., and Robertson, J. (2000). Interpretation of Raman spectra of disordered and amorphous carbon. *Phys. Rev. B, 61*(20): 14095.

Ferreira, A., Xu, X., Tan, C.-L., Bae, S.-K., Peres, N., Hong, B.-H., Özyilmaz, B., and Neto, A. C. (2011). Transport properties of graphene with one-dimensional charge defects. *EPL (Europhysics Letters), 94*(2): 28003.

First Solar Builds the Highest Efficiency Thin Film PV Cell on Record. Retrieved from http://investor.firstsolar.com/releasedetail.cfm?ReleaseID=864426

Fitzer, E., Kochling, K.-H., Boehm, H., and Marsh, H. (1995). Recommended terminology for the description of carbon as a solid (IUPAC Recommendations 1995). *Pure and Applied Chemistry, 67*(3): 473-506.

Freitag, M., Teuscher, J., Saygili, Y., Zhang, X., Giordano, F., Liska, P., Hua, J., Zakeeruddin, S. M., Moser, J.-E., and Grätzel, M. (2017). Dye-sensitized solar cells for efficient power generation under ambient lighting. *Nature Photonics*.

Fugallo, G., Cepellotti, A., Paulatto, L., Lazzeri, M., Marzari, N., and Mauri, F. (2014). Thermal conductivity of graphene and graphite: collective excitations and mean free paths. *Nano letters, 14*(11): 6109-6114.

Fujishima, A., Zhang, X., and Tryk, D. A. (2008). TiO_2 photocatalysis and related surface phenomena. *Surface Science Reports, 63*(12): 515-582.

Fukai, Y., Kondo, Y., Mori, S., and Suzuki, E. (2007). Highly efficient dye-sensitized SnO 2 solar cells having sufficient electron diffusion length. *Electrochemistry Communications, 9*(7): 1439-1443.

Geim, A. K. (2009). Graphene: status and prospects. *science, 324*(5934): 1530-1534.

Geng, D., Wang, H., and Yu, G. (2015). Graphene Single Crystals: Size and Morphology Engineering. *Advanced Materials, 27*(18): 2821-2837.

Geng, X., Niu, L., Xing, Z., Song, R., Liu, G., Sun, M., Cheng, G., Zhong, H., Liu, Z., and Zhang, Z. (2010). Aqueous‐Processable Noncovalent Chemically Converted Graphene–Quantum Dot Composites for Flexible and Transparent Optoelectronic Films. *Advanced Materials, 22*(5): 638-642.

Gerischer, H., Michel-Beyerle, M., Rebentrost, F., and Tributsch, H. (1968). Sensitization of charge injection into semiconductors with large band gap. *Electrochimica Acta, 13*(6): 1509-1515.

Ghann, W., Kang, H., Sheikh, T., Yadav, S., Chavez-Gil, T., Nesbitt, F., and Uddin, J. (2017). Fabrication, Optimization and Characterization of Natural Dye Sensitized Solar Cell. *Scientific Reports, 7*.

Gharavi, P. M., and Mohammadi, M. (2015). The improvement of light scattering of dye-sensitized solar cells aided by a new dandelion-like TiO_2 nanostructures. *Solar Energy Materials and Solar Cells, 137*: 113-123.

Ghasemi, S., Hosseini, S. R., and Mousavi, F. (2017). Electrophoretic deposition of graphene nanosheets: A suitable method for fabrication of silver-graphene counter electrode for dye-sensitized solar cell. *Colloids and Surfaces A: Physicochemical and Engineering Aspects, 520*: 477-487.

Giannouli, M. (2013). Nanostructured ZnO, TiO_2, and composite ZnO/TiO_2 films for application in dye-sensitized solar cells. *International Journal of Photoenergy, 2013*.

Gong, J., Liang, J., and Sumathy, K. (2012). Review on dye-sensitized solar cells (DSSCs): fundamental concepts and novel materials. *Renewable and Sustainable Energy Reviews, 16*(8): 5848-5860.

Grätzel, M. (2001). Photoelectrochemical cells. *Nature, 414*(6861): 338.

Grätzel, M. (2003). Dye-sensitized solar cells. *Journal of Photochemistry and Photobiology C: Photochemistry Reviews, 4*(2): 145-153.

Green, M. A. (1981). Solar cell fill factors: General graph and empirical expressions. *Solid State Electron., 24*(8): 788-789.

Green, M. A., Emery, K., Hishikawa, Y., Warta, W., and Dunlop, E. D. (2015). Solar cell efficiency tables (Version 45). *Progress in photovoltaics: research and applications, 23*(1): 1-9.

Guo, J., Li, Y., Zhu, S., Chen, Z., Liu, Q., Zhang, D., Moon, W.-J., and Song, D.-M. (2012). Synthesis of WO 3@ Graphene composite for enhanced photocatalytic oxygen evolution from water. *Rsc Advances, 2*(4): 1356-1363.

Guo, J., Zhu, S., Chen, Z., Li, Y., Yu, Z., Liu, Q., Li, J., Feng, C., and Zhang, D. (2011). Sonochemical synthesis of TiO_2 nanoparticles on graphene for use as photocatalyst. *Ultrasonics sonochemistry, 18*(5): 1082-1090.

Guo, X., Lu, G., and Chen, J. (2015). Graphene-based materials for photoanodes in dye-sensitized solar cells. *Frontiers in Energy Research, 3*: 50.

Gupta, S. M., and Tripathi, M. (2011). A review of TiO_2 nanoparticles. *Chinese Science Bulletin, 56*(16): 1639-1657.

Gupta, S. M., and Tripathi, M. (2012). A review on the synthesis of TiO_2 nanoparticles by solution route. *Central European Journal of Chemistry, 10*(2): 279-294.

Gurunathan, S., Han, J. W., and Kim, J.-H. (2013). Green chemistry approach for the synthesis of biocompatible graphene. *Int J Nanomedicine, 8*: 2719-2732.

Gwon, H., Kim, H.-S., Lee, K. U., Seo, D.-H., Park, Y. C., Lee, Y.-S., Ahn, B. T., and Kang, K. (2011). Flexible energy storage devices based on graphene paper. *Energy & Environmental Science, 4*(4): 1277-1283.

Ha, N. T., Long, P. D., Trung, N. T., and Hong, L. V. (2016). Graphene Effect on Efficiency of TiO_2-based Dye Sensitized Solar Cells (DSSC). *Communications in Physics, 26*(1): 43.

Hagfeldt, A. (2012). Brief overview of dye-sensitized solar cells. *Ambio, 41*(2): 151-155.

Hagfeldt, A., Boschloo, G., Sun, L., Kloo, L., and Pettersson, H. (2010a). Dye-sensitized solar cells. *Chem. Rev., 110*(11): 6595-6663.

Hagfeldt, A., Boschloo, G., Sun, L., Kloo, L., and Pettersson, H. (2010b). Dye-sensitized solar cells. *Chemical reviews, 110*(11): 6595-6663.

Haldorai, Y., Rengaraj, A., Kwak, C. H., Huh, Y. S., and Han, Y.-K. (2014). Fabrication of nano TiO_2@ graphene composite: reusable photocatalyst for hydrogen production, degradation of organic and inorganic pollutants. *Synthetic Metals, 198*: 10-18.

Hamadanian, M., and Jabbari, V. (2011). Investigation on the energy conversion of dye-sensitized solar cells based on TiO_2 core/shell using metal oxide as a barrier layer. *Applied Solar Energy, 47*(4): 281-288.

Hamid, S. B. A., Tan, T. L., Lai, C. W., and Samsudin, E. M. (2014a). Multiwalled carbon nanotube/TiO_2 nanocomposite as a highly active photocatalyst for photodegradation of Reactive Black 5 dye. *Chinese J. Catal., 35*(12).

Hamid, S. B. A., Tan, T. L., Lai, C. W., and Samsudin, E. M. (2014b). Multiwalled carbon nanotube/TiO_2 nanocomposite as a highly active photocatalyst for photodegradation of Reactive Black 5 dye. *Chinese Journal of Catalysis, 35*(12).

Han, D.-W., Heo, J.-H., Kwak, D.-J., Han, C.-H., and Sung, Y.-M. (2009). Texture, Morphology and Photovoltaic Characteristics of Nanoporous F: SnO_2 Films. *Journal of Electrical Engineering & Technology, 4*(1): 93-97.

Hanaor, D. A., and Sorrell, C. C. (2011). Review of the anatase to rutile phase transformation. *Journal of Materials science, 46*(4): 855-874.

Hardcastle, F. (2011). Raman spectroscopy of titania (TiO_2) nanotubular water-splitting catalysts. *J. Ark. Acad. Sci., 65*: 43-48.

Hardcastle, F. D., and Wachs, I. E. (1991). Determination of vanadium-oxygen bond distances and bond orders by Raman spectroscopy. *J. Phys. Chem., 95*(13): 5031-5041.

Hasan, M. R., Lai, C. W., Bee Abd Hamid, S., and Jeffrey Basirun, W. (2014). Effect of Ce doping on RGO-TiO_2 nanocomposite for high photoelectrocatalytic behavior. *International Journal of Photoenergy, 2014*.

Hasaneen, R., Elsayed, N. A., and Barrufet, M. A. (2014). Analysis of the technical, microeconomic, and political impact of a carbon tax on carbon dioxide sequestration resulting from liquefied natural gas production. *Clean Technologies and Environmental Policy, 16*(8): 1597-1613.

Hashimoto, K., Irie, H., and Fujishima, A. (2005). TiO_2 photocatalysis: a historical overview and future prospects. *Japanese journal of applied physics, 44*(12R): 8269.

He, C.-N., Huang, W.-Q., Xu, L., Yang, Y.-C., Zhou, B.-X., Huang, G.-F., Peng, P., and Liu, W.-M. (2015). Tuning near-gap electronic structure, interface charge transfer and visible light response of hybrid doped graphene and Ag3PO4 composite: Dopant effects. *arXiv preprint arXiv:1510.08137*.

He, H., Chen, A., Lv, H., Dong, H., Chang, M., and Li, C. (2013). Hydrothermal fabrication of Ni_3S_2/TiO_2 nanotube composite films on Ni anode and application in photoassisted water electrolysis. *Journal of Alloys and Compounds, 574*: 217-220.

He, Z., Guai, G., Liu, J., Guo, C., Loo, J. S. C., Li, C. M., and Tan, T. T. Y. (2011). Nanostructure control of graphene-composited TiO_2 by a one-step solvothermal approach for high performance dye-sensitized solar cells. *Nanoscale, 3*(11): 4613-4616.

Hernandez, Y., Nicolosi, V., Lotya, M., Blighe, F. M., Sun, Z., De, S., McGovern, I., Holland, B., Byrne, M., and Gun'Ko, Y. K. (2008). High-yield production of graphene by liquid-phase exfoliation of graphite. *Nature nanotechnology, 3*(9): 563-568.

Hoffmann, M. R., Martin, S. T., Choi, W., and Bahnemann, D. W. (1995). Environmental applications of semiconductor photocatalysis. *Chemical reviews, 95*(1): 69-96.

Hofmann, U., and Holst, R. (1939). Über die Säurenatur und die Methylierung von Graphitoxyd. *Berichte der deutschen chemischen Gesellschaft (A and B Series), 72*(4): 754-771.

Hoogwijk, M., Faaij, A., Van Den Broek, R., Berndes, G., Gielen, D., and Turkenburg, W. (2003). Exploration of the ranges of the global potential of biomass for energy. *Biomass and bioenergy, 25*(2): 119-133.

Hou, Y., Li, X. Y., Zhao, Q. D., Quan, X., and Chen, G. H. (2010). Electrochemical method for synthesis of a ZnFe2O4/TiO_2 composite nanotube array modified electrode with enhanced photoelectrochemical activity. *Advanced functional materials, 20*(13): 2165-2174.

Howatt, G., Breckenridge, R., and Brownlow, J. (1947). Fabrication of thin ceramic sheets for capacitors. *Journal of the American Ceramic Society, 30*(8): 237-242.

Hsu, C.-H., Lai, C.-C., Chen, L.-C., and Chan, P.-S. (2014a). Enhanced Performance of Dye-Sensitized Solar Cells with Graphene/ZnO Nanoparticles Bilayer Structure. *Journal of Nanomaterials, 2014*.

Hsu, C.-H., Lai, C.-C., Chen, L.-C., and Chan, P.-S. (2014b). Enhanced performance of dye-sensitized solar cells with graphene/ZnO nanoparticles bilayer structure. *Journal of Nanomaterials, 2014*: 4.

Huang, C., Chang, K., and Hsu, C. (2015). TiO_2 compact layers prepared for high performance dye-sensitized solar cells. *Electrochimica Acta, 170*: 256-262.

Huang, C., Li, C., and Shi, G. (2012a). Graphene based catalysts. *Energy & Environmental Science, 5*(10): 8848-8868.

Huang, N., Lim, H., Chia, C. H., Yarmo, M. A., and Muhamad, M. (2011). Simple room-temperature preparation of high-yield large-area graphene oxide. *International journal of nanomedicine, 6*: 3443-3448.

Huang, W.-C., Tseng, C.-H., Chang, S.-H., Tuan, H.-Y., Chiang, C.-C., Lyu, L.-M., and Huang, M. H. (2012b). Solvothermal synthesis of zincblende and wurtzite CuInS2 nanocrystals and their photovoltaic application. *Langmuir, 28*(22): 8496-8501.

Huc, V., Bendiab, N., Rosman, N., Ebbesen, T., Delacour, C., and Bouchiat, V. (2008). Large and flat graphene flakes produced by epoxy bonding and reverse exfoliation of highly oriented pyrolytic graphite. *Nanotechnology, 19*(45): 455601.

Hummers Jr, W. S., and Offeman, R. E. (1958). Preparation of graphitic oxide. *Journal of the American Chemical Society, 80*(6): 1339-1339.

Hung, I., and Bhattacharjee, R. (2016). Effect of Photoanode Design on the Photoelectrochemical Performance of Dye-Sensitized Solar Cells Based on SnO2 Nanocomposite. *Energies, 9*(8): 641.

Hussein, K., Muta, I., Hoshino, T., and Osakada, M. (1995). Maximum photovoltaic power tracking: an algorithm for rapidly changing atmospheric conditions. *IEE Proceedings-Generation, Transmission and Distribution, 142*(1): 59-64.

Islam, M., Sampe, J., Kamal, N., and Nadzirin, H. (2016). Architecture of low power energy harvester using hybrid input of solar and thermal for laptop or notebook: A review.

Jasim, D. A., Lozano, N., and Kostarelos, K. (2016). Synthesis of few-layered, high-purity graphene oxide sheets from different graphite sources for biology. *2D Materials, 3*(1): 014006.

Jeng, M.-J., Wung, Y.-L., Chang, L.-B., and Chow, L. (2013). Dye-Sensitized Solar Cells with Anatase TiO_2 Nanorods Prepared by Hydrothermal Method. *Int. J. Photoenergy, 2013*.

Jeon, N. J., Noh, J. H., Kim, Y. C., Yang, W. S., Ryu, S., and Seok, S. I. (2014). Solvent engineering for high-performance inorganic–organic hybrid perovskite solar cells. *Nature materials*, *13*(9): 897-903.

Jiang, B., Tian, C., Pan, Q., Jiang, Z., Wang, J.-Q., Yan, W., and Fu, H. (2011). Enhanced photocatalytic activity and electron transfer mechanisms of graphene/TiO_2 with exposed {001} facets. *The Journal of Physical Chemistry C, 115*(48): 23718-23725.

Jin, Y.-S., Kim, K.-H., Kim, W.-J., Jang, K.-U., and Choi, H.-W. (2012). The effect of RF-sputtered TiO_2 passivating layer on the performance of dye sensitized solar cells. *Ceramics International, 38*: S505-S509.

Jin, Y. S., and Choi, H. W. (2012). Properties of dye-sensitized solar cells with TiO_2 passivating layers prepared by electron-beam evaporation. *Journal of nanoscience and nanotechnology, 12*(1): 662-667.

JING, L., and FU HG, W. B. (2005). Effects of Sn dopant on the photocatalytic activity of TiO_2 nanoparticles. *Applied Catalysis, B, 62*: 282-291.

Jose, R., Kumar, A., Thavasi, V., Fujihara, K., Uchida, S., and Ramakrishna, S. (2008). Relationship between the molecular orbital structure of the dyes and photocurrent density in the dye-sensitized solar cells. *Applied Physics Letters, 93*(2): 023125.

Juang, Z.-Y., Wu, C.-Y., Lu, A.-Y., Su, C.-Y., Leou, K.-C., Chen, F.-R., and Tsai, C.-H. (2010). Graphene synthesis by chemical vapor deposition and transfer by a roll-to-roll process. *Carbon*, *48*(11): 3169-3174.

Kadachi, Z., Karoui, M. B., Azizi, T., and Gharbi, R. (2016). Effect of TiO_2 blocking layer synthesised by a sol–gel method in performances of fluorine-doped tin oxide/TiO_2/dyed-TiO_2/electrolyte/pt/fluorine-doped tin oxide solar cells based on natural mallow dye. *Micro & Nano Letters, 11*(2): 94-98.

Kanta, U.-a., Thongpool, V., Sangkhun, W., Wongyao, N., and Wootthikanokkhan, J. (2017). Preparations, Characterizations, and a Comparative Study on Photovoltaic Performance of Two Different Types of Graphene/TiO_2 Nanocomposites Photoelectrodes. *Journal of Nanomaterials, 2017*.

Karim, M. R., Hatakeyama, K., Matsui, T., Takehira, H., Taniguchi, T., Koinuma, M., Matsumoto, Y., Akutagawa, T., Nakamura, T., and Noro, S.-i. (2013). Graphene oxide nanosheet with high proton conductivity. *Journal of the American Chemical Society, 135*(22): 8097-8100.

Kato, R., Koga, Y., Matsuishi, K., and Hasegawa, M. (2017). Strain analysis of plasma CVD graphene for roll-to-roll production by scanning transmission electron microscopy and Raman spectroscopy. *Japanese Journal of Applied Physics, 56*(3): 030307.

Kayes, B. M., Nie, H., Twist, R., Spruytte, S. G., Reinhardt, F., Kizilyalli, I. C., and Higashi, G. S. (2011). 27.6% conversion efficiency, a new record for single-junction solar cells under 1 sun illumination. *Photovoltaic Specialists Conference (PVSC), 2011 37th IEEE*: 000004-000008.

Khalid, N., Ahmed, E., Hong, Z., Sana, L., and Ahmed, M. (2013). Enhanced photocatalytic activity of graphene–TiO_2 composite under visible light irradiation. *Current Applied Physics, 13*(4): 659-663.

Khan, S. U., Al-Shahry, M., and Ingler, W. B. (2002). Efficient photochemical water splitting by a chemically modified n-TiO_2. *science, 297*(5590): 2243-2245.

Kim, D. W., Kim, D., Min, B. H., Lee, H., and Jung, H.-T. (2015a). Sonication-free dispersion of large-area graphene oxide sheets using internal pressure from release of intercalated carbon dioxide. *Carbon, 88*: 126-132.

Kim, H.-N., Yoo, H., and Moon, J. H. (2013). Graphene-embedded 3D TiO_2 inverse opal electrodes for highly efficient dye-sensitized solar cells: morphological characteristics and photocurrent enhancement. *Nanoscale, 5*(10): 4200-4204.

Kim, S.-B., Park, J.-Y., Kim, C.-S., Okuyama, K., Lee, S.-E., Jang, H.-D., and Kim, T.-O. (2015b). Effects of graphene in dye-sensitized solar cells based on nitrogen-doped TiO_2 composite. *The Journal of Physical Chemistry C, 119*(29): 16552-16559.

Kim, S. R., Parvez, M. K., and Chhowalla, M. (2009). UV-reduction of graphene oxide and its application as an interfacial layer to reduce the back-transport reactions in dye-sensitized solar cells. *Chemical Physics Letters, 483*(1): 124-127.

Ko, H.-S., Han, H.-J., Na, G., Lee, A.-R., Yun, J.-J., and Han, E.-M. (2013). Efficiency Characteristics of Dye-Sensitized Solar Cells (DSSCs) by Incorporation of TiO_2-Reduced Graphene Oxide Composite Electrodes. *Mol. Cryst. Liq. Cryst., 579*(1): 83-88.

Komiya, R., Fukui, A., Murofushi, N., Koide, N., Yamanaka, R., and Katayama, H. (2011). Improvement of the conversion efficiency of a monolithic type dye-sensitized solar cell module. *Technical Digest, 21st International Photovoltaic Science and Engineering Conference*: 2C-5O.

Kothari, R., Tyagi, V., and Pathak, A. (2010). Waste-to-energy: A way from renewable energy sources to sustainable development. *Renewable and Sustainable Energy Reviews, 14*(9): 3164-3170.

Kovtyukhova, N. I., Ollivier, P. J., Martin, B. R., Mallouk, T. E., Chizhik, S. A., Buzaneva, E. V., and Gorchinskiy, A. D. (1999). Layer-by-layer assembly of ultrathin composite films from micron-sized graphite oxide sheets and polycations. *Chemistry of Materials, 11*(3): 771-778.

Kuila, T., Bose, S., Khanra, P., Mishra, A. K., Kim, N. H., and Lee, J. H. (2012). A green approach for the reduction of graphene oxide by wild carrot root. *Carbon, 50*(3): 914-921.

Kumar, R., Singh, R. K., Dubey, P. K., Singh, D. P., Yadav, R. M., and Tiwari, R. S. (2015). Hydrothermal synthesis of a uniformly dispersed hybrid graphene–TiO_2 nanostructure for optical and enhanced electrochemical applications. *RSC Advances, 5*(10): 7112-7120.

Kumari, J., Sanjeevadharshini, N., Dissanayake, M., Senadeera, G., and Thotawatthage, C. (2016). The effect of TiO_2 photo anode film thickness on photovoltaic properties of dye-sensitized solar cells. *Ceylon Journal of Science, 45*(1).

Kusumawati, Y., Martoprawiro, M., and Pauporté, T. (2014). Effects of graphene in graphene/TiO_2 composite films applied to solar cell photoelectrode. *The Journal of Physical Chemistry C, 118*(19): 9974-9981.

Lambert, T. N., Chavez, C. A., Hernandez-Sanchez, B., Lu, P., Bell, N. S., Ambrosini, A., Friedman, T., Boyle, T. J., Wheeler, D. R., and Huber, D. L. (2009). Synthesis and characterization of titania− graphene nanocomposites. *The Journal of Physical Chemistry C, 113*(46): 19812-19823.

Larcher, D., and Tarascon, J.-M. (2015). Towards greener and more sustainable batteries for electrical energy storage. *Nature chemistry, 7*(1): 19-29.

Lee, E., Ryu, J., and Jang, J. (2013). Fabrication of graphene quantum dots via size-selective precipitation and their application in upconversion-based DSSCs. *Chemical Communications, 49*(85): 9995-9997.

Lee, J.-K., and Yang, M. (2011). Progress in light harvesting and charge injection of dye-sensitized solar cells. *Materials Science and Engineering: B, 176*(15): 1142-1160.

Lee, J. S., You, K. H., and Park, C. B. (2012). Highly photoactive, low bandgap TiO_2 nanoparticles wrapped by graphene. *Advanced Materials, 24*(8): 1084-1088.

Lee, K. E., Gomez, M. A., Elouatik, S., and Demopoulos, G. P. (2010a). Further understanding of the adsorption mechanism of N719 sensitizer on anatase TiO_2 films for DSSC applications using vibrational spectroscopy and confocal Raman imaging. *Langmuir, 26*(12): 9575-9583.

Lee, K. S., Lee, H. K., Wang, D. H., Park, N.-G., Lee, J. Y., Park, O. O., and Park, J. H. (2010b). Dye-sensitized solar cells with Pt-and TCO-free counter electrodes. *Chemical communications, 46*(25): 4505-4507.

Lee, Y. K., Choi, H., Lee, H., Lee, C., Choi, J. S., Choi, C.-G., Hwang, E., and Park, J. Y. (2016). Hot carrier multiplication on graphene/TiO_2 Schottky nanodiodes. *Scientific reports, 6*.

Li, B., Cao, H., Yin, G., Lu, Y., and Yin, J. (2011a). Cu 2 O@ reduced graphene oxide composite for removal of contaminants from water and supercapacitors. *Journal of Materials Chemistry, 21*(29): 10645-10648.

Li, J., Wan, W., Zhou, H., Li, J., and Xu, D. (2011b). Hydrothermal synthesis of TiO_2 (B) nanowires with ultrahigh surface area and their fast charging and discharging properties in Li-ion batteries. *Chemical Communications, 47*(12): 3439-3441.

Li, K., Xiong, J., Chen, T., Yan, L., Dai, Y., Song, D., Lv, Y., and Zeng, Z. (2013). Preparation of graphene/TiO_2 composites by nonionic surfactant strategy and their simulated sunlight and visible light photocatalytic activity towards representative aqueous POPs degradation. *Journal of hazardous materials, 250*: 19-28.

Li, N., Liu, G., Zhen, C., Li, F., Zhang, L., and Cheng, H. M. (2011c). Battery Performance and Photocatalytic Activity of Mesoporous Anatase TiO_2 Nanospheres/Graphene Composites by Template ‐ Free Self ‐ Assembly. *Advanced Functional Materials, 21*(9): 1717-1722.

Li, P. C. (1961). Preparation of single-crystal graphite from melts. *Nature, 192*(4805): 864-865.

Li, R., Chen, G., Dong, G., and Sun, X. (2014). Controllable synthesis of nanostructured TiO_2 by CTAB-assisted hydrothermal route. *New Journal of Chemistry, 38*(10): 4684-4689.

Li, S., Luo, Y., Lv, W., Yu, W., Wu, S., Hou, P., Yang, Q., Meng, Q., Liu, C., and Cheng, H. M. (2011d). Vertically Aligned Carbon Nanotubes Grown on Graphene Paper as Electrodes in Lithium ‐ Ion Batteries and Dye ‐ Sensitized Solar Cells. *Advanced Energy Materials, 1*(4): 486-490.

Liang, D., Cui, C., Hu, H., Wang, Y., Xu, S., Ying, B., Li, P., Lu, B., and Shen, H. (2014). One-step hydrothermal synthesis of anatase TiO_2/reduced graphene oxide nanocomposites with enhanced photocatalytic activity. *Journal of Alloys and Compounds, 582*: 236-240.

Liang, Y., Wang, H., Casalongue, H. S., Chen, Z., and Dai, H. (2010). TiO_2 nanocrystals grown on graphene as advanced photocatalytic hybrid materials. *Nano Research, 3*(10): 701-705.

Liang, Y. T., Vijayan, B. K., Lyandres, O., Gray, K. A., and Hersam, M. C. (2012). Effect of dimensionality on the photocatalytic behavior of carbon–titania nanosheet composites: charge transfer at nanomaterial interfaces. *The Journal of Physical Chemistry Letters, 3*(13): 1760-1765.

Lim, S. P., Pandikumar, A., Huang, N. M., and Lim, H. N. (2015a). Reduced graphene oxide – titania nanocomposite ‐ modified photoanode for efficient dye ‐ sensitized solar cells. *Int. J. Energ. Res., 39*(6): 812-824.

Lim, S. P., Pandikumar, A., Huang, N. M., and Lim, H. N. (2015b). Reduced graphene oxide – titania nanocomposite ‐ modified photoanode for efficient dye ‐ sensitized solar cells. *International Journal of Energy Research, 39*(6): 812-824.

Lin, F., Tong, X., Wang, Y., Bao, J., and Wang, Z. M. (2015). Graphene oxide liquid crystals: synthesis, phase transition, rheological property, and applications in optoelectronics and display. *Nanoscale research letters, 10*(1): 435.

Lin, L.-Y., Lee, C.-P., Vittal, R., and Ho, K.-C. (2011). Improving the durability of dye-sensitized solar cells through back illumination. *Journal of Power Sources, 196*(3): 1671-1676.

Lin, Y.-C., Chen, Y.-T., and Yao, P.-C. (2013). Effect of post-heat-treated NiO x overlayer on performance of nanocrystalline TiO_2 thin films for dye-sensitized solar cells. *Journal of Power Sources, 240*: 705-712.

Liu, B., Wang, X., Cai, G., Wen, L., Song, Y., and Zhao, X. (2009a). Low temperature fabrication of V-doped TiO_2 nanoparticles, structure and photocatalytic studies. *Journal of hazardous materials, 169*(1): 1112-1118.

Liu, H., Cao, K., Xu, X., Jiao, L., Wang, Y., and Yuan, H. (2015a). Ultrasmall TiO_2 nanoparticles in situ growth on graphene hybrid as superior anode material for sodium/lithium ion batteries. *ACS applied materials & interfaces, 7*(21): 11239-11245.

Liu, H., Zhang, L., Guo, Y., Cheng, C., Yang, L., Jiang, L., Yu, G., Hu, W., Liu, Y., and Zhu, D. (2013a). Reduction of graphene oxide to highly conductive graphene by Lawesson's reagent and its electrical applications. *J. Mater. Chem. C, 1*(18): 3104-3109.

Liu, J., Fu, X., Cao, D.-P., Mao, L., Wang, J., Mu, D.-H., Mi, B.-X., Zhao, B.-M., and Gao, Z.-Q. (2015b). Stacked graphene–TiO_2 photoanode via electrospray deposition for highly efficient dye-sensitized solar cells. *Organic Electronics, 23*: 158-163.

Liu, L., Zhang, Y., Zhang, B., and Feng, Y. (2017). A detailed investigation on the performance of dye-sensitized solar cells based on reduced graphene oxide-doped TiO_2 photoanode. *Journal of Materials Science, 52*(13): 8070-8083.

Liu, S.-Y., Perng, Y.-H., and Ho, Y.-F. (2013b). The effect of renewable energy application on Taiwan buildings: What are the challenges and strategies for solar energy exploitation? *Renewable and Sustainable Energy Reviews, 28*: 92-106.

Liu, X.-w., Shen, L.-y., and Hu, Y.-h. (2016a). Preparation of TiO2-Graphene Composite by a Two-Step Solvothermal Method and its Adsorption-Photocatalysis Property. *Water, Air, & Soil Pollution, 227*(5): 1-12.

Liu, X., Balla, I., Bergeron, H., and Hersam, M. C. (2016b). Point defects and grain boundaries in rotationally commensurate MoS_2 on epitaxial graphene. *The Journal of Physical Chemistry C, 120*(37): 20798-20805.

Liu, X., Pan, L., Lv, T., Zhu, G., Lu, T., Sun, Z., and Sun, C. (2011a). Microwave-assisted synthesis of TiO_2-reduced graphene oxide composites for the photocatalytic reduction of Cr (vi). *RSC Adv., 1*(7): 1245-1249.

Liu, X., Pan, L., Lv, T., Zhu, G., Sun, Z., and Sun, C. (2011b). Microwave-assisted synthesis of CdS–reduced graphene oxide composites for photocatalytic reduction of Cr (vi). *Chemical Communications, 47*(43): 11984-11986.

Liu, Y. (2014). Hydrothermal synthesis of TiO_2–RGO composites and their improved photocatalytic activity in visible light. *RSC Advances, 4*(68): 36040-36045.

Liu, Z., Suenaga, K., Harris, P. J., and Iijima, S. (2009b). Open and closed edges of graphene layers. *Physical review letters, 102*(1): 015501.

Loryuenyong, V., Totepvimarn, K., Eimburanapravat, P., Boonchompoo, W., and Buasri, A. (2013). Preparation and characterization of reduced graphene oxide sheets via water-based exfoliation and reduction methods. *Advances in Materials Science and Engineering, 2013*.

Lotya, M., King, P. J., Khan, U., De, S., and Coleman, J. N. (2010). High-concentration, surfactant-stabilized graphene dispersions. *ACS nano, 4*(6): 3155-3162.

Low, F. W., Lai, C. W., and Abd Hamid, S. B. (2015a). Facile synthesis of high quality graphene oxide from graphite flakes using improved Hummer's technique. *J. Nanosci. Nanotechnol., 15*(9): 6769.

Low, F. W., Lai, C. W., and Hamid, S. B. A. (2015b). Easy preparation of ultrathin reduced graphene oxide sheets at a high stirring speed. *Ceramics International, 41*(4): 5798-5806.

Low, F. W., Lai, C. W., and Hamid, S. B. A. (2015c). Easy preparation of ultrathin reduced graphene oxide sheets at a high stirring speed. *Ceram. Int., 41*(4): 5798.

Low, F. W., Lai, C. W., and Hamid, S. B. A. (2017a). Study of reduced graphene oxide film incorporated of TiO_2 species for efficient visible light driven dye-sensitized solar cell. *Journal of Materials Science: Materials in Electronics, 28*(4): 3819-3836.

Low, F. W., Lai, C. W., and Hamid, S. B. A. (2017b). Surface modification of reduced graphene oxide film by Ti ion implantation technique for high dye-sensitized solar cells performance. *Ceramics International, 43*(1): 625-633.

Luan, X., Chen, L., Zhang, J., Qu, G., Flake, J. C., and Wang, Y. (2013). Electrophoretic deposition of reduced graphene oxide nanosheets on TiO_2 nanotube arrays for dye-sensitized solar cells. *Electrochimica Acta, 111*: 216-222.

Machado, B. F., and Serp, P. (2012). Graphene-based materials for catalysis. *Catalysis Science & Technology, 2*(1): 54-75.

Maeda, K., Xiong, A., Yoshinaga, T., Ikeda, T., Sakamoto, N., Hisatomi, T., Takashima, M., Lu, D., Kanehara, M., and Setoyama, T. (2010). Photocatalytic overall water splitting promoted by two different cocatalysts for hydrogen and oxygen evolution under visible light. *Angewandte Chemie, 122*(24): 4190-4193.

Mali, S. S., Kim, H., Shim, C. S., Bae, W. R., Tarwal, N., Sadale, S. B., Patil, P. S., Kim, J.-H., and Hong, C. K. (2013). Single-step synthesis of 3D nanostructured TiO_2 as a scattering layer for vertically aligned 1D nanorod photoanodes and their dye-sensitized solar cell properties. *CrystEngComm, 15*(28): 5660-5667.

Mao, X., Zhou, R., Zhang, S., Ding, L., Wan, L., Qin, S., Chen, Z., Xu, J., and Miao, S. (2016). High efficiency dye-sensitized solar cells constructed with composites of TiO_2 and the hot-bubbling synthesized ultra-small SnO2 nanocrystals. *Scientific reports, 6*.

Marcano, D. C., Kosynkin, D. V., Berlin, J. M., Sinitskii, A., Sun, Z., Slesarev, A., Alemany, L. B., Lu, W., and Tour, J. M. (2010). Improved synthesis of graphene oxide. *ACS nano, 4*(8): 4806-4814.

Mathew, S., Yella, A., Gao, P., Humphry-Baker, R., Curchod, B. F., Ashari-Astani, N., Tavernelli, I., Rothlisberger, U., Nazeeruddin, M. K., and Grätzel, M. (2014). Dye-sensitized solar cells with 13% efficiency achieved through the molecular engineering of porphyrin sensitizers. *Nature chemistry, 6*(3): 242-247.

Matsui, T., Sai, H., Suezaki, T., Matsumoto, M., Saito, K., Yoshida, I., and Kondo, M. (2013). Development of highly stable and efficient amorphous silicon based solar cells. *Proc. 28th European Photovoltaic Solar Energy Conference*: 2213-2217.

Matsumura, M., Matsudaira, S., Tsubomura, H., Takata, M., and Yanagida, H. (1980). Dye sensitization and surface structures of semiconductor electrodes. *Industrial & Engineering Chemistry Product Research and Development, 19*(3): 415-421.

McCann, E., and Koshino, M. (2013). The electronic properties of bilayer graphene. *Reports on Progress in Physics, 76*(5): 056503.

Meng, L., and Li, C. (2011). Blocking layer effect on dye-sensitized solar cells assembled with TiO2 nanorods prepared by DC reactive magnetron sputtering. *Nanoscience and Nanotechnology Letters, 3*(2): 181-185.

Method of producing high dielectric high insulation ceramic plates. (1952). Google Patents.

Min, Y., Zhang, K., Zhao, W., Zheng, F., Chen, Y., and Zhang, Y. (2012). Enhanced chemical interaction between TiO_2 and graphene oxide for photocatalytic decolorization of methylene blue. *Chemical Engineering Journal, 193*: 203-210.

Mirkin, C. A., and Tuominen, M. (2011). Synthesis, processing, and manufacturing of components, devices, and systems *Nanotechnology Research Directions for Societal Needs in 2020* (pp. 109-158): Springer.

Mitchell, I. K., and Walinga, J. (2017). The creative imperative: The role of creativity, creative problem solving and insight as key drivers for sustainability. *Journal of Cleaner Production, 140*: 1872-1884.

Mogilevsky, G., Chen, Q., Kleinhammes, A., and Wu, Y. (2008). The structure of multilayered titania nanotubes based on delaminated anatase. *Chemical Physics Letters, 460*(4): 517-520.

Momeni, M. M. (2016). Dye-sensitized solar cell and photocatalytic performance of nanocomposite photocatalyst prepared by electrochemical anodization. *Bulletin of Materials Science, 39*(6): 1389-1395.

Moo, J. G. S., Khezri, B., Webster, R. D., and Pumera, M. (2014). Graphene Oxides Prepared by Hummers ' , Hofmann ' s, and Staudenmaier ' s Methods: Dramatic Influences on Heavy ‐ Metal ‐ Ion Adsorption. *ChemPhysChem, 15*(14): 2922-2929.

Morais, A., Alves, J. P. C., Lima, F. A. S., Lira-Cantu, M., and Nogueira, A. F. (2015). Enhanced photovoltaic performance of inverted hybrid bulk-heterojunction solar cells using TiO_2/reduced graphene oxide films as electron transport layers. *Journal of Photonics for Energy, 5*(1): 057408-057408.

Morais, A., Longo, C., Araujo, J. R., Barroso, M., Durrant, J. R., and Nogueira, A. F. (2016). Nanocrystalline anatase TiO_2/reduced graphene oxide composite films as photoanodes for photoelectrochemical water splitting studies: the role of reduced graphene oxide. *Physical Chemistry Chemical Physics, 18*(4): 2608-2616.

Mori, S., Oh-oka, H., Nakao, H., Gotanda, T., Nakano, Y., Jung, H., Iida, A., Hayase, R., Shida, N., and Saito, M. (2015). Organic photovoltaic module development with inverted device structure. *Symposium U Organic Photovoltaics Fundamentals, Materials and Devices*.

Morishige, K., and Hamada, T. (2005). Iron oxide pillared graphite. *Langmuir, 21*(14): 6277-6281.

Mukherji, A., Seger, B., Lu, G. Q., and Wang, L. (2011). Nitrogen doped $Sr_2Ta_2O_7$ coupled with graphene sheets as photocatalysts for increased photocatalytic hydrogen production. *ACS nano, 5*(5): 3483-3492.

Muniz, E., Goes, M., Silva, J., Varela, J. A., Joanni, E., Parra, R., and Bueno, P. (2011). Synthesis and characterization of mesoporous TiO_2 nanostructured films prepared by a modified sol–gel method for application in dye solar cells. *Ceramics International, 37*(3): 1017-1024.

Neto, A. C., Guinea, F., Peres, N. M., Novoselov, K. S., and Geim, A. K. (2009). The electronic properties of graphene. *Reviews of modern physics, 81*(1): 109.

Ng, Y. H., Iwase, A., Kudo, A., and Amal, R. (2010). Reducing graphene oxide on a visible-light $BiVO_4$ photocatalyst for an enhanced photoelectrochemical water splitting. *The Journal of Physical Chemistry Letters, 1*(17): 2607-2612.

Noh, Y., Kim, K., Choi, M., and Song, O. (2016). Properties of Blocking Layer with Ag Nano Powder in a Dye Sensitized Solar Cell. *Journal of the Korean Ceramic Society, 53*(1): 105-109.

Norrish, K., and Taylor, R. M. (1962). Quantitative analysis by X-ray diffraction. *Clay Miner. Bull, 5*(28): 98-109.

Nouri, E., Mohammadi, M. R., and Lianos, P. (2016). Impact of preparation method of TiO_2-RGO nanocomposite photoanodes on the performance of dye-sensitized solar cells. *Electrochimica Acta, 219*: 38-48.

Novoselov, K. S., Geim, A. K., Morozov, S., Jiang, D., Zhang, Y., Dubonos, S., Grigorieva, I., and Firsov, A. (2004). Electric field effect in atomically thin carbon films. *science, 306*(5696): 666-669.

O'regan, B., and Grätzel, M. (1991). A low-cost, high-efficiency solar cell based on dye-sensitized colloidal TiO2 films. *Nature, 353*: 737.

O’regan, B., and Grfitzeli, M. (1991). A low-cost, high-efficiency solar cell based on dye-sensitized. *nature, 353*(6346): 737-740.

Oh, T. H., Pang, S. Y., and Chua, S. C. (2010). Energy policy and alternative energy in Malaysia: issues and challenges for sustainable growth. *Renewable and Sustainable Energy Reviews, 14*(4): 1241-1252.

Ohsaki, Y., Masaki, N., Kitamura, T., Wada, Y., Okamoto, T., Sekino, T., Niihara, K., and Yanagida, S. (2005). Dye-sensitized TiO_2 nanotube solar cells: fabrication and electronic characterization. *Phys. Chem. Chem. Phys., 7*(24): 4157-4163.

Ong, W. J., Tan, L. L., Chai, S. P., Yong, S. T., and Mohamed, A. R. (2014). Facet‐Dependent Photocatalytic Properties of TiO_2‐Based Composites for Energy Conversion and Environmental Remediation. *ChemSusChem, 7*(3): 690-719.

Paek, S.-M., Yoo, E., and Honma, I. (2008). Enhanced cyclic performance and lithium storage capacity of SnO_2/graphene nanoporous electrodes with three-dimensionally delaminated flexible structure. *Nano letters, 9*(1): 72-75.

Pan, J. H., Bahnemann, D. W., Wang, Q., Wang, C., and Zhang, X. (2014). Solar Energy Conversion by Nanostructured TiO_2. *International Journal of Photoenergy, 2014*.

Pan, X., Zhao, Y., Liu, S., Korzeniewski, C. L., Wang, S., and Fan, Z. (2012a). Comparing graphene-TiO_2 nanowire and graphene-TiO_2 nanoparticle composite photocatalysts. *ACS applied materials & interfaces, 4*(8): 3944-3950.

Pan, X., Zhao, Y., Liu, S., Korzeniewski, C. L., Wang, S., and Fan, Z. (2012b). Comparing graphene-TiO2 nanowire and graphene-TiO_2 nanoparticle composite photocatalysts. *ACS Appl. Mater. Interfaces, 4*(8): 3944-3950.

Panwar, N., Kaushik, S., and Kothari, S. (2011). Role of renewable energy sources in environmental protection: a review. *Renewable and Sustainable Energy Reviews, 15*(3): 1513-1524.

Park, C., Kefayat, U., Vikram, N., Ghosh, T., Oh, W., and Cho, K. (2013). Preparation of novel CdS-graphene/TiO_2 composites with high photocatalytic activity for methylene blue dye under visible light. *Bulletin of Materials Science, 36*(5): 869-876.

Park, J. H., Kim, S., and Bard, A. J. (2006). Novel carbon-doped TiO_2 nanotube arrays with high aspect ratios for efficient solar water splitting. *Nano letters, 6*(1): 24-28.

Park, S., and Ruoff, R. S. (2009). Chemical methods for the production of graphenes. *Nature nanotechnology, 4*(4): 217-224.

Parvez, K., Wu, Z.-S., Li, R., Liu, X., Graf, R., Feng, X., and Müllen, K. (2014). Exfoliation of graphite into graphene in aqueous solutions of inorganic salts. *Journal of the American Chemical Society, 136*(16): 6083-6091.

Patil, S. A., Hwang, H.-J., Yu, M.-H., Shrestha, N. K., and Kim, H.-S. (2017). Photonic sintering of a ZnO nanosheet photoanode using flash white light combined with deep UV irradiation for dye-sensitized solar cells. *RSC Advances, 7*(11): 6565-6573.

Pavasupree, S., Ngamsinlapasathian, S., Nakajima, M., Suzuki, Y., and Yoshikawa, S. (2006a). Synthesis, characterization, photocatalytic activity and dye-sensitized solar cell performance of nanorods/nanoparticles TiO_2 with mesoporous structure. *J. Photochem. Photobio. A: Chem., 184*(1): 163-169.

Pavasupree, S., Ngamsinlapasathian, S., Suzuki, Y., and Yoshikawa, S. (2006b). One-dimensional nanostructured TiO_2 for photocatalytic activity and dye-sensitized solar cells applications. *The 2nd Joint International Conference on Sustainable Energy and Environment*: 21-23.

Pena, R., Clare, J., and Asher, G. (1996). Doubly fed induction generator using back-to-back PWM converters and its application to variable-speed wind-energy generation. *IEE Proceedings-Electric Power Applications, 143*(3): 231-241.

Pessoa, R., Fraga, M., Santos, L., Massi, M., and Maciel, H. (2015). Nanostructured thin films based on TiO_2 and/or SiC for use in photoelectrochemical cells: A review of the material characteristics, synthesis and recent applications. *Materials Science in Semiconductor Processing, 29*: 56-68.

Poortmans, J., and Arkhipov, V. (2006). *Thin film solar cells: fabrication, characterization and applications* (Vol. 5): John Wiley & Sons.

Pop, E., Varshney, V., and Roy, A. K. (2012). Thermal properties of graphene: Fundamentals and applications. *MRS bulletin, 37*(12): 1273-1281.

Pradhan, B., Batabyal, S. K., and Pal, A. J. (2007). Vertically aligned ZnO nanowire arrays in Rose Bengal-based dye-sensitized solar cells. *Solar Energy Materials and Solar Cells, 91*(9): 769-773.

Rahmanian, A., Naji, L., and Javanbakht, M. (2015). Electrochemical Study of Hydrogen Adsorption/Reduction (HAR) Reaction on Graphene Oxide as Electrocatalyst for Proton Exchange Membrane Fuel Cells. *Iranian Journal of Hydrogen & Fuel Cell, 2*(2): 99-107.

Raj, C. C., and Prasanth, R. (2016). A critical review of recent developments in nanomaterials for photoelectrodes in dye sensitized solar cells. *Journal of Power Sources, 317*: 120-132.

Raja, R., Govindaraj, M., Antony, M. D., Krishnan, K., Velusamy, E., Sambandam, A., Subbaiah, M., and Rayar, V. W. (2017). Effect of TiO_2/reduced graphene oxide composite thin film as a blocking layer on the efficiency of dye-sensitized solar cells. *Journal of Solid State Electrochemistry, 21*(3): 891-903.

Ramamoorthy, R., Karthika, K., Dayana, A. M., Maheswari, G., Eswaramoorthi, V., Pavithra, N., Anandan, S., and Williams, R. V. (2017). Reduced graphene oxide embedded titanium dioxide nanocomposite as novel photoanode material in natural dye-sensitized solar cells. *Journal of Materials Science: Materials in Electronics*: 1-12.

Release, S. P. (2014). *Solibro Beats World Record for Solar Cells*

Robertson, A. W., and Warner, J. H. (2011). Hexagonal single crystal domains of few-layer graphene on copper foils. *Nano letters, 11*(3): 1182-1189.

Roy-Mayhew, J. D., and Aksay, I. A. (2014a). Graphene materials and their use in dye-sensitized solar cells. *Chemical reviews, 114*(12): 6323-6348.

Roy-Mayhew, J. D., and Aksay, I. A. (2014b). Graphene materials and their use in dye-sensitized solar cells. *Chem. Rev., 114*(12): 6323-6348.

Rozhkov, A., Sboychakov, A., Rakhmanov, A., and Nori, F. (2016). Electronic properties of graphene-based bilayer systems. *Physics Reports, 648*: 1-104.

Safarpour, M., Khataee, A., and Vatanpour, V. (2015). Effect of reduced graphene oxide/TiO_2 nanocomposite with different molar ratios on the performance of PVDF ultrafiltration membranes. *Separation and Purification Technology, 140*: 32-42.

Sahu, S., Awasthy, R. K., Patel, M., AGNIHOTRI, P., and Tiwari, S. (2016). Fabrication and Characterization of nanoporous TiO_2 layer on photoanode by using Doctor Blade Method for dye-sensitized solar cells. *International Conference on Fibre Optics and Photonics*: Th3A. 9.

Sakthivel, S., and Kisch, H. (2003). Daylight photocatalysis by carbon‐modified titanium dioxide. *Angewandte Chemie International Edition, 42*(40): 4908-4911.

Salam, Z., Vijayakumar, E., Subramania, A., Sivasankar, N., and Mallick, S. (2015). Graphene quantum dots decorated electrospun TiO_2 nanofibers as an effective photoanode for dye sensitized solar cells. *Solar Energy Materials and Solar Cells, 143*: 250-259.

Sauvage, F., Chhor, S., Marchioro, A., Moser, J.-E., and Graetzel, M. (2011). Butyronitrile-based electrolyte for dye-sensitized solar cells. *Journal of the American Chemical Society, 133*(33): 13103-13109.

Šćepanović, M. J., Grujić-Brojčin, M., Dohčević-Mitrović, Z., and Popović, Z. (2009). Characterization of anatase TiO2 nanopowder by variable-temperature Raman spectroscopy. *Science of Sintering, 41*(1): 67-73.

Schiermeier, Q., Tollefson, J., Scully, T., Witze, A., and Morton, O. (2008). Electricity without carbon. *Nature, 454*(7206): 816.

Sedghi, A., and Miankushki, H. N. (2012). Influence of TiO_2 electrode properties on performance of dye-sensitized solar cells. *Int. J. Electrochem. Sci., 7*: 12078-12089.

Seema, H., Kemp, K. C., Chandra, V., and Kim, K. S. (2012). Graphene–SnO_2 composites for highly efficient photocatalytic degradation of methylene blue under sunlight. *Nanotechnology, 23*(35): 355705.

Sellappan, R., Sun, J., Galeckas, A., Lindvall, N., Yurgens, A., Kuznetsov, A. Y., and Chakarov, D. (2013). Influence of graphene synthesizing techniques on the photocatalytic performance of graphene–TiO_2 nanocomposites. *Physical Chemistry Chemical Physics, 15*(37): 15528-15537.

Shahriary, L., and Athawale, A. A. (2014). Graphene oxide synthesized by using modified hummers approach. *Int. J. Renew. Energy Environ. Eng, 2*(01): 58-63.

Shakir, S., and Abd-ur-Rehman, H. M. (2016). Enhancement in Photovoltaic Performance of Dye Sensitized Solar Cells Using Cu and Cu: Ag Co-Doped TiO_2 Photoanode. *ASME 2016 Power Conference collocated with the ASME 2016 10th International Conference on Energy Sustainability and the ASME 2016 14th International Conference on Fuel Cell Science, Engineering and Technology*: V001T008A016-V001T008A016.

Shanmugam, M., Durcan, C., Gedrim, R. J., Bansal, T., and Yu, B. (2013). Oxygenated-graphene-enabled recombination barrier layer for high performance dye-sensitized solar cell. *Carbon, 60*: 523-530.

SharmilaDevi, R., Venckatesh R., RajeshwariSivaraj. (2014). Synthesis of titanium dioxide nanoparticles by sol-gel technique. *International Journal of Innovative Research in Science, Engineering and Technology, 3*(8): 15206-15211.

Sheehan, S., Surolia, P., Byrne, O., Garner, S., Cimo, P., Li, X., Dowling, D., and Thampi, K. (2015). Flexible glass substrate based dye sensitized solar cells. *Solar Energy Materials and Solar Cells, 132*: 237-244.

Shen, J., Yan, B., Shi, M., Ma, H., Li, N., and Ye, M. (2011). One step hydrothermal synthesis of TiO_2-reduced graphene oxide sheets. *Journal of Materials Chemistry, 21*(10): 3415-3421.

Sheng, J., Hu, L., Xu, S., Liu, W., Mo, L. e., Tian, H., and Dai, S. (2011). Characteristics of dye-sensitized solar cells based on the TiO_2 nanotube/nanoparticle composite electrodes. *Journal of Materials Chemistry, 21*(14): 5457-5463.

Sher Shah, M. S. A., Park, A. R., Zhang, K., Park, J. H., and Yoo, P. J. (2012). Green synthesis of biphasic TiO$_2$–reduced graphene oxide nanocomposites with highly enhanced photocatalytic activity. *ACS applied materials & interfaces, 4*(8): 3893-3901.

Shu, W., Liu, Y., Peng, Z., Chen, K., Zhang, C., and Chen, W. (2013a). Synthesis and photovoltaic performance of reduced graphene oxide–TiO$_2$ nanoparticles composites by solvothermal method. *Journal of Alloys and Compounds, 563*: 229-233.

Shu, W., Liu, Y., Peng, Z., Chen, K., Zhang, C., and Chen, W. (2013b). Synthesis and photovoltaic performance of reduced graphene oxide–TiO$_2$ nanoparticles composites by solvothermal method. *J. Alloy. Compd., 563*: 229-233.

Sim, L. C., Leong, K. H., Ibrahim, S., and Saravanan, P. (2014). Graphene oxide and Ag engulfed TiO$_2$ nanotube arrays for enhanced electron mobility and visible-light-driven photocatalytic performance. *Journal of Materials Chemistry A, 2*(15): 5315-5322.

Singh, V., Joung, D., Zhai, L., Das, S., Khondaker, S. I., and Seal, S. (2011). Graphene based materials: past, present and future. *Progress in materials science, 56*(8): 1178-1271.

Singhbabu, Y., Kumari, P., Parida, S., and Sahu, R. K. (2014). Conversion of pyrazoline to pyrazole in hydrazine treated N-substituted reduced graphene oxide films obtained by ion bombardment and their electrical properties. *Carbon, 74*: 32-43.

Sipahutar, R., Bernas, S. M., and Imanuddin, M. S. (2013). Renewable energy and hydropower utilization tendency worldwide. *Renewable and Sustainable Energy Reviews, 17*: 213-215.

Soldano, C., Mahmood, A., and Dujardin, E. (2010). Production, properties and potential of graphene. *Carbon, 48*(8): 2127-2150.

Song, C., Qiang, Y., Zhao, Y., Gu, X., Zhu, L., Song, J., and Liu, X. (2014). Dye-sensitized solar cells based on graphene-TiO$_2$ nanoparticles/TiO$_2$ nanotubes composite films. *Int. J. Electrochem. Sci, 9*: 8090-8096.

Song, J., Yin, Z., Yang, Z., Amaladass, P., Wu, S., Ye, J., Zhao, Y., Deng, W. Q., Zhang, H., and Liu, X. W. (2011). Enhancement of photogenerated electron transport in dye‐sensitized solar cells with introduction of a reduced graphene oxide‐TiO$_2$ junction. *Chemistry-A European Journal, 17*(39): 10832-10837.

Song, Z., Hrbek, J., and Osgood, R. (2005). Formation of TiO$_2$ nanoparticles by reactive-layer-assisted deposition and characterization by XPS and STM. *Nano letters, 5*(7): 1327-1332.

Staudenmaier, L. (1898). Verfahren zur darstellung der graphitsäure. *European Journal of Inorganic Chemistry, 31*(2): 1481-1487.

Stubrov, Y., Nikolenko, A., Strelchuk, V., Nedilko, S., and Chornii, V. (2017). Structural Modification of Single-Layer Graphene Under Laser Irradiation Featured by Micro-Raman Spectroscopy. *Nanoscale Research Letters, 12*(1): 297.

Su, C.-Y., Lu, A.-Y., Wu, C.-Y., Li, Y.-T., Liu, K.-K., Zhang, W., Lin, S.-Y., Juang, Z.-Y., Zhong, Y.-L., and Chen, F.-R. (2011). Direct formation of wafer scale graphene thin layers on insulating substrates by chemical vapor deposition. *Nano letters, 11*(9): 3612-3616.

Su, C.-Y., Xu, Y., Zhang, W., Zhao, J., Tang, X., Tsai, C.-H., and Li, L.-J. (2009). Electrical and spectroscopic characterizations of ultra-large reduced graphene oxide monolayers. *Chemistry of Materials*, *21*(23): 5674-5680.

Subramanian, A., Ho, C.-Y., and Wang, H. (2013). Investigation of various photoanode structures on dye-sensitized solar cell performance using mixed-phase TiO_2. *Journal of Alloys and Compounds, 572*: 11-16.

Sun, S., Gao, L., and Liu, Y. (2010a). Enhanced dye-sensitized solar cell using graphene-TiO_2 photoanode prepared by heterogeneous coagulation. *Applied Physics Letters, 96*(8): 3113.

Sun, S., Gao, L., and Liu, Y. (2010b). Enhanced dye-sensitized solar cell using graphene-TiO_2 photoanode prepared by heterogeneous coagulation. *Applied physics letters, 96*(8): 083113.

Sur, U. K. (2012). Graphene: A rising star on the horizon of materials science. *International Journal of Electrochemistry, 2012*.

Sutthana, S., Hongsith, N., and Choopun, S. (2010). AZO/Ag/AZO multilayer films prepared by DC magnetron sputtering for dye-sensitized solar cell application. *Current Applied Physics, 10*(3): 813-816.

Tacchini, I., Ansón-Casaos, A., Yu, Y., Martinez, M. T., and Lira-Cantú, M. (2012). Hydrothermal synthesis of 1D TiO_2 nanostructures for dye sensitized solar cells. *Materials Science and Engineering: B, 177*(1): 19-26.

Taguchi, M., Yano, A., Tohoda, S., Matsuyama, K., Nakamura, Y., Nishiwaki, T., Fujita, K., and Maruyama, E. (2014). 24.7% record efficiency HIT solar cell on thin silicon wafer. *IEEE Journal of Photovoltaics, 4*(1): 96-99.

Tan, B., and Wu, Y. (2006). Dye-sensitized solar cells based on anatase TiO_2 nanoparticle/nanowire composites. *J. Phys. Chem. B, 110*(32): 15932-15938.

Tan, L.-L., Ong, W.-J., Chai, S.-P., and Mohamed, A. R. (2013a). Reduced graphene oxide-TiO_2 nanocomposite as a promising visible-light-active photocatalyst for the conversion of carbon dioxide. *Nanoscale research letters, 8*(1): 1-9.

Tan, L.-L., Ong, W.-J., Chai, S.-P., and Mohamed, A. R. (2013b). Reduced graphene oxide-TiO_2 nanocomposite as a promising visible-light-active photocatalyst for the conversion of carbon dioxide. *Nanoscale research letters, 8*(1): 465.

Tan, L.-L., Ong, W.-J., Chai, S.-P., and Mohamed, A. R. (2013c). Reduced graphene oxide-TiO_2 nanocomposite as a promising visible-light-active photocatalyst for the conversion of carbon dioxide. *Nanoscale Res. Lett., 8*(1): 1-9.

Tan, L. L., Chai, S. P., and Mohamed, A. R. (2012). Synthesis and Applications of Graphene‐Based TiO_2 Photocatalysts. *Chem. Sus. Chem., 5*(10): 1868-1882.

Tang, B., and Hu, G. (2012). Two kinds of graphene-based composites for photoanode applying in dye-sensitized solar cell. *Journal of Power Sources, 220*: 95-102.

Tang, B., Hu, G., Gao, H., and Shi, Z. (2013). Three-dimensional graphene network assisted high performance dye sensitized solar cells. *Journal of Power Sources, 234*: 60-68.

Tang, H., Prasad, K., Sanjines, R., Schmid, P., and Levy, F. (1994). Electrical and optical properties of TiO_2 anatase thin films. *Journal of Applied Physics, 75*(4): 2042-2047.

Tang, J., and Gomez, A. (2015). Control of the mesoporous structure of dye-sensitized solar cells with electrospray deposition. *Journal of Materials Chemistry A, 3*(15): 7830-7839.

Tang, Y.-B., Lee, C.-S., Xu, J., Liu, Z.-T., Chen, Z.-H., He, Z., Cao, Y.-L., Yuan, G., Song, H., and Chen, L. (2010). Incorporation of graphenes in nanostructured TiO_2 films via molecular grafting for dye-sensitized solar cell application. *Acs Nano, 4*(6): 3482-3488.

Thakur, S., and Karak, N. (2012). Green reduction of graphene oxide by aqueous phytoextracts. *Carbon, 50*(14): 5331-5339.

Thema, F., Moloto, M., Dikio, E., Nyangiwe, N., Kotsedi, L., Maaza, M., and Khenfouch, M. (2012). Synthesis and characterization of graphene thin films by chemical reduction of exfoliated and intercalated graphite oxide. *Journal of chemistry, 2013*.

Thien, G. S., Omar, F. S., Blya, N. I. S. A., Chiu, W. S., Lim, H. N., Yousefi, R., Sheini, F.-J., and Huang, N. M. (2014). Improved Synthesis of Reduced Graphene Oxide-Titanium Dioxide Composite with Highly Exposed 001 Facets and Its Photoelectrochemical Response. *International Journal of Photoenergy, 2014*.

Titelman, G., Gelman, V., Bron, S., Khalfin, R., Cohen, Y., and Bianco-Peled, H. (2005). Characteristics and microstructure of aqueous colloidal dispersions of graphite oxide. *Carbon, 43*(3): 641-649.

TRIBUTSCH, H. (1972). Reaction of excited chlorophyll molecules at electrodes and in photosynthesis. *Photochemistry and Photobiology, 16*(4): 261-269.

Tributsch, H., and Calvin, M. (1971). Electrochemistry of Excited Molecules: Photo‐Electrochemical Reactions of Chlorophylls. *Photochemistry and Photobiology, 14*(2): 95-112.

Tritt, T. M., Böttner, H., and Chen, L. (2008). Thermoelectrics: Direct solar thermal energy conversion. *MRS bulletin, 33*(04): 366-368.

Tryba, B., Morawski, A., and Inagaki, M. (2003). Application of TiO_2-mounted activated carbon to the removal of phenol from water. *Applied Catalysis B: Environmental, 41*(4): 427-433.

Tsai, T.-H., Chiou, S.-C., and Chen, S.-M. (2011). Enhancement of dye-sensitized solar cells by using graphene-TiO_2 composites as photoelectrochemical working electrode. *Int. J. Electrochem. Sci, 6*(8): 3333-3343.

Umrao, S., Abraham, S., Theil, F., Pandey, S., Ciobota, V., Shukla, P., Rupp, C. J., Chakraborty, S., Ahuja, R., and Popp, J. (2014a). A possible mechanism for the emergence of an additional band gap due to a Ti–O–C bond in the TiO_2–graphene hybrid system for enhanced photodegradation of methylene blue under visible light. *RSC Advances, 4*(104): 59890-59901.

Umrao, S., Abraham, S., Theil, F., Pandey, S., Ciobota, V., Shukla, P. K., Rupp, C. J., Chakraborty, S., Ahuja, R., Popp, J., Dietzek, B., and Srivastava, A. (2014b). A possible mechanism for the emergence of an additional band gap due to a Ti-O-C bond in the

TiO_2-graphene hybrid system for enhanced photodegradation of methylene blue under visible light. *RSC Adv., 4*(104): 59890-59901. doi:10.1039/C4RA10572A

Valencia, S., Marín, J. M., and Restrepo, G. (2010). Study of the bandgap of synthesized titanium dioxide nanoparticules using the sol-gel method and a hydrothermal treatment. *Open Materials Science Journal, 4*(1): 9-14.

Van de Lagemaat, J., Park, N.-G., and Frank, A. (2000). Influence of electrical potential distribution, charge transport, and recombination on the photopotential and photocurrent conversion efficiency of dye-sensitized nanocrystalline TiO_2 solar cells: a study by electrical impedance and optical modulation techniques. *J. Phys. Chem. B, 104*(9): 2044-2052.

Velasco-Soto, M., Pérez-García, S., Alvarez-Quintana, J., Cao, Y., Nyborg, L., and Licea-Jiménez, L. (2015). Selective band gap manipulation of graphene oxide by its reduction with mild reagents. *Carbon, 93*: 967-973.

Vicarelli, L., Heerema, S. J., Dekker, C., and Zandbergen, H. W. (2015). Controlling defects in graphene for optimizing the electrical properties of graphene nanodevices. *ACS nano, 9*(4): 3428.

W Lai, C., W Low, F., W Chong, S., PP Wong, C., Siddick, B. M., Siti, Z., C Juan, J., and B Abdul Hamid, S. (2015). An Overview: Recent Development of Titanium Dioxide Loaded Graphene Nanocomposite Film for Solar Application. *Current Organic Chemistry, 19*(19): 1882-1895.

Waita, S. M., Aduda, B. O., Mwabora, J. M., Granqvist, C. G., Lindquist, S.-E., Niklasson, G. A., Hagfeldt, A., and Boschloo, G. (2007). Electron transport and recombination in dye sensitized solar cells fabricated from obliquely sputter deposited and thermally annealed TiO_2 films. *Journal of Electroanalytical Chemistry, 605*(2): 151-156.

Wang, B., Zhang, G., Leng, X., Sun, Z., and Zheng, S. (2015). Characterization and improved solar light activity of vanadium doped TiO_2/diatomite hybrid catalysts. *Journal of hazardous materials, 285*: 212-220.

Wang, D., Choi, D., Li, J., Yang, Z., Nie, Z., Kou, R., Hu, D., Wang, C., Saraf, L. V., and Zhang, J. (2009a). Self-assembled TiO_2–graphene hybrid nanostructures for enhanced Li-ion insertion. *ACS nano, 3*(4): 907-914.

Wang, D., Choi, D., Li, J., Yang, Z., Nie, Z., Kou, R., Hu, D., Wang, C., Saraf, L. V., and Zhang, J. (2009b). Self-assembled TiO_2–graphene hybrid nanostructures for enhanced Li-ion insertion. *ACS Nano., 3*(4): 907-914.

Wang, D., Kou, R., Choi, D., Yang, Z., Nie, Z., Li, J., Saraf, L. V., Hu, D., Zhang, J., and Graff, G. L. (2010). Ternary self-assembly of ordered metal oxide− graphene nanocomposites for electrochemical energy storage. *ACS nano, 4*(3): 1587-1595.

Wang, D., Li, X., Chen, J., and Tao, X. (2012a). Enhanced photoelectrocatalytic activity of reduced graphene oxide/TiO_2 composite films for dye degradation. *Chemical engineering journal, 198*: 547-554.

Wang, F., and Zhang, K. (2011). Reduced graphene oxide–TiO_2 nanocomposite with high photocatalytic activity for the degradation of rhodamine B. *Journal of Molecular Catalysis A: Chemical, 345*(1): 101-107.

Wang, H., Zhang, X., Su, Y., Yu, H., Chen, S., Quan, X., and Yang, F. (2014a). Photoelectrocatalytic oxidation of aqueous ammonia using TiO_2 nanotube arrays. *Applied Surface Science, 311*: 851-857.

Wang, P., Ao, Y., Wang, C., Hou, J., and Qian, J. (2012b). Enhanced photoelectrocatalytic activity for dye degradation by graphene–titania composite film electrodes. *Journal of hazardous materials, 223*: 79-83.

Wang, P., Wang, J., Wang, X., Yu, H., Yu, J., Lei, M., and Wang, Y. (2013). One-step synthesis of easy-recycling TiO_2-rGO nanocomposite photocatalysts with enhanced photocatalytic activity. *Appl. Catal. B: Env., 132*: 452-459.

Wang, P., Zhai, Y., Wang, D., and Dong, S. (2011a). Synthesis of reduced graphene oxide-anatase TiO_2 nanocomposite and its improved photo-induced charge transfer properties. *Nanoscale, 3*(4): 1640-1645.

Wang, Q., Ito, S., Grätzel, M., Fabregat-Santiago, F., Mora-Sero, I., Bisquert, J., Bessho, T., and Imai, H. (2006a). Characteristics of high efficiency dye-sensitized solar cells. *J. Phys. Chem. B, 110*(50): 25210-25221.

Wang, Q., Ito, S., Grätzel, M., Fabregat-Santiago, F., Mora-Sero, I., Bisquert, J., Bessho, T., and Imai, H. (2006b). Characteristics of high efficiency dye-sensitized solar cells. *The Journal of Physical Chemistry B, 110*(50): 25210-25221.

Wang, X., Zhi, L., and Müllen, K. (2008a). Transparent, conductive graphene electrodes for dye-sensitized solar cells. *Nano Lett., 8*(1): 323-327.

Wang, Y., Li, Z., He, Y., Li, F., Liu, X., and Yang, J. (2014b). Low-temperature solvothermal synthesis of graphene–TiO_2 nanocomposite and its photocatalytic activity for dye degradation. *Materials Letters, 134*: 115-118.

Wang, Y., Shi, Z., and Yin, J. (2011b). Facile synthesis of soluble graphene via a green reduction of graphene oxide in tea solution and its biocomposites. *ACS Appl. Mater. Interfaces, 3*(4): 1127-1133.

Wang, Y., Shi, Z., and Yin, J. (2011c). Facile synthesis of soluble graphene via a green reduction of graphene oxide in tea solution and its biocomposites. *ACS applied materials & interfaces, 3*(4): 1127-1133.

Wang, Y., Zhang, Z., Zhu, Y., Li, Z., Vajtai, R., Ci, L., and Ajayan, P. M. (2008b). Nanostructured VO_2 photocatalysts for hydrogen production. *Acs Nano, 2*(7): 1492-1496.

Warner, J. H., Schaffel, F., Rummeli, M., and Bachmatiuk, A. (2012). *Graphene: fundamentals and emergent applications*: Newnes.

Wei, L., Chen, S., Yang, Y., Dong, Y., Song, W., and Fan, R. (2016). Reduced graphene oxide modified TiO_2 semiconductor materials for dye-sensitized solar cells. *RSC Advances, 6*(103): 100866-100875.

Wei, Z., Yao, Y., Huang, T., and Yu, A. (2011). Solvothermal growth of Well-Aligned TiO_2 Nanowire Arrays for Dye-Sensitized Solar Cell: Dependence of morphology and vertical orientation upon substrate pretreatment. *Int. J. Electrochem. Sci, 6*: 1871-1879.

Williams, G., and Kamat, P. V. (2009). Graphene− Semiconductor Nanocomposites: Excited-State Interactions between ZnO Nanoparticles and Graphene Oxide†. *Langmuir, 25*(24): 13869-13873.

Williams, G., Seger, B., and Kamat, P. V. (2008). TiO2-graphene nanocomposites. UV-assisted photocatalytic reduction of graphene oxide. *ACS Nano., 2*(7): 1487-1491.

Woan, K., Pyrgiotakis, G., and Sigmund, W. (2009). Photocatalytic Carbon ‐ Nanotube ‐ TiO_2 Composites. *Advanced Materials, 21*(21): 2233-2239.

Wojtoniszak, M., Chen, X., Kalenczuk, R. J., Wajda, A., Łapczuk, J., Kurzewski, M., Drozdzik, M., Chu, P. K., and Borowiak-Palen, E. (2012a). Synthesis, dispersion, and cytocompatibility of graphene oxide and reduced graphene oxide. *Colloids and Surfaces B: Biointerfaces, 89*: 79-85.

Wojtoniszak, M., Zielinska, B., Chen, X., Kalenczuk, R. J., and Borowiak-Palen, E. (2012b). Synthesis and photocatalytic performance of TiO_2 nanospheres–graphene nanocomposite under visible and UV light irradiation. *Journal of Materials Science, 47*(7): 3185-3190.

Wu, J., Wang, J., Lin, J., Xiao, Y., Yue, G., Huang, M., Lan, Z., Huang, Y., Fan, L., and Yin, S. (2013). Dual functions of YF3: Eu^{3+} for improving photovoltaic performance of dye-sensitized solar cells. *Scientific reports, 3*.

Wulff, J., Moffatt, W., Pearsall, G., Brophy, J., Rose, R., Hayden, H., Shepard, L., and Klerer, J. (1967). The structure and properties of materials. *Journal of The Electrochemical Society, 114*(9): 243C-250C.

Xiang, Q., Yu, J., and Jaroniec, M. (2011a). Enhanced photocatalytic H_2-production activity of graphene-modified titania nanosheets. *Nanoscale, 3*(9): 3670-3678.

Xiang, Q., Yu, J., and Jaroniec, M. (2011b). Preparation and enhanced visible-light photocatalytic H_2-production activity of graphene/C_3N_4 composites. *The Journal of Physical Chemistry C, 115*(15): 7355-7363.

Xiang, Q., Yu, J., and Jaroniec, M. (2012a). Graphene-based semiconductor photocatalysts. *Chemical Society Reviews, 41*(2): 782-796.

Xiang, Q., Yu, J., and Jaroniec, M. (2012b). Synergetic effect of MoS_2 and graphene as cocatalysts for enhanced photocatalytic H2 production activity of TiO_2 nanoparticles. *Journal of the American Chemical Society, 134*(15): 6575-6578.

Xiang, Z., Zhou, X., Wan, G., Zhang, G., and Cao, D. (2014). Improving Energy Conversion Efficiency of Dye-Sensitized Solar Cells by Modifying TiO2 Photoanodes with Nitrogen-Reduced Graphene Oxide. *ACS Sust. Chem. Eng., 2*(5): 1234-1240.

Xing, H., Wen, W., and Wu, J.-M. (2016). One-pot low-temperature synthesis of TiO_2 nanowire/rGO composites with enhanced photocatalytic activity. *RSC Advances, 6*(96): 94092-94097.

Xu, C., Wang, X., and Zhu, J. (2008). Graphene− metal particle nanocomposites. *The Journal of Physical Chemistry C, 112*(50): 19841-19845.

Xu, Z., Yin, M., Sun, J., Ding, G., Lu, L., Chang, P., Chen, X., and Li, D. (2016). 3D periodic multiscale TiO_2 architecture: a platform decorated with graphene quantum dots for enhanced photoelectrochemical water splitting. *Nanotechnology, 27*(11): 115401.

Yamasaki, A. (2003). An overview of CO_2 mitigation options for global warming—emphasizing CO_2 sequestration options. *Journal of Chemical Engineering of Japan, 36*(4): 361-375.

Yanagisawa, K., and Ovenstone, J. (1999). Crystallization of anatase from amorphous titania using the hydrothermal technique: effects of starting material and temperature. *The Journal of Physical Chemistry B, 103*(37): 7781-7787.

Yang, H., Guo, L., Yan, W., and Liu, H. (2006). A novel composite photocatalyst for water splitting hydrogen production. *Journal of Power Sources, 159*(2): 1305-1309.

Yang, N., Zhai, J., Wang, D., Chen, Y., and Jiang, L. (2010a). Two-dimensional graphene bridges enhanced photoinduced charge transport in dye-sensitized solar cells. *ACS nano, 4*(2): 887-894.

Yang, S.-T., Chen, S., Chang, Y., Cao, A., Liu, Y., and Wang, H. (2011). Removal of methylene blue from aqueous solution by graphene oxide. *Journal of colloid and interface science, 359*(1): 24-29.

Yang, S., Feng, X., Ivanovici, S., and Müllen, K. (2010b). Fabrication of graphene‐encapsulated oxide nanoparticles: towards high‐performance anode materials for lithium storage. *Angewandte Chemie International Edition, 49*(45): 8408-8411.

Yang, W., Chen, G., Shi, Z., Liu, C.-C., Zhang, L., Xie, G., Cheng, M., Wang, D., Yang, R., and Shi, D. (2013). Epitaxial growth of single-domain graphene on hexagonal boron nitride. *Nature materials, 12*(9): 792-797.

Yang, W. S., Noh, J. H., Jeon, N. J., Kim, Y. C., Ryu, S., Seo, J., and Seok, S. I. (2015). High-performance photovoltaic perovskite layers fabricated through intramolecular exchange. *Science, 348*(6240): 1234-1237.

Yao, N., Huang, J., Fu, K., Deng, X., Ding, M., Zhang, S., and Xu, X. (2016). Improving the photovoltaic performance of dye sensitized solar cells based on a hierarchical structure with up/down converters. *RSC Advances, 6*(14): 11880-11887.

Yao, Z., Jia, F., Tian, S., Li, C., Jiang, Z., and Bai, X. (2010). Microporous Ni-doped TiO_2 film photocatalyst by plasma electrolytic oxidation. *ACS applied materials & interfaces, 2*(9): 2617-2622.

Yeh, M. H., Lin, L. Y., Chang, L. Y., Leu, Y. A., Cheng, W. Y., Lin, J. J., and Ho, K. C. (2014). Dye‐Sensitized Solar Cells with Reduced Graphene Oxide as the Counter Electrode Prepared by a Green Photothermal Reduction Process. *Chem. Phys. Chem., 15*(6): 1175-1181.

Yella, A., Lee, H.-W., Tsao, H. N., Yi, C., Chandiran, A. K., Nazeeruddin, M. K., Diau, E. W.-G., Yeh, C.-Y., Zakeeruddin, S. M., and Grätzel, M. (2011). Porphyrin-sensitized solar cells with cobalt (II/III)–based redox electrolyte exceed 12 percent efficiency. *Science, 334*(6056): 629.

Yen, C.-C., Wang, D.-Y., Chang, L.-S., Shih, M.-H., and Shih, H. C. (2011). Improving conversion efficiency of dye-sensitized solar cells by metal plasma ion implantation of ruthenium ions. *Thin Solid Films, 519*(15): 4717-4720.

Yen, Y.-C., Chen, P.-H., Chen, J.-Z., Chen, J.-A., and Lin, K.-J. (2015). Plasmon-induced efficiency enhancement on dye-sensitized solar cell by a 3D TNW-AuNP layer. *ACS applied materials & interfaces, 7*(3): 1892-1898.

Yin, Z., Zhu, J., He, Q., Cao, X., Tan, C., Chen, H., Yan, Q., and Zhang, H. (2014). Graphene‐Based Materials for Solar Cell Applications. *Adv. Energy Mater., 4*(1).

Yoo, S., Akbar, S. A., and Sandhage, K. H. (2004). Nanocarving of titania (TiO_2): a novel approach for fabricating chemical sensing platform. *Ceramics International, 30*(7): 1121-1126.

Yu, H., Xiao, P., Tian, J., Wang, F., and Yu, J. (2016a). Phenylamine-Functionalized rGO/TiO_2 Photocatalysts: Spatially Separated Adsorption Sites and Tunable Photocatalytic Selectivity. *ACS Applied Materials & Interfaces, 8*(43): 29470-29477.

Yu, H., Zhang, B., Bulin, C., Li, R., and Xing, R. (2016b). High-efficient Synthesis of Graphene Oxide Based on Improved Hummers Method. *Scientific reports, 6*.

Yuan, S., Tang, Q., Hu, B., Ma, C., Duan, J., and He, B. (2014). Efficient quasi-solid-state dye-sensitized solar cells from graphene incorporated conducting gel electrolytes. *Journal of Materials Chemistry A, 2*(8): 2814-2821.

Yum, J.-H., Baranoff, E., Wenger, S., Nazeeruddin, M. K., and Grätzel, M. (2011). Panchromatic engineering for dye-sensitized solar cells. *Energy & Environmental Science, 4*(3): 842-857.

Yusuf, S., Azzahari, A., Selvanathan, V., Yahya, R., Careem, M., and Arof, A. (2017). Improvement of N-phthaloylchitosan based gel polymer electrolyte in dye-sensitized solar cells using a binary salt system. *Carbohydrate Polymers, 157*: 938-944.

Zaaba, N., Foo, K., Hashim, U., Tan, S., Liu, W.-W., and Voon, C. (2017). Synthesis of Graphene Oxide using Modified Hummers Method: Solvent Influence. *Procedia Engineering, 184*: 469-477.

Zallen, R., and Moret, M. (2006). The optical absorption edge of brookite TiO_2. *Solid State Communications, 137*(3): 154-157.

Zang, X., and Lin, L. (2014). Graphene synthesis via droplet CVD AND its photonic applications. *Micro Electro Mechanical Systems (MEMS), 2014 IEEE 27th International Conference on*: 486-489.

Zang, X., Zhou, Q., Chang, J., Teh, K. S., Wei, M., Zettl, A., and Lin, L. (2017). Synthesis of Single‐Layer Graphene on Nickel Using a Droplet CVD Process. *Advanced Materials Interfaces, 4*(4).

Zeng, F., Sun, Z., Sang, X., Diamond, D., Lau, K. T., Liu, X., and Su, D. S. (2011). In situ one‐step electrochemical preparation of graphene oxide nanosheet‐modified electrodes for biosensors. *ChemSusChem, 4*(11): 1587-1591.

Zeng, Q., Li, H., Duan, H., Guo, Y., Liu, X., Zhang, Y., and Liu, H. (2015). A green method to prepare TiO_2/MWCNT nanocomposites with high photocatalytic activity and insights into the effect of heat treatment on photocatalytic activity. *RSC Advances, 5*(18): 13430-13436.

Zeng, W., Cao, Y., Bai, Y., Wang, Y., Shi, Y., Zhang, M., Wang, F., Pan, C., and Wang, P. (2010). Efficient dye-sensitized solar cells with an organic photosensitizer featuring orderly conjugated ethylenedioxythiophene and dithienosilole blocks. *Chemistry of Materials, 22*(5): 1915-1925.

Zhang, H., Lv, X., Li, Y., Wang, Y., and Li, J. (2009a). P25-graphene composite as a high performance photocatalyst. *ACS nano, 4*(1): 380-386.

Zhang, H., Lv, X., Li, Y., Wang, Y., and Li, J. (2009b). P25-graphene composite as a high performance photocatalyst. *ACS Nano., 4*(1): 380-386.

Zhang, H., Xu, P., Du, G., Chen, Z., Oh, K., Pan, D., and Jiao, Z. (2011a). A facile one-step synthesis of TiO_2/graphene composites for photodegradation of methyl orange. *Nano Research, 4*(3): 274-283.

Zhang, J., Pan, C., Fang, P., Wei, J., and Xiong, R. (2010a). Mo+ C codoped TiO_2 using thermal oxidation for enhancing photocatalytic activity. *ACS applied materials & interfaces, 2*(4): 1173-1176.

Zhang, Q., He, Y., Chen, X., Hu, D., Li, L., Yin, T., and Ji, L. (2011b). Structure and photocatalytic properties of TiO_2-graphene oxide intercalated composite. *Chinese Science Bulletin, 56*(3): 331-339.

Zhang, S., Deng, W., Pan, X., Jiao, H., Chen, D., Huang, H., Cui, Y., Xu, J., Feng, J., and Zhong, M. (2015). 335Watt world record P-type mono-crystalline module with 20.6% efficiency PERC solar cells. *Photovoltaic Specialist Conference (PVSC), 2015 IEEE 42nd*: 1-6.

Zhang, T., Zhang, D., and Shen, M. (2009c). A low-cost method for preliminary separation of reduced graphene oxide nanosheets. *Materials Letters, 63*(23): 2051-2054.

Zhang, X.-Y., Li, H.-P., Cui, X.-L., and Lin, Y. (2010b). Graphene/TiO_2 nanocomposites: synthesis, characterization and application in hydrogen evolution from water photocatalytic splitting. *J. Mater. Chem., 20*(14): 2801-2806.

Zhang, X.-Y., Li, H.-P., Cui, X.-L., and Lin, Y. (2010c). Graphene/TiO_2 nanocomposites: synthesis, characterization and application in hydrogen evolution from water photocatalytic splitting. *Journal of Materials Chemistry, 20*(14): 2801-2806.

Zhang, X., and Cui, X. (2012). Graphene/Semiconductor Nanocomposites: Preparation and Application for Photocatalytic Hydrogen Evolution.

Zhang, X., Sun, Y., Cui, X., and Jiang, Z. (2012a). A green and facile synthesis of TiO_2/graphene nanocomposites and their photocatalytic activity for hydrogen evolution. *international journal of hydrogen energy, 37*(1): 811-815.

Zhang, Y., Li, D., Tan, X., Zhang, B., Ruan, X., Liu, H., Pan, C., Liao, L., Zhai, T., and Bando, Y. (2013). High quality graphene sheets from graphene oxide by hot-pressing. *Carbon, 54*: 143-148.

Zhang, Y., and Pan, C. (2011). TiO_2/graphene composite from thermal reaction of graphene oxide and its photocatalytic activity in visible light. *Journal of Materials Science, 46*(8): 2622-2626.

Zhang, Y., Tang, Z.-R., Fu, X., and Xu, Y.-J. (2011c). Engineering the unique 2D mat of graphene to achieve graphene-TiO_2 nanocomposite for photocatalytic selective transformation: what advantage does graphene have over its forebear carbon nanotube? *ACS nano, 5*(9): 7426-7435.

Zhang, Y., Wang, C., Yuan, Z., Zhang, L., and Yin, L. (2017a). Reduced Graphene Oxide Wrapped Mesoporous Hierarchical TiO_2 ‐ CdS as a Photoanode for High ‐ Performance Dye ‐ Sensitized Solar Cells. *European Journal of Inorganic Chemistry, 2017*(16): 2281-2288.

Zhang, Y., Wang, C., Yuan, Z., Zhang, L., and Yin, L. (2017b). Reduced Graphene Oxide Wrapped Mesoporous Hierarchical TiO_2 ‐ CdS as a Photoanode for High ‐ Performance Dye ‐ Sensitized Solar Cells. *European Journal of Inorganic Chemistry*.

Zhang, Y., Zhang, N., Tang, Z.-R., and Xu, Y.-J. (2012b). Improving the photocatalytic performance of graphene–TiO_2 nanocomposites via a combined strategy of decreasing defects of graphene and increasing interfacial contact. *Physical Chemistry Chemical Physics, 14*(25): 9167-9175.

Zhao, J., Wu, J., Yu, F., Zhang, X., Lan, Z., and Lin, J. (2013). Improving the photovoltaic performance of cadmium sulfide quantum dots-sensitized solar cell by graphene/titania photoanode. *Electrochimica Acta, 96*: 110-116.

Zhao, L., Chen, X., Wang, X., Zhang, Y., Wei, W., Sun, Y., Antonietti, M., and Titirici, M. M. (2010). One ‐ Step Solvothermal Synthesis of a Carbon@ TiO_2 Dyade Structure Effectively Promoting Visible ‐ Light Photocatalysis. *Advanced Materials, 22*(30): 3317-3321.

Zheng, Q., Li, Z., Yang, J., and Kim, J.-K. (2014). Graphene oxide-based transparent conductive films. *Progress in Materials Science, 64*: 200-247.

Zhou, X., and Liu, Z. (2010). A scalable, solution-phase processing route to graphene oxide and graphene ultralarge sheets. *Chemical Communications, 46*(15): 2611-2613.

Zhu, M., Li, X., Liu, W., and Cui, Y. (2014). An investigation on the photoelectrochemical properties of dye-sensitized solar cells based on graphene–TiO_2 composite photoanodes. *Journal of Power Sources, 262*: 349-355.

Zhu, P., Nair, A. S., Shengjie, P., Shengyuan, Y., and Ramakrishna, S. (2012). Facile fabrication of TiO_2–graphene composite with enhanced photovoltaic and photocatalytic properties by electrospinning. *ACS applied materials & interfaces, 4*(2): 581-585.

Zhu, P., Shen, M., Xiao, S., and Zhang, D. (2011). Experimental study on the reducibility of graphene oxide by hydrazine hydrate. *Physica B: Condensed Matter, 406*(3): 498-502.

Zhu, Y., Murali, S., Cai, W., Li, X., Suk, J. W., Potts, J. R., and Ruoff, R. S. (2010). Graphene and graphene oxide: synthesis, properties, and applications. *Advanced materials, 22*(35): 3906-3924.

Zhuang, S., Xu, X., Feng, B., Hu, J., Pang, Y., Zhou, G., Tong, L., and Zhou, Y. (2013). Photogenerated Carriers Transfer in Dye–Graphene–SnO_2 Composites for Highly Efficient Visible-Light Photocatalysis. *ACS applied materials & interfaces*, *6*(1): 613-621.

LIST OF PUBLICATIONS AND PAPERS PRESENTED

List of Book Chapter:

1. Chin Wei Lai*, Foo Wah Low, Siti Zubaidah Binti Mohamed Siddick, Joon Ching Juan, Graphene/TiO_2 Nanocomposites: Synthesis Routes, Characterization, and Solar Cell Applications, *Advanced Materials Book Series*. 2018, Pp. 1-49.

List of Publications:

1. Foo Wah Low, Chin Wei Lai, Kian Mun Lee, Joon Ching Juan (2018). Enhance of TiO_2 dopants incorporated reduced graphene oxide via RF magnetron sputtering for efficient dye-sensitised solar cells. *Rare Metals*. 1-17. DOI : 10.1007/s12598-018-1064-4
2. Foo Wah Low, Chin Wei Lai, Sharifah Bee Abd Hamid (2018). One-step hydrothermal synthesis of titanium dioxide decorated on reduced graphene oxide for dye-sensitised solar cells application, Int. J. Nanotechnol., Vol. 15, Nos. 1/2/3, 2018. DOI: https://doi.org/10.1504/IJNT.2018.089561
3. Foo Wah Low, Chin Wei Lai (2017). Recent developments of graphene-TiO_2 composite nanomaterials as efficient photoelectrodes in dye-sensitized solar cells: A review. Renewable and Sustainable Energy Reviews, 82(1), 103-125. DOI: https://doi.org/10.1016/j.rser.2017.09.024
4. Foo Wah Low, Chin Wei & Sharifah Bee Abd Hamid (2016). Surface Modification of Reduced Graphene Oxide Film by Ti Ion Implantation Technique for High Dye-Sensitized Solar Cells Performance. Ceramics International, *43*(1), 625-633. DOI: http://dx.doi.org/10.1016/j.ceramint.2016.09.205
5. Foo Wah Low, Chin Wei Lai & Sharifah Bee Abd Hamid (2016). Study of Reduced Graphene Oxide Film Incorporated of TiO_2 Species for Efficient Visible Light Driven Dye-Sensitized Solar Cell. *Journal of Materials Science: Materials in Electronics (JMSE)*, 1-18. DOI: 10.1007/s10854-016-5993-0

6. Low, F. W., Lai, C. W., & Hamid, S. B. A. (2015). Easy preparation of ultrathin reduced graphene oxide sheets at a high stirring speed. *Ceramics International*, *41*(4), 5798-5806. DOI: http://dx.doi.org/10.1016/j.ceramint.2015.01.008
7. W Lai, C., W Low, F., W Chong, S., PP Wong, C., Siddick, B. M., Siti, Z., & B Abdul Hamid, S. (2015). An Overview: Recent Development of Titanium Dioxide Loaded Graphene Nanocomposite Film for Solar Application. *Current Organic Chemistry*, *19*(19), 1882-1895. DOI: 10.2174/1385272819666150605230240
8. Chong, S. W., Lai, C. W., Abd Hamid, S. B., Low, F. W., & Liu, W. W. (2015). Simple preparation of exfoliated graphene oxide sheets via simplified hummer's method. In *Advanced Materials Research* (Vol. 1109, pp. 390-394). DOI: 10.4028/www.scientific.net/AMR.1109.390
9. Low, F. W., Lai, C. W., & Abd Hamid, S. B. (2015). Facile Synthesis of High Quality Graphene Oxide from Graphite Flakes Using Improved Hummer's Technique. *Journal of Nanoscience and Nanotechnology*, *15*(9), 6769-6773. DOI: 10.1166/jnn.2015.10903
10. Low, F. W., Lai, C. W., Abd Hamid, S. B., Chong, S. W., & Liu, W. W. (2015). High Yield Preparation of Graphene Oxide Film Using Improved Hummer's Technique for Current-Voltage Characteristic. In *Advanced Materials Research* (Vol. 1109, pp. 385-389). DOI: 10.4028/www.scientific.net/AMR.1109.385